UNIVERSITY OF SOUTHAMPTON

FACULTY OF ENGINEERING, SCIENCE AND
MATHEMATICS
SCHOOL OF ELECTRONICS AND COMPUTER SCIENCE

THE DESIGN AND FABRICATION OF A MAGNETICALLY ACTUATED MICROFLUIDIC DISPENSING DEVICE

by Benjamin Husband

A thesis submitted for the degree of Doctor of Philosophy

July 2007

UNIVERSITY OF SOUTHAMPTON

ABSTRACT

FACULTY OF ENGINEERING, SCIENCE AND MATHEMATICS
SCHOOL OF ELECTRONICS AND COMPUTER SCIENCE

Doctor of Philosophy

THE DESIGN AND FABRICATION OF A MAGNETICALLY ACTUATED MICROFLUIDIC DISPENSING DEVICE

by Benjamin Husband

Examples of microfluidic and nanofluidic devices for biological and chemical fluid analysis, processing, and manipulation have increased in number in the last twenty years. Integrated microfluidic structures, called Lab-on-a-chip have been fabricated and utilised. A major limitation of existing fluidic structures is that methods for introducing nanolitre volumes of reagents are not available in an integrated format. There are currently only a few workable devices as 'stand alone' components. The aim of this thesis is to investigate the design, fabrication technique and testing methods for a novel dispensing device, targeted for pipetting precise volumes of fluid into integrated fluidic devices.

A novel technique to displace fluid, in the nanolitre volume range, using a paramagnetic bead plug was proposed and subsequently demonstrated. Actuation of the dispensing technique is achieved using (i) a moving permanent magnet and (ii) sequentially actuated electromagnets. The use of magnetically actuated paramagnetic bead plugs of different sizes in fluidic channels, was proven to provide an approach to displace nanolitre volumes of fluid.

Following this demonstration, an integrated microfabricated silicon device was designed and fabricated. The integrated microdevice includes thick gold microcoils and a fluidic channel containing the paramagnetic beads. The transport and separation of paramagnetic beads was demonstrated and quantified.

The fluid displacement technique investigated here is compact and simple to produce and the device has no moving parts. It was shown to be possible to carry out repeatable dispensing, of variable volumes of fluid, using a reciprocating paramagnetic bead plug. This is the first practical demonstration of the pipetting of small volumes, within a fluidic channel, utilising paramagnetic beads as a plunger. An integrated silicon microdevice was fabricated to demonstrate the feasibility for fluid dispensing.

Contents

List of Figures

List of Tables

Acknowledgements

First and foremost I must thank my three supervisors: Dr. Tracy Melvin, who has guided me throughout my research and has been indispensable in completing my thesis. Prof. Alan Evans, who helped with my research, especially with the theoretical and fabrication parts and has continued to help me despite retiring over 12 months ago, Prof. James Wilkinson, who took over from Alan, and has played a key role in helping to complete my research and the writing of my thesis. In the later stages of the thesis writing, Dr Eleanor Tarbox was kind enough to go through my thesis and point out the difference between fowl and foul, which was an immense help. Thank you to the NSI group, who supported me from the start and then the ORC who allowed me to use their temporary facilities and office after the fire.

Thank you to everyone at Innos who were responsible for completing my fabrication, despite all the problems that came up. I must especially thank Janet, Nasser, Mir, Tony Blackburn, Tonny Coppens, Brian, Corry, Neil, Sally, Pejwaak, Jean and Mike, for there advice and help throughout my research. Plus the one person who was a good friend, a fellow PhD student and an Innos development engineer, Enrico. Not forgetting, that I could not have achieved such great gold plating if it was not for Gareth Lewis, who allowed me to use his plating system and taught me how to use it. Not forgetting the countless discussions about who had the best electrodeposited gold.

During the hard times after the fire, I was appreciative of any outside help that I received. Thanks to Hefin Griffiths, Colin Welch and Mike Stokeley at OPT, who did some very tricky DRIE for me, when it looked like no one else could do it. I will certainly recommend OPT plasma etchers where ever I go. Thank you to Prof. Bruce Hamilton for allowing me to use the wire bonding facilities at Manchester University. Also thanks to Mal who gave me a crash course in wire bonding, then allowed me to get on with it. Without this I would never have completed my fabrication. Thank you to Dr. Liz Tull from electrochemistry, who near the end of my research kept providing me with different ways to clean my microfluidic channels.

Thank you to my fellow students, who made it possible to drink so many cups of tea and take regular trips to the The Crown for 'crown in burgers', Tim, Andrew, Chris, Daniel, Mukhzeer, Chien and Hamish. Not forgetting the ones that got away, Lit Ho, Toma, Christoph and Manoucher. You have all made this time more enjoyable. I should also thank two project students, Jo Chambers and Ben Crundwell, for helping with the proof of concept experiments.

Finally, I must thank Julia who is the one person who kept telling me that it was all worth it and of course for always being there for me to go home to.

List of Symbols

a	-	Channel width $[m]$
A	-	Microchannel area $[m^2]$
α	-	Radius of coil $[m]$
b	-	Channel height $[m]$
B	-	Magnetic flux density $[T]$
β	-	Distance between two straight wires $[m]$
C	-	Piezo actuator capacitance $[F]$
C_p	-	Specific heat capacity $[J\ kg^{-1}\ K^{-1}]$
χ	-	Magnetic susceptibility $[-]$
D_h	-	Hydraulic diameter $[m]$
η	-	Dynamic viscosity $[Pa\ s]$
F_B	-	Bead force $[N]$
F_{cap}	-	Capillary force $[N]$
F_{sum}	-	Sum of all forces in the system $[N]$
γ	-	Fluid free surface energy $[J\ m^{-2}]$
Γ	-	Radius point from centre of circular fluidic channel $[m]$
h	-	Microchannel height $[m]$
H	-	Magnetic field $[A\ m^{-1}]$
I	-	Electrical current $[A]$
K	-	Head loss factor $[-]$
l	-	Length of wire $[m]$
L	-	Length of channel $[m]$
L_{coil}	-	Length of wrapped coil $[m]$
m	-	Magnetic dipole moment $[N\ m]$
M	-	Total volume magnetization $[A\ m^2\ Kg^{-1}]$
μ	-	Permeability $[N\ A^{-2}]$
μ_0	-	Permeability of free space $[N\ A^{-2}]$
μ_r	-	Relative permeability $[-]$
n	-	Wrapped coil turn density $[m^{-1}]$
N	-	Number of coil turns $[-]$
$\bar{\nu}$	-	Average fluid velocity $[m\ s^{-1}]$
ν_m	-	Maximum fluid velocity $[m\ s^{-1}]$
ν_r	-	Fluid velocity at radius r $[m\ s^{-1}]$
ν_y	-	Fluid velocity at distance y from surface $[m\ s^{-1}]$
ω	-	Contact angle of the fluid and the surface $[°]$
ω_{GLASS}	-	Contact angle of the fluid and the glass surface $[°]$
$\omega_{MODIFIED}$	-	Contact angle of the fluid and the modified surface $[°]$
p	-	Pressure in microchannel $[Pa]$
P	-	Power input to system $[W]$

P_{wet}	-	Microchannel wetted perimeter $[m]$
Q	-	Volume flow rate $[m^3\ s^{-1}]$
Q_{duct}	-	Volume flow rate in a duct $[m^3\ s^{-1}]$
r	-	Distance from point of interest to centre of current loop $[m]$
R	-	Radius of microchannel $[m]$
R_B	-	Radius of a bead $[m]$
R_{duct}	-	Radius of duct $[m]$
R_h	-	Hydraulic radius $[m]$
$R_{Transistor}$	-	Transistor resistance $[\Omega]$
Re	-	Reynolds number $[-]$
$\Re$	-	Resistance to flow $[Pa\ s\ m^{-3}]$
ρ	-	Mass density $[kg\ m^{-3}]$
σ	-	A point from the coil centre $[m]$
t	-	Time $[s]$
T	-	Temperature $[^\circ\ K]$
T_{Switch}	-	Switching delay of photovoltaic transistor circuit $[s]$
T_{ON}	-	Switching 'ON' delay of photovoltaic transistor $[s]$
T_{OFF}	-	Switching 'OFF' delay of photovoltaic transistor $[s]$
V	-	Volume $[m^3]$
V_B	-	Paramagnetic bead Volume $[m^3]$
w	-	Microchannel width $[m]$
x	-	Distance from the coil centre along the x-axis $[m]$
y	-	Distance from the fluidic channel surface $[m]$
z	-	Distance from the surface of a coil along the z-axis $[m]$

List of Abbreviations

ASE	-	Advanced silicon etch
dpi	-	Dots per inch
DIL	-	Dual in line
DNA	-	Deoxyribonucleic acid
DRIE	-	Deep reactive ion etching
EOF	-	Electroosmotic flow
FET	-	Field-effect transistor
FNA	-	Fuming nitric acid
HF	-	Hydrofluoric acid
KOH	-	Potassium hydroxide
LED	-	Light emitting diode
MEMS	-	Microelectromechanical systems
μTAS	-	Micro total analysis system
PCR	-	Polymerase chain reaction
PZT	-	Lead zirconate titanate
RIE	-	Reactive ion etching
SOI	-	Silicon on insulator
STS	-	Surface technology systems

Chapter 1

Introduction

1.1 Overview

The development of microsystems for the control and manipulation of fluids has increased dramatically in the last twenty years [1; 2; 3], driven by the realization of a complete lab-on-a-chip system. Such microsystems boast faster analysis and decreased sample / reagent volumes, allowing for massively parallel analysis to be carried out. This is due to the reduced size of the systems and the integration of actuation, sensing and optical elements [4; 5; 6]. Several types of microfluidic structure have been developed, including mixers [7; 8], pumps [3; 9], valves [10; 11; 12] and pipettors [13; 14]. These systems have been produced to handle both discrete droplets of fluid and continuous fluid flow.

With the advancement of high throughput, massively parallel methods used for analysis, there is an increasing need for fluidic technologies for dispensing microlitre and sub-microlitre volumes of fluid. Many bioanalytical assays require sequential addition of different bioreagents into bioanalysis solutions. The ability to precisely dispense fluid in defined volumes in a reproducible fashion is most desirable. A further desirable function of a dispensing device is the ability to adjust the volume of the dispensed fluid. The fluids and the contents (in particular fluids containing biomolecules) can be sensitive to thermal and mechanical stress, thus it is important that the structural and actuation approaches are appropriately designed to take this into account.

Fluid dispensing using microdevices is a mature technology, an example of this is the inkjet which was developed for printing [15; 16]. Inkjets provide a method to dispense *picolitre volumes of fluid as droplets into air*. In recent years, the inkjet system has been developed to provide pipetting devices for bioassays, typically with lead zirconate titanate (PZT) actuation [17; 18]. At present the key microdispenser systems rely upon either thermal or PZT actuated methods. The configuration of the two technologies are illustrated in Figure 1.1.

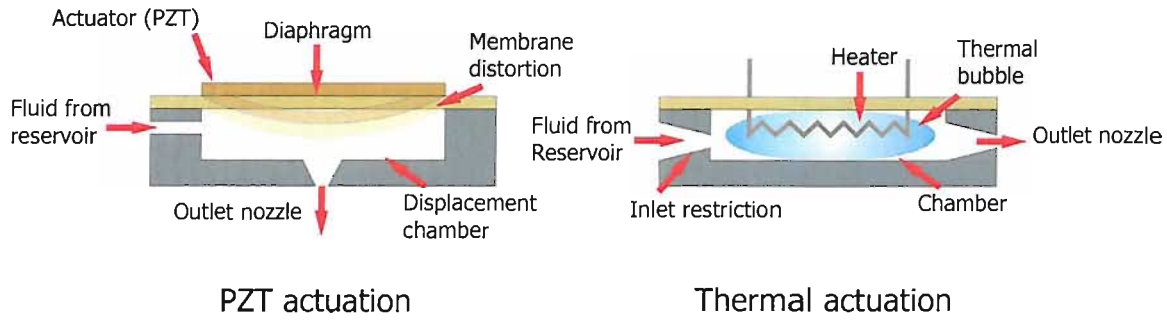

Figure 1.1: Configuration of PZT actuation and Thermal actuation showing the inlet, outlet nozzle, displacement chamber and actuator.

Inkjet print heads with piezo electric actuation consist of a diaphragm, which is electrically actuated with a PZT element to provide displacement. This displacement is used to apply a force to the fluid to push it out of the displacement chamber via a nozzle ($20 - 30\ \mu m$). The volume of fluid which is dispensed is dependant upon the volume displacement of the diaphragm, but also on the fluid viscosity, chamber size and the relative resistance to flow (back to the reservoir versus out of the nozzle). PZT actuated inkjet print heads tend to be more robust and the print heads can be reused by replacing the ink reservoir. The alternative thermal technique involves the use of integrated heating elements; to produce vapour bubbles within a displacement chamber thus fluid is forced out of the device via the nozzle. Typical devices can produce a temperature increase of up to $300°C$ in the dispensed fluid [19]. The thermal technique has a more limited lifetime due to a tendency of the ink to foul the displacement chamber; however an advantage is that the requirements on the fluid viscosity are less stringent. A major drawback of both PZT and thermal actuation techniques for dispensing solutions containing thermally sensitive biomolecules is the increase in the temperature of the fluid being dispensed.

Studies have shown that commercial PZT and thermal technologies can be used to print biomaterials, having been used to print mammalian and Eukaryotic cells, Deoxyribonucleic acid (DNA) and proteins [20; 21; 22; 23]. It is clear that there are biological systems that can withstand the thermal stress exerted by thermal inkjet printers; however such stress will not be suitable for printing all biomolecular solutions. Ideally these would be dispensed at low temperatures ($< 50°C$). PZT inkjet printing technology is less popular for 'bio-printing', because the viscosity of the required 'ink' is device dependent; printing of biomaterials can be problematic as, if the viscosity is too low, the fluid tends to leach out of the pipetting device [20]. This is an advantage of thermal inkjet technology because the viscosity of the ink used for printing is typically 2 $mPa\ s$. The viscosity and surface tension of the dispensed fluid will influence the release rate of the droplet, prevent the fluid from leeching out of the nozzle and finally prevent clogging of the nozzle [21]. The typical viscosity of the solutions used to print proteins and cells is 8 $mPa\ s$.

There are currently no methods to dispense miscible aliquots of fluid at the sub-microlitre scale into another miscible fluid. In particular, for fluid volumes between the nanolitre and microlitre range; so far the lower limit for fluid dispensing into a channel is two microlitre volumes for mixing [24]. Microfluidic T-junctions have been investigated to form droplets in a microchannel of two immiscible fluids (i.e. water droplets into oil) [25; 26]. Finally hydrodynamic focusing has been used to produce picolitre to nanolitre volume droplets within fluid filled microchannels [27], but similar to the previous T-junction examples the droplets are produced in an immiscible fluid. However all of these devices require constant fluid velocities of the two fluids to produce droplets in the immiscible fluid and therefore are not suitable for this application.

Devices similar to those used for inkjet applications (either thermal or PZT systems) could be adapted for dispensing into another miscible fluid and eventually be integrated within lab-on-a-chip devices. If a droplet is to be dispensed into a fluidic channel containing fluid, a positive fluidic pressure is required for the 'dispense actuation'. After the fluid is dispensed there must be minimal drawback of fluid into the pipetting device. To achieve this, the actuation method used must be such that there is a directional difference in the pressure applied to the fluid.

Most existing microfabricated dispensers are used to release droplets into air. The introduction of a fluid droplet into a 'closed' microfluidic system is more complicated. Once the droplet has been dispensed, a method for refilling has to be built into the system, which should not enable fluid to be drawn back into the pipettor. A scheme showing the appropriate sequence for achieving this is outlined in Figure 1.2:

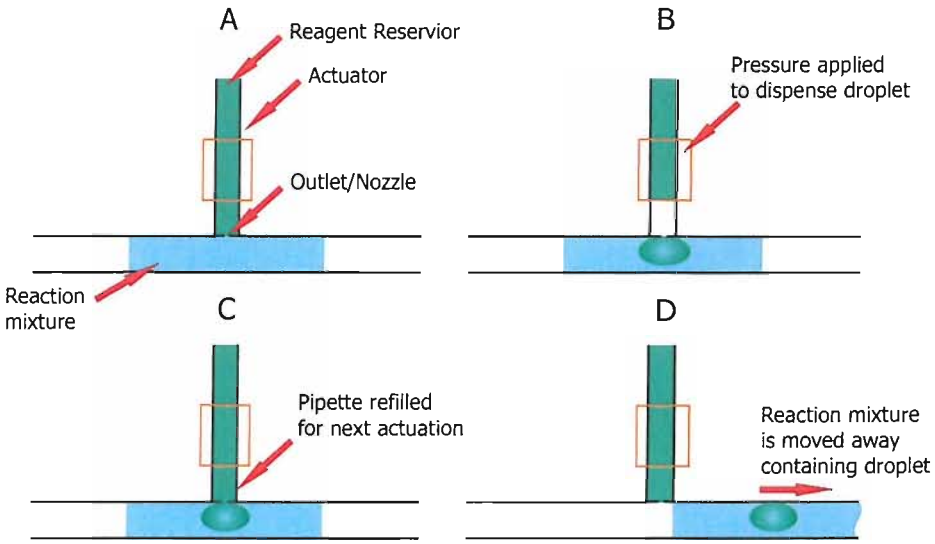

Figure 1.2: Illustration of the technique required to dispense sub-microlitre fluids into an adjacent microchannel. (A) starting position, (B) volume of fluid dispensed by pressure, (C) integrated pipette filled from reservoir and (D) reaction mixture moved away.

The steps are as follows:

(A) First a droplet of fluid (reagent) is introduced into an adjacent fluid (reaction mixture); this will require an actuation technique which can be used to apply a unidirectional pressure.

(B) This pressure will be used to dispense a droplet into the fluid.

(C) Once the pressure has been applied to introduce the droplet (reagent), fluid fills the reaction chamber from the reservoir without draw back.

(D) The fluid (reaction mixture) will then be transported away. There will be no back flow of fluid into the dispenser.

The program of research presented in this thesis addresses dispensing devices, which satisfy the requirements illustrated in Figure 1.2. An investigation was first carried out using a peristaltic micropump, which was designed to manipulate a $1\,\mu m$ droplet. The system was subsequently used to transport a droplet through a series of temperature

controlled chambers [28; 29]. The droplet was transported using air pressure, generated using a peristaltic micropump driven by piezo electric elements. Pressure is an alternative method for fluid dispensing, using an external or internal source to form and manipulate fluid droplets through a microfluidic system [30; 31]. The investigation of the micropump was done to gain a familiarity with microelectromechanical systems (MEMS) fluidic devices to gain 'hands on' experience whilst developing ideas for new approaches for fluid dispensing using the scheme of Figure 1.2. The practical studies demonstrated that the dispensing of variable volumes of fluid using the PZT actuation of a diaphragm, would require a highly complex alternative approach than that devised here.

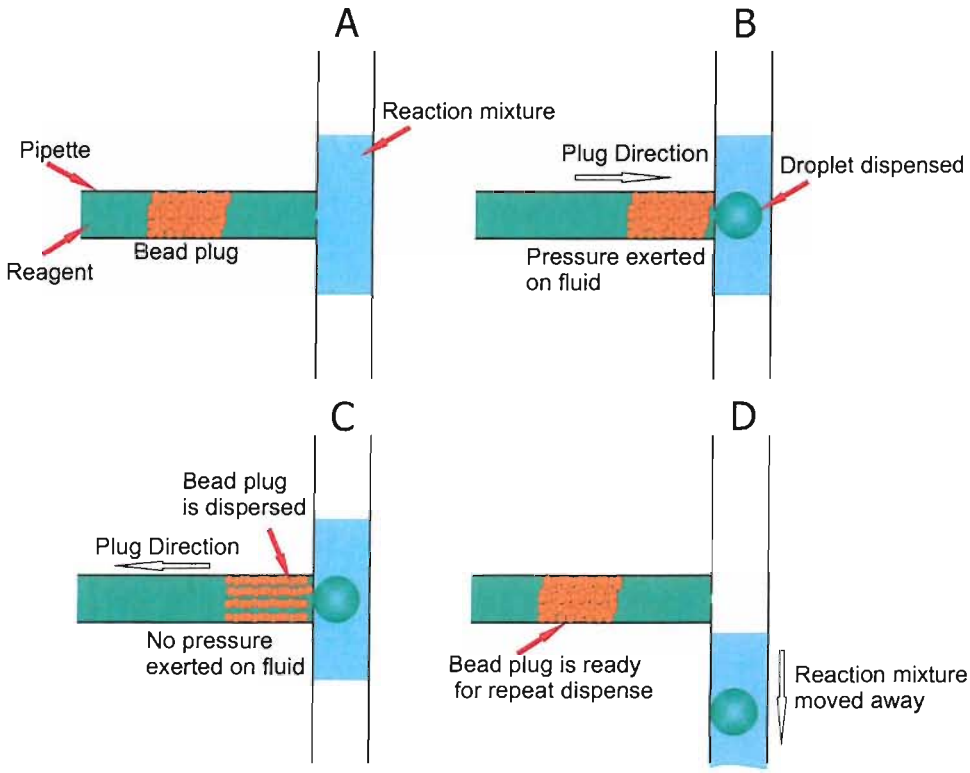

Figure 1.3: Proposed actuation principle to dispense defined volumes of fluid into an adjacent microchannel using a paramagnetic bead plug. (A) the bead plug is formed, (B) a volume of fluid is dispensed by pressure, (C)the bead plug is dispersed on return to the start position and (D) the reaction mixture is moved away, ready for a repeat dispense.

While magnetic pipetting devices have been produced using ferrofluid [32; 14], paramagnetic beads are used for the work of this thesis. These beads offer a biocompatible alternative to ferrofluid, which can also be moved through fluid, to obtain the requirements of the system outlined in Figure 1.2. The paramagnetic beads will be used to

form a plunger, which can be translated along a microchannel to displace fluid. Although paramagnetic beads have found significant applications [33; 34; 35], none have been proposed for pipetting. Various ways of using magnetic bead plugs for pipetting were investigated. As a result of investigations on plug dynamics a pipetting scheme was designed, as illustrated in Figure 1.3. Dispensing of a defined volume of fluid into a fluid filled channel requires a number of steps, whereby fluid is forced under pressure into a channel and then the pipettor is refilled by a process with zero or low pressure by the actuator.

The steps are as follows:

(A) First a bead plug is formed.

(B) Then the bead plug is moved toward the microchannel, resulting in pressure being exerted on the fluid, displacing and creating a droplet.

(C) The next step is the return of the paramagnetic beads to the start position. To achieve this, the bead plug is dispersed (decreased bead density for a given volume) such that it can be moved through the fluid. This results in a minimum displacement of the fluid in the channel back into the pipette.

(D) The beads are now repositioned for a repeat dispense.

This thesis details the research into a magnetically actuated MEMS device for the precise dispensing of nanolitre volumes of fluid, which satisfy the requirements given in Figure 1.2. The structure for the proposed dispenser will be produced using MEMS microfabrication techniques. This technology enables the precise fabrication of fluidic channels to be produced with micron and sub-micron dimensions [36]. The first proof of concept experiments using permanent magnets to move a paramagnetic bead plug to displace fluid are described, followed by the design and fabrication of an integrated microstructure containing microcoils. This is the first example of the application of microcoils for the pipetting of small volumes within a fluidic channel utilising paramagnetic beads as a plunger.

1.2 Project aim

The aim of this research is to produce an integrated pipetting device, which can be used to dispense nanolitre volumes of fluid, into another miscible fluid, in an accurate and repeatable fashion. It is essential that the fluid being dispensed is not affected by the actuation technique, in particular the dispensed fluid should not be exposed to high temperatures.

1.3 Summary of main achievements

During this research a number of original contributions have been made. These are outlined briefly here:

A novel actuation system for a peristaltic micropump was produced, which was used to successfully demonstrate air pumping using a peristaltic micropump and the dynamic deflection of the diaphragms of the peristaltic micropump was determined using a Michelson interferometer.

A novel technique to displace fluid, in the nanolitre range, using a paramagnetic bead plug was proposed and demonstrated, using a moving permanent magnet and sequentially actuated electromagnets. Paramagnetic bead plugs of different sizes were used to displace varying volumes of fluid, illustrating that this technique can be used to form a repeatable dispensing device.

An integrated microdevice was designed and fabricated, to utilise the paramagnetic bead plug technique. The integrated microdevice includes thick gold microcoils, with a minimum separation between the microcoils and the fluidic channel containing the paramagnetic beads. The transport and separation of paramagnetic beads was demonstrated and quantified using the integrated electromagnetic microdevice.

1.4 Thesis structure

Chapter 2 details the investigation of a peristaltic micropump, produced for displacing air to move a $1\mu m$ droplet of fluid through a series of temperature controlled chambers. The design and production of an actuation system, used to achieve air pumping, is described here. A Michelson interferometer was set up and used to measure the deflection of the micropump diaphragms to confirm the operation of the micropump.

Chapter 3 is a review of current technologies used for pipetting and dispensing using microdevices. Once it was decided that paramagnetic beads were going to be used to produce a pipetting device, a further review was carried out, in Chapter 4, to determine the current technology used for manipulating paramagnetic beads within microdevices.

A technique for fluid displacement was proposed, which is proven to work using proof of concept experiments, detailed in Chapter 5. The proposed paramagnetic bead plug technique is described and demonstrated; fluid is displaced using a paramagnetic bead actuated using a permanent magnet and a series of hand wound electromagnets.

The design and fabrication of an integrated microdevice for manipulating paramagnetic beads is detailed in Chapter 6. The first half of this chapter contains the design of the microcoils, including magnetostatic and thermal simulations. The second half of this chapter, from Section 6.3, contains the process development of the fabrication used to produce the electromagnetic microdevice which is evaluated in Chapter 7.

Chapter 7 details the test strategies that were used to determine the effectiveness of the integrated microdevice, for producing a pipette device with paramagnetic bead plugs. Two strategies were used to indirectly determine the magnetic field and the magnetic force on a paramagnetic bead, using the actuation of the microcoils on the integrated microdevice.

Chapter 8 contains the conclusion and overall achievements of this research, which is followed by suggestions for future work.

Chapter 2

Fluidic droplet control using a micropump

2.1 Introduction

The main focus of this thesis is the design, fabrication and testing of a novel fluid dispensing device. To gain experience in the fabrication and actuation of microfluidic devices, used for droplet manipulation, the actuation and testing of an in-house peristaltic micropump was completed. The micropump was designed and fabricated by Bu et al. [29]; Bu [37] as part of a Polymerase Chain Reaction (PCR) device. Part of this research includes the design of the actuation system which was used to achieve air pumping with the peristaltic micropump, where the results presented by Bu et al. [29]; Bu [37] for volume flow rate were obtained using this actuation system. An interferometer was set up and used to determine the dynamic deflection of the micropump diaphragms, which were obtained as part of this research. This was an essential part of learning techniques that have aided the subsequent research, which was the investigation of a new actuation technique for fluid dispensing. In the early stages a piezo-electric actuated system was considered as one of the possible approaches to develop a novel pipetting system. This investigation was carried out separate to the main research topic of dispensing and therefore is treated as a 'stand alone' chapter.

A large number of microfluidic devices have been developed over the last decade [38; 6; 5; 4]. One of the more difficult fluid handling requirements for microfluidic devices is droplet creation and manipulation. Droplet creation is conventionally carried out using microfluidic devices by rapid actuation of a membrane using either a piezo transducer or a thermal actuation approach, for instance inkjet printers [39; 40], which will be discussed in Section 3.3.1. Manipulation of droplets in microchannels has been achieved using an air pump [10; 41] or electrodynamic systems [42] which is discussed in Section 3.3.3.

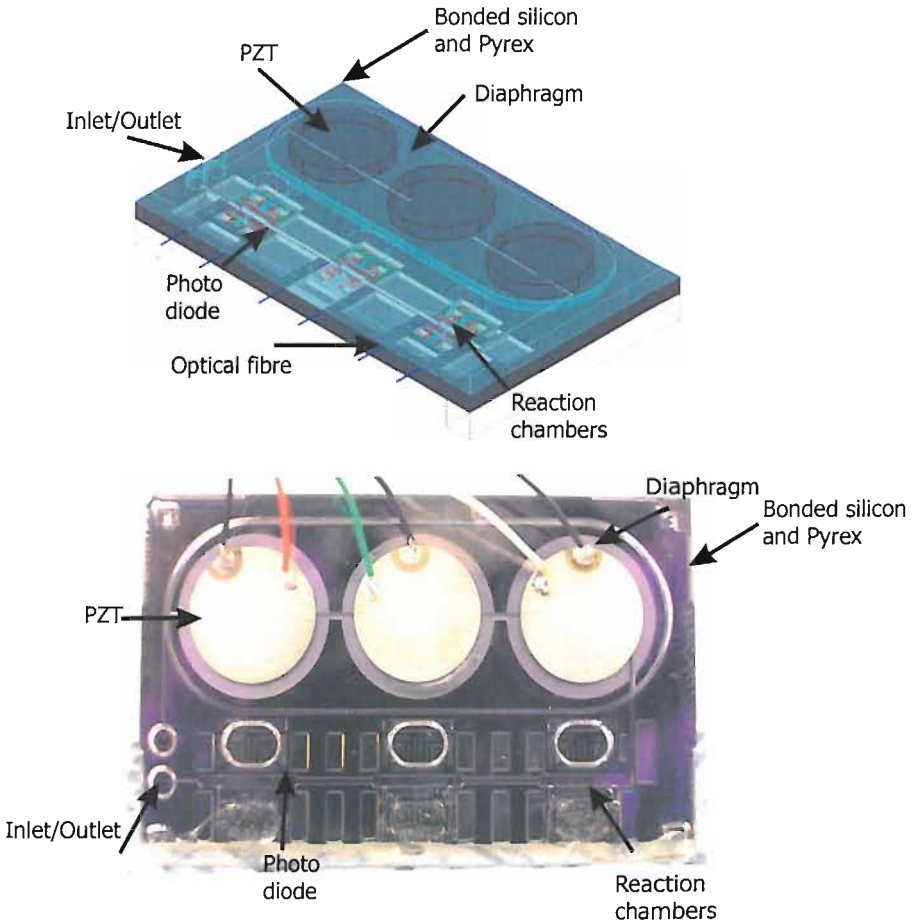

Figure 2.1: PCR device, including peristaltic micropump [29]

Figure 2.1 illustrates a microdevice produced by Bu et al. [28, 29] at the University of Southampton for PCR. This offers several advantages over traditional microsystems for PCR such as quicker thermal cycling times, higher through put and lower sample/reagent volumes [28; 29]. This is achieved by using microfabrication approaches, because of the ability to produce small dimension devices (microns). The microdevice produced by Bu et al. [28] consists of thermally controlled reaction chambers, a micro-

pump and optical detection. The optical fibres and pn-diodes, integrated into the micro-device, are designed to control a fluid droplet of $1\mu l$ through the device.

PCR devices have been previously produced; these are typically flow-through systems [43; 44; 45; 46], whereas the device which has been investigated here exploits a micropump to displace air. This air displacement is used to move a single droplet of fluid through the three reaction chambers, which are fixed at different temperatures. The droplet is then moved back to the first chamber and this process is typically repeated for 20 times. The device designed and fabricated by Bu et al. [28, 29] is illustrated in Figure 2.1 and required a pumping system to enable air displacement. The micropump investigated during this research utilises a peristaltic action to provide air displacement to move a fluid droplet. The peristaltic design eliminates the necessity for valves and allows for bidirectional pumping. The actuation of the pump is provided by three PZT discs. The pumping technique implemented here is used to provide both the sequence and the driving voltage required to actuate each of the three PZT discs, and is described in detail later in Section 2.3. In short, the system operates at ± 100 v, at frequencies up to $100Hz$. The system consists of a sequencer and a driver; the sequencer is required to achieve three different pump sequences, one for each of the diaphragms. The actuation system was subsequently used with the micropump to successfully demonstrate the pumping of air, to move a fluid droplet.

To understand why a peristaltic micropump was used to manipulate the fluid droplet within the PCR device, different diaphragm micropump methods are reviewed, consisting of single and peristaltic techniques. The system which was produced during this investigation to actuate the micropump is described, including the testing strategy that was used to determine the performance of the micropump. An interferometer was set up and used to determine the dynamic deflection of the micropump diaphragms. In addition to the diaphragm deflection the rate of actuation can be estimated which is essential in determining the frequency limitations of the micropump. The results obtained from the micropump actuation are presented and accompanied by analysis. Conclusions are drawn about the micropump operation, with suggested work which might be considered for further development of the micropump.

2.2 A review of fabricated diaphragm micropumps

Micropumps have been fabricated using a number of configurations, these include PZT actuated diaphragm devices [47; 48; 49; 50; 51], ferrofluid actuated devices [52; 53; 54], thermo pneumatic actuated diaphragm devices [55; 56; 57; 58; 59], thermal bubble [60; 61], magnetically actuated diaphragm devices [62], pneumatic actuated diaphragm devices [63] and electroosmotic flow (EOF) [64; 65] . Microstructures for biological and medical applications have been produced and continue to be developed. Micropumps have been developed, where volume flow rates from $78nl\ min^{-1}$ to $1500\mu l\ min^{-1}$ have been achieved. These have been integrated into systems, or used as component parts, and are used to move the fluid through microchannels and reaction chambers [43; 44; 45; 46]. The micropumps can be used to displace microlitre volumes of fluid and some designs can achieve bidirectional pumping.

During the design of micropumps the dead volume is an important consideration. The dead volume is the volume within the displacement chamber minus the stroke volume of the pump diaphragm. The dead volume can cause problems because fluid or air can become trapped. During the design of a micropump the ratio between the stroke volume and dead volume is made as small as possible. This is critical for air pumping or bubble tolerant devices [66].

Diaphragm micropumps are classified here into three types, which are as follows:

1. single chamber with dynamic valves [47; 48; 51; 57]
2. single chamber with active valves [67; 68; 69; 49; 56; 62]
3. multi chamber peristaltic systems [70; 55; 63]

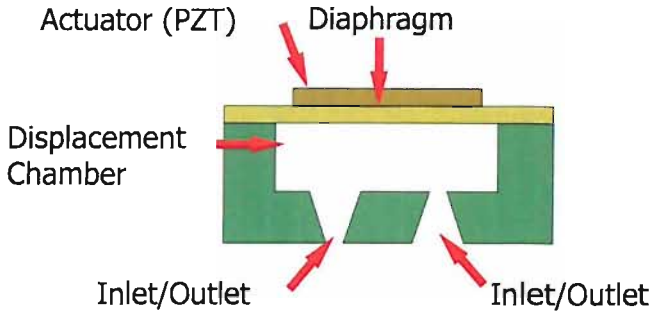

Figure 2.2: Schematic of a single chamber diaphragm micropump, including dynamic valves and a PZT actuation technique.

1.) The simplest diaphragm micropump consists of a single displacement chamber, with dynamic valves. A detailed discussion of dynamic valve operation can be found in Section 3.4, page 54 [71]. A schematic of a single diaphragm micropump is illustrated in Figure 2.2 which includes the main components used to produce positive displacement of fluid, these are as follows:

- Inlet
- Outlet
- Displacement chamber
- Diaphragm
- Actuator

The micropump is operated by deflecting the diaphragm up and down using an actuator. For this example PZT is illustrated, but other actuation techniques could be used; magnetic or thermal to name two. The actuated diaphragm deflects up and down creating a negative and positive pressure difference, respectively, within the displacement chamber. A negative pressure difference will draw fluid into the displacement chamber via the inlet and the positive pressure difference will force fluid out of the displacement chamber via the outlet. To obtain positive displacement of fluid, valves must be included in the system. Failure to provide a valve system will result in fluid simply being drawn in and out of the device via both the inlet and outlet. The valves provide a mechanism for producing a net flow from the inlet to the outlet over one cycle of operation.

Diffuser/nozzle valves are used to provide directional flow, requiring relatively simple fabrication. Valves have been produced in the same plane as the displacement chamber [57; 47] and out of plane, perpendicular to the displacement chamber [48; 51]. Both of these techniques allow for easy integration with other fluidic devices. Using diffuser/nozzle valves does not completely stop the flow in either direction, but results in a higher restriction to the fluid in one direction than for the other. The fluid resistance is directly proportional to the flow velocity used. To use diffuser/nozzle valves, high frequencies up to $2kHz$ are used to produce a difference between the restriction due to the inlet and outlet [48]. During pumping, fluid will be forced out and drawn in through both the diffuser and the nozzle, but overall the fluid will be moved in one direction, this however will result in a poor pumping efficiency. By tuning the frequency it is possible to produce pumping in either direction using single diaphragm micropumps with diffuser/nozzle valves.

Kim et al. [57] produced a thermally actuated single diaphragm micropump with a 3.5 mm diameter diaphragm and an actuation voltage of 55 v at 6 Hz, achieving a volume flow rate up to 78 $nl\ min^{-1}$. A PZT actuated device was produced by Olsson et al. [47], which consists of two $6mm$ diameter diaphragms, working together. This device was actuated with 145 v to produce volume flow rates up to 2300 $\mu l\ min^{-1}$. Further PZT actuated micropumps were produced by Koch et al. [48] and Schabmueller et al. [51]. The micropump of Koch et al. [48] consists of an 8x4 mm diaphragm which was actuated with 600 v at 2 kHz, achieving a pump rate of 155 $\mu l\ min^{-1}$. The micropump produced by Schabmueller et al. [51], achieved volume flow rates up to 1500 $\mu l\ min^{-1}$, with a 7x7 mm diaphragm and an actuation voltage of 190 v at 2.5 kHz.

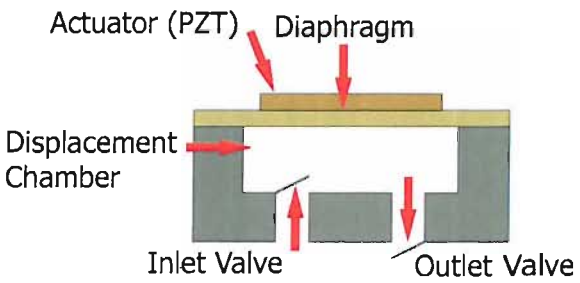

Figure 2.3: Schematic of a single chamber diaphragm micropump, including active valve structures and a PZT actuation technique.

2.) The efficiency of dynamic valves is poor; there will always be a fraction of flow in and out of both ports during pumping. To improve the performance active valves have been introduced at the inlet and outlet. A schematic of a single diaphragm micropump with active valves is in illustrated in Figure 2.3. Although the valves will require a pressure in order to be opened or closed, it is possible to completely stop the fluid flow in one or the other direction. To operate these devices, the diaphragm is deflected upwards, opening the inlet valve and closing the outlet valve. This will draw fluid into the displacement chamber. The diaphragm is then deflected downwards, closing the inlet valve and opening the outlet, thus forcing fluid out of the displacement chamber. Single diaphragm micropumps have been produced with valves, fabricated in silicon and glass, though other materials have been used. Micropumps with valves provide better pumping efficiency, but the fabrication is more complex because multi-layers are used. The devices will be more expensive to fabricate and more complicated to integrate with other fluidic components. The valve structure usually prevents these micropumps from bidirectional operation.

Koch et al. [68] have produced a PZT actuated micropump using silicon, which contains a valve at the inlet and outlet. This device (8 x 4 mm) was used to achieve pump rates of up to 120 $\mu l\ min^{-1}$, which is comparable to a similar diffuser/nozzle device [48]. However this is at a lower actuation frequency of 200 Hz compared to 2 kHz, illustrating that the active valve device is more efficient. Maillefer et al. [49] have also produced a PZT actuated micropump, using silicon and Pyrex. The device is 6 x 10 mm, with a stroke volume of 160 nl. During testing, the micropump was used to achieve pump rates of up to 33 $\mu l\ min^{-1}$ at $3Hz$. The efficiency of this device is excellent and Maillefer et al. [49] report that over a long term test of 600 days the device sustains the delivery of 160 nl for every actuation; $160nl$ is the stroke volume of the diaphragm. Similar micropumps have been produced by Meng et al. [69] (pneumatic and solenoid, 75 $\mu l\ min^{-1}$ at 13 Hz), Wego and Pagel [56] (thermal actuation, 11 $\mu l\ min^{-1}$ at 1.8 Hz) and Santra et al. [62] (magnetic actuation, 250 $\mu l\ min^{-1}$ at 5 Hz, 13 mm device). All of these devices have been demonstrated to produce similar volume flow rates to the diffuser/nozzle configuration devices, but at much lower pump rates.

A final example of a micropump has been produced by Zengerle et al. [67]; this

pump has been demonstrated for bidirectional pumping. This has been achieved by considering the resonant frequency of the actual valves. The pump was used to achieve a pump rate of up to 200 $\mu l\ min^{-1}$ at 833 Hz and 300 $\mu l\ min^{-1}$ at 1666 Hz in the reverse direction. This illustrates that it is possible to produce bidirectional pumping with a single diaphragm micropump with active valves.

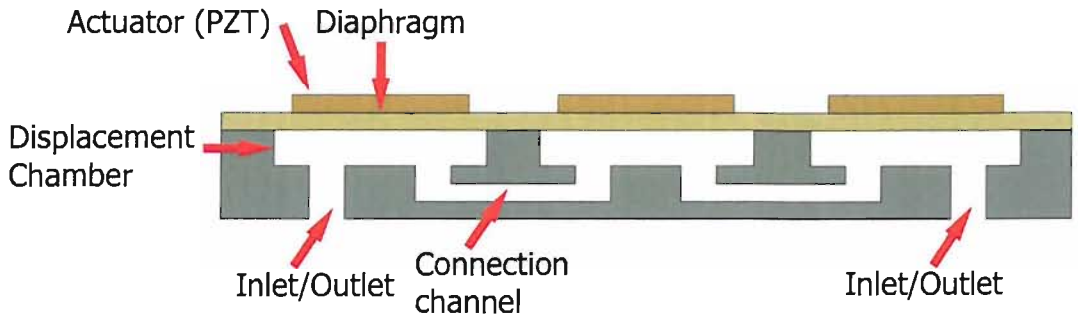

Figure 2.4: Schematic of a bidirectional 3 chamber peristaltic micropump, including a PZT actuation technique.

3.) The fabrication of active valves is complicated, so a peristaltic action can be used to simplify fabrication, whilst still obtaining a more efficient pumping system. To increase the micropump efficiency, and allow for easy bidirectional pumping, peristaltic micropumps have been produced [70; 55; 66; 50; 63]. Peristaltic micropumps typically have three diaphragms in series, as illustrated in Figure 2.4. This illustration shows a schematic of a peristaltic micropump, with three displacement chambers. The inlet/outlet is located at either end of the device and each chamber is connected via a channel within the device. The operation of the pump can be considered to be similar to a single diaphragm micropump (centre chamber), with two active valves (left and right chambers), which are opened and closed to produce fluid pumping. Each diaphragm acts as both a pumping and valve element. Each actuation of a pump diaphragm results in the displacement of fluid. Using a sequential opening of each diaphragm, air is drawn across the system. Using an appropriate pump sequence, displacement of fluid through the device can be achieved in both directions with a high pumping efficiency. An example of a peristaltic pump sequence is illustrated in Figure 2.5 in Section 2.3.

The physical dimensions of peristaltic micropumps tend to be larger in size because three diaphragms are used. Nguyen and Huang [50] have produced a three diaphragm peristaltic micropump with PZT actuation. The three diaphragms (8 mm) are config-

ured such that two are on one side of the device and the third is on the opposite side, enabling the device dimensions to be reduced. The micropump was used to achieve pump rates up to 1500 $\mu l\ min^{-1}$ at 50 Hz. Mover over a thermal pneumatic actuated peristaltic micropump has been produced by Folta et al. [70]. The device consists of three diaphragms in series and the overall dimensions of the device are 10 x 3 mm. The maximum pump rate achieved with this device was 120 $\mu l\ min^{-1}$ at 16 Hz. There is no real indication, with any of these devices, of the pumping efficiency, though it is expected to be high due to the use of diaphragms as valves . However the pump rates of peristaltic micropumps are comparable to single diaphragm micropumps, but the pumps are bidirectional.

All three micropump types discussed here can be used to displace air which could be used to manipulate fluid for a pipette device. The single diaphragm devices with active valves and peristaltic micropumps offer the best pumping efficiency. However the peristaltic micropump can be used to produce bidirectional pumping, but a more complicated actuation system is required. The single diaphragm micropumps are generally smaller in size, so for pipetting single droplets of fluid, a single diaphragm micropump could be a possible solution.

The peristaltic micropump was selected for this work due to bidirectional pumping capability. The pump layout and design is relatively simple though the dimensions of the diaphragm were calculated so that the device could be used to produce the pump rate required for the microdevice. Due to the simplicity of the peristaltic pump design all of the elements can be produced in the plane of two wafers; these are connection channels, displacement chambers and diaphragms. This allows for the straightforward integration of additional elements within these wafers, such as thermal heating and sensor elements to form a PCR device [28; 29].

2.3 PZT micropump principle

The complete conceptual design, simulation, fabrication and testing of a peristaltic micropump was carried out by Bu [37]; the focus of this investigation here was the actuation of the micropump. The micropump is used to displace air, which can then

be used to manipulate a 1 μl droplet of fluid through the rest of the microdevice. This micropump has the potential to be used as a pipetting device. The operation of the technique is essentially pneumatic; therefore the only contact with the droplet will be with air and the channel surface. This is advantageous because fluid could get trapped in the pump diaphragms, or heated due to an increase in temperature associated with the PZT actuators. However the device alone could not be used as a pipetting device, because there is no potential for metering of fluid, to form droplets.

The micropump consists of three diaphragms; each actuated using a PZT disc. The device has been designed to be actuated with $\pm$100 v at a frequency of 10 Hz. It should be possible to achieve a volume flow rate of up to 188 $\mu l\ min^{-1}$, if it is assumed that each cycle displaces a volume equal to the calculated displaced volume of 314 nl. This has been calculated assuming that the diaphragm deflection will be 6 μm. This is an ideal approximation and does not consider any leakage.

A peristaltic micropump was chosen for this work because it is possible to pump in both directions (required for the PCR device) and can be produced using just two layers. In this case silicon was used to produce the connection channels and the displacement chambers and Pyrex was used to produce the diaphragms and the capping layer for the connection channels. Peristaltic pumps have been successfully demonstrated by Folta et al. [70], Berg et al. [63] and Grosjean and Tai [55]. These pumps are operated using three diaphragms in a given sequence to produce a peristaltic action. An example of an appropriate pump sequence is illustrated in Figure 2.5. The pump sequence illustrated in Figure 2.5 has been successfully used to produce pumping by Grosjean and Tai [55]. To pump in the opposite direction, the sequence is simply reversed.

The peristaltic micropump produced for this work (Figure 2.6) is actuated using PZT discs; 10 mm in diameter and 200 μm thick (855, APC International, Ltd., Mackeyville, PA, USA). These offer quick (μs) and large displacements (10 μm), but require a high operating voltage ($\pm$100 v). The peristaltic micropump consists of three Pyrex diaphragms, anodically bonded to silicon. The silicon contains connection channels between each diaphragm and displacement chambers, etched by deep reactive ion etching (DRIE). The PZT is attached to the surface of the Pyrex diaphragm using cyanoacrylate superglue (GD105, Glue-Direct, www.glue-direct.com). When the PZT is actuated it

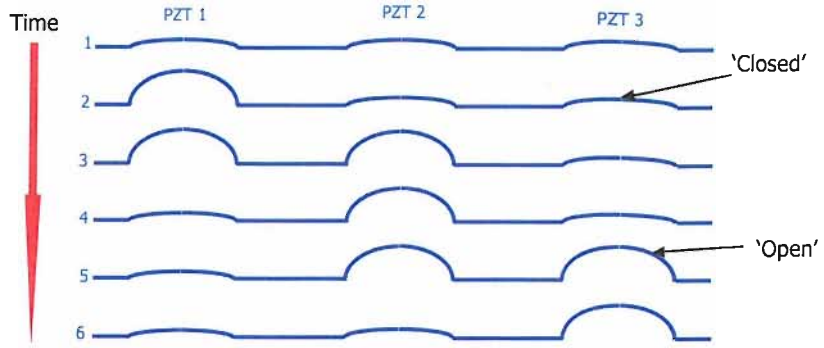

Figure 2.5: Six stage pump actuation sequence, illustrating the 'open' and 'closed' position of each of the three diaphragms in a six stage sequence.

will change dimensions. If the actuation voltage is applied in the poling direction of the material, it will expand and become thinner, however if the actuation voltage is applied in the opposite direction of the poling direction the material will contract and become thicker. As the PZT is attached to the Pyrex diaphragm the movement will be limited, resulting in a deflection up or down of the diaphragm. This results in the diaphragm moving up or down, creating a positive or negative pressure within the displacement chamber. The PZT was actuated using a high voltage square wave at ± 100 v. The frequency of this signal was varied between frequencies of 10 and 100 Hz to obtain the optimum pump rate. The frequency and voltage used will determine the pump rate of the device.

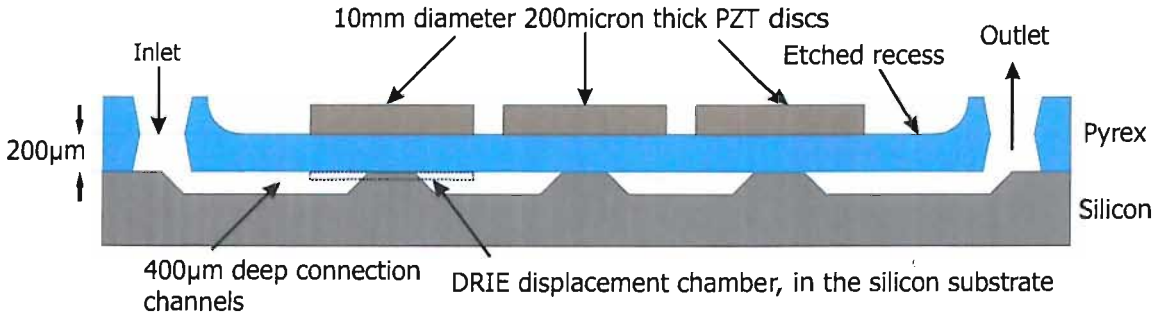

Figure 2.6: Cross section of the peristaltic micropump including critical dimensions.

The micropump was required to move a 1 μl droplet of fluid in both directions; using air to displace the fluid. The micropump needs to be used to produce volume flow rates from 100 *to* 200$\mu l\ min^{-1}$, to move the 1 μm droplet between the chambers quickly ($< 2\ s$) to achieve high PCR cycle times. To obtain this volume flow rate, the pump must be actuated at frequencies up to $100Hz$.

The sequence required to actuate the peristaltic micropump is illustrated in Figure 2.5, which can be used to produce a displacement of fluid from left to right. By reversing this sequence the pump direction will be reversed and therefore the micropump is bidirectional.

2.4 Micropump actuation

To achieve air pumping using the peristaltic micropump, an actuation system was designed and produced as a part of this research [72; 73]. For simplicity, the system was divided into two parts. A sequencer was used to produce the three signals required to control each of the PZT discs, but at low voltage ($0 - 5$ v). A driver was produced to gain the high voltage (± 100 v) to create the designed deflection of the diaphragms; and was controlled using the sequencer.

2.4.1 Sequencer

The sequence of six steps used to actuate the peristaltic micropump is illustrated in Figure 2.5. During the micropump testing stage it was considered advantageous to be able to vary the diaphragm actuation sequence. The sequencer solution uses software (Labview, National Instruments), allowing for a greater amount of user control. The software sequencer was used in conjunction with a National Instruments data acquisition card (PCI-6014). The user can change the pump sequence time and the sequence. Figure 2.7 illustrates the user input of the software sequencer. This illustrates the user controls for each diaphragm in the sequence and the timing input control.

The sequencer can be used to produce the 'six stage sequence' required for the peristaltic micropump. The effective cycle frequency of the sequencer ranges from 0.1 to 166 Hz. The output of the sequencer from the data acquisition card consists of three digital signals, which can be either high (5 v) or low (0 v). A typical output from the sequencer is illustrated later in Section 2.6 in Figure 2.12, which shows the three outputs; one for each PZT driver.

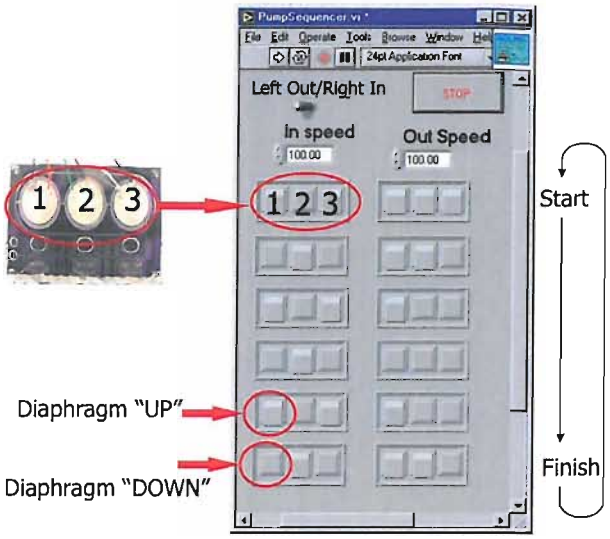

Figure 2.7: The user interface for the software sequencer using Labview (National Instruments). Each Stage of the sequence allows for the individual diaphragms to be *Open* or *Closed*. The pump sequence starts at the top, goes through each stage and then repeats until the program is terminated.

2.4.2 Driver circuit

The second part of the actuation system is the driver circuit. The PZT discs actuating the diaphragms require a high voltage (± 100 v) to produce the required deflection. The large deflection is required to be able to produce a high enough pump rate for the device. The driver circuit needs to actuate each PZT; controlled by the sequencer and operate at frequencies up to 100 Hz. The solution chosen to drive the PZT discs consists of photovoltaic transistors (PVR33N, International Rectifier) to allow low frequency, unlimited switching of the PZT. The photovoltaic devices consist of field-effect transistors (FET) with no gate connection, packaged with a light emitting diode (LED). When the LED is switched on using a low voltage ($1 - 5$ v), light is emitted and the transistor will be turned on. The transistor can be used to switch up to 300 v d.c. These devices are ideal for this application because there is no risk of mixing the high and low voltage, which could result in damaging the data acquisition card. The photovoltaic transistors can switch at frequencies up to 350 Hz, with a $T_{ON} = 150\ \mu s$ and $T_{OFF} = 125\ \mu s$. These devices are slow (maximum frequency of 340 Hz), but have a long switching life and have no mechanical parts.

An illustration of the driver circuit is shown in Figure 2.8. The circuit contains two photovoltaic devices for each PZT output; one 'pull-up' and one 'pull-down'. The same type of device is being used for the pull-up and the pull-down, so the circuit timing will be symmetrical. A logical inverter decodes the output from the computer, such that when one transistor is 'ON' the other transistor is 'OFF'. When the photovoltaic transistors are activated using the sequencer signal, the output will be pulled up or down depending on the signal. To ensure that the circuit will not delay the operation of the PZT actuator, the time delay of the circuit is considered. Using the Equation 2.1, the maximum time delay for each switch transition can be calculated, where C is the PZT capacitance and $R_{Transistor}$ is the transistor 'ON' resistance.

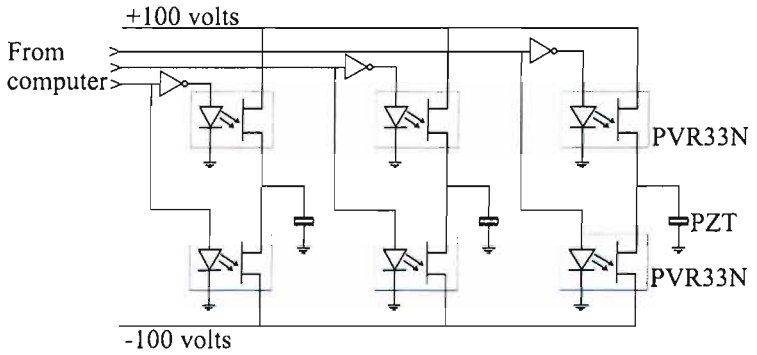

Figure 2.8: Driver circuit including PVR33N photo voltaic transistors (International Rectifier)

$$T_{Switch} = C * R_{Transistor} + T_{ON} \tag{2.1}$$

Using Equation 2.1 T_{Switch} has been calculated to be 150 μs, where $R_{Transistor} = 24\ \Omega$, the PZT ceramic disc capacitance = 5.9 nF and T_{ON} = 150 μs. This is dominated by the switching time of the device. This is considered acceptable because the circuit does not have to be operated at frequencies above 100 Hz.

2.5 Testing procedure for the peristaltic micropump

2.5.1 Diaphragm deflection using an interferometer

Initial experiments indicated that the system could effectively be used to pump fluid and displace a 1 μl volume droplet of water [37]. However to test the system more rigorously and establish the efficiency, the following experiments were conducted. A driving voltage of ± 100 v is predicted to achieve a diaphragm deflection of 6 μm as described in Section 2.3 [28]. A Michelson interferometer method to determine this small deflection during actuation of the diaphragm was set up as part of this investigation. Interference of a fixed wavelength of coherent light provides an accurate approach for measuring the deflection of the diaphragm up and down in the nanometre range. The interferometer is used here for the temporal evaluation of the diaphragm displacement 'UP' or 'DOWN'. This interferometer method was used to determine the deflection of each pump diaphragm, during actuation. In addition to the diaphragm deflection, it was possible to determine the time taken for the deflection. This was useful to determine the efficiency of the micropump.

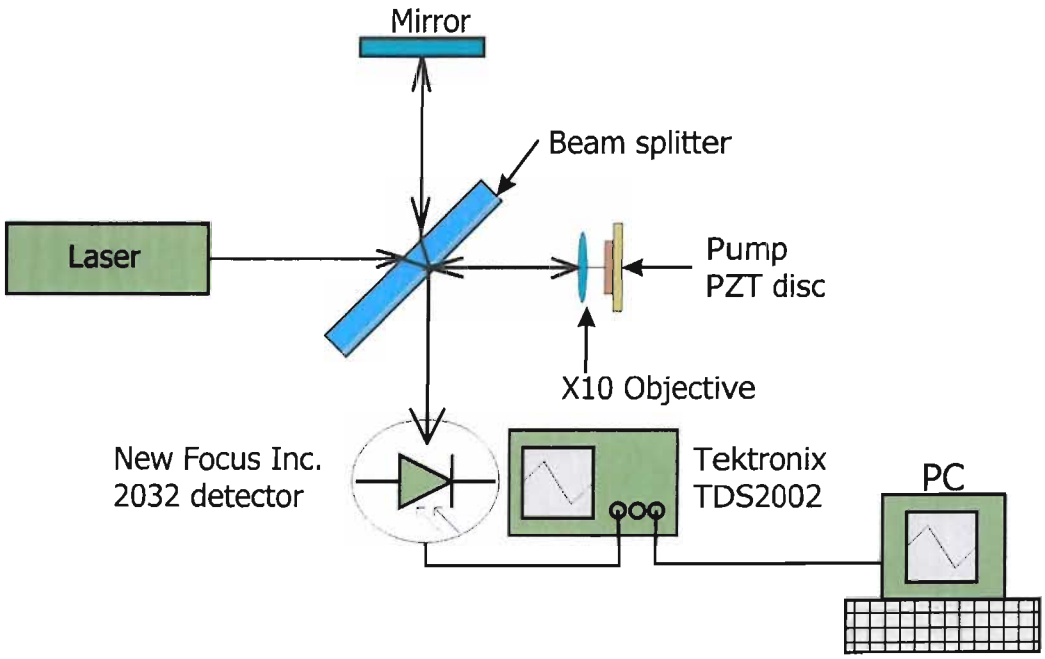

Figure 2.9: Schematic of the interferometer set up including the detection method used to collect the interference fringes.

The interferometric method consists of a standard Michelson Interferometer in conjunction with a fast photodiode linked to an oscilloscope. The data obtained was transferred to a computer, to enable the deflection of the diaphragm to be determined. The set up of the interferometer is illustrated by the schematic in Figure 2.9. The light source for the interferometer is a Helium Neon laser (HeNe 633nm, Melles Griot). The coherent light beam from the laser is split by the beam splitter; $\approx$ 50% of the light is directed toward a fixed mirror and the other $\approx$ 50% is directed toward the sample mirror. Both of these beams are reflected back to the beam splitter and recombine. The two light beams interfere constructively or destructively depending upon the phase difference. The light intensity was measured using a New Focus 2032 photodetector which has a large 5.8 mm diameter silicon detector. This can be used to detect wavelengths of light from 190 to 1100 nm with a temporal response of 900 kHz. The photodetector was used at a single point to detect light and dark fringes while the diaphragm was actuated.

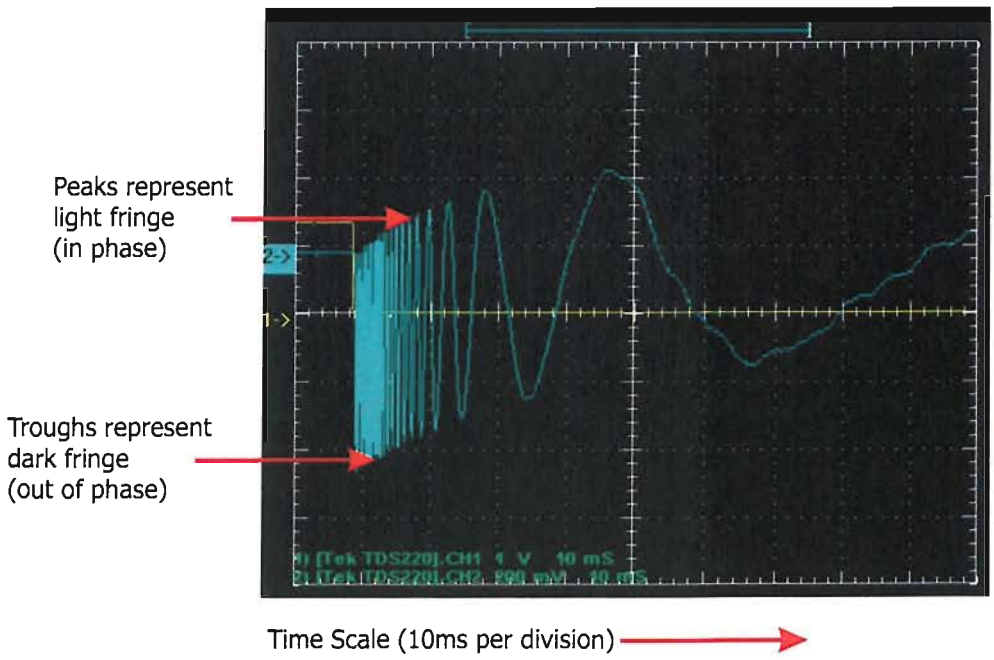

Figure 2.10: An example of the output from the photodetector; illustrating the light and dark fringes passing a single point. The number of peaks and the time at each peak occurs is recorded to determine the deflection of the PZT and the time, however the amplitude of the signal is not required

At the detector the two reflected rays will be observed from the mirror and the sample mirror where destructive and constructive interference will result. As the sample

is displaced by the diaphragm, a distance of $n\lambda/2$ is moved (n is the number of $\lambda/2$ which the diaphragm deflects), resulting in destructive then constructive interference; continued displacement results in light and dark fringes [74]. The photodetector was placed at a single point and was used to detect each light and each dark fringe which occurred. The output from the photodetector is illustrated in Figure 2.10. In the photodetector output, peaks represent light fringes and troughs represent dark fringes. No difference in the fringe patterned is observed for the upward and downward motion of the diaphragm. To ensure the deflection of the centre of the diaphragm was measured, an objective (x10) was added to the system to focus the beam to a small spot. To enhance the reflection from the PZT, a small mirror was attached. Reflection from this small mirror enabled measurements of deflection of the PZT, and therefore the diaphragm, during actuation.

2.5.2 Fluid displacement using micropump

The micropump has been developed as part of the PCR device to manipulate a 1 μl droplet through three reaction chambers. To correlate the diaphragm displacement data with pumping rate, it was necessary to make some measurements as follows. Initial pump testing used the actuation system discussed, using the pump sequence illustrated in Figure 2.5. This testing was carried out to determine the pump rates which could be achieved with the peristaltic micropump. To determine the pump rates the driving voltage was kept constant while varying the frequency of the actuating sequence. Similar actuation voltages were used, as for the displacement measurements described previously. To obtain results for volume flow rate a tube (5 mm internal diameter.) was connected to the device. A 1 μl droplet of water was introduced into the attached tube. During actuation of the micropump air would be displaced and thus move the droplet. The distance moved by the droplet and the time taken were recorded; results for volume flow rate were obtained for different frequencies up to $180\,Hz$.

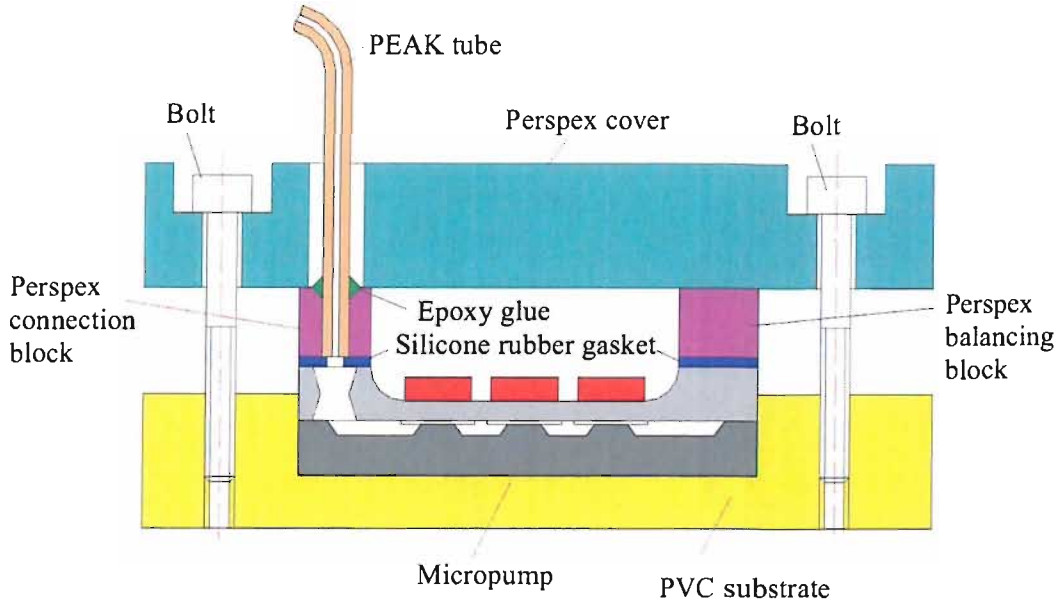

Figure 2.11: Schematic of the clamp used to connect a 5 mm (internal diameter) PEAK tube to the peristaltic micropump during testing [37].

2.6 Results and discussion

The first part of this investigation was to produce an actuation system to drive the peristaltic micropump, using the correct diaphragm actuation sequence. This was successfully produced and a typical output from both the sequencer and the corresponding driver circuit output are illustrated in Figure 2.12. The actuation system was used during all of the subsequent testing.

The dynamic deflection of each of the diaphragms was successfully measured using the Michelson Interferometer. Figure 2.13 illustrates the temporal displacement of each of the diaphragms during actuation up and down. During displacement measurements, the other two diaphragms were held open using a 100 v drive. The results illustrate both the overall deflection and the time taken to reach a maximum displacement. The deflection for different driving voltages was determined, however results for pumping are only shown for actuation voltages of ± 100 v. These results illustrate that the actuation times for each of the diaphragms is different. The deflection results are summarized in Table 2.1, for an actuation voltage of ± 100 v. The deflection and time for the left and right diaphragms is similar, and by allowing for a small error (± 633 nm), can be considered to be the same. The interference fringes were manually counted to determine

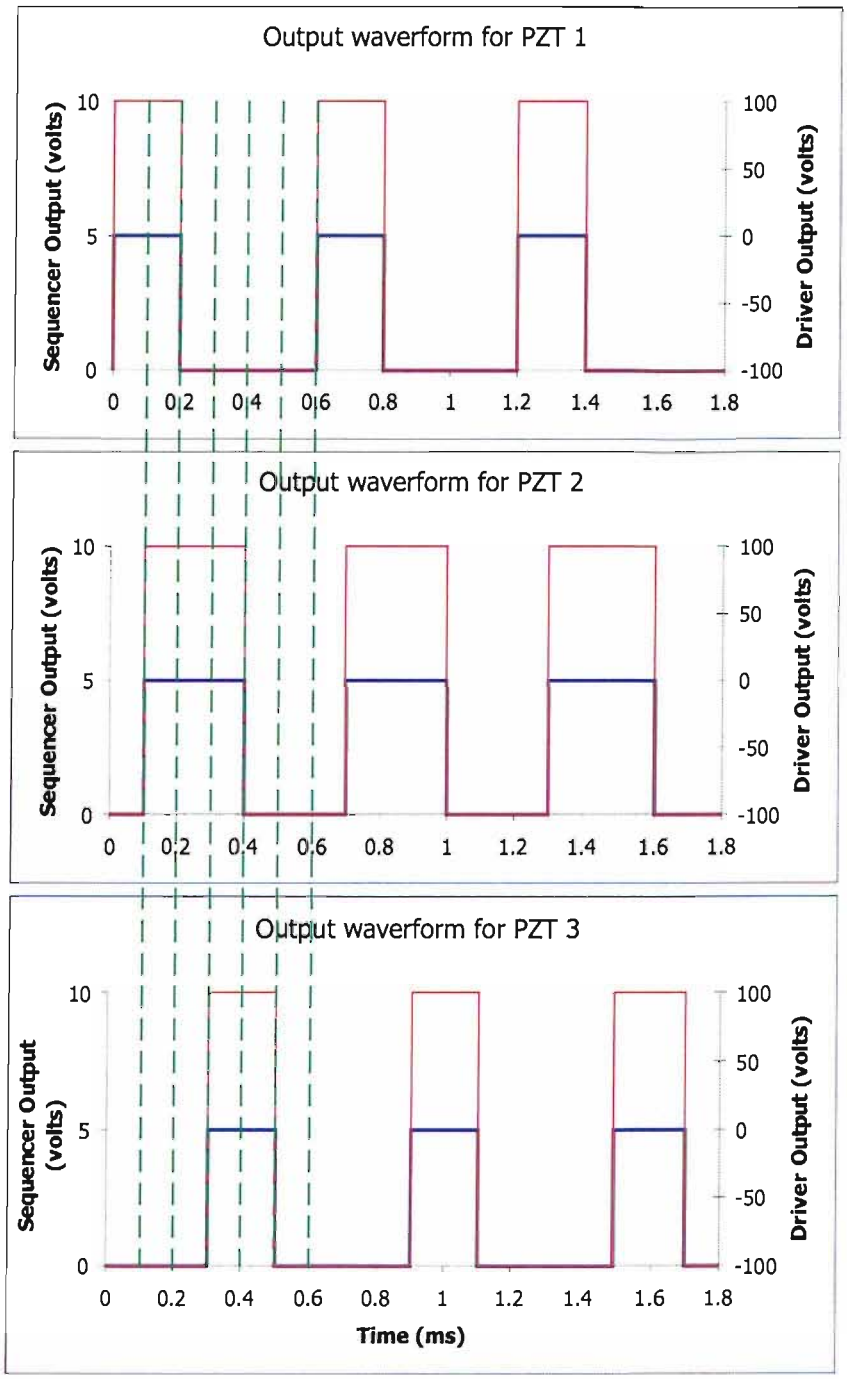

Figure 2.12: Typical sequencer and driver system outputs for the three PZT discs. The sequencer is represented by the thick blue line and the driver output is represented by the thin red line.

the deflection; therefore an error of two fringes was considered reasonable. The centre diaphragm reaches a similar deflection point, but the time taken is longer ($\approx 1\ ms$). This could be attributed to the difference in the spacing between the connection channels which are etched beneath each of the diaphragms (Figure 2.14) and the resulting restriction to flow of air into/out of the diaphragm chamber. To illustrate this finding, Figure 2.14 shows an image of a completed micropump (without the PZT discs). This illustrates that the spacing between the connection channels is different for the outer pump chambers ($8\ mm$) and the centre pump chamber ($1.3\ mm$). Due to the decreased spacing of these channels for the outer chambers, more of the channel is exposed once the Pyrex layer is bonded. The result of this is that the resistance to the air will be less due to a larger opening; therefore the diaphragms will deflect quicker.

Diaphragm	**Deflection** ($\mu m \pm 633\ nm$)	**OPEN Time** ($ms \pm 0.1\ ms$)	**CLOSE TIME** ($ms \pm 0.1\ ms$)
Left	9	2.6	3.5
Centre	9.8	3.8	4.5
Right	9	2.6	3.6

Table 2.1: Summary of interferometer data, including deflection and OPEN/CLOSE times for an actuation voltage of ± 100 v.

The results, illustrated in Figure 2.15, are for pumping using the previously described six stage pump sequence. These results show that the pump rate increases with increasing pump frequency. The maximum pump rate achieved out of the device was $835\ \mu l\ min^{-1}$ for a six stage sequence. It is clear from the results there is a difference in pump rate for each pumping direction. It is believed that this is due to an asymmetry of the 'overall' device. The design of the micropump is symmetrical about the centre of the middle diaphragm (Figure 2.14), excluding the inlet and outlet connecting channels (although a small asymmetry may be introduced into the device during the attachment of the PZT actuators). During actuation, the order in which the diaphragms are actuated is different. However all three diaphragms are deflected up and down once for one complete one pump cycle, therefore there is no asymmetry introduced here.

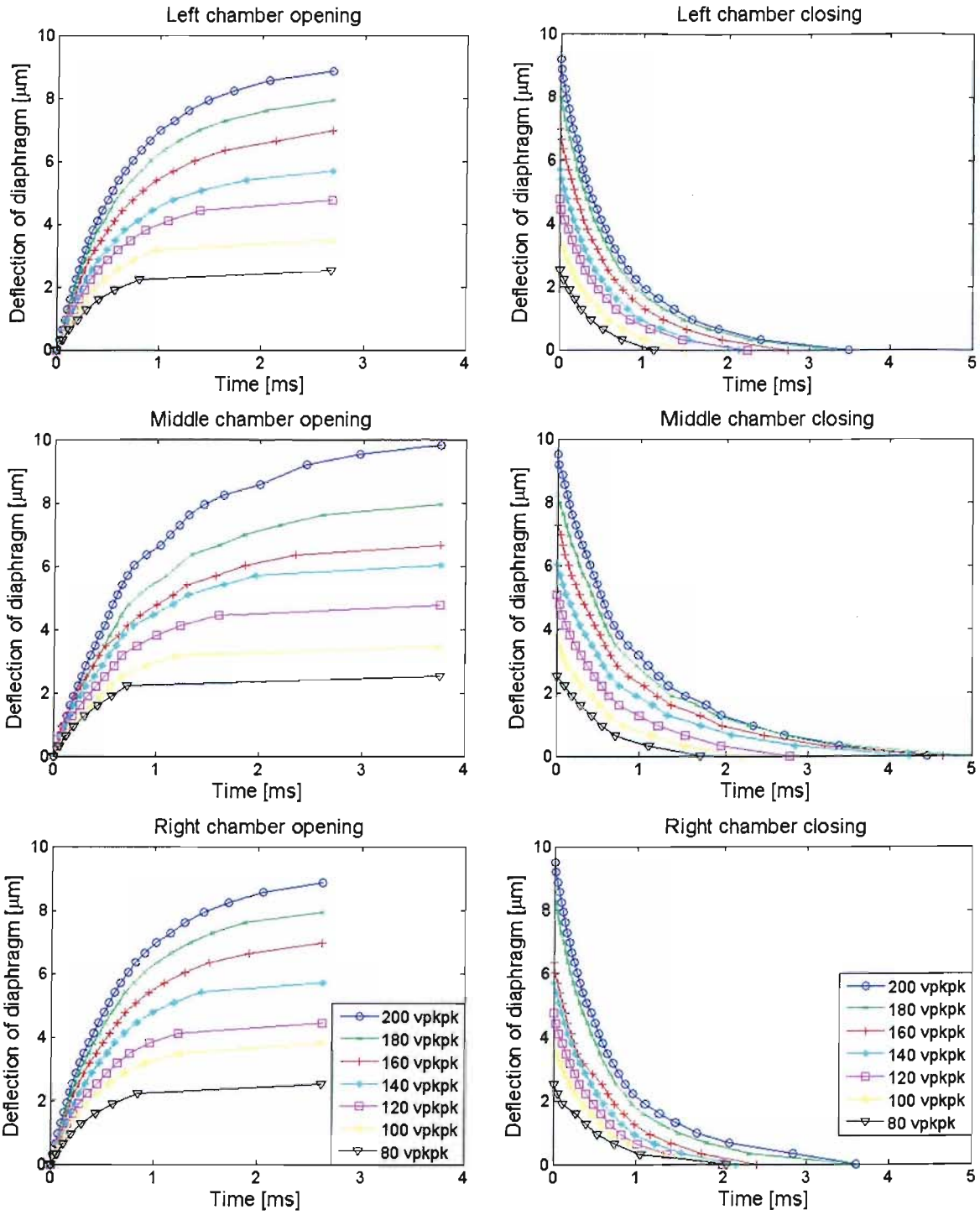

Figure 2.13: Interferometer results for upward and downward movement of the three diaphragms of the micropump.

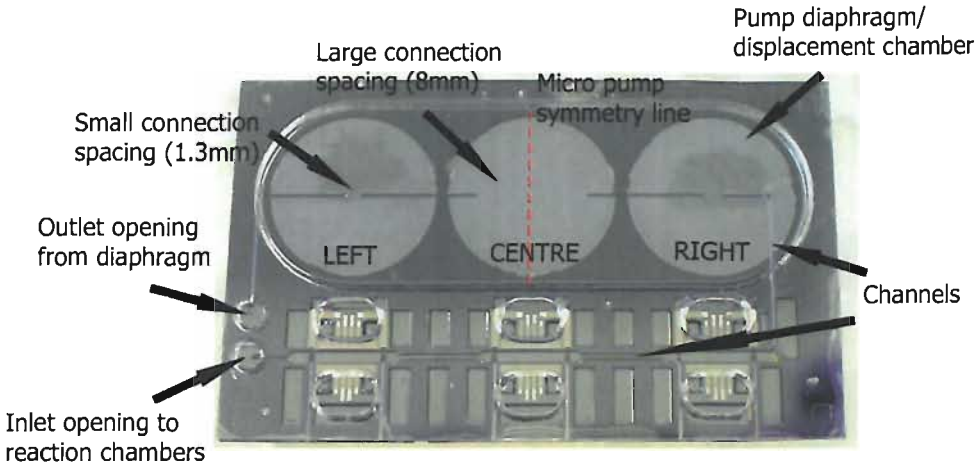

Figure 2.14: Illustration of a bonded micropump, showing the spacing of the connection channels, but without PZT disks.

The only asymmetry of the device is in length of the connection channel to the inlet (via the reaction chambers) and the connection channel to the outlet and the pump. A higher resistance to flow of the air will occur in the longer channel. For inward pumping (toward the outlet) the air will be moved through the longer inlet channel for more stages of the pumping cycle than the shorter outlet channel, therefore the overall resistance for the entire pump cycle will be greater, resulting in a higher overall resistance to flow for forward pumping. To rectify this asymmetrical pumping in forward and reverse direction the inlet and outlet channels must be made the same.

The interferometer results provide information about when the deflection time of the diaphragms will begin to attenuate the pump rate. If the opening and closing of the micropump diaphragms was achieved in zero time, then the pump rate would increase linearly with increasing actuation frequency. However this is not the case. It is possible to obtain a theoretical maximum pump frequency; this can be evaluated for conditions where the deflection time of the diaphragms is so fast that the system no longer has effective pumping. This is because the diaphragms do not reach the maximum deflection for a given actuation voltage. However the pump rate will still increase, due to an increase in actuation frequency, but the pump rate will not increase linearly. The theoretical frequency can be calculated using the total *open* and *closing* times for each of the diaphragms for a given actuation voltage, summarized in Table 2.1. The theoretical maximum pump frequency for an actuation voltage of 100 v, where the pump rate will no longer be linear, is 48.6 $\pm$ 1.4 Hz as calculated from Table 2.1. This

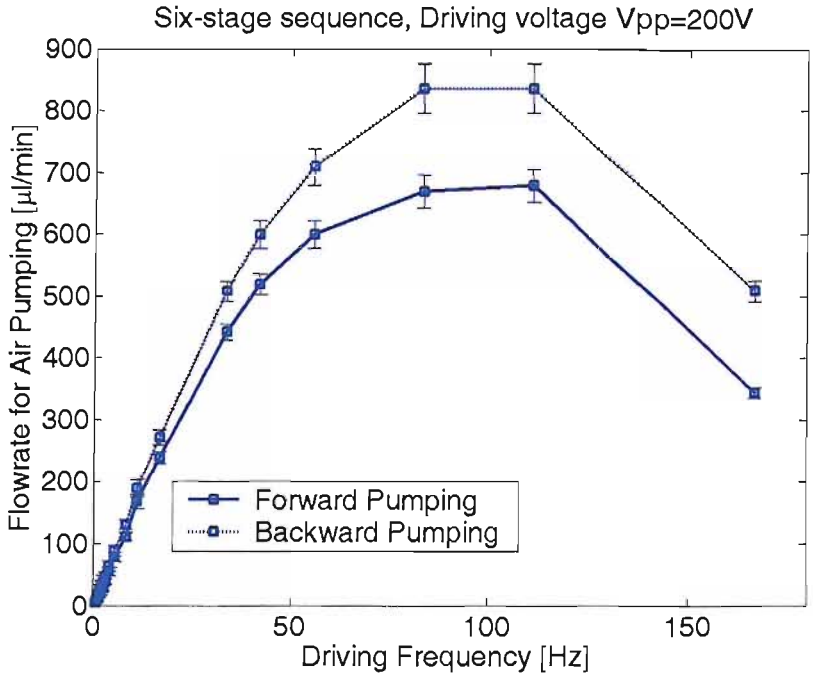

Figure 2.15: Graph of flow rate against actuation frequency for the six stage actuation sequence [37].

frequency was determined by finding the inverse of the sum the three pump chambers opening and closing times. It has a good correlation with the results in Figure 2.15, which shows that the pump rate ceases to be linear above 40 Hz.

To determine the pumping efficiency of the micropump the theoretical pump rate which can be achieved needs to be found using the diaphragm displacement data obtained using the Michelson interferometer. The theoretical pump rate of 188 $\mu l\ min^{-1}$ at 10 Hz was predicted, on the basis that the diaphragms would be deflected by 6 μm (resulting in a displaced volume of 314 nl by Bu et al. [28]). The pump rate is calculated on the basis that each cycle displaces a volume of 314 nl; with no leakage or air compression. The deflection of the micropump was recorded as approximately 9 μm, so the theoretical pump rate can be recalculated by predicting the total volume of air which is displaced at a frequency of 10 Hz. A deflection of 9 μm produces a volume of approximately 500 nl, predicted using the volume of a spherical segment. Using the same principle, the theoretical pump rate at 10 Hz should be 300 $\mu l\ min^{-1}$. This is clearly higher than the achieved pump rate at 10 Hz of 125 $\mu l\ min^{-1}$, resulting in an effective pumping efficiency of ≈ 40 %.

The reasons for this pumping efficiency have not been investigated, but it could be attributed to one of the following factors:

- Leakage of air when diaphragms are in the 'down' position
- Non-uniform deformation of the diaphragm, resulting in the analytical model for displaced volume being incorrect
- Diaphragm movement being different from PZT movement, which was measured using the interferometer
- Air compression

The actuation system and the optical detection method for determining the diaphragm deflection, specifically produced for the peristaltic micropump, have been described. These have been successfully used to actuate the micropump in order to displace a fluid droplet in this research and used by Bu [37] to obtain further data. The deflection and movement times of each diaphragm have been recorded, which complements the pump data, which was obtained. More results of the micropump actuation, not shown here were obtained by Bu [37], this includes different pump sequences and back pressure measurements. The data obtained during this research was used to optimize the micropump operation and to understand the limiting factors which affect the device performance.

2.6.1 Applicability of PZT for dispensing device

There was a possibility that a similar PZT actuated device could have been used for the pipetting device in this work. The requirements for this pipetting device are to produce a droplet metering and manipulation technique within a microdevice. The device should not contaminate, or increase the temperature of, the sample and it must be possible to be used to define precise volumes of fluid. There are two possible methods which could be implemented using PZT actuation.

The first implementation would be similar to the micropump investigated here which uses air to manipulate a droplet. This is advantageous because there is no contact with

the fluid droplet and the droplet does not enter the pump diaphragm. This will reduce any risks of heating associated with PZT actuators and minimise any loss of fluid. The configuration of the micropump could be just a single diaphragm micropump.

The second implementation would be to use a PZT actuated diaphragm to produce the displacement of fluid via direct contact with the diaphragm. There is a risk of heating from the PZT actuator. This would have to be a single diaphragm implementation, with additional valves to meter and pipette single droplets, making the design more complicated.

Although PZT has been used in the production of pipetting devices and shown here to displace fluid by air pressure, it was decided at this point to find an alternative technique to displace fluid for a dispensing device.

2.7 Conclusion

An actuation system has been produced for the operation of a peristaltic micropump which is part of a PCR device. The micropump has been used to demonstrate manipulation of a 1 μl droplet of fluid through the PCR device, in both directions. The micropump has been successfully actuated at frequencies up to 100 Hz, with a maximum recorded pump rate of 835 $\mu l\ min^{-1}$ at 80 Hz.

The pumping results illustrate an asymmetry for pumping in different directions. The asymmetry was observed during actuation of more than one fabricated micropump, therefore it cannot be a result of the production of the device used to obtain these results. This asymmetry has been attributed to an asymmetry in the overall device. These phenomena could be investigated further by producing a completely symmetrical device. To achieve a symmetrical device, the connection channels between the inlet/outlet and the micropump, must be the same length, unlike the device investigated here.

To determine the deflection of the diaphragms of the micropump an interferometer was used successfully to measure the dynamic deflection of the three diaphragms of the peristaltic micropump. The total deflection of the diaphragm in the centre was measured to be approximately $9\mu m$, which occurred in approximately $3 - 5\ ms$ using

$\pm$100 v. The data from this investigation has been an essential tool in determining the limits of the micropump actuation frequency and pump rate. This method is limited to only measuring the deflection of a single point of the diaphragm, due to the set up used for the interferometer. It would be useful to be able to determine the deflection of an entire deflected diaphragm and not just a single point. This could be achieved by scanning over the surface of the diaphragm. A complete scan over the diaphragm surface would enable the production of a three dimensional representation of the diaphragm and therefore the determination of the exact displaced volume. This information could be used to produce a more accurate theoretical pump rate.

Much knowledge has been gained in the processing and testing of microfluidic devices during this work. The results gained from this investigation have been useful in researching the peristaltic micropump. The investigation has been continued, to further characterise the micropump beyond the scope of this work. The micropump has been demonstrated to move a 1 μl droplet back and forth through the reaction chambers within the microdevice (see Figure 2.1, Section 2.1). Further results and analysis of this micropump have been documented by Bu [37]. Investigations of the use of the micropump for the production of a pipetting system were not continued, because a new technique which is described in Chapter 4 was proposed.

Chapter 3

Review of microstructured injectors and dispensers

3.1 Introduction

Microfluidic devices are being produced to replace current technology used for the biomedical sciences [75; 38; 6; 5; 4]. These fluidic devices, sometimes referred to as micro total analysis systems (μTAS) or Lab-on-a-Chip, will enable smaller reagent and sample volumes to be used and allow for higher parallel processing [76; 77; 78]. These μTAS will combine all of the components needed for sample handling and processing. These components include pumps([9; 54; 60; 61]), pipettes [32; 13; 14] and mixers [79; 80; 81] for instance. Pipettes form an important part of any microfluidic system and are necessary for the precise metering and dispensing of controlled volumes of fluid. The fluid which is dispensed could be a sample or reagent to be mixed for subsequent processing.

The aim of this thesis is the design, fabrication and testing of a novel dispensing device, required for pipetting precise fluid volumes. Though the behaviour of introducing droplets into fluid flow has been studied [82; 83], there have been few workable devices produced for this application. Here current dispensing and injection principles will be discussed, including examples of microdevices. Analysis of suitable techniques which can be exploited further for a pipettor will be discussed and evaluated.

The following review examines the most significant physical effects that are observed when reducing the dimensions of devices to the microscale. This is followed by examples of current pipette techniques, devices, and how these devices are designed to overcome the difficulties of fluid handling in microdevices. The review concludes with examples of valves/structures to aid the design of a novel pipette device. Pipette design requires the discussion of fluid control (or pumping) to move samples through the microdevice and valving to ensure that the flow is only in one direction; toward the outlet. These areas are discussed in the following sections.

3.2 Microfluidics

When reducing fluidic devices to the micrometre scale, physical phenomena not encountered at the macro scale must be considered [1; 78; 76; 84; 36]. These effects can be both detrimental and useful when producing fluidic devices. The most significant phenomena that must be considered for the design of a pipette device are discussed, these are flow regime, fluid resistance and surface tension.

3.2.1 Flow regime

The flow regime describes the transport of the fluid through an enclosed channel or duct. The fluid transport can be separated into either laminar or turbulent flow. The Reynolds (Re) number is used to classify which type of flow is present in a microchannel, and can be calculated using Equation 3.1 [85; 84; 86], where ρ is the fluid density, $\bar{\nu}$ is the average fluid velocity, D_h is the hydraulic diameter of the channel and η is the viscosity of the fluid. The hydraulic diameter of the microchannel is a ratio of the cross-sectional area of the channel (A) to the wetted perimeter(P_{wet}) as given in Equation 3.2.

$$Re = \frac{\rho \bar{\nu} D_h}{\eta} \tag{3.1}$$

$$D_h = \frac{4A}{P_{wet}} \tag{3.2}$$

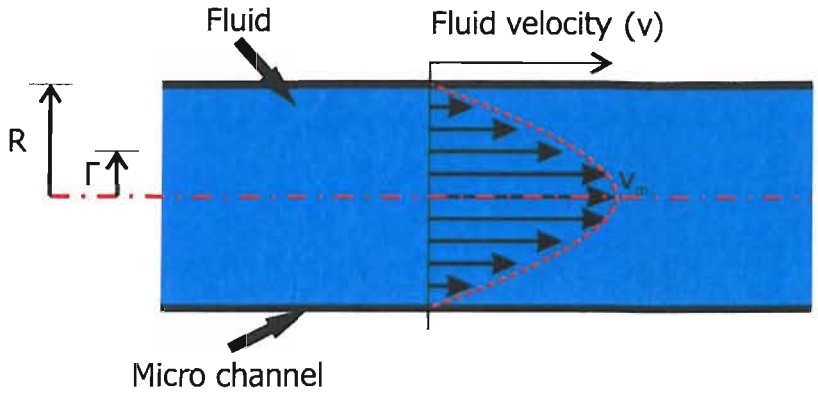

Figure 3.1: Microchannel profile, illustrating normalised flow, with a parabolic fluid front.

The velocity profile for a circular channel, as illustrated in Figure 3.1, can be predicted using Equation 3.3, where ν_m is the maximum velocity, R is the channel radius. The velocity (ν_r) of the fluid will be determined as a function of the radius, at a point Γ. The maximum fluid velocity in the centre of the channel can be predicted using Equation 3.4, where Δp is the pressure difference over the channel length L.

$$\nu_r = \nu_m \left(1 - \frac{\Gamma^2}{R^2}\right) \tag{3.3}$$

$$\nu_m = \frac{1}{4\eta}\frac{\Delta p}{L}R^2 \tag{3.4}$$

If the Reynolds number is calculated to be less than 2300 the flow is termed laminar. As the name suggests, a laminar flow regime consists of sheets of fluid flowing smoothly and steadily through the channel. The velocity of a particle in a laminar fluid stream will not be random with time [84], therefore the flow is predictable. Figure 3.1 illustrates the fluid velocity across a channel, showing the parabolic flow distribution. Due to this distribution most calculations involving the fluid velocity will consider the average fluid velocity across the channel. The drawback of laminar flow is that it is difficult to mix fluids; the only way to effect mixing is by diffusion. If two fluids are introduced separately into a microchannel and the two fluid streams flow in contact, then mixing occurs due to molecular diffusion. Fluidic devices for passive mixing can be enhanced by creating several laminations of the fluidic streams [87; 88; 89; 90].

3.2.2 Fluid resistance

Fluidic resistance is a result of the interaction between the fluid and channel walls. This effect is greater in microdevices because the ratio of the cross sectional area of the channel to the channel perimeter is greater in microdevices. The fluid resistance in a closed channel can be described using $\Re = \Delta p/Q$, where $\Re$ is the resistance, Δp is the pressure drop along the length of the channel and Q is the volume flow rate [85; 84; 86]. The viscous flow resistance due to a circular duct can be calculated using a result from the work of Hagen-Poiseuille, as shown in Equation 3.5 where η is the fluid viscosity, L is the channel length and R is the radius of the channel. The volume flow rate within a circular duct is given in Equation 3.6.

$$\Re = \frac{8\eta L}{\pi R^4} \tag{3.5}$$

$$Q = \frac{\pi R^3 \Delta p}{8\eta L} \tag{3.6}$$

The circular channel is the most commonly evaluated theoretically, but it is easier to produce channels with a rectangular cross section by microfabrication techniques. The fluid resistance due to a rectangular channel can be expressed simply by using Equation 3.7, where η is the fluid viscosity, L the length of the channel, w is the channel width and h is the channel height. This can be used only when the width of the channel is much greater than the height ($w >> h$). This is because this expression is for the fluid resistance due to two parallel plates and therefore it is assumed that the contribution to fluid resistance, due to the side walls of the microchannel, is much less than the resistance due to the upper and lower walls.

$$\Re = \frac{12\eta L}{wh^4} \tag{3.7}$$

3.2.3 Surface tension

Surface tension is the measure of how much free energy a surface contains [84; 91] and is the result of the interaction of the liquid molecules with the surface. The molecules deep within the fluid are densely packed and therefore experience cohesive forces between all neighbouring molecules and therefore all the forces will be balanced. The molecules at the surface of the liquid are less densely packed and half of the liquid molecules are missing at the surface, due to a liquid/gas or liquid/liquid interface, resulting in an imbalance of the cohesive forces. This mechanical effect is known as surface tension [85].

The liquid/surface interaction must also be considered, because this will affect the surface tension of the fluid. The forces between the fluid molecules and the surface molecules will result in adhesion between the fluid and the solid boundary. The molecular attraction within the fluid, results in cohesion. If the adhesion force between the fluid and the surface boundary is greater than the cohesion force between the fluid molecules, the fluid molecules will crowd towards the solid surface. This results in the fluid spreading over the solid surface, wetting the surface, and decreasing the contact angle; this surface is defined as hydrophilic. If the opposite occurs; the cohesion force exceeds the adhesion force the contact angle will increase and it is defined as a hydrophobic surface [86]. Figure 3.2 illustrates two droplets, on a hydrophobic and hydrophilic surface, showing the change in contact angle.

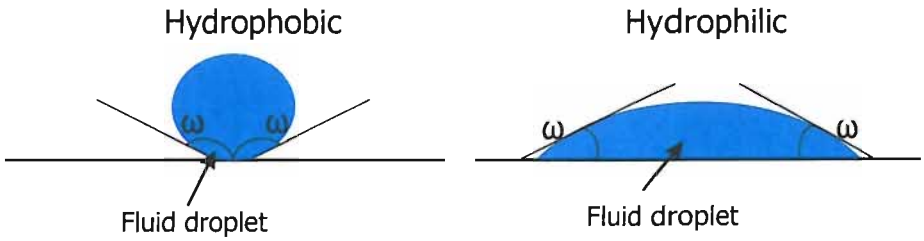

Figure 3.2: Illustration of a fluid droplet on a hydrophobic and hydrophilic surface, showing the contact angles between the fluid and the surface.

The surface tension of a liquid droplet with perpendicular radii of curvature can be expressed mathematically as a pressure drop (Δp) across the liquid/gas interface, by using Young's Laplace Equation 3.8, where γ is the free surface energy of the fluid and ω_1 and ω_2 are the contact angles of the fluid and the surface.

$$\Delta p = \gamma \left(\frac{1}{\omega_1} + \frac{1}{\omega_2} \right) \tag{3.8}$$

This expression can be simplified for a droplet of fluid to Equation 3.9, such that the pressure contained within a fluid droplet can be calculated, because the contact angles are equal.

$$\Delta p = \frac{2\gamma}{\omega} \tag{3.9}$$

The implication of surface tension is that there is an additional force which must be considered when moving fluid droplets through a microchannel, which is the capillary force. To enable the transport of a droplet through a microchannel, both fluid resistance and the capillary force due to the surface tension must be overcome. The capillary force (F_{cap}) due to the surface tension can be calculated using Equation 3.10, where ω is the contact angle of the fluid and the surface and R is the channel radius. The capillary force is due to the surface tension at the tail end of the droplet, given by Equation 3.10 (as shown in Figure 3.3) .

$$F_{cap} = 2\pi R\gamma cos(\omega) \tag{3.10}$$

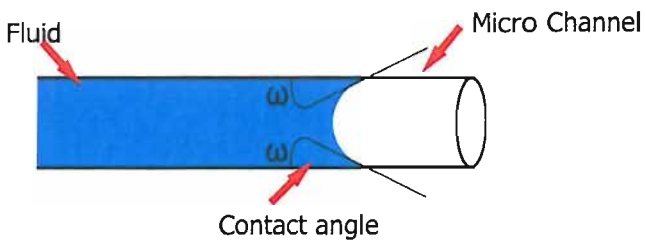

Figure 3.3: Illustration of a fluid meniscus showing the contact between the fluid and the channel surface.

If a droplet is introduced into a microchannel the capillary force will act at both ends. This will result in the droplet remaining stationary because the forces will be equal in magnitude and in opposite directions, as illustrated in Figure 3.4. However if fluid is introduced at one end of a channel, the fluid will be drawn into the channel

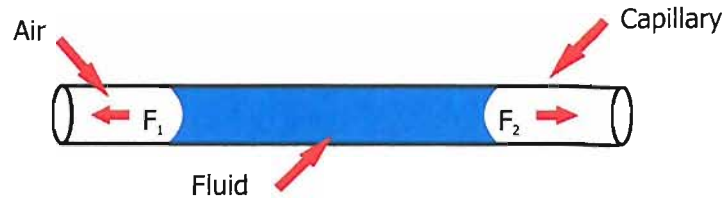

Figure 3.4: Illustration of a fluid droplet in a microchannel, showing that because there is no resultant forces the droplet will remain stationary ($F_1 = F_2$).

due to the capillary force. This movement of fluid will continue until an opposing force acting on the fluid counteracts it.

Surface tension is useful in microsystems because capillary action will enable priming of microdevices with a fluid that experiences no other external forces. However, the capillary action can be detrimental to some applications because moving droplets is more difficult on the microscale since the surface tension must be overcome to move a droplet through a channel.

The surface tension or capillary force is calculated using the contact angle between the fluid and the surface or the radius of curvature. If the contact angle is less than 90° the surface is hydrophobic and if the contact angle is greater than 90° the surface is hydrophilic. It is possible to change the contact angle by modification of the channel surface [41], and by doing so, it is possible to decrease or increase the capillary force. Techniques such as the deposition of Carbon Hydro-Trifluoride (CHF_3) or Octafluorocyclobutane (C_4F_8) patches on the microchannel surface have been used to produce devices which exploit surface effects [92; 41; 91; 10; 93; 94].

3.3 Fluid dispensing technologies

3.3.1 Pipettors and injectors

Pipetting devices are widely used for inkjet printing; picolitre volumes of fluid are repeatedly dispensed [95; 96; 97; 40; 98; 99]. Pipetting devices are a crucial part of microsystems; providing a technique for the precise dispensing of fluid volumes [100; 101]. Techniques for actuating pipette devices include thermal, PZT and plunger actuators.

Injection devices are commonly used to dispense fluid droplets into air. To make this possible the droplet must be given sufficient energy such that it is released from the nozzle. The energy in this case will be kinetic due to the velocity of the droplet [102]. Once the fluid has reached the nozzle of the device, this energy must be great enough such the surface effects of the fluid and nozzle can be overcome. If the release is not complete, a tail or satellite droplets are formed which follow the main droplet which is highly significant for printing because it will affect the image.

Printing devices require arrays of nozzles to produce characters and images with high resolution. This has been transferred to microsystems where arrays of pipette nozzles are used for spotting and filling well plates used in biosystem analysis. These systems differ from conventional printing devices because usually all the nozzles are used to dispense fluid simultaneously; in contrast to printing technology where each nozzle is individually addressable. The actuation approach, used to produce single pipettes, arrays and inkjet devices, will be discussed further below.

PZT actuation

Lead zirconate titanate (PZT) is a piezoelectric material that is used for actuators in microsystems, due to the speed and displacement that can be achieved. PZT is generally used in conjunction with a diaphragm to form a bimorph actuator. The PZT is attached to the diaphragm, which constricts the motion of the PZT. This motion would typically be a dimension change for planar PZT ceramics. If the PZT is actuated the length will increase, but because it is attached to a diaphragm this is not possible, therefore the diaphragm will bend up or down. Using this technique displacements of up to 10 μm have been achieved in $1 - 10\mu s$, using 100 v [37].

Injection devices using PZT are usually of the form used to produce micropumps (see Chapter 2). These are typically known as bend-mode pipettes, because the diaphragm is bent down into the displacement chamber. Alternate methods include shear and push mode technologies [103]. The configuration of a bend-mode injection device is illustrated in Figure 3.5. The device includes many components similar to those used in a single diaphragm micropump design [48; 51]. The components include an inlet

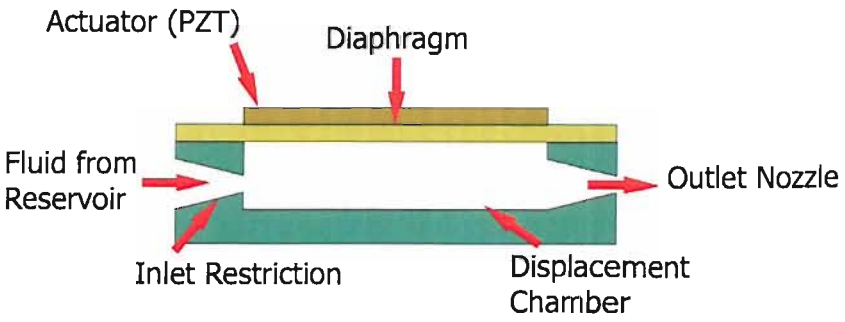

Figure 3.5: A pipette device including a PZT actuator in a bend mode configuration.

restriction, displacement chamber, diaphragm, PZT actuator and outlet nozzle. The fluid is drawn into the device due to capillary action and fills the displacement chamber. When the PZT is actuated the diaphragm will deflect down, displacing a volume of fluid. The volume of fluid which is dispensed at the outlet nozzle is dependant on the volume displaced by the diaphragm and the difference between the fluid resistance to the reservoir and the outlet nozzle. By ensuring that the resistance back to the reservoir is greater than the resistance to the outlet nozzle, the majority of the fluid will be dispensed at the outlet nozzle. When the voltage is removed from the PZT actuator the diaphragm will relax back to the original position, thus refilling the displacement chamber. The force of the actuator is not great enough to overcome the capillary force at the nozzle, so no air will be drawn into the device.

Drop on demand devices have been produced which use the structure described above, with some modifications. Single pipette devices have been produced by Chen et al. [104] (45 *pl*, 25 v actuation), Laurell et al. [105] (100 *pl*, 50 v actuation), Luginbuhl et al. [106] (3.6 *fl*), Bergkvist et al. [107] and (60 *pl*, 33 v actuation) implementing a bend mode technique. The devices are fabricated in a variety of materials including nickel, silicon and Pyrex. The configuration of the devices is similar to Figure 3.5, but the nozzle position is different, forming an up or down shooting injection device. The different configuration is illustrated in Figure 3.6. The devices have been used to produce droplets down to femtolitre volumes, using actuation voltages up to 70 v.

An alternative configuration of the bend-mode has been produced by Lam et al. [108], which uses a circular actuator. The actuator is situated around the nozzle of the injector device. The device can be used to dispense volumes of fluid similar in volume to

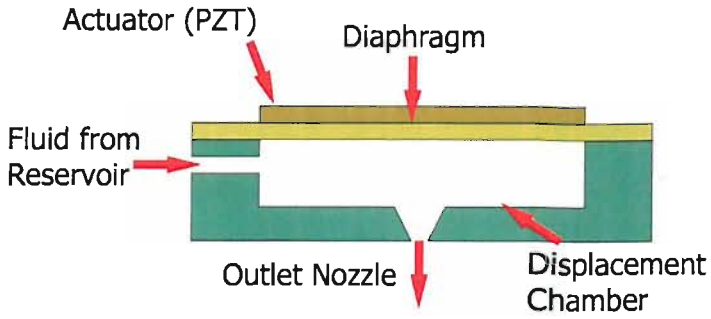

Figure 3.6: An alternative configuration of a bend mode pipette device realised for upward or downward fluid injection.

other PZT devices, with a reduced actuation voltage. This is possible because the PZT used has higher piezo electric coefficients, making it possible to produce displacements ten times higher for a given actuation voltage.

A simple device has been produced by Streule et al. [109], which uses the same principle as a PZT actuated pipette. The device consists of a polymer tube to dispense fluid, using a mechanical plunger. The tube is connected to a reservoir which is used to fill the tube by capillary action. The plunger squeezes the tube from above in a fast downward motion, dispensing fluid at the open end of the tube. The plunger is slowly retracted and the tube refills from the reservoir. No air or fluid enters the open end of the tube because of the capillary forces. This device was used to repeatably dispense a droplet of 22.6 nl, using an actuation frequency of 0.1 Hz.

Thermal actuation

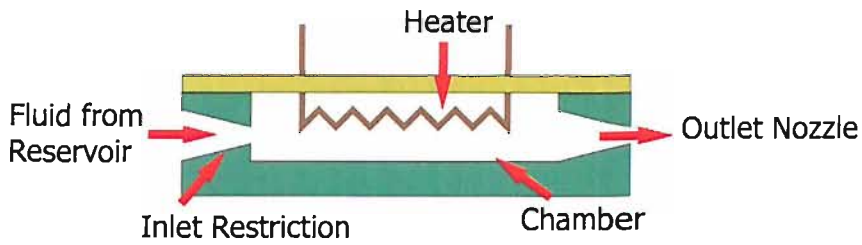

Figure 3.7: A pipette device which includes a heating element for thermal actuation.

Thermal actuation is another typical actuation approach used in printing pipettor/inkjet systems, sometimes known as bubble jet printing [96; 97; 95; 110; 60; 61]. A lot of research on this technology was carried out by printer manufacturers such as

Hewlett Packard [16; 15] and IBM [111; 112; 113] between the 1970's and the 1990's. Today the technology boasts up to 4800 dots per inch (dpi) using the current inkjet technology. The principle of displacing fluid from a chamber is similar to the PZT actuation technique described previously. The configuration of a typical thermal injection device is illustrated in Figure 3.7. The device is actuated using an electrical heater, within the fluid chamber. When a voltage is applied to the heater element, the temperature of the heater and the fluid will increase such that the fluid vaporises. This results in a bubble formation in the chamber, which is used to force fluid out of the chamber via the outlet nozzle. Similar to the PZT actuated device, some fluid will be displaced back to the reservoir, but this is kept to a minimum using a flow restriction between the reservoir and the chamber. When the voltage is removed from the heater element the bubble will collapse and fluid will be drawn back into the chamber from the reservoir.

The simple diagram in Figure 3.7 illustrates the configuration of a thermal pipette device, but actual thermal devices are designed with a number of configurations, an example is illustrated in Figure 3.8. Devices with this alternative configuration have been produced by Tseng et al. [114, 115, 116], Baek et al. [40, 98, 117], Shin et al. [99] and Bae et al. [118] for inkjet print heads. The heater for these devices is usually located either side of the nozzle, but examples have also been produced with the heater opposite the nozzle. Two heating elements have been integrated to reduce dispensing without a fluid tail. Most of the research for these devices has been focused toward printing technologies; therefore the focus has been to produce smaller perfect dots. The two heaters are used simultaneously to produce vapour bubbles in the fluid. The two bubbles increase in size until the bubbles combine, cutting the droplet off in the nozzle and separating the droplet from the bulk of the fluid in the fluid chamber.

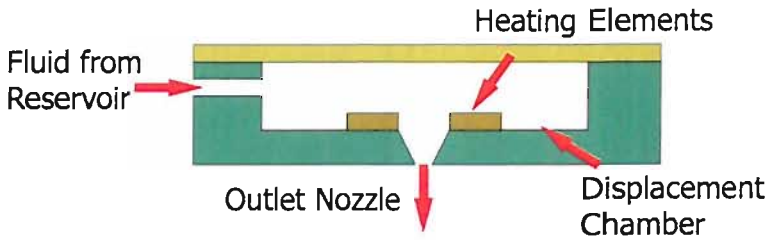

Figure 3.8: An illustration of a possible commercial thermal print head configuration.

As mentioned above, the biggest problem with this approach for droplet ejection is the production of perfect droplets without satellite droplets. This has been overcome by altering the frequency of actuation, the heater energy, the nozzle design and the heater design [119; 120]. Thermal devices have been fabricated which have been used to produce droplets down to 30 pl in volume at a frequency up to 12 kHz [40; 98; 117] and down to 1 pl at a frequency of 35 kHz [115; 116], allowing for 1200 dpi to be achieved.

All the devices that have been discussed dispense fluid into air. It is only if the fluid has enough energy to overcome the surface effects in the nozzle that the droplet is released. No fluid or air is drawn back into these types of injection devices via the nozzle due to capillary forces at the outlet orifice. This capillary force, within the device, is very advantageous. However, for the device being produced for this research fluid is to be dispensed into another stationary fluid. For the proposed device, a mechanism to separate the dispensed fluid from the remaining fluid in the displacement chamber will be needed.

Thermally actuated devices have the advantage of fluidic separation of the droplet from the reservoir because the bubbles produced in the fluid, will automatically cut off the dispensed fluid. However this thermal technique is not suitable for all biological applications due to the sensitivity of such systems to high temperatures.

Plunger actuation

The techniques described so far have been developed specifically for microfabricated pipette devices. However devices have been produced which use a simple syringe-like technique to dispense fluid by implementing a plunger within a microchannel. This technique is less 'main stream' and uses a ferrofluid which is a stable colloidal suspension of magnetic particles with an average diameter of 10 nm, in an oil liquid carrier to form a plunger [121]. These particles are coated with a stabilizing dispersing agent to prevent the formation of a large mass and to maintain an even dispersion of particles.

The ferrofluid can be introduced into a microchannel and controlled using an external magnetic field. When the ferrofluid is introduced into a microchannel, without the presence of a magnetic field, the magnetic moments of the particles are randomly

distributed. When a magnetic field is applied the moments of the particles orientate along the magnetic field. However when the magnetic field is removed the moments become random again very quickly. This is because the size of the magnetic particles is only approximately 10 *nm*. In a magnetic field gradient the ferrofluid responds as a homogeneous magnetic liquid, moving towards the highest magnetic field region. The retention force and therefore the force which can be applied with a ferrofluid plug is proportional to the gradient of the external field and the magnetization value of the fluid.

Pipette devices have been produced which utilise ferrofluid actuation. Greivell and Hannaford [32] have produced an electromagnetic pipette device using a magnetite (iron oxide) suspended in a light-hydrocarbon based oil. The device consists of a Tefzel tube containing a 22 *mm* long ferrofluid plug. Three external electromagnets are positioned around the outside of the tube. The electromagnets are actuated in turn to move the ferrofluid plug along the channel. To use this device to dispense fluid there is a valve structure, which is used to allow fluid into the device when the ferrofluid plunger is moved away from the outlet. When the plug is moved towards the outlet the fluid will be forced out of the device.

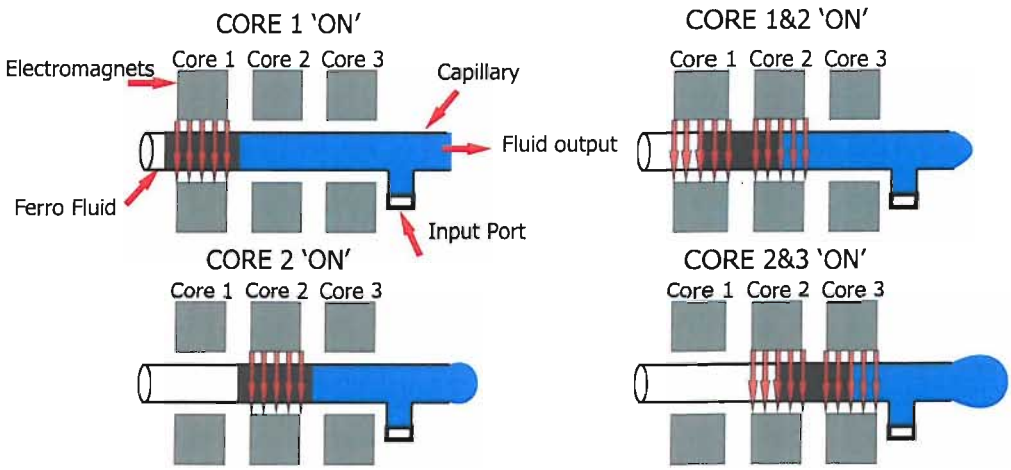

Figure 3.9: An illustration of the ferrofluid pipette device produced by Greivell and Hannaford [32], to dispense fluid using electromagnetic actuation of a plunger of ferrofluid. The ferrofluid plug is moved to the right using an electromagnet sequence thus dispensing the fluid from the capillary.

A second device has been produce by Ahn et al. [14] where an external permanent magnet is used. The device consists of a channel etched in silicon which is capped with

Pyrex. The channel is circular allowing the magnet to be moved using a motorised rotation stage. This device can be used to successfully dispense fluid, but the device must be refilled via the outlet using a similar method to that for a syringe. This device has obvious drawbacks, because the total volume of fluid which can be dispensed is limited by the volume in the device channel.

The application of ferrofluid in a microchannel is a very simple technique for dispensing fluid, producing a syringe like device. The main problem with this device is that ferrofluids are generally oil based, thus limiting the applications. The utilisation of ferrofluids with biological solutions will result in degradation of the biological sample. An alternative bio-compatible fluid would be required to make this technique more valuable for biological MEMS applications.

3.3.2 Spotting/printing microtechnologies

There has been significant effort devoted to the development of large arrays of spotting/printing techniques. These are generally spotting devices used either to load many samples into a well plate [122] (well plates are used for massively parallel analysis) or to spot large numbers of samples and reagents onto surfaces, such as microarrays [123]. A requirement is that these devices can be used to repeatedly dispense the same volume of fluid without cross contamination between each dispensing nozzle; this is important because different nozzles could be used for different samples or reagents.

The most commonly used method for dispensing, for such spotting or well plate devices, is to apply pressure [123; 124; 125; 122]. Figure 3.10 illustrates the configuration of one pipette device, which could be produced in a matrix of many devices as developed by Koltay et al. [125, 122]. The reservoir containing the sample is connected via a channel to the displacement chamber. The displacement chamber is filled and refilled by capillary action. The reservoir can be filled by more conventional hand pipettes suitable for higher volumes (800 nl). When a pressure pulse is applied to the top surface of the device the fluid is forced out of the nozzle. The pressure is applied across the top of the entire device, to prevent the fluid flowing back to the reservoir. Typically the dispensed volumes for the devices produced by Koltay et al. [125, 122] are approximately 50 nl.

The disadvantage of this technique is that the device can only be used for up to 16 doses before refilling.

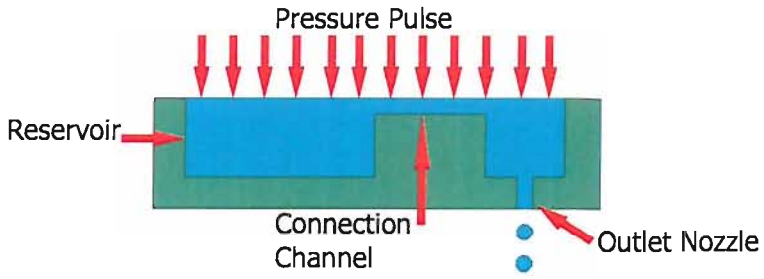

Figure 3.10: Illustration of the TopSpot technique for highly parallel fluid dispensing ([125; 122]).

An alternative configuration has been produced by Ducree et al. [123] and de Heij et al. [124] and is illustrated in Figure 3.11. The difference with this configuration is that the pressure pulse is only applied to the nozzle chambers and not to the reservoir. This means that the operation of the device relies on the resistance to the reservoir being greater than the resistance of the nozzle, therefore a greater volume of fluid will be dispensed at the outlet. The pressure pulse is applied using an elastomer compressed by a PZT actuated piston [124; 17] or a cushion of air actuated using a pneumatic actuator [123]. These devices have been used to dispense fluid volumes from 60 nl to 800 nl using different actuation techniques.

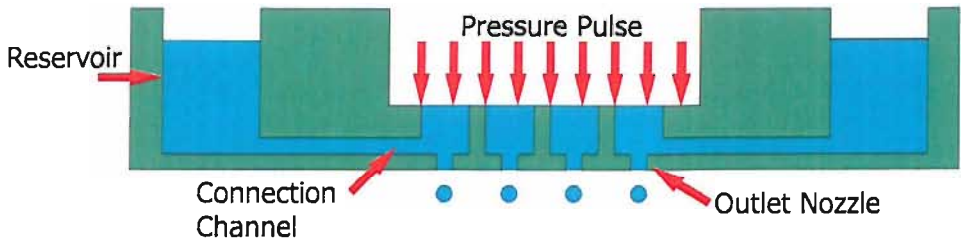

Figure 3.11: Illustration of an alternative method for highly parallel fluid dispensing, applying pressure only to the fluid outlet chambers ([123; 124]).

An electrostatically actuated device has been produced by Takagi et al. [126] to form a dispensing biochip. It is based upon an electrostatic inkjet print head. An electrostatic force is used to actuate a pressure plate. This is used to create a negative pressure drop within the ink cavity, drawing ink in from the reservoir. When the pressure plate is actuated in the opposite direction the fluid is forced out of the device and not back to

the reservoir. This device has 128 nozzles with a dispensed fluid volume of approximately 15 *pl*.

These highly parallel devices are suited to delivering many samples simultaneously. The dispensing technique is simple; using pressure from an external plunger, which could be applied to a single pipette device. A potential problem with this device is that the droplet delivery is into air in common with the inkjet printing technologies. This prevents fluid from being drawn back into the displacement chamber during refilling. However if a droplet is simply dispensed into an adjacent fluid, the sample could be drawn back in when refilling the displacement chamber. The device being developed during this work is for droplet delivery into fluid. The other problem is that the pressure pulse is generally applied externally. For highly parallel dispensing systems (with many nozzles) this is acceptable. However, for a single dispensing device, a large external actuator may be unacceptable. The technique would be more appropriate if the actuator providing the pressure pulse could be integrated in the device.

3.3.3 Fluid metering

Precise metering of fluid within microsystems is achieved by separating a droplet of fluid from a bulk of fluid. A metered volume of fluid is an aliquot of fluid of a defined volume. Most of the pipette techniques which have been discussed so far dispense fluid into air, thus the metering of the fluid is achieved when the droplet is released from the device. This is not always the case as fluid dispensing might be required within a microsystem, therefore techniques to precisely meter a fluid droplet within a microdevice are required. Precise fluid metering has been successfully achieved within microsystems by combining hydrophobic regions and air pressure within a microchannel [127; 128; 129].

Surface tension has already been discussed in Section 3.2.3, which is the principle used here for fluid metering. The surface tension at either end of a droplet results in a pressure difference between the fluid and the air. Figure 3.12 illustrates a droplet in a microchannel and the resulting pressure difference created due to the surface tension. This previously discussed result is for a circular channel, but the same principle can be applied to a rectangular channel. Equation 3.11 illustrates how the pressure drop, due

to the surface tension of the droplet, can be used in the case of a rectangular channel, where γ is the surface energy of the fluid, ω is the fluid/surface contact angle, h and w are the height and width of the channel respectively.

$$\Delta p = \gamma \, cos\omega \frac{2h + 2w}{hw} \tag{3.11}$$

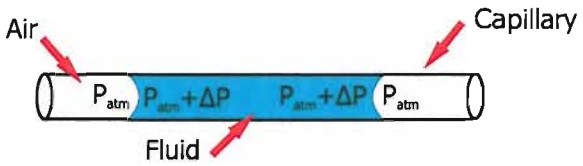

Figure 3.12: An illustration of a microchannel containing a fluid droplet, to demonstrate the Laplace equation.

The pressure difference across the liquid gas interface can be used to form a valve within a microchannel which forms part of this metering technique. If the surface of the microchannel is modified to be more hydrophobic or hydrophilic, the contact angle of the fluid will be altered and therefore the pressure drop will change. The pressure difference, calculated using Equation 3.11, is the minimum pressure which is required for the fluid to be moved past a region in a microchannel. This pressure difference results because the contact angle between the fluid and the channel surface will be higher in the modified region than in the rest of the channel, which will be unmodified.

To be able to use this technique, the channel surface has to be modified, which can be carried out chemically when the channel is complete [41]. If it is not possible to carry out the modification once the channel is complete, this can be achieved during the fabrication process. If not all of the walls of a rectangular channel are modified, Equation 3.11 can be adapted to take into account of the different channel surface materials. Equation 3.12 can be used to predict the pressure required to overcome a modified hydrophobic region which covers the bottom and side walls of a microchannel; the top of the channel is formed with unmodified glass [10]. This alone can be used as a stop valve for fluid in a microchannel, an example has been produced by Feng et al. [41]. Two types of hydrophobic modifications were used; a chemical octadecyltrichlorosiliane (OTS) and plasma deposited triflouromethane (CHF_3). These were demonstrated to produce a stop pressure of approximately 490 Pa.

$$\Delta p = \gamma \cos(\omega_{MODIFIED}) \frac{2h + w}{hw} + \gamma \cos(\omega_{GLASS}) \frac{w}{hw} \tag{3.12}$$

To be able to use this technique to meter fluid, air pressure is used. A region of a microchannel is modified such that it is hydrophobic. The fluid is introduced into the microchannel, which will fill up to the hydrophobic region due to capillary forces. For this technique to be work, the fluid must be hydrophilic. When the fluid has reached the hydrophobic region, air pressure is applied to the fluid from a side channel, to overcome the hydrophobic region [127; 128; 129; 130; 131], as illustrated in Figure 3.13. The surface of any pressure vent is also modified, such that no fluid will escape. When the fluid is over the hydrophobic region there is no longer a pressure difference, so the fluid will continue to flow. The air pressure will be used to continue to move the metered volume of fluid over the region until there is no fluid in the modified region of the channel. At this point the air pressure is removed and the device will be refilled by capillary action up to the modified region.

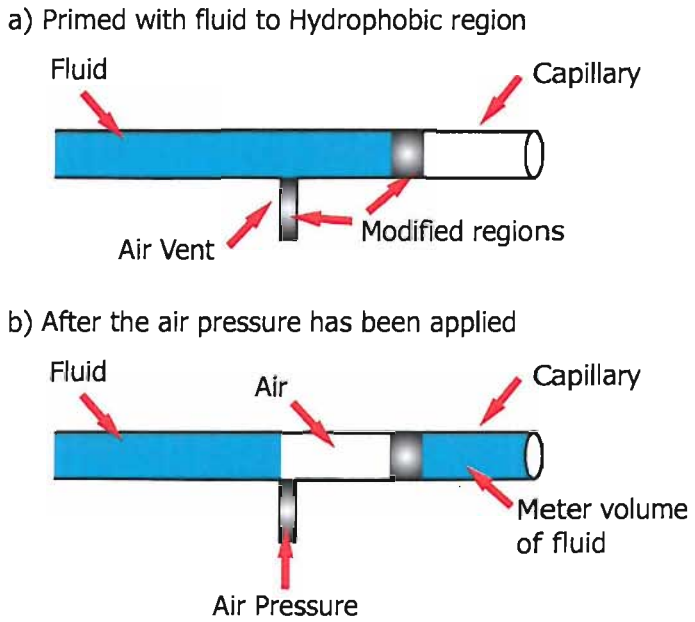

Figure 3.13: An illustration of a hydrophobic pressure valve.

Handique et al. [127, 128, 129] have produced devices similar to those shown in Figure 3.13. Areas in a fabricated microchannel were modified using a silanization treatment. The modified areas were patterned using a metal (aluminium or titanium) mask. The devices consist of 20 μm and 40 μm deep microchannels, used to accurately

meter volumes of fluid between 5 and 50 nl. Burns et al. [130, 131] and Lee et al. [30, 31] have used this technique of fluid metering within a nanolitre analysis/reaction device. Structures similar to the ones illustrated in Figure 3.13 were used to meter the correct quantity of samples at the entrance of this analysis device. These techniques have been typically used to meter volumes of fluid in the nanolitre range.

A device which uses a similar technique has been produced by Hosokawa et al. [132, 133, 134] for fluid metering of picolitre samples. Instead of simply using hydrophobic regions to stop the fluid, this technique implements microcapillaries produced using Polydimethylsiloxane (PDMS), which is inherently hydrophobic. Figure 3.14 illustrates the device configuration and shows how the device operates. The fluid is introduced from the left hand side of the microchannel (100 μm wide, 25 μm deep), where the fluid will be drawn into the device up to the microcapillaries. The fluid stops at the microcapillaries, because the surface is hydrophobic, and the dimensions of the microcapillaries are much smaller than the proceeding microchannel. Once the channel is filled up to the valve, air is introduced at the side vent which separates a droplet from the main bulk of fluid. The device was used to meter volumes of fluid as small as 600 pl. The theoretical pressure required to drive fluid past the valve was predicted to be 27 kPa, using an expression of the form of Equation 3.11, but it was found experimentally to be $30 - 35$ kPa.

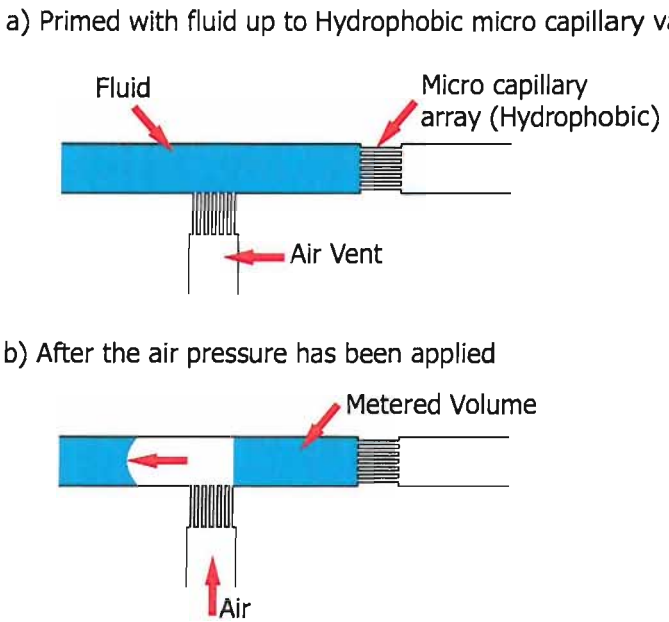

Figure 3.14: An illustration of a hydrophobic pressure valve, using microcapillaries.

The technique of combining modified surfaces and pressure is a very simple method for dispensing fluid. Examples have been identified which are used to precisely meter nano volumes of fluid. The metered volumes of fluid have then been transported within a microdevice for analysis or for mixing with other metered volumes. To be able to produce a device for metering and manipulating droplets a more complicated channel structure would be required to be used in conjunction with an air pressure system. Air pressure would be required to both produce a droplet and move it within the microdevice. The air pressure could be provided externally or by using an integrated pump.

3.4 Nozzles and valves

Nozzles and valves can be separated into two types, dynamic and active. These structures were discussed earlier in Chapter 2 when used in micropumps. Dynamic valves are structures which can be used to create a pressure drop that is dependant on physical parameters, such as fluid velocity. Active valves are used to create a barrier for the fluid and can be actuated open or closed. This type of valve may also be dependant on pressure, but could be used to completely stop fluid flow.

Dynamic valves usually take the form of a dimension change within a microchannel. This could be a sudden or gradual change, which results in a change in the fluid flow velocity. The change in velocity is due to the change in dimension and occurs because the volume flow rate remains constant. The pressure difference which results due to the fluid expansion, or contraction, in the microchannel can be calculated using Equation 3.13, where Δp is the pressure difference, K is the head loss factor, η is the fluid viscosity and $\bar{\nu}$ is the average fluid velocity through the microchannel. The head loss factor can be expressed as a dimensionless factor and it is normally determined experimentally [71] and is used to evaluate the total pressure across a part of a system.

$$\Delta p = K\left(\frac{1}{2}\eta\bar{\nu}^2\right) \tag{3.13}$$

The head loss factor for channel expansions and contractions, both sudden and gradual, has been obtained experimentally, these are presented in Table 3.1

Sudden contraction	Sudden expansion	Gradual contraction	Gradual expansion
0.44	1	0.1 (35.3°)	1 *to* 1.2 (35.3°)
		< 0.02 (2.6°)	0.25 (2.6°)

Table 3.1: Experimentally obtained 'head loss factor' for a gradual and sudden expansion and contraction within a closed fluidic system [71].

If a diffuser and nozzle structure is implemented for the input and output of a micropump it is possible to produce a positive displacement of fluid. This is possible because the head loss coefficient of a diffuser is different from that of a nozzle. Figure 3.15 illustrates an example of a micropump which has diffuser/nozzle valves, labelled as *Duct* 1 and *Duct* 2. When the diaphragm is actuated in an upward direction, fluid is drawn into the device. *Duct* 1 (diffuser) will have a greater pressure drop than *Duct* 2 (nozzle), therefore more fluid will be drawn into the displacement chamber via *Duct* 2. When the diaphragm is moved in a downward direction fluid is forced out of the device and the diffuser and nozzle are switched because of the change in fluid direction. Now more fluid will be forced out of *Duct* 1 (nozzle), than *Duct* 2 (diffuser). The result is positive displacement of fluid from right to left, with respect to the device in Figure 3.15 or described as fluid flow from *Duct* 2 to *Duct* 1. Devices have been successfully produced by Koch et al. [48] with this technique, which was used to pump against a back pressure of 550 Pa.

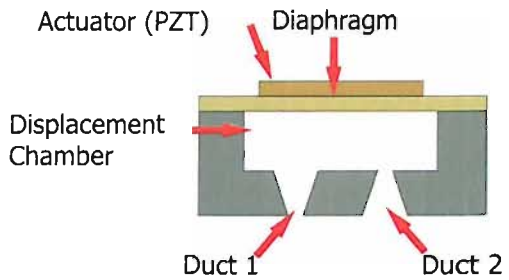

Figure 3.15: An illustration of a single chamber micropump, with dynamic valves.

A technique which consists of a nozzle followed by a sudden expansion has been used as a unidirectional stop valve, by Man et al. [92] as illustrated in Figure 3.16. This can be used to stop flow because of the increase in the channel dimension going

from a nozzle to a sudden expansion, illustrated in Figure 3.16. When a fluid meniscus approaches the orifice of the nozzle by capillary force (from left to right in Figure 3.16), the contact angle will change because of the sudden expansion that precedes the gradual contraction. This will result in a change in the contact angle and therefore decrease the surface energy of the fluid. To move the fluid through the structure an external pressure must be applied. However if fluid is applied at the opposite end of the device (from right to left in Figure 3.16), no barrier effect is observed. The structures in this device were used to produce a pressure barrier of up to $1kPa$.

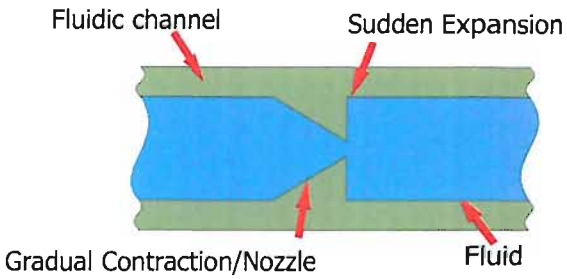

Figure 3.16: A unidirectional stop valve, with a nozzle followed by a sudden expansion [92].

A similar technique has been used by Melina et al. [135] to create a valve for fluid, which prevents flow unless both fluids are present at a junction within the device, illustrated in Figure 3.17. If fluid is only introduced at one of the inlets of the device, the fluid will stop where the two channels come together; illustrated in Figure 3.17. This structure alters the contact angle, resulting in a decrease in surface energy. When fluids are applied to both inlets, the fluids come together and can flow through the device. The device was used to provide a barrier pressure of 7.3 kPa.

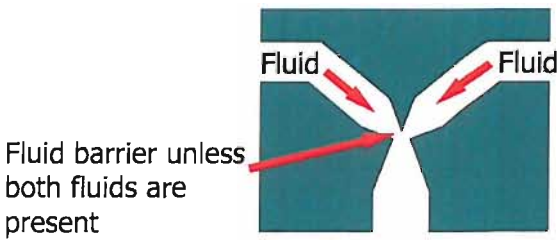

Figure 3.17: An illustration of a device which uses the contact angle of fluid to control fluid flow.

Dynamic valves and other channel structures can be used to impede fluid flow. The problem is that these structures are dynamic devices and therefore the resulting pressure

drop is dependant on the fluid velocity. For micropumps and inkjet injection devices high fluid velocities are used, but if the fluid velocity is low, these structures will provide little or no pressure drop across the structure. If however a diffuser or nozzle structure was implemented in a pipetting device, it has the advantage that the fabrication is simple because it could be easily introduced as part of a microchannel design.

A active valve is a solid obstruction which is placed in the path of the fluid flow. Active valves are used to produce higher pressure barriers. There will still be a finite pressure which can be stopped using such valves. This will be dependant upon the actuation technique used. Active valves have been used in micropumps, because the efficiency of the device will be better than a dynamic structure. The micropumps produced by Koch et al. [68] and Meng et al. [69] have silicon or Parylene microvalves on the inlet and outlet. The fluid being displaced by the diaphragm will force the valves to open, and close, as the fluid is forced out of and drawn into the device. The valves in these two devices require 2 kPa and up to 5.9 kPa, respectively, to be opened. An illustration of a single diaphragm micropump with physical valves is shown in Figure 3.18.

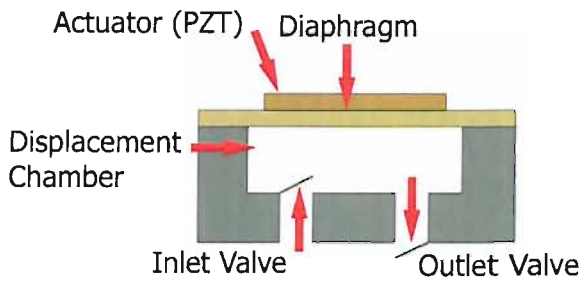

Figure 3.18: An illustration of a single chamber micropump with active valves to produce fluid flow from left to right.

Standalone passive valves have been produced for fluid flow control and take a similar form to that illustrated in Figure 3.19. These use a diaphragm technique to close the valve. This approach yields a restriction or barrier, thus preventing fluid from flowing through the microchannel. Parameters (of examples) of such valve devices are illustrated in Table 3.2. The valve will be opened by releasing the externally exerted pressure, thus enabling the fluid to be pumped through the device. The holding pressure which this type of device can maintain is dependant upon the actuation technique used.

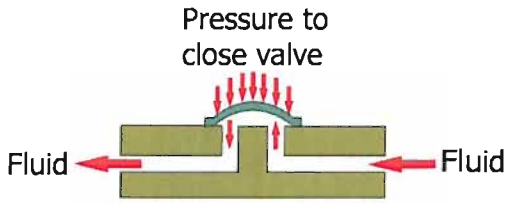

Figure 3.19: An illustration of a single fluid control valve.

Author	Flow rate, Leak Pressure	Actuation
Ohori et al. [136]	-, -	Pneumatic
Vandelli et al. [137]	3.2 $ml\ min^{-1}$, 10 kPa	Electrostatic
Xuen et al. [138]	80 $\mu l\ min^{-1}$, 965 kPa	-
Pilarskia et al. [139]	-, -	Servo motor
Grover et al. [140]	380 $nl\ min^{-1}$, 75 kPa	Pneumatic
Capanu et al. [141]	7.5 $\mu l\ min^{-1}$, 7 kPa	Electromagnetic
Luque et al. [12]	-,262kPa	Pneumatic
Bohm et al. [142]	72 $\mu l\ min^{-1}$, 5 kPa	Electromagnetic
Carlen and Mastrangelo [143]	-, -	Paraffin
Kirby et al. [144]	-, 5.5 MPa	Electrokinetic

Table 3.2: Summary of flow rate and leak pressures of actuated physical valves

The majority of the valves listed in Table 3.2 have been developed to control fluid flow and not to stop it. These designs were considered for the pipetting system, at the design stage, because these approaches could be used to prevent or control fluid flow back and forth at different flow rates. The majority of the designs given in Table 3.2, including the fully integrated valves, are actuated by using electrostatic [144] or electromagnetic [141; 142] approaches. The disadvantage of these valves structures is that the fabrication tends to be complicated.

The final type of valve to be considered incorporates a ferrofluid or paraffin to plug a channel and prevent fluid flow [145; 53]. In common with the ferrofluid pipette [32], discussed earlier in Section 3.3.1, this device is actuated using an external magnet. The ferrofluid plug can be used to stop the flow of fluid up to pressures of 12 kPa. This valve technique would not be suitable for the pipette device researched here because an oil based ferrofluid is used. If an alternative could be found this technique would be more appropriate.

Using a similar approach to Menz et al. [145] and Hartshorne et al. [53] a single-use valve, which uses a plug of paraffin to stop fluid flow by Liu et al. [11]. When the paraffin is heated, using integrated heating elements, the paraffin will be displaced by the fluid moving through the channel. Paraffin microvalves have been used as part of an integrated biochip [6]. The valves are used to control the release of samples and reagents into the device. For one-time use, analysis devices, this technique is useful for controlling the release of samples at the correct time, but it is not appropriate for repeated use.

3.5 Conclusion

Principles for dispensing fluid have been discussed. These use a variety of actuation techniques, including PZT, thermal, pressure and magnetic. Much of the work that has been carried out for inkjet printing and array spotting relies on the fluid being dispensed into air. This is not the requirement for this work, which adds an extra complication to the design. For this work the fluid will be dispensed into another fluid. Hence some

of these techniques appear to be inappropriate in the current form of the device; a new device configuration must be devised if these techniques are used.

Each technique described has merits, but two techniques stand out for simplicity and novelty and these are of most interest. The first uses a ferrofluid plug to dispense fluid from a microchannel [32; 52; 14]. This technique is simple, but could contaminate the sample being dispensed. If an alternative to ferrofluid could be sourced this technique could be used to pipette fluid. The second technique uses modified channel surfaces and pressure to meter volumes of fluid. Once the fluid has been metered, pressure is required to actually pipette the fluid. Though for this work the volume of fluid would not actually leave the device; unlike printing technology, the fluid will be moved to a different position within the device.

The use of ferrofluid to dispense fluid in a syringe-like method has been identified as an interesting and appropriate technique. However to eliminate the possibly of contamination, an alternative to ferrofluid was identified. The proposed alternative is paramagnetic beads which are biocompatible, which will be used in a similar way to the ferrofluid, using a magnetic field from either a permanent magnet or electromagnets to move the beads. As it has been proposed to use magnetic actuation approach, Chapter 4 describes magnetic microdevices that have been produced, which utilise paramagnetic beads.

Chapter 4

Review of magnetic devices and materials

4.1 Introduction

An approach to dispense nanolitre volumes of fluid was proposed in Chapter 1. Actuation approaches for dispensing volumes of fluid were considered and discussed in Chapter 3. A new approach is now proposed. Magnetic actuation was considered appropriate for the dispensing of sensitive biomolecule containing fluids, above other actuator approaches for microdevices, i.e. air pressure [31], thermal [96; 60] and piezo electric [104]. Examples of magnetically actuated devices with designs that could be adapted for use for a microdispenser, were reported by Greivell and Hannaford [32] and Ahn et al. [14] as discussed in Section 3.3.1. Here a magnetic ferrofluid is used within a microchannel, actuated with an external magnetic field. The ferrofluid acts as a plunger. The external magnetic field is translated along the channel and this results in displacement of the ferrofluid plug. The pressure produced by moving the plug results in fluid displacement. The volume of fluid which is displaced will be equivalent to the volume by which the ferrofluid plug is moved, thus it is 100% efficient. Ferrofluids are typically oil based and unsuitable for biomaterials. An alternative to ferrofluid was proposed for this work, polymer paramagnetic beads of the type commercialised by Invitrogen [146] (formerly Dynal), these are discussed in Section 4.2.2.

The proposed technique will use paramagnetic beads to displace fluid. To enable these to be utilised in a magnetic dispensing device, the properties of the beads are reviewed in this chapter. The aim of this research is to produce an integrated microdevice, so the principles of magnetic microdevices are described and existing magnetic microdevices are reviewed, including the operation and the fabrication process that was used.

4.2 Magnetic materials

4.2.1 Ferromagnetic, paramagnetic and diamagnetic materials

The proposed dispensing technique exploits magnetic actuation within a microfluidic structure. Commercially available paramagnetic polymer beads will be used in the proposed magnetic plunger technique. Materials with magnetic properties are classed as diamagnetic, paramagnetic and ferromagnetic. The magnetic susceptibility of a material is defined as the ratio of the magnetic moment per unit volume to the applied magnetic field [147]. Diamagnetic and paramagnetic materials have a negative and positive susceptibility to magnetic fields respectively. The susceptibility values of ferromagnetic materials are dependant on the applied magnetic field and are positive.

A magnetic material is one that is attracted or repelled when placed in a magnetic field. At the atomic level there are two sources of magnetic moment, (i) the permanent magnetic moment due to the spin of unpaired electrons and (ii) the induced magnetic moments due to the application of a magnetic field which exerts a non-specific influence on the electrons in the highest occupied orbits.

All materials have a diamagnetic component because all materials contain most or all the electrons in closed shells. The spin moments and orbits of individual atoms will be balanced, resulting in a zero net magnetic moment. However, in the presence of a magnetic field, the orbits of the electrons are altered slightly, resulting in a small net magnetic moment, in the opposite direction of the applied field. The electron spins

remain tightly coupled and thus do not contribute to the net magnetic moment.

Conversely the magnetic moment of paramagnetic materials is due to both the change in the electron orbit and the electron spin. A permanent magnetic moment due to the electron spin is always present but, due to the thermal randomisation of individual electron spins, the net magnetic field is zero.

Similarly, ferromagnetic materials have unpaired electrons and thus a net magnetic moment. Many of these magnetic moments are aligned in 'domains' within the bulk material. Within each 'domain' there is a high net magnetism. However the orientation of these 'domains' is random and the net magnetization of the material is zero in the absence of a magnetic field. When a magnetic field is present these 'domains' become aligned and this yields a strong magnetism. When the external magnetic field is removed the magnetization of the material remains.

4.2.2 Magnetic polymer beads

The creation of polymer spheres has resulted in a successful new bio-analysis applications that can be applied in the medical and life-sciences, for example cell separation. However when the spheres were originally produced these applications were far from the inventors' thoughts. The technology used to produce these polymer spheres was invented by the well known, Norwegian, Professor Ugelstad in 1979 [148]. Professor Ugelstad took on the challenge of producing polymer spheres with micron scale diameter. Previously it was believed that it would only be possible to produce spheres with these dimensions in space, because gravity would prevent the formation of perfect spheres. Indeed, American scientists and NASA planned to carry out experimental production of microscopic spheres in space.

Later, paramagnetic beads were successfully formed. These are uniform spheres with an even dispersion of maghemite (20% Fe_2O_3). Each bead is coated with a thin polymer shell which encases the magnetic material and provides the surface for the coupling of molecules. The beads are manufactured with a uniform size and shape to ensure the consistency of the chemical and physical properties. The beads are available commercially from Invitrogen [146], Seradyn [149] and Polyscience [150].

Surface functionalised magnetic or paramagnetic beads are used as solid phase carriers and these surface attached molecules selectively bind to the target molecules. Examples of these are bio-recognition molecules such as antibodies or single DNA strands that are covalently attached to the bead surface, as illustrated in Figure 4.1. The modified beads are placed in a solution containing substrates (i.e. antigens or a complementary DNA sequence) and the bio-recognition binding event takes place. The beads are collected and removed from the solution using an external permanent magnet. The target molecules are then released from the recognition molecules on the surface (Invitrogen).

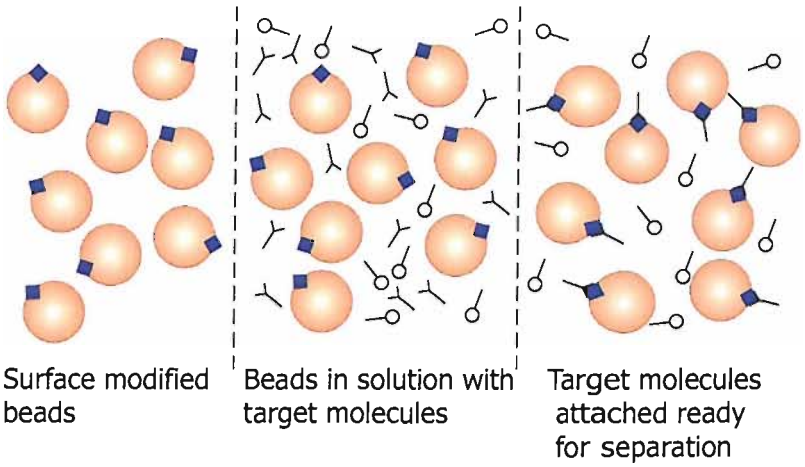

Figure 4.1: An illustration of the bio separation technique.

The magnetic force acting on a single bead in a magnetic field is given by Equation 4.1, where F_B is the force acting on a single bead, m is the magnetic dipole moment, μ is the permeability and B is the magnetic flux density (Zborowski et al. [151]; Gijis [33]).

$$F_B = \frac{1}{\mu}\nabla(m \cdot B) \tag{4.1}$$

If it is assumed that the magnetic field does not vary in space ([152]) then F_B can be determined using Equation 4.2.

$$F_B \approx \frac{1}{\mu}(m \cdot \nabla)B \tag{4.2}$$

The total magnetic dipole moment can be described by Equation 4.3, where V_B is the volume of the bead and M is the total volume magnetization.

$$m = V_B \mu M \tag{4.3}$$

The total volume magnetization is obtained using Equation 4.4, where $\Delta\chi$ is the effective magnetic susceptibility and H is the external magnetic field.

$$M = \Delta\chi H \tag{4.4}$$

B can be obtained from H using the permeability μ, as shown in Equation 4.5.

$$B = \mu H \tag{4.5}$$

To obtain the force acting on a single bead Equations 4.2 to 4.5 are combined to produce Equation 4.6.

$$F_B = \frac{V_B \Delta\chi}{\mu}(B \cdot \nabla)B \tag{4.6}$$

$$\frac{1}{2}\nabla B^2 = (B \cdot \nabla)B \tag{4.7}$$

Substitution of Equation 4.7 into Equation 4.6 to establish the force acting on a single bead (F_B) yields Equation 4.8.

$$F_B = \frac{1}{2}\frac{V_B \Delta\chi}{\mu}\nabla B^2 \tag{4.8}$$

Equation 4.8 can be used to predict the force of a single bead due to the gradient of the magnetic flux density squared in all directions, as illustrated in Figure 4.2. The overall predicted force is a vector sum of the bead forces. However the force can be specified in one direction, by using the gradient of the squared magnetic field, in the direction of interest. Therefore the dependent magnetic variable which will be used to determine the magnetic force will be ∇B^2 throughout this thesis.

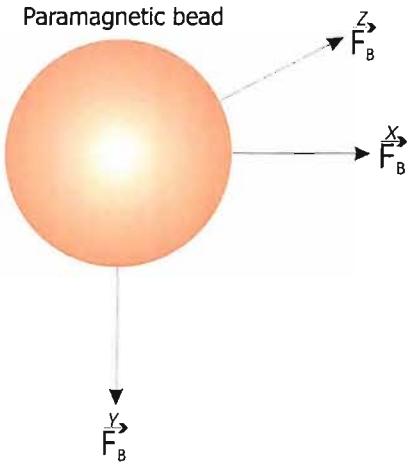

Figure 4.2: BeadForce.

The magnetic properties of the beads depend upon the bead manufacturer. The beads used for this work are 4.5 μm radius epoxy coated (M-450 Epoxy), from Invitrogen. The characteristics of the beads are as follows: diameter 4.5 μm, density 1500 $kg\ m^{-3}$, surface area 900 $m^2\ kg^{-1}$ and iron content $\approx$ 20%. The susceptibility will depend on the magnitude of the magnetic flux density, which will be discussed later in this section.

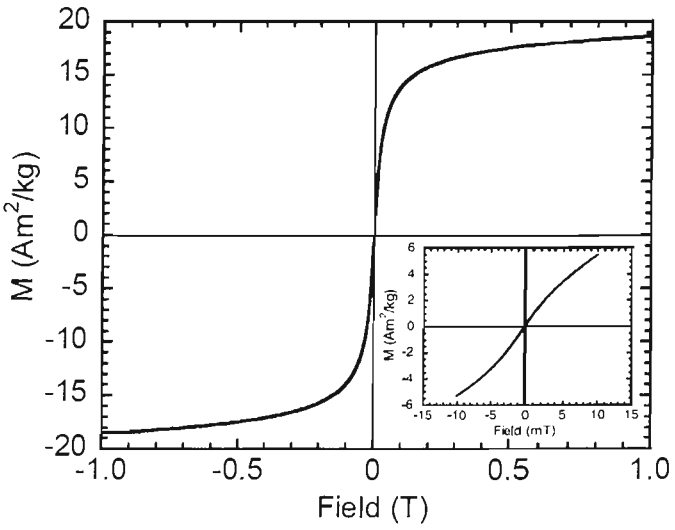

Figure 4.3: Plot of magnetization against applied magnetic field for M-450 Dynalbeads [153].

Fonnum et al. [153] determined the magnetic properties of the paramagnetic beads used for this work (Invitrogen, M-450). The beads contain an even dispersion of maghemite (20% Fe_2O_3), but Fonnum et al. [153] showed that the maghemite particles are present in clusters of approximately 20 nm, which are evenly dispersed within the porous polymer structure of the beads. The susceptibility of the paramagnetic beads has been obtained experimentally, by moving the paramagnetic beads in a magnetic field and measuring the induced magnetization. This was carried out in a vibrating sample magnetometer; Figure 4.3 shows a graph of the measured magnetization of the paramagnetic beads. The initial susceptibility was determined to be 1.6, at a magnetic field of 10 mT, from the measurement results. However the susceptibility at higher magnetic flux densities of 0.2 T was determined to be approximately 0.02 from the experimental results. In comparison bulk maghemite is ferromagnetic and has a susceptibility of approximately $2 - 2.5$ [154; 155]. This is due to interaction of the individual grains within the bulk material. The susceptibility of bulk maghemite is dependant on the grain size, temperature and the microstructure.

One of the reasons for selecting magnetic actuation was because of the demonstrated use of ferrofluid for fluid displacement. Here fluid displacement is demonstrated using paramagnetic beads, which are chemically inert and uniform in shape and size. Due to the manufacturing process each bead has an even dispersion of maghemite, encapsulated in a polymer shell. The main difference between the ferrofluid and the paramagnetic beads, is that there is no fluid carrier and the beads will have a lower magnetization in a given magnetic flux density [156]. A fluid plunger will be formed, which can be used to dispense different volumes of fluid, as described later in this chapter.

4.2.3 Paramagnetic bead structures

It has been shown that paramagnetic beads can be used to form ordered structures of pillars and chains [157; 158]. The beads align along the magnetic field lines resulting in chains. At a low bead density, sparse uniformly spaced chains or pillars are formed. With increasing density of the beads (per volume), a decrease in the spacing between the individual chains occurs until the density of beads is such that there is a solid bead structure.

An ordered structure is created when the paramagnetic beads are introduced into a non-uniform magnetic field. The beads will move toward the point of highest magnetic gradient. However only one bead can occupy a single space and each bead will locate as near as possible to the point of highest magnetic gradient. This results in the formation of a cubic close pack ordered structure, as illustrated in Figure 4.4. The Kepler conjecture states that the cubic close pack arrangement of spheres results in a bead density of 74.048% per volume [159]. Any ordered structure formed using spherical beads cannot exceed this value of packing density.

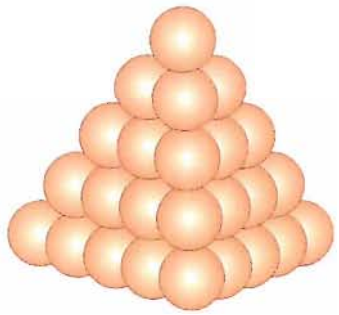

Figure 4.4: Cubic close pack formation of spheres.

4.3 Magnetic device structure design

Geometries of electromagnets will be studied theoretically to estimate the expected magnetic field and allow the selection of structures for experimental work. Electromagnets can be used for the separation or purification of paramagnetic beads within microdevices. The separation of the paramagnetic beads is possible if the force exerted on the particles is greater than the bead drag force. The force exerted on the beads is directly proportional to ∇B^2, as discussed earlier, resulting from the actuation of the microcoils, therefore channels with integrated microcoils are designed so that this product is greatest in the microchannel. Different forms of electromagnets have been used, these are loops [160], meanders [161] and wrapped coils [162]. Each of these electromagnet structures are fabricated near the surface of the microfluidic channel into which the paramagnetic beads are moved.

The separation of paramagnetic beads within microdevices can be achieved by using a fixed magnetic field for purification, as described in Section 4.2.2. The ability to

relocate the beads within a microdevice is desirable for further analysis or reaction of the surface attached molecules. A moving magnetic field provides a moving force along the microchannel for the transport of beads. This can be achieved by sequential actuation of integrated microcoils along the microchannel. The coils are actuated sequentially one after the other, thus yielding a *moving* magnetic field. This *moving* magnetic field is used to collect and transport the beads along the path of the electromagnets within the microchannel. In order to transport the beads, the magnetic flux density between the coils must be high enough to result in the beads moving from one coil to the next.

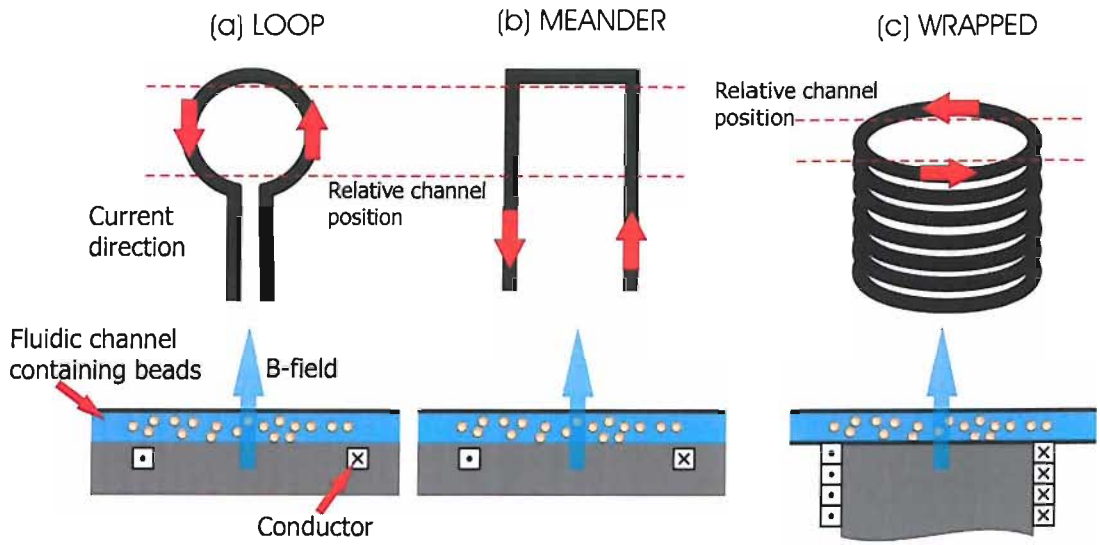

Figure 4.5: Electromagnet structures (TOP) with associated position (BOTTOM) of the fluid channel containing the paramagnetic beads, for (a) Loop, (b) Meander and (c) wrapped.

Figure 4.5 illustrates three forms of electromagnetic coil structures, including the relative position of the coils within the fluidic channel. The loops and meanders would be typically produced below the channel, whereas the wrapped coil structures are formed at the side of the channel. Structures of these forms have been fabricated in micrometer dimensions [162; 161; 163; 164; 160; 165].

(a) Loop structure:

If current is applied to a loop structure, Figure 4.5a, a magnetic field is produced. The magnetic field in the centre of a current loop can be estimated using the Biot-Savart law [166], in Equation 4.9. The magnetic field B_z along the z-axis (z) can be estimated by using Equation 4.10, where I is the current, α is the radius of the loop, z is the distance from the centre of the loop and μ is the permeability ($\mu_0 * \mu_r$, where μ_0 is the

permeability in free space and μ_r is the relative permeability of the material) [166]. An illustration of the loop system is shown in Figure 4.6. The magnetic flux density has been predicted for a current loop with an actuation current of 1 A and a diameter of 100 μm, shown in Figure 4.7a. The predicted magnetic flux density, was used to find the values of ∇B^2 theoretically, as shown in the graph in Figure 4.7b.

$$d\vec{B} = \frac{\mu}{4\pi} I \frac{d\vec{l} \times \hat{\sigma}}{\sigma^2} \tag{4.9}$$

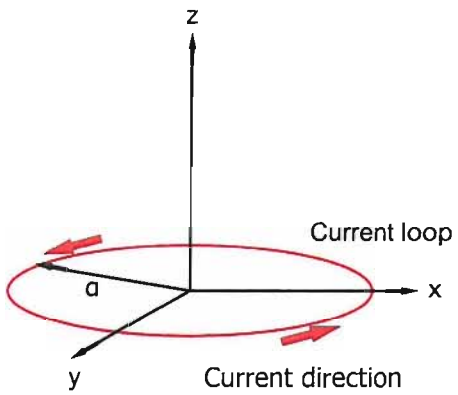

Figure 4.6: Illustration of a current loop, showing the current direction.

$$B_z = \frac{\mu \alpha^2 I}{2(z^2 + \alpha^2)^{3/2}} \tag{4.10}$$

A loop coil of with a 100μm diameter and an actuation current of 1 A can theoretically produce the highest magnetic flux density and ∇B^2 of 4.1 $T^2\ m^{-1}$ at 25 μm from the centre of the coil, as illustrated in the graphs in Figure 4.7. The magnetic flux density from a planar current loop is increased by the addition of more loops. This will result in a higher magnetic flux density in the centre of the structure and a lower magnetic flux density at the edge, because the outer loop will be larger than the central loop and therefore will have a lower magnetic flux density. A multiturn loop or spiral structure would be acceptable for magnetic bead separation techniques, but bead transportation would require a number of high magnetic field points close together, such that the beads could be moved from one coil to the next. Therefore it is preferable to produce many single turn loops in close proximity.

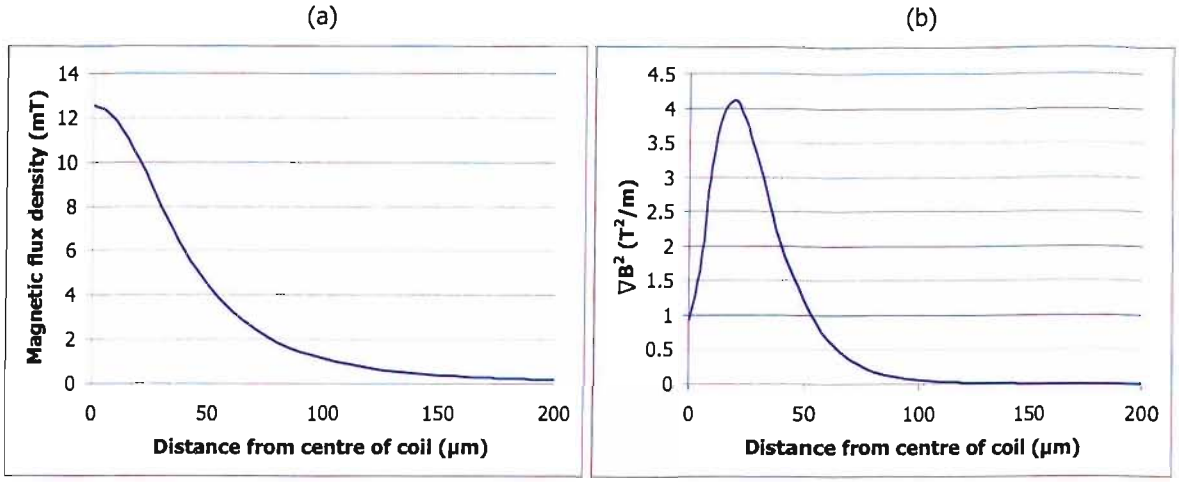

Figure 4.7: (a) Graph of the magnetic flux density against the distance from the centre of a current loop, and (b) graph of ∇B^2 against the distance from the centre of a current loop.

(b) Meander structure:

A meander structure consists of parallel current carrying wires, where each wire yields a magnetic field. A single meander is illustrated in Figure 4.5b, however a microcoil meander would typically be formed of many meanders. The magnetic flux density from this meander structure is a result of the sum of the magnetic flux density from each wire with the neighbouring wires. The magnetic field B_{wire} using a single conductor is predicted by Equation 4.11, where μ is the permeability, I is the current and β is the distance from the wire. This relationship assumes that the wire is infinitely long, so the magnetic flux density will be constant on a line parallel to the conductor ([166]). The maximum density of field lines will be in the centre of two conductors. The magnetic flux density and ∇B^2 have been predicted for two parallel wires, with an actuation current of $1A$ and a separation of $100\mu m$, as shown in Figure 4.8.

$$B_{wire} = \frac{\mu I}{2\pi\beta} \tag{4.11}$$

The meander coil is predicted to produce a ∇B^2 of up to 1.6 $T^2\ m^{-1}$ at 25 μm, shown in the plot in Figure 4.8b. The magnetic field gradients with these structures are typically lower than the wrapped coil structures. This meander coil is ideal for the separation of magnetic beads from solution [161] because the field is constant parallel to the conductor providing a large area for bead trapping. In addition the field can be established over a large distance (the length of the conductor) thus establishing a struc-

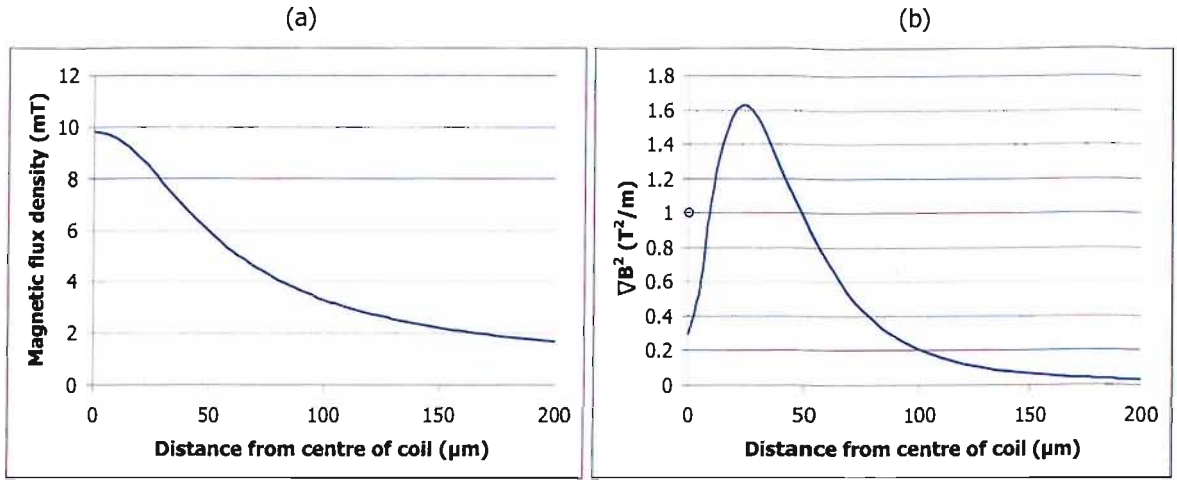

Figure 4.8: (a) Graph of magnetic flux density against the distance from the centre of two parallel wires, and (b) graph of ∇B^2 against the distance from the centre of two parallel wires.

ture with many high magnetic field points within a microfluidic device. An advantage of the meander structure is that it is relatively simple to fabricate and can be fabricated as a single element. Although a meander coil has many advantages the predicted value of ∇B^2, of interest, is lower than that of a current loop for these examples.

(c) Wrapped structure:

Wrapped structures consist of a conductor coiled around an appropriate core, commonly known as a solenoid, illustrated in Figure 4.5c. The field in the centre of the solenoid is concentrated and uniform perpendicular to the current flowing in the conductor; however the field is weak and divergent outside the solenoid. The field in the centre of an air core solenoid can be predicted using Equation 4.12, where μ is the permeability, n is the turn density (N/L) and I is the current. To increase the field produced using a wrapped coil, a core of higher permeability can be added. This satisfies $\mu = \mu_0\mu_r$, where μ_0 is the permeability of free space and μ_r is the relative permeability of the core material.

$$B_{solenoid} = \mu n I \tag{4.12}$$

The magnetic field due to a wrapped coil, outside of the core along the axis, can be predicted using Equation 4.13, where L_{coil} is the length of the wrapped coil, μ_0 is the permeability of free space, μ_r is the relative permeability, I is the current, N is the

number of turns, x is the distance along the axis from the centre of the coil and α is the radius of the coil [167]. Figure 4.9 illustrates the coil configuration. The magnetic flux density has been obtained for a wrapped coil with an actuation current of $1\,A$, a diameter of $100\mu m$, with 100 turns in a distance of 1 mm, giving a turn density (L_{coil}) of 1000 m^{-1}, Figure 4.10a. Values for ∇B^2 were obtained from the magnetic flux density and are shown in the graph in Figure 4.10b.

$$B_x(x) = \frac{\mu_r \mu_o I N}{2L_{coil}} \left[\frac{L_{coil}/2 - x}{\sqrt{\alpha^2 + (x - L_{coil}/2)^2}} + \frac{L_{coil}/2 + x}{\sqrt{\alpha^2 + (x + L_{coil}/2)^2}} \right] \tag{4.13}$$

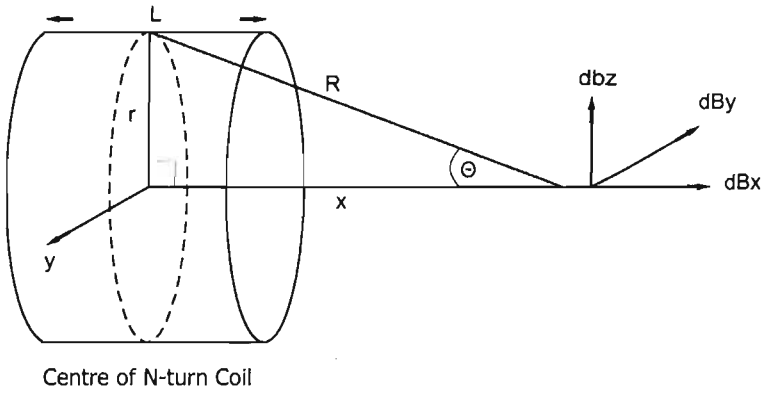

Figure 4.9: Illustration of a wrapped coil configuration.

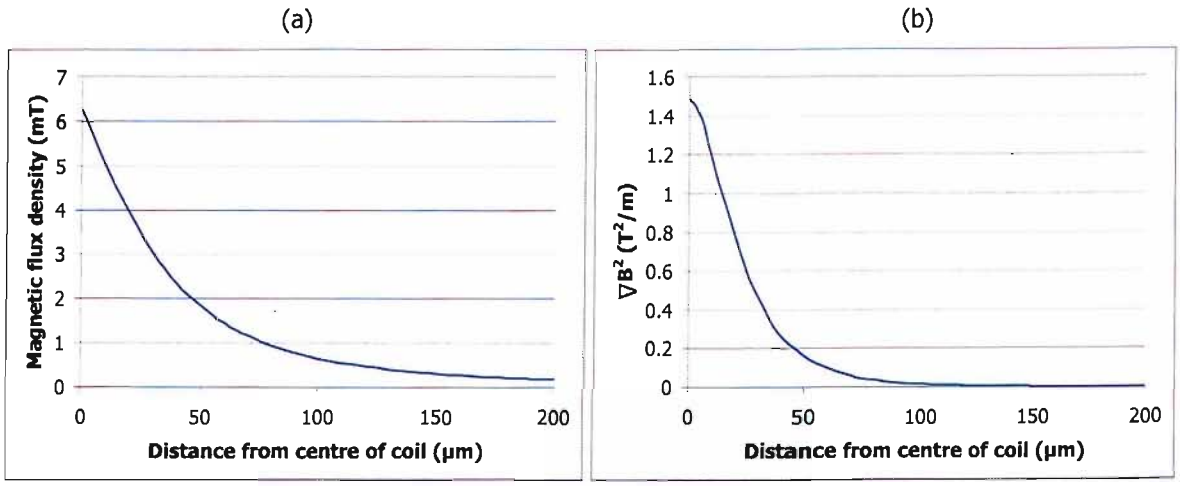

Figure 4.10: (a) Graph of magnetic flux density against the distance from the end of the wrapped coil, and (b) graph of ∇B^2 against the distance from the end of the wrapped coil.

As shown by the plot in Figure 4.10b, the wrapped coil structure is predicted to produce the lowest value for ∇B^2 of up to 1.5 $T^2\ m^{-1}$ at 25 μm. This is mainly

because the field outside the wrapped coil is low and divergent compared to the field inside the coil. The predicted magnetic field would be increased by introducing a core with higher permittivity (see Equation 4.13), but this could also result in remanence. Remanence is the amount of a material that remains magnetised after the magnetic field has been removed. Thus the use of a material that has a high remanence would be disadvantageous for bead transportation.

To transport magnetic beads a series of high magnetic field points, positioned close together must be achieved. To transport paramagnetic beads a series of coils, meanders or loops, positioned below the channel must be actuated one after the other to produce a moving magnetic field. The force on the bead due to the 'next' coil must be great enough to move it from the 'previous' one; therefore the coils need to be closely packed. For transportation the best coil structures would be either loops on the bottom of the channel or wrapped structures at opposing edges of the channel.

4.4 Review of paramagnetic bead microdevices

There has been significant interest in the development of microfabricated devices for the manipulation of magnetic beads, to enable the separation technique of biomolecules, as described in Section 4.2.2, within microdevices. The magnetic bead separation technique already developed by companies like Invitrogen, is used within these microdevices for the separation of target molecules from a solution in an efficient and non-destructive way. The microdevices are used to precisely locate the separated beads within a microfluidic channel.

4.4.1 Permanent magnetic bead devices

The separation approach developed by Invitrogen is conventionally carried out using a permanent magnet to remove the beads from *ml* volumes of solution, but not for microlitre and sub-microlitre volumes. There are two main strategies that have been developed for sample purification. In the first strategy, the beads are self assembled into a fixed assembly [168; 169; 170; 157; 158; 34], which fluid sample is flowed through.

Here the target molecules will attach to the molecules on the surface of the beads. In the second strategy, integrated microcoils are used as electromagnets to precisely place and transport paramagnetic beads within a microdevice [171]. Though studies using self assembled structures have been carried out, the emphasis was placed on the bead formation and its use. Critical information regarding the number of beads or bead densities was not specified.

As described previously novel separation devices have been created, with the self assembly of paramagnetic beads ($1 - 2\mu m$). The beads have been used to define separation structures within microchannels [157] for purification, as illustrated in Figure 4.11a. These structures can be used to carry out rapid, reproducible, inexpensive purification. The structures are typically a matrix of pillars of a fixed diameter and spacing. An external magnetic field is used to form these structures within microchannels. The external magnetic field is first used at the surface of the microchannel to collect paramagnetic beads to form a close-packed bed at the point of high magnetic field gradient. Once collected, the magnetic field is removed to allow the beads to return to a colloidal state. The magnetic field ($10 - 100mT$) is then reapplied at a distance from the microchannel [168; 170], resulting in the formation of pillars.

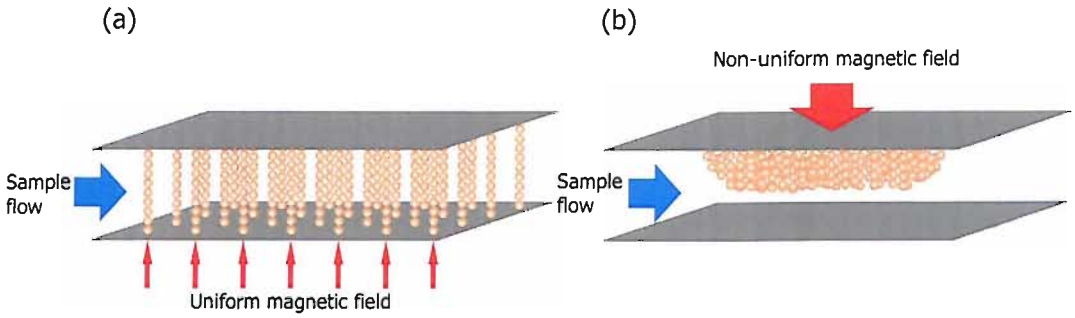

Figure 4.11: An illustration of bead chains formed in a fluidic channel using a uniform magnetic field (a), an illustration of a packed bead formed at the edge of a channel using a non-uniform magnetic field (b).

The formation of regular bead structures depends on (i) the paramagnetic bead concentration, (ii) the magnetic field gradient and (iii) the height of the channel [157; 158]. A bead concentration of approximately $1 - 2\%$ volume is used to form pillar structures within the microchannel. An example of pillar structures are those used by Minc et al. [157, 158] to monitor the behaviour of DNA flowing through a microfluidic

array containing $100 - 600$ posts of paramagnetic beads (600 nm diameter).

By increasing the concentration of beads more dense pillars are formed until the spacing between the bead columns is less than 1 μm [34]. At higher bead concentrations a less ordered structure is formed, consisting of a 'labyrinth-like' form [34], with nanometre pores. The 'labyrinth-like' structure remains stable in the microchannel as a result of a thermodynamic equilibrium between the magnetic energy and the thermal agitation energy.

The second parameter that defines the structure of magnetic bead assemblies is the magnetic field used. At high magnetic field gradients a clump of beads will form at the point of highest magnetic field gradient, as illustrated in Figure 4.11b. Hayes et al. [169] have produced packed bead beds within a 50 μm diameter capillary. Paramagnetic beads with $1 - 2$ μm diameter were used to form a $2.4\text{x}10^{-12}$ m^3 volume bead plug, of approximately 1.2 mm in length, using a permanent magnet with a magnetic flux density of 0.24 T. The bead plug was held in place while fluid was flowed through the capillary ($50\mu m$ diameter capillary) and through the bead plug. Once the system is stabilized the solution is passed through the microchannel and the analyte is detected. The advantage of using a bead plug is that it allows for a higher surface area to volume ratio for binding molecules than when using just a flat surface on a microchannel. If the magnetic source is moved away from the channel the beads will disperse, as the magnetic field gradient is reduced and the field becomes uniform. Alternatively multiple magnets can be used to obtain parallel field lines and these align the beads in a collinear fashion [34].

The final parameter that defines the structure of bead assemblies is the channel height. If the number of beads used in a channel is constant, but the channel height is increased, the self assembled pillars are less dense, with increased pillar separation. The centre to centre spacing between the pillars is suggested to be due to the microchannel height. As the microchannel height increases the pillar length increases, thus increasing the magnetic dipole; this results in a greater spacing between the pillars.

4.4.2 Microcoil electromagnetic bead devices

The fabrication of microcoils will be discussed later in Section 4.5 and here examples of microdevices containing microcoils, of the form discussed previously, will be reviewed. The most simple microdevice for the capture of magnetic beads from fluid was reported by Lee et al. [160] and is a single current loop of 50 μm diameter. The current loop was fabricated with an insulation layer between the loop and the fluid to prevent electrical shorting between the particles and the wires. This enables the capture of the beads for purification, while still being able to view the device from above. The loop trap is illustrated in Figure 4.12, where $1 - 20$ nm magnetite particles are trapped from a droplet of water with an applied current of 0.35 A. Under this operating condition the magnetic flux density is 2.7 mT above the insulation layer at the centre of the loop.

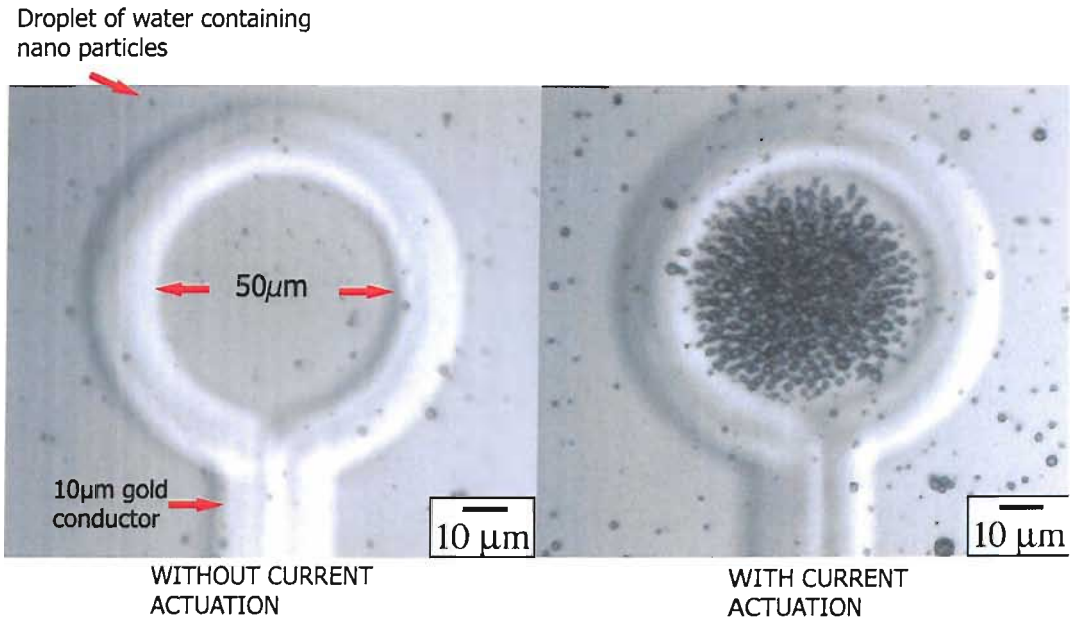

Figure 4.12: Trapped nanoparticles from a droplet of water above a ring trap with $I = 0.35$ A [160].

If additional loops are integrated (spiral), the magnetic field at the centre of the coil will be greater. However, the field due to a circular coil is proportional to $1/R^3$ therefore the field will not double, with the addition of a loop, because the second loop must be bigger than the first. Smistrup et al. [165] has fabricated multiple turn planar coils, with twelve turns. The conductors are 60 μm wide, 25 μm thick, with a spacing of 20μm. The coils were used to successfully separate 1 μm diameter beads from a solution within the capillary running through the centre of the device.

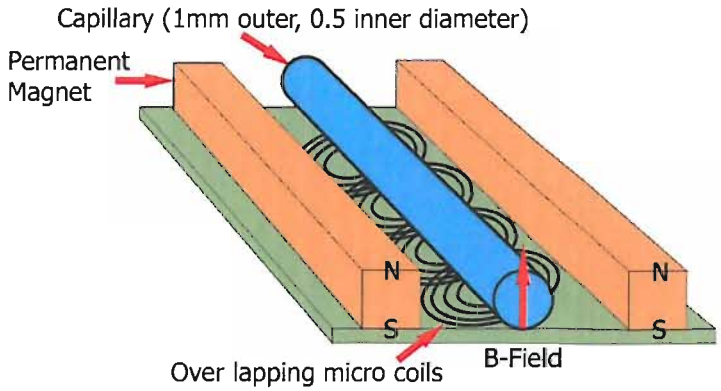

Figure 4.13: Proposed design of a microcoil array to transport magnetic beads over long distances [171]

Rida et al. [171] suggested that it is practically difficult to produce a high enough magnetic field to move paramagnetic particles over 'long distances' using just planar coils within a microdevice. Rida et al. [171] suggested that the transport of paramagnetic beads requires an overlap of the magnetic fields from each coil to enable the movement of beads from one coil to the next. To enhance the magnetic field a device was fabricated which consisted of overlapped microcoils, in conjunction with two permanent magnets placed on either side, as shown in Figure 4.13. The static magnetic field from the permanent magnets provides the magnetization of the beads, while the sequentially actuated planar coils provide a *moving* magnetic field. Thus the integrated coils provide a means for 'long distance' transportation of the beads. The coils were fabricated using simple printed circuit board (PCB) technology. The coils have up to 10 complete turns with a conductor width and spacing of approximately 100 μm, providing a magnetic field of $1 - 4\ mT$ with an applied current of 1 A. This system was used to successfully transport complete clusters of beads with an effective velocity of 1 $mm\ s^{-1}$.

As explained earlier using a core material with a higher permeability than air within a microcoil produces a higher magnetic field (Equation 4.10). Liakopoulos et al. [172] and Choi et al. [163] have fabricated coil structures with integrated magnetic cores, as illustrated in Figure 4.14. The core material used for both of these structures was a nickel-iron (Ni-Fe) permalloy, which has a permeability of approximately 6000. The disadvantage of a magnetic core material with a high relative permeability is that this can result in a high remanence.

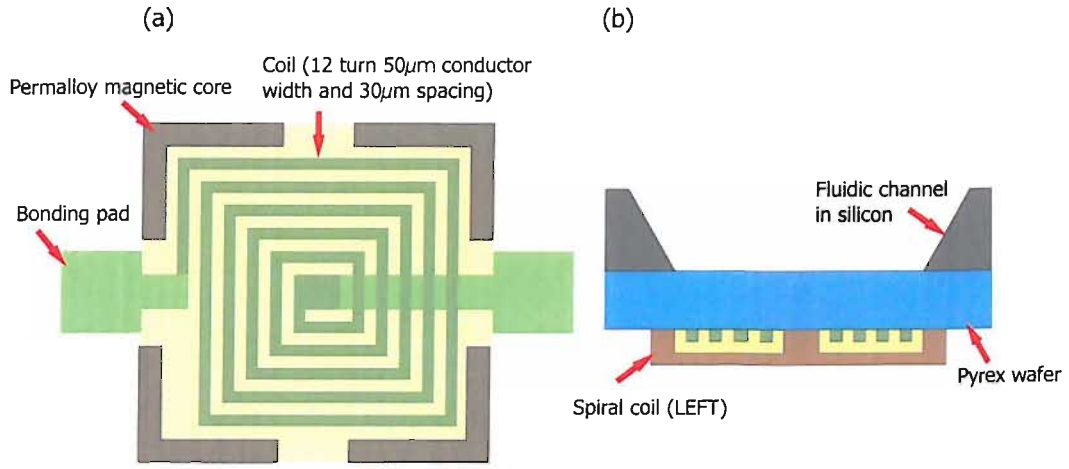

Figure 4.14: Multi-turn loop or spiral coil with integrated nickel-iron core (a). A fluidic channel above the microcoil structure (b) [172; 163].

A meander microcoil structure has been produced by Choi et al. [161], for the separation of paramagnetic beads ($0.8-1.3\ \mu m$ diameter) which is illustrated in Figure 4.15. The meandering wire has a 10 μm width and spacing. The microcoils are separated from the fluid flow, containing the paramagnetic beads, by a 1 μm layer of silicon dioxide. To achieve a higher magnetic flux density for separation of the paramagnetic beads, the minimum distance between the coil and the microchannel must be achieved.

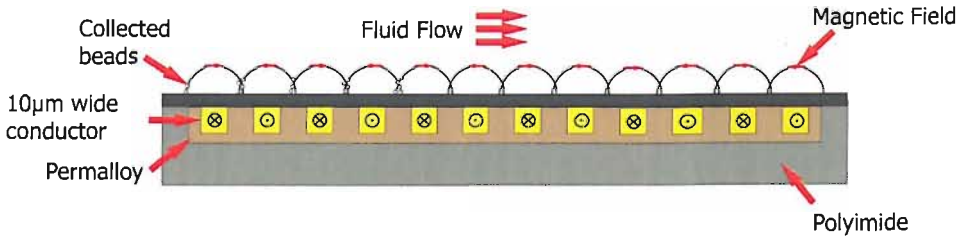

Figure 4.15: Serpentine conductor with semi-encapsulated permalloy [161; 163].

Another example of a meander coil has been fabricated by Deng et al. [164] for transporting paramagnetic beads. This example contains two serpentine wires which have been fabricated within the device structure and is illustrated in Figure 4.16. The magnetic beads experience a strong local magnetic field produced by the serpentine wires and a strong magnetic field from two straight wires either side of the serpentine. The straight wires are used to trap and 'magnetize' the beads within the device, such that the beads can be controlled by the magnetic field from the serpentine wires. The two serpentine patterned tracks have been fabricated to be in close proximity (50 μm)

to one another and are offset linearly by 200 μm. Each serpentine track is actuated in an alternate fashion using a current of 10 A, such that the beads move between each track as illustrated in Figure 4.16. Using the serpentine wires and current carrying wires either side, approximately 200 beads (Dynal M-450) were transported along a channel in hexagonal ordering.

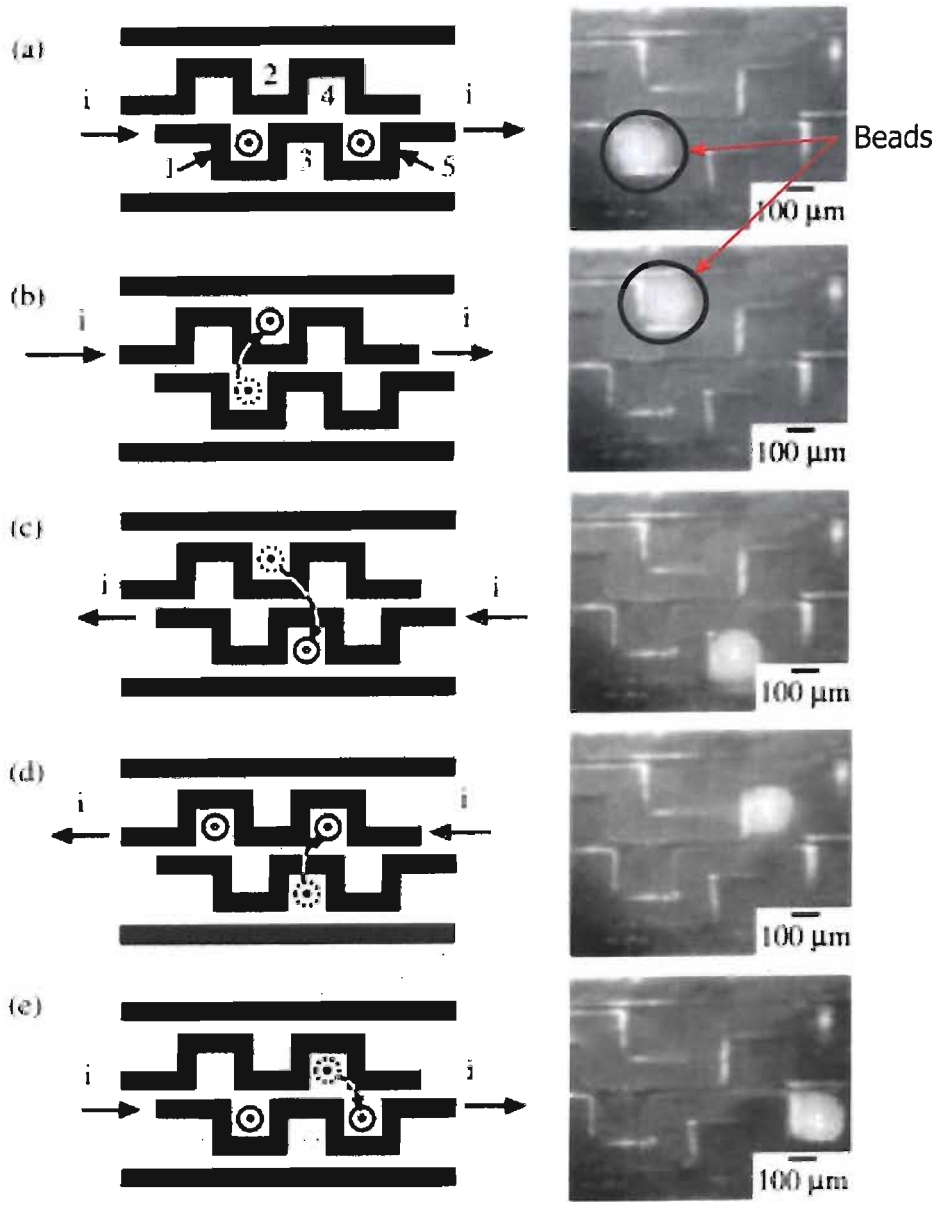

Figure 4.16: Micromagnetic system fabricated using soft lithography [164], illustrating beads trapped and transported within serpentine conductors actuated by current i. (a) The path that the beads will be moved $(1-5)$, (b) beads moved from position 1 to 2, (c) beads moved from position 2 to 3, (d) beads moved from position 3 to 4, (e) beads moved from position 4 to 5.

The first example of a wrapped coil structure considered here has been fabricated by Ahn et al. [162]. The device consists of electromagnets produced either side of a fluidic channel, using toroidal-meander-type inductors. The electromagnets are terminated at the edge of a fluidic channel for the separation of paramagnetic beads, as illustrated in Figure 4.17. The coils are fabricated in copper, with a nickel / iron permalloy magnetic core. The device is used to separate $0.8 - 1.3\ \mu m$ beads, suspended in fluid at the magnetic dipoles, as illustrated in Figure 4.17. The coils are actuated using 500 mA, achieving a magnetic flux density of 0.03 T in the centre of the magnetic poles.

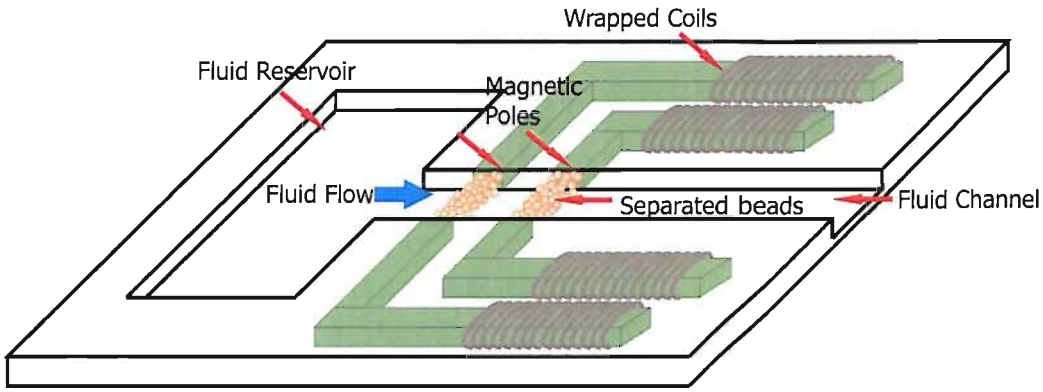

Figure 4.17: Schematic drawing of an electromagnetic device for bead separation from fluid flow ([162]).

A simple example for bead transportation has been reported by Joung et al. [167], using a series of wrapped electromagnets placed either side of a capillary; these coils are clearly not integrated. The electromagnets are turned 'ON' and 'OFF' to control the movement of the beads (Dynal beads) in a zig-zag pattern, as illustrated in Figure 4.18. The electromagnets were used to achieve greater forces on the beads than the predicted drag force of 33 pN (at 1 $mm\ s^{-1}$ in water, viscosity of 1 $mPa\ s$). The electromagnets used for this device consist of iron cores (0.15 mm radius and 20 mm in length) with high relative permeability and approximately 300 turns of copper wire, corresponding to 30 000 turns per metre. An actuation current of $1\,A$ was used to produce a magnetic flux density and high magnetic gradient. This device is designed to move 2 μm diameter beads through a solution in a glass capillary with an internal diameter of 0.4 mm. The paramagnetic beads are moved through the capillary at approximately 1 $mm\ s^{-1}$.

The transportation and the separation of paramagnetic beads have been achieved using fabricated coils, used as electromagnets. For the separation of the paramagnetic

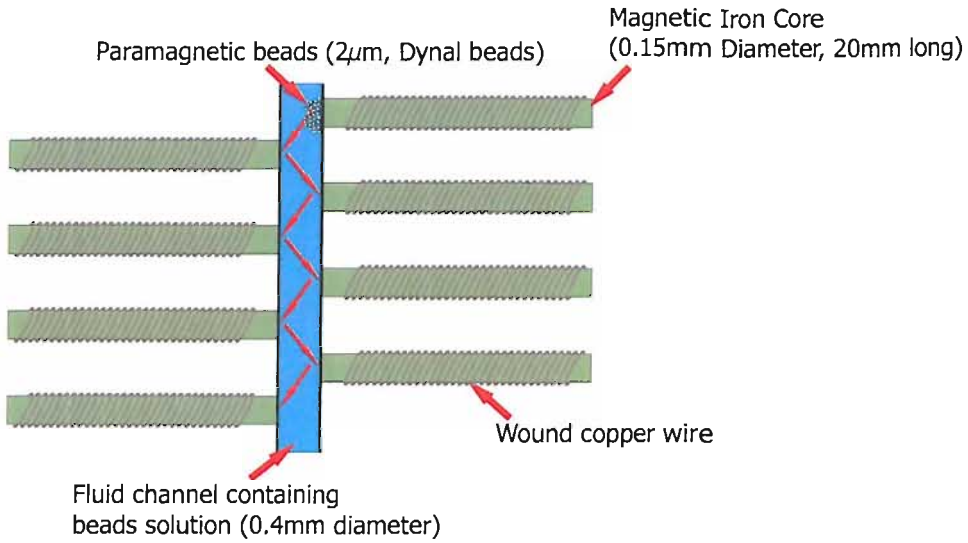

Figure 4.18: Schematic drawing of the proposed pumping system for paramagnetic beads [167].

beads all types of coils discussed here are suitable, because all that is required is a magnetic field gradient within the microchannel. However it is clear that the use of multiple loops and meanders is preferred due to the lower complexity of fabrication relative to the wrapped coils.

The transportation of paramagnetic beads requires a series of high magnetic field points along the channel path. These are required to produce a moving magnetic field to transport the beads from one coil to the next. For this purpose loops [171] and wrapped coils [162; 167] are more effective, because it is possible to fabricate a series of coils which can be actuated to yield the required moving magnetic field. It has been shown that by overlapping the loop coils it is possible to successfully achieve bead transportation along a microchannel [171]. However in the example produce by Rida et al. [171] permanent magnets were also used to magnetise the paramagnetic beads to aid the movement. Finally, meander coils are typically used for separation [161], although an example has been produced, implementing two meanders, which was demonstrated to transport beads through fluid in a zig-zag path [164].

In its current form the example of Deng et al. [164] does not appear to be suitable for transporting a bead plug seamlessly through a microchannel to displace fluid. However, if the electromagnets are placed much closer together, it might be possible to overlap the magnetic field from one electromagnet to the next. This would make it possible to

move a plug of beads seamlessly through a microchannel instead of moving the beads in a zig-zag formation. In addition the internal diameter of the microchannel could be reduced compared to that used by Deng et al. [164] and/or the number of beads increased. This would restrict the movement of the beads, therefore making the beads move in a more linear fashion through the microchannel.

4.5 Microcoil fabrication techniques

There are two essential approaches for the fabrication of microcoils. Two dimensional planar coil structures are fabricated by the electrodeposition of thick films ($< 35\mu m$), as explained by Coutrot et al. [173]; Lee et al. [160]; Choi et al. [163] (Figure 4.19a). The electrodeposition is achieved by using a patterned sputtered or evaporated film as a seed layer. Three dimensional coil structures are formed around a core material to form *wrapped* structures as described by Wagner et al. [174]; Yamada et al. [175]; Sadler et al. [176](Figure 4.19b). Alternatively a multi wafer approach is used where structures are aligned to form contacts on each wafer, reported by Velten et al. [177](Figure 4.19c).

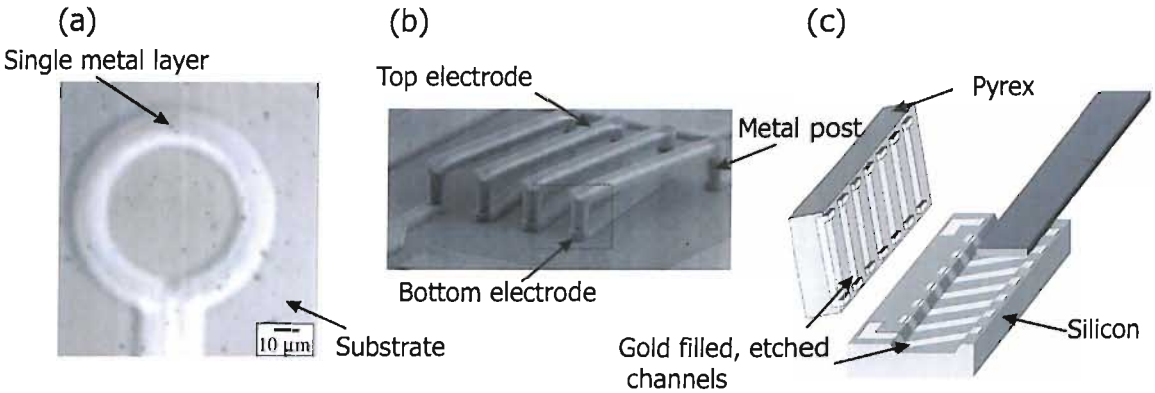

Figure 4.19: Example electroplated structures: a two dimensional planar structure [160] (a), a three dimensional wrapped structure, with three layers [178] (b) and a three dimensional structure, produced on multiple wafers [177](c).

Simple two dimensional structures are formed using a seed layer, followed by electrodeposition into a resist mould. Coutrot et al. [173] and Lee et al. [160] have produced two dimensional structures using electrodeposition of gold. The initial step is to evaporate or sputter a seed layer (as shown in Figure 4.20). The seed layer is patterned after

the evaporation or sputtering using a photolithography mask followed by a wet etch or ion beam milling. Once the seed layer has been patterned, a thick resist mould is produced ($5 - 25\mu m$) to define the coil thickness and to enable good aspect ratio structures to be produced. If the electrodeposition is carried out without a resist mould the metal is deposited all over the surface, as illustrated in Figure 4.20a. The coil structure is then deposited by electrodeposition, so that the metal that creates the coil will only be deposited on the exposed seed layer, within the photoresist mould (Figure 4.20b). The seed layer is used as the working electrode for the deposition process for the reduction of cations from the plating solution. The thickness of the photoresist defines the maximum possible thickness of the deposited metal. The rate of the electrodeposition must be calibrated before the final structure is fabricated as there is not a simple method to predict the growth of the metal structure in the mould (Figure 4.20c).

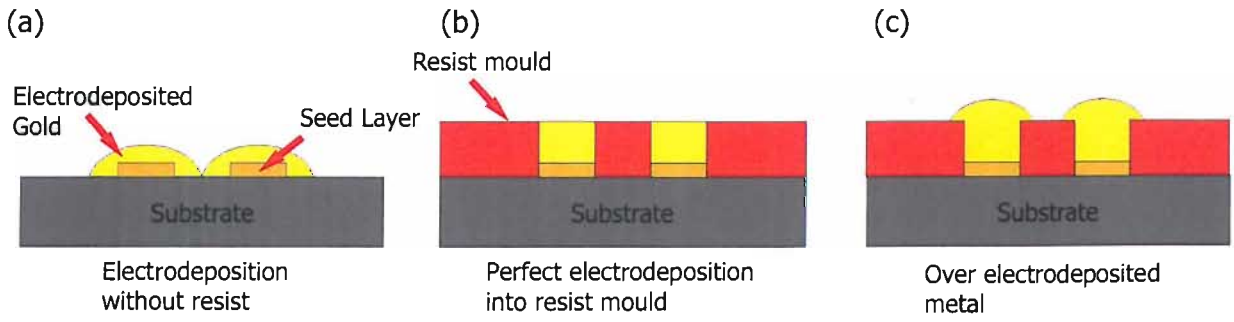

Figure 4.20: Schematic of electrodeposition to explain the technique.

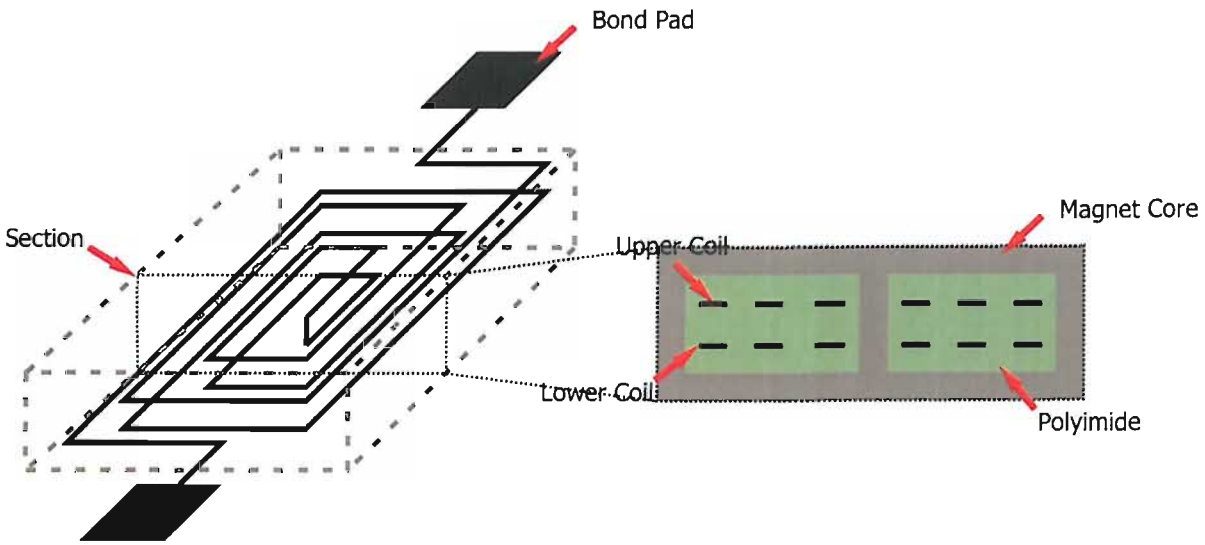

Figure 4.21: Multilayer planar coil structure, produced using a polyimide insulating layer [179].

An alternative technique for producing two dimensional planar coils has been used by Coutrot et al. [173]. This technique differs from the previously described process because the seed layer is patterned after the electrodeposition stage. The seed layer is left unpatterned until after the electrodeposition. Wet etching is used to remove the unwanted seed layer, utilising the electrodeposited layer as a masking layer. This is possible because the thickness of the electrodeposited gold is at least tens times thicker than the seed layer. The advantage of patterning the seed layer after the electrodeposition is that the structures do not have to be connected via a common electrode for the electrodeposition. The disadvantage however is that there could be a degree of under etching when removing the remaining seed layer.

This simple microfabrication technique can only be used to produce single turn microcoils of two dimensional structures. If multiple turn or multiple layer planar coils are required the fabrication must be carried out in a number of stages. Indeed this multilayer approach has been carried out by Ahn and Allen [179]; Sadler et al. [180] to make microcoils. Ahn and Allen [179] fabricated the coils by metal sputtering and lithography defined patterning. The core was fabricated by electrodeposition into a thick resist mould. To isolate the lower part of the coil, polyimide is used which has 'through-connections' made to allow for electrical contacts between the upper and lower part of the coil structure.

Three dimensional structures are more complex due to the requirement for vias, or connections, to be made between the multiple layers. Three dimensional structures have been produced with (i) solid cores (insulation/magnetic core combination) on single wafers, (ii) air cores on single wafers and (iii) air cores on multiple wafers. The simplest form of three dimensional structures is a solenoid produced using a solid core, which is typically a combination of an insulator and a magnetic core. These structures have been produced using three main steps [175; 176]. Firstly the lower conductive wires are deposited in a resist mould using a seed layer, similar to the previously described planar structures. The second step is to produce the magnetic core and the electrical vias to connect the upper and lower conducting wires. This is achieved using a thick resist mould once again. The resist mould is first patterned, and then hard cured to form a permanent dielectric layer. The hard curing also reflows the resist such that

it is planarized for subsequent steps. The vias are then electroplated, using a new seed layer deposited on the planarized resist surface. The final step is to produce the upper conductive wires, which are produced using a seed layer and a thick resist mould. The final conductors will make contact with the electrical wires and thus complete the electrical circuit. Due to the use of resist and the magnetic core these structures are rigid.

The previously described solenoid structures were produced using an appropriate core to increase the magnetic field, however electrical inductors have been produced using similar fabrication techniques with air cores [178]. The removal of the solid core from the solenoid structures increases the complexity of fabrication and makes the final device more fragile. Solenoids with air cores have been produced using the same technique to those produced with a solid core, with the exception of the removal of the thick photoresist post-electrodeposition. An example of a solenoid structure produced using this technique is illustrated in Figure 4.22.

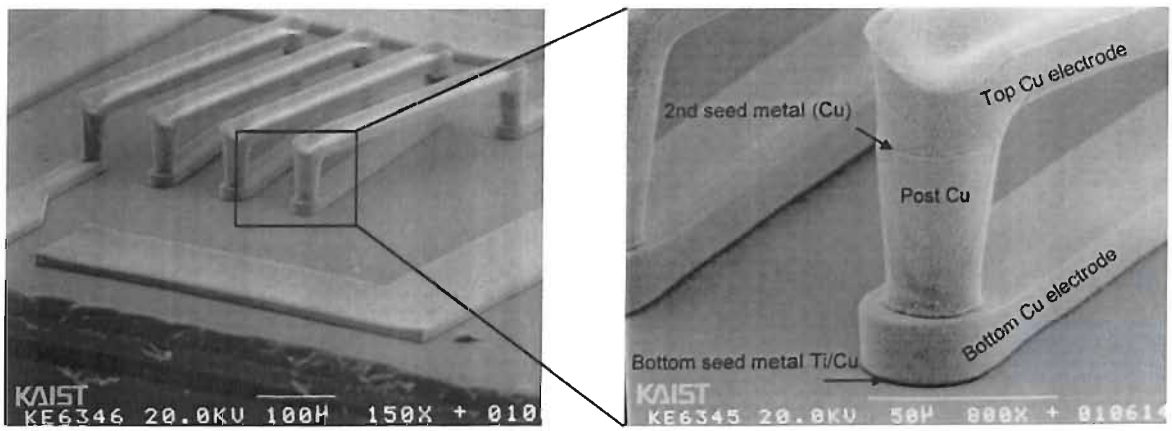

Figure 4.22: SEM of microfabricated solenoid structures using a three stage electrodeposition process [178].

The final example of three dimensional coil structures has been produced using multiple substrates by Velten et al. [177]. This tuneable coil has been produced as a sensor. The structure consists of a microfabricated solenoid, with an air core, used to introduce a core after fabrication which can be moved freely. The coils are produced in two parts. The first part is produced in silicon, in which an anisotropic potassium hydroxide (KOH) etched channel is formed to allow for the introduction of the core. Reactive ion etching (RIE) is used to produce shallow channels (10 μm), which are filled

using electrodeposition. The wires are insulated with a 1 μm layer of silicon dioxide, produced before the electrodeposition. To allow for two substrates to be connected electrically, copper bumps are deposited at the end of each conducting wire. The lower part of the solenoid is illustrated in Figure 4.23. The left hand side shows the etch trenches which are subsequently filled with gold; this is shown on the right hand side of Figure 4.23. The second part of the solenoid is produced in a glass wafer using the same fabrication process, with the exception of the KOH etched channel which is not required. The upper part of the solenoid in the glass has copper bumps deposited at the end of each conductor to make electrical connections between the upper and lower part of the solenoid. Before the solenoid is completed the copper bumps on the upper solenoid substrate are also plated with a lead/tin alloy, which will be used to make the connection between the upper and lower parts of the solenoid. Finally the two wafers are aligned and bonded.

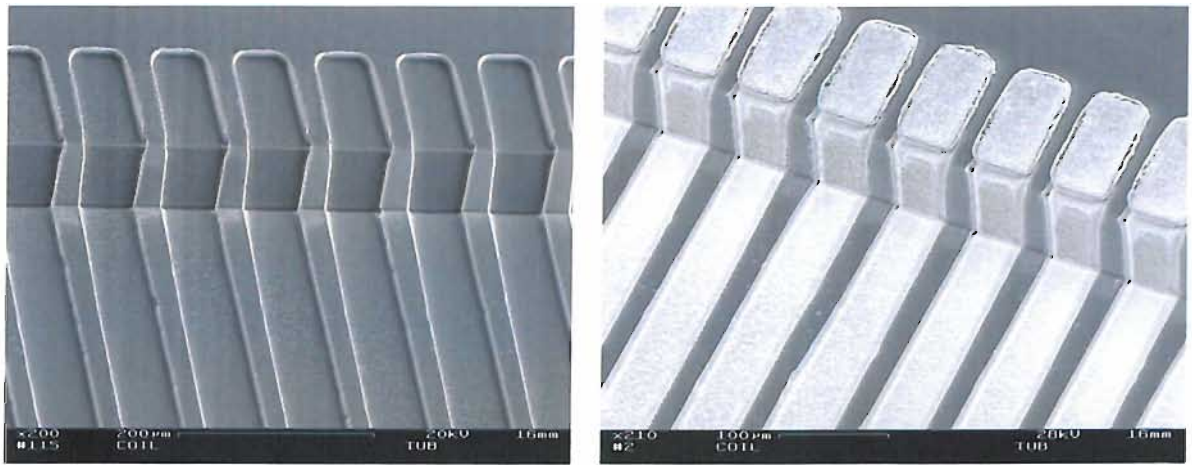

Figure 4.23: DRIE trenches for the lower part of the wrapped coil structure (LEFT), electrodeposited conductors to the form lower part of the wrapped coil structure, in the DRIE trenches (RIGHT) [177].

It is clear that the most effective fabrication approach for producing microcoils or conductors in microdevices is electrodeposition. Electrodeposition has been applied to produce metal coil structures of between $5-35\mu m$ thick which cannot be easily produced using alternative microfabrication techniques, such as sputtering or evaporation.

The electrodeposition of metals discussed here will be limited to non-cyanide gold plating techniques, described in detail by Sclesinger and Paunovic [181] and by Margesin et al. [182]. For electrodeposition, two electrodes are used, the working (structure) elec-

trode (cathode) and the counter electrode (anode). The two electrodes are submersed into an aqueous solution containing metal salts, illustrated simplistically in Figure 4.24. The plating solution used for this work is ammonium gold sulphite (Metalor, ECF64D). Non-cyanide gold electrodeposition is used because it has higher compatibility with photoresists and the residual stress of the deposited metals can be controlled [182].

Before current is applied to the electrodes of the plating set up, the electrode potential will equilibrate. The metal working electrode (Au) is submersed into the aqueous solution containing metal ions (Au^{+3}). At the metal-solution interphase, the Au^{+3} ions from the solution will be reduced (consumes electrons), while the Au will be oxidised (liberates an electron). This results in a transfer of Au^{+3} ions to the metal lattice and the Au entering the solution. A dynamic equilibrium is reached once there is a neutral charge at the metal-solution interphase region. The reduction and oxidation of gold is described by Equation 4.14.

$$Au^{+3} + 3e \rightleftharpoons Au \tag{4.14}$$

A galvanostatic transient electrodeposition technique is used for this work, where current is applied between the working electrode and the counter electrode [183]. The current is held constant, while the potential is measured between the working electrode and a reference electrode which is placed in the solution. The current is applied and the potential is measured and recorded as a function of time using an Autolab PGSTAT302. First the potential increases as the current flow charges the double-layer at the metal-solution interphase, up to a potential, known as the overpotential, where the electrode reaction can proceed [183]. The overpotential is the result of charge transfer across the double-layer, diffusion, chemical reaction and crystallisation. When the overpotential reaches a constant value, the reaction begins at a measurable rate. At this point the charge transfer will be constant and the deposition of the gold will begin at the working electrode. As illustrated simplistically in Figure 4.24, the working electrode to be plated is the cathode and the counter electrode is the anode. When current is applied to the circuit positive ions of Au^{+3} (cations) are reduced at the cathode, consuming three electrons. This reaction is shown in Equation 4.14. To equilibrate the system anions oxidise at the anode (three electrons are liberated).

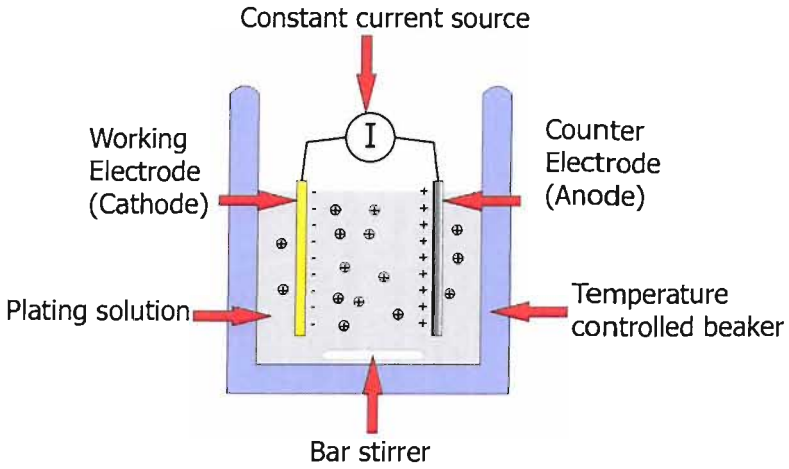

Figure 4.24: Illustration of the electrodeposition set up.

The stress formed in the deposited metal can be controlled by the temperature of the solution, the current density used and by selecting an appropriate plating bath solution. Using a temperature of $50°C$ and a current density between $50A\ m^{-2}$, gives a low stress deposit, which is recommended by the manufacturer. It has also been shown that ECF64D, results in a lower stress than other plating bath solutions and a temperature of approximately $50°C$ can be used to produced lower stress deposited gold [182]. Agitation of the plating solution helps to maintain a constant concentration of gold ions in the solution. This is particular important at the metal-solution interphase, where the reduction of cations at the cathode, will result in a lower concentration, thus reducing the deposition rate.

Electrodeposition has been used to produce coils of varying dimensions and with different metals. Examples used for microfabrication of metallic structures and dimensions which have been achieved, are summarized in Table 4.1. The information contained in Table 4.1 clearly illustrates that electrodeposition of conductors to form microcoils can be achieved. The three metals which have mainly been used for electrodeposition of coils are gold, copper and nickel. For this work the most important property is the resistivity, as this will determine the resistance and therefore the power dissipation of the deposited structure. Copper has the lowest resistivity at 16.78 $n\Omega\ m$, gold and nickel are 22.14 $n\Omega\ m$, 69.3 $n\Omega\ m$ respectively. These materials have been used to achieve structures up to 35 μm thick, with an aspect ratio of 2 : 1 (width: thickness). The other important aspect to consider with this technique is the production of the

Material	Thickness (μm)	Width (μm)	Author Reference
Copper	18	10	Inoue et al. [184]
Copper	$10 - 20$	50	Sadler et al. [180]
Gold	35	(-)	Liakopoulos et al. [172]
Gold	10	50	Velten et al. [177]
Gold	(-)	10	Lee et al. [160]
Gold	10	100	Deng et al. [164]
Nickel/Iron permalloy	25	50	Choi et al. [163]
Nickel permalloy	10	25	Do et al. [185]
Nickel	25	60	Smistrup et al. [186]

Table 4.1: Summary of electrodeposited materials for microdevices, including material and critical dimensions.

thick mould. A variety of materials have been used to produce thick moulds; Polyimide ([184]), AZ-photoresist ([172; 180; 163]) and SU8 ([185])). The critical part of the mould is the aspect ratio, because it is very difficult to successfully produce patterns with high aspect ratios. The thickness of the metal structure and the physical pattern for the thick resist mould must be carefully considered during the coil and mask design.

4.6 Conclusion

The use of paramagnetic beads has been identified as a means to form physical structures such as pillars [157] and plugs with a random fluid path [169]. These structures have been used for the separation of molecules in a fluid flow. This relies on the beads being held in place by the application of a magnetic field gradient from permanent magnets. It was hypothesised that it should be possible to apply a plug of paramagnetic beads to exert a force on a fluid in a microchannel by a similar approach to that used by others where ferrofluid was used [32; 52; 53]. The effectiveness of this approach will depend upon the paramagnetic bead plug structure, which is formed in the microchannel, and the size of the force which can be applied on the fluid using the plug of paramagnetic beads.

Although successful separation of paramagnetic beads has been achieved using microcoils [164; 171], it is microdevices configured for the transportation of paramagnetic beads that is of the most interest for this study. The most suitable example which could be applied for the proposed bead transportation for this work, is a microdevice, that was produced by Rida et al. [171], see Figure 4.13. However this example relies upon the use of overlapped coils, which is difficult to fabricate, because a double conducting layer is required. The examples produce by Deng et al. [164]; Rida et al. [171], use a magnetic field to magnetise the beads, before the 'microcoils' are sequentially actuated to move the beads. It should be possible to achieve the same movement of the beads without this initial magnetisation.

The multiple turn coils produced by Rida et al. [171] are very large (4 mm diameter), therefore it would be better to use many smaller single loops (100 μm) in which a similar magnetic flux density can be theoretically achieved. Indeed, single loops coils have been shown to produce similar magnetic flux densities (3 mT, Lee et al. [160]) as spiral coils ($1-4$ mT, Rida et al. [171]). The example produced by Rida et al. [171] has a distance of 250 μm between the coils and the channel; obviously by reducing this distance the magnetic flux density in the channel could be increased. Indeed, Choi et al. [161] have achieved a separation of just 1 μm between the microchannel and the coil structures. These loop structures will be valuable for integration with fluidic microchannels for the creation of a dispensing device, as described in Chapter 6.

Chapter 5

Displacing and dispensing using paramagnetic beads

5.1 Introduction

As outlined in Chapter 4 the new concept behind this research is a novel method for fluid displacement, which is achieved by the magnetic actuation of paramagnetic beads to dispense fluid. In the past, magnetic devices have been fabricated where ferrofluid is used for fluid displacement ([32; 52; 14; 54]), such structures include micropumps and pipettes. Permanent magnets or coil structures wrapped around fluid channels were used to move a plug of ferrofluid along a channel to displace a non-miscible aqueous fluid in front of it. Here paramagnetic beads were considered as a bio-compatible alternative to ferrofluid; paramagnetic beads have been present in other microdevices which have been used for different biological applications ([168; 169; 170; 157; 158; 34]). The most notable of these are microstructures where well defined pillars of beads are self assembled [170; 157; 158]. Although bead plugs with random fluid flow paths have also been created [168; 169]. Here it is proposed to create a microdevice for magnetic bead manipulation, as outlined in Chapter 6. The device will be used to create bead structures that are highly dense to act as a plunger for fluid displacement, the plug is then dispersed to form a less dense structure to enable the beads to be moved to the starting location for re-dispensing.

The proposed technique will use thousands of beads within a microchannel. For previous systems, as discussed in Chapter 4, the paramagnetic beads have been used in microdevices as vehicles for the association of biomolecules on the surface for transport [164; 171]. Here the purpose of the paramagnetic beads is for the creation of a plug to act as a plunger and physically block the channel. It has been shown that it is possible to produce bead plugs, using a non-uniform magnetic field, which fill the channel [168] (see Section 4.4). It may not be possible to completely block the microchannel as the beads are spherical and packed in a cubic close pack structure. It was considered that a sufficiently long bead plug could be used to create a force to push fluid along in the channel. In effect by moving the plug through the microchannel, fluid would be displaced in front and behind the plug.

To form a dispensing device using this technique a varying plug density is required. A dispensing device requires a pressure to pipette fluid, but also a method of refilling. The force which can be applied using a single bead within a non-uniform magnetic field has already been discussed in Section 4.2.2. Firstly, it is assumed that a plug of beads can be used to apply a force which is equal to the sum of the forces of all the beads. This plug of beads can be used to apply a pressure within a fluid filled microchannel. Providing that the pressure exerted using the bead plug does not exceed the pressure derived from the resistance to flow of the fluid, and then the bead plug can be used to displace the fluid at an increasing velocity. However when the pressure derived from the resistance to flow is greater than the pressure exerted using the bead plug, it is proposed that the fluid will begin to move through the bead plug. This is because the fluid will cause the beads to separate thus allowing the passage of fluid through the plug.

The proposed technique will use a bead plug in two defined states; plugging and slipping. When the pressure which can be exerted using a bead plug is greater than the force required to displace the fluid at a given velocity, the bead plug will be in the plugging state. It is assumed that beads will be packed closely together in a cubic close pack structure. The Kepler conjecture states a packed volume of spheres cannot exceed a density greater than that of the face-centred cubic packing, resulting in a density of 74.048% [159]. When the plug pressure is exceeded, the plug will be in the slipping state. This technique is proposed to dispense fluid by moving the bead plug in the

plugging state in one direction and returning it to the start position in the slipping state. The system and forces acting on the bead plug are illustrated in Figure 5.1. This system assumes that there is an infinite volume of fluid at each end of the capillary and therefore there will be no capillary forces acting upon the fluid at the air-liquid interface.

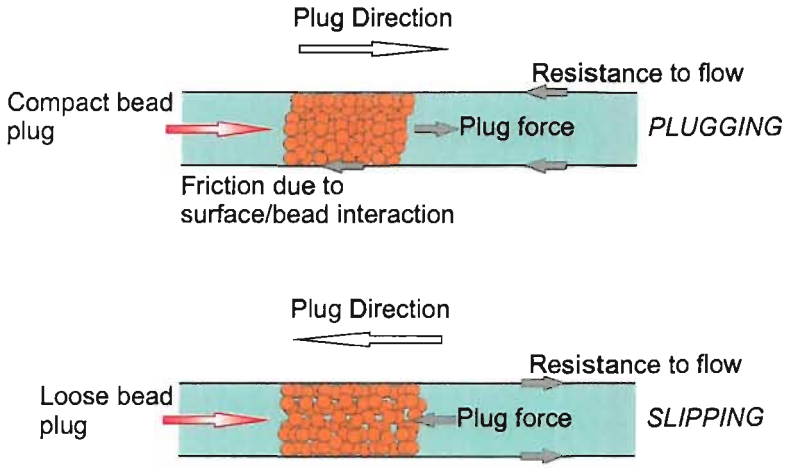

Figure 5.1: Illustration of the plugging and slipping state of a paramagnetic bead plug being moved through a fluid filled microchannel.

Limited information exists at present in the literature, and public domain, about the behaviour of a plug of paramagnetic beads and movement of this plug when displacing fluid. For this reason a simple series of experiments were performed to establish whether a bead plug could be used as an actuation method within a novel pipette device and to determine the requirements of this technique for fluid displacement.

5.2 Dispensing technique theory

As described in Section 5.1, it is proposed that when the bead plug is in the 'plugging state' and moved through a fluid filled microchannel, a volume of fluid equal to the volume moved through will be displaced. However once the bead plug is in the 'slipping state', the fluid will move through the plug. The following experiments were carried out to test the proposed principles.

The major force which is opposing the bead plug force as it is drawn through the microchannel, by the applied magnetic field, is the viscous flow, as discussed in Sec-

tion 3.2.2. The pressure drop across a fluid channel can be predicted for a given flow velocity. This theoretical pressure drop can be approximated using the theory of steady state laminar flow between parallel planes [86] and assuming that the microchannel is horizontal. The flow is considered to be parabolic across the centre plane, midway between to the two plates. This approach considers that the flow resistance due to the upper and lower plates is considerably greater than the resistance due to the two sides of the microchannel. The duct dimensions are channel width (a) and channel height (b) such that $a >> b$, where Q_{duct} is the volume flow rate within the channel, μ is the fluid viscosity and $\frac{dp}{dL}$ is the pressure gradient, illustrated in Figure 5.2. Thus the volume flow rate Q_{duct} is defined by Equation 5.1.

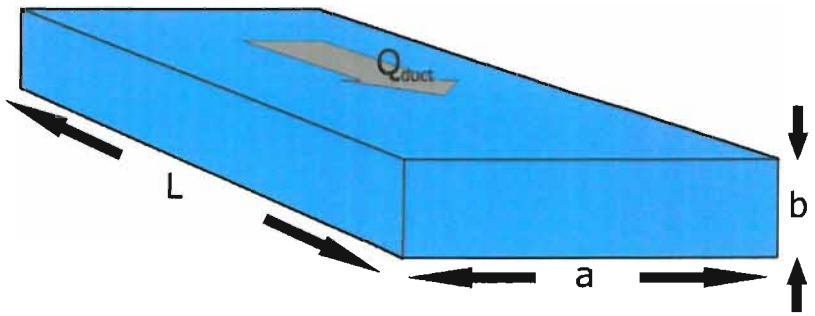

Figure 5.2: Rectangular duct, illustrating the terms used in Equation 5.1.

$$Q_{duct} = \frac{ba^3}{12\mu}\left(\frac{-dp}{dL}\right) \tag{5.1}$$

The pressure gradient $\frac{-dp}{dL}$ is replaced with a pressure difference ΔP, over a distance L to obtain Equation 5.2.

$$Q_{duct} = \frac{ba^3\Delta p}{12\mu L} \tag{5.2}$$

While this simple theory holds true for the flow of fluids through channels where the width is much greater that the height, the relationship of volume flow rate for viscous flow in a circular duct can be applied, as studied experimentally by Hagen and Poiseuille [85]. Equation 5.3 is for the volume flow rate for a circular pipe, where R_{duct} is the radius of the duct. This is obtained by integrating for the pipe flow of a fluid through a circular duct. It is assumed that there is fully developed laminar flow with

a paraboloid of revolution about the centre line. The pressure gradient is negative and thus the flow rate will be positive.

$$Q_{duct} = \frac{\pi {R_{duct}}^4}{8\mu}\left(\frac{-dp}{dL}\right) \tag{5.3}$$

To apply this theory, Equation 5.3, valid for a non-circular duct, the hydraulic radius of the duct must be considered. The hydraulic radius (R_h) is obtained using the wetted perimeter (P_{wet}) and the cross-sectional-area (A) of the duct; Equation 5.4.

$$R_h = \frac{2A}{P_{wet}} \tag{5.4}$$

The hydraulic radius can be used to replace the circular radius in the Hagen-Poiseuille equation. First consider that $\pi {R_{duct}}^2 = Area$. Secondly consider the $Area = a * b$ for the rectangular duct, where a is the channel width and b is the channel height. If this is replaced in Equation 5.3, Equation 5.5 is obtained.

$$Q_{duct} = \frac{Area{R_{duct}}^2}{8\mu}\left(\frac{-dp}{dL}\right) \tag{5.5}$$

By replacing R_{duct} with R_h from Equation 5.4 and simplifying where appropriate, the result is a relationship which can be used to determine the volume flow rate for a given pressure gradient and channel dimension; Equation 5.6.

$$Q_{duct} = \frac{a^3 b^3}{8\mu(a+b)^2}\left(-\frac{dp}{dL}\right) \tag{5.6}$$

Equation 5.6 is expressed in terms of pressure gradient along the channel of length L; Equation 5.7 indicates the flow rate which will result for a given channel, with an applied pressure ΔP.

$$Q_{duct} = \frac{a^3 b^3 \Delta P}{8\mu(a+b)^2 L} \tag{5.7}$$

It is important to note that there are already examples of devices which have been created to transport paramagnetic beads through fluid using a magnetic field. Most

notable is an example produced by Joung et al. [167], where electromagnets are used to transport paramagnetic beads through a fluid capillary (see Section 4.4). For this example, the design is based on the assumption that the beads are being moved through the fluid and therefore the beads will experience a frictional drag force. For the proposed device in this work it is assumed that the beads and fluid are moving at the same velocity and therefore there will be no drag force on the beads.

5.3 Initial permanent magnet investigation

5.3.1 Introduction

A microchannel was produced for these proof of concept experiments. The microchannel was fabricated in silicon and Pyrex. Single fluidic channels were fabricated and are described fully in Section 6.3.1. The channels were etched by deep reactive ion etching (DRIE) in silicon and capped with a Pyrex wafer by anodic bonding. The channels are 100 μm wide, 27 μm deep and 30 mm long. Fluidic connections are made to the microchannels via channels sawn into the Pyrex substrate. This allows for a connection to be made in the same plane as the channel, as illustrated in Figure 5.3. Paramagnetic beads are introduced into the microchannel and these are moved through the channel, in a plug, using the linear translation of a permanent magnet. The volume of fluid which is displaced using the bead plug is recorded as a function of the velocity of the magnet.

The channel dimensions used for this experiment were chosen for three reasons. (1) To ensure that it was possible to observe fluid slip past the bead plug. (2) To ensure that it would be possible to measure the volume dispensed. (3) To dispense nanolitre volumes of fluid.

5.3.2 Experimental apparatus and procedure

The particular paramagnetic beads (M-450, Invitrogen) used for this work have an epoxy group on the surface. The epoxy group makes the surface of the beads hydrophobic, promoting possible aggregation and adhesion of the beads to the silicon (hydrophobic)

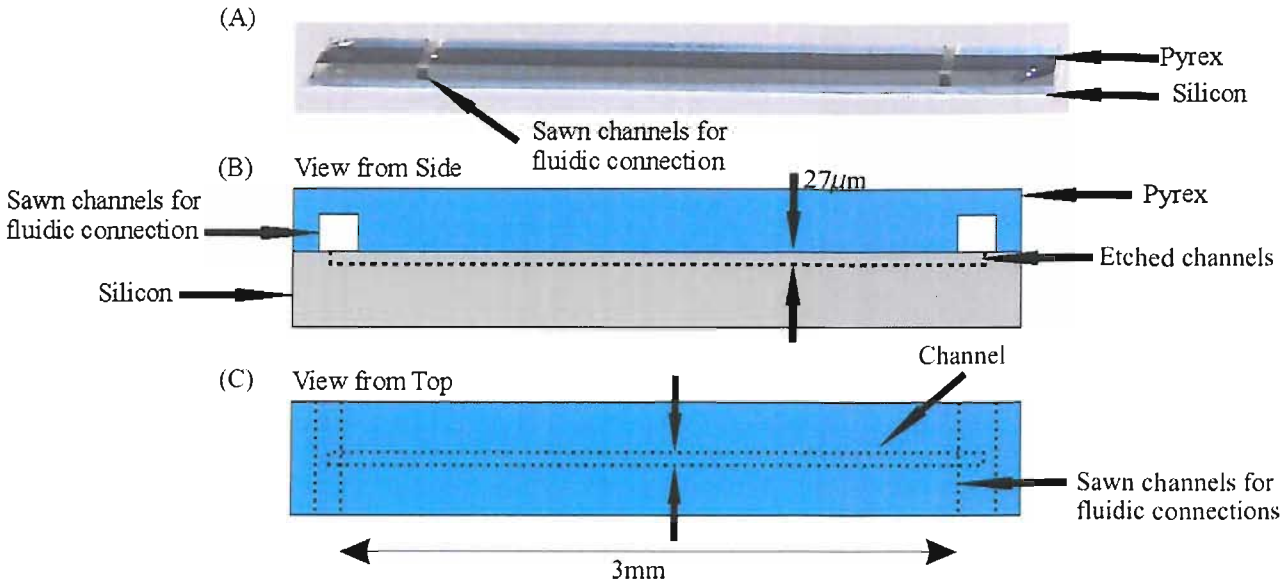

Figure 5.3: (A) Image of the silicon and Pyrex fabricated microchannel, (B) diagram of the silicon and Pyrex microchannel, (C) view of channel from above.

surface during experiments. To further tune the surface properties of the beads a 1% Triton (Triton X-100, Fisher BioReagents) solution was used in these experiments. The 'soap-like' hydrocarbon chain (hydrophobic) of the Triton is proposed to interact with the epoxy group on the bead surface. Thus the hydrophilic hydrogen-oxygen group of the Triton X-100 will be on the outside of this bead surface; this will make the bead more stable in the water solution as the bead will be more hydrophilic.

The theoretical pressure drop along the length of the channel was calculated using Equation 5.7, where the volume flow rate was determined using flow velocities from 0 *to* 1 $mm\ s^{-1}$, and is shown in the graph in Figure 5.8 by the diagonal line, on page 103. The dimensions of the channel were taken as: $a = 100\ \mu m$, $b = 27\ \mu m$ and $L = 30\ mm$. The viscosity of the fluid used (1% Triton solution) was measured using a viscometer (Poulten, Selfe & Lee Ltd, BS/IP/SL(S) Size2) prior to the experiment and was found to be 1.1 $mPa\ s$.

The microfabricated channels, produced to determine the potential of a bead plug based technique, must be included in an experimental set up such that the volume which is displaced using a bead plug can be determined. The experimental apparatus is illustrated in Figure 5.4, showing the fabricated device with additional components. Due to the small dimensions of the channels used for the experiment it is important to

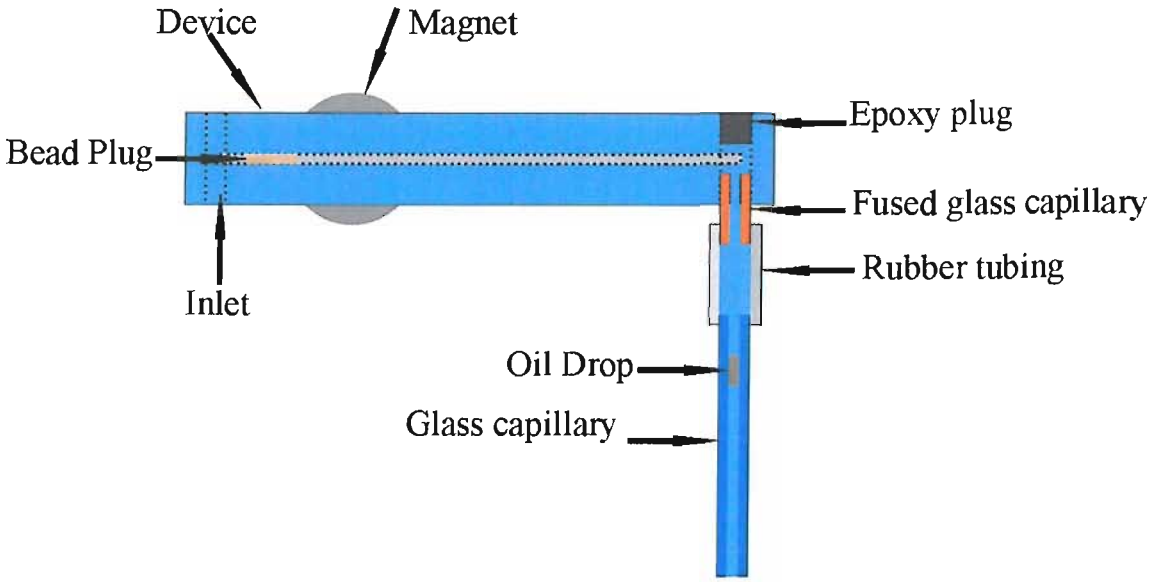

Figure 5.4: Experimental apparatus, illustrating the fabricated device, connected to a glass capillary used to determine the volume of fluid which is displaced by the bead plug (plan view).

ensure that the flow being measured is due to the pressure exerted using the magnetic bead plug under actuation by a moving magnet and not an artifact such as capillary force. The channel is primed with an aqueous solution of a 1% Triton, introduced into the inlet of the device and allowed to fill the channel, as a result of the inherent capillary forces. Once filled, the fluid is drawn through the remaining apparatus using a syringe to avoid bubble formation. The beads are then drawn into the microchannel with a permanent magnet. The beads are held within the microchannel using the magnet until required.

A fused glass capillary is fixed at the outlet using epoxy glue (B&Q, repositionable epoxy glue). A plug of epoxy glue is used to block the other part of the outlet. Connected to this fused capillary is a glass capillary (Cammag, 0.5 μl, 140 μm internal diameter), which is connected via a piece of rubber tubing (SF Medical 0.5 mm internal diameter). The glass capillary will be used to measure the flow induced by the bead plug. Finally, in order to determine the flow within the microchannel, an oil droplet has been introduced into the glass capillary. The purpose of the oil is to provide a marker to measure the flow due to the bead plug. The minimum volume which can be determined is 1 nl, which corresponds to the oil droplet moving 6 μm in the glass capillary, within the apparatus shown in Figure 5.4. The device is illustrated in Figure 5.3.

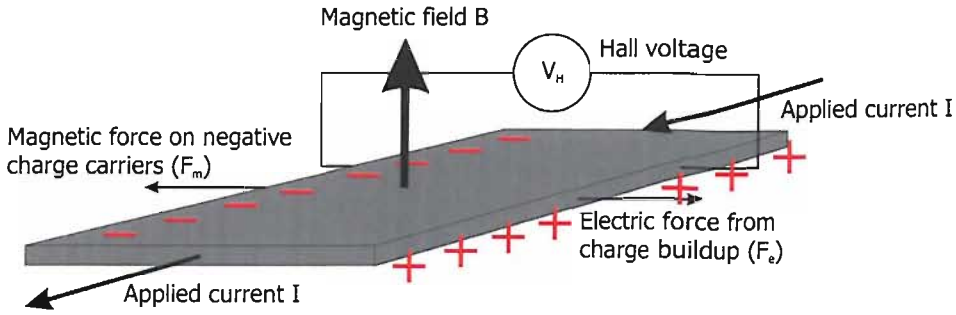

Figure 5.5: Illustration of a Hall probe configuration.

A piece of rubber tubing was attached to the open end of the glass capillary (Figure 5.4), which was used as a reservoir. During the experiment it was ensured that the inlet and reservoir was always full of fluid; this is done to avoid any potential meniscus, which could impede the fluid movement. The meniscus in the rubber tubing would produce a force acting in the same direction as the fluid movement, therefore if this were contributing a force, it would increase the fluid flow, resulting in a higher displacement force than predicted.

The magnetic field for these experiments was provided by a bullet magnet from Assemtech (M1219-5). This is a neodymium iron boron magnet with a high magnetic field (0.35 T, Assemtech) and a diameter of 9 mm. To ensure that the theoretical plug force could be calculated accurately the magnetic flux density of the magnet was measured using a Hall probe (Allegro Microsystems, UGN-3501M). A Hall probe contains a thin flat conductor through which a current is applied, as illustrated in Figure 5.5. When this conductor is placed into a magnetic field, a force which is dependant on the field strength is experienced by the moving charge carriers. This yields a build up of charge at the edges of the conductor. A measurable voltage between the two sides of the conductor, perpendicular to the applied current direction, results. The measured voltage is known as the Hall voltage and is proportional to the magnetic field. In the case of the Hall probe used here (Allegro Microsystems, UGN-3501M) this proportionality is 0.36 T v^{-1}.

The measured magnetic flux density using a Hall probe was recorded at the surface of the magnet and at 0.25 mm and 0.50 mm from the surface. The measurement was carried out at different distances to determine how the magnetic flux density differed

across the depth of the microchannel. Figure 5.6 illustrates the measured magnetic flux density values measured using the Hall probe. From the measured magnetic field at the surface of the magnet, the magnetic flux density and a value for ∇B^2 were estimated to be 0.24 T and 70 $T^2\ m^{-1}$ respectively, at the edge of the magnet. The edge of the magnet has the highest field gradient and therefore a bead plug will form at this point.

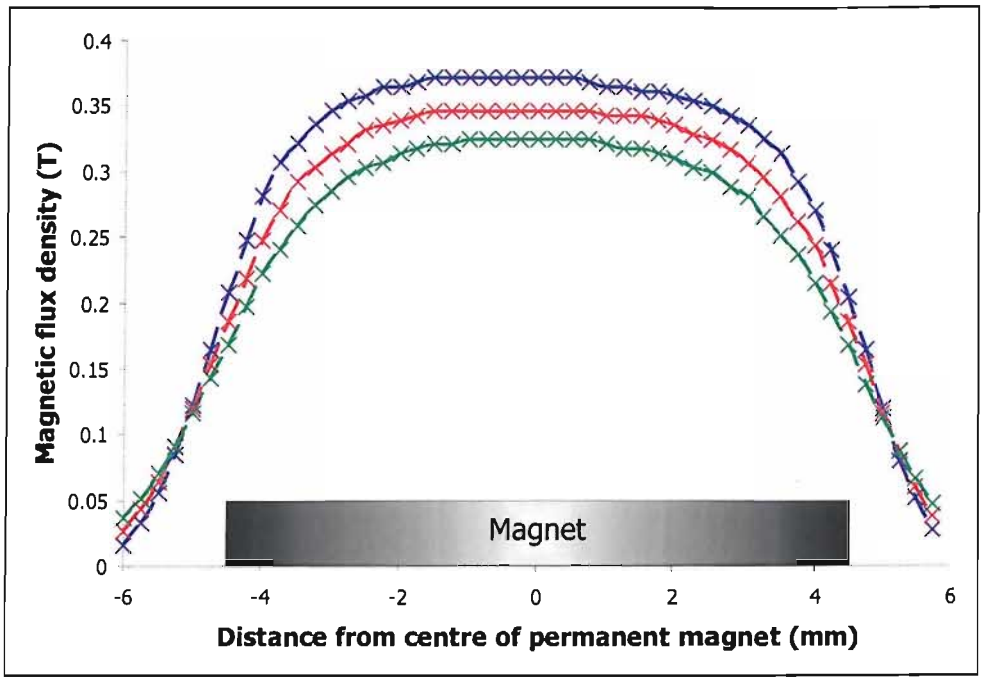

Figure 5.6: Graph of magnetic flux density against the distance from the centre of the permanent magnet (Assemtech M1219-5), taken at the magnet surface (-x-) and 0.25 mm away (-x-) and 0.50 mm (-x-) from the magnet surface.

The Hall probe which was used to measure the magnetic flux density is unfortunately sealed within an eight pin dual in line (DIL) package. Due to this the magnetic flux density which has been measured is approximately 500 μm away from the sensing element within the DIL package. However, the microchannel used within the experimental apparatus, has been produced in silicon which is approximately 500 μm thick. Therefore the magnetic flux density within the microchannel can be approximated to be the magnetic flux density which was measured at the surface of the magnet using the Hall probe, as illustrated in the graph in Figure 5.6. The uniformity of the measured magnetic flux density of the magnet is due to experimental error.

A variation in the magnetic flux density was detected by the Hall probe as it was moved away from the magnet surface. The magnetic flux density must be constant

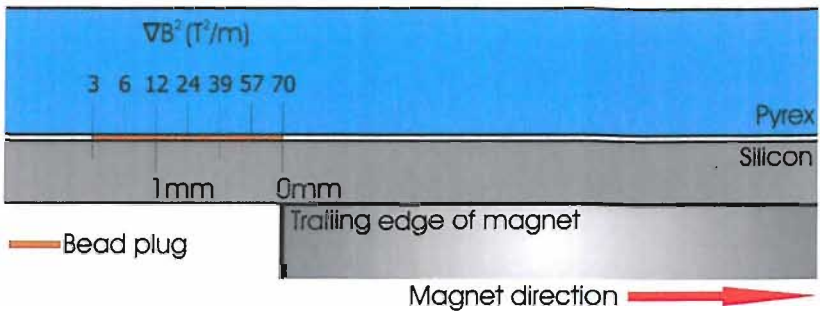

Figure 5.7: Illustration of a 1.5 mm bead plug within a microchannel, showing ∇B^2 ($T^2\ m^{-1}$) of the permanent magnet at discrete points (every 0.25 mm) along the microchannel.

across the depth of the channel to establish the theoretical plug force which can be produced. The variation of magnetic density over a distance of 250 μm was measured to be approximately 0.025 T. The magnetic flux density will decrease across the depth of the channel (27 μm) to a much smaller degree, so it is considered to be constant.

The theoretical bead force for a single bead was discussed in Section 4.2.2, Equation 4.8. A value for ∇B^2 was estimated from the graph in Figure 5.6, along the length of the microchannel up to 1.5 mm away, in 0.25 mm increments, as shown in Figure 5.7. The force was calculated theoretically with values for ∇B^2, estimated from the graph in Figure 5.6 using Equation 4.8, along the length of each bead plug. The theoretical plug force was predicted for four different plug lengths. The theoretical pressure was predicted from the plug force, by dividing it by the area of the microchannel ($3\text{x}10^{-9}\ m^2$), as shown in Figure 5.8 (horizontal lines).

The theoretical fluid pressure in the graph in Figure 5.8 has been predicted using Equation 5.7. For this prediction it is assumed that the length of the fluid in the channel (L) remains constant, because as fluid is being forced out of the end of the channel in front of the bead plug, fluid is drawn into the other end of the channel behind the bead plug. When the fluid pressure within the microchannel was predicted theoretically, for velocities up to 1 $mm\ s^{-1}$, the additional fluidic structures connected to the device were also considered. These are a glass capillary with an internal diameter of 140 μm and a length of 3 cm and a piece of rubber tubing with an internal diameter of 0.5 mm and a length of 1 cm.

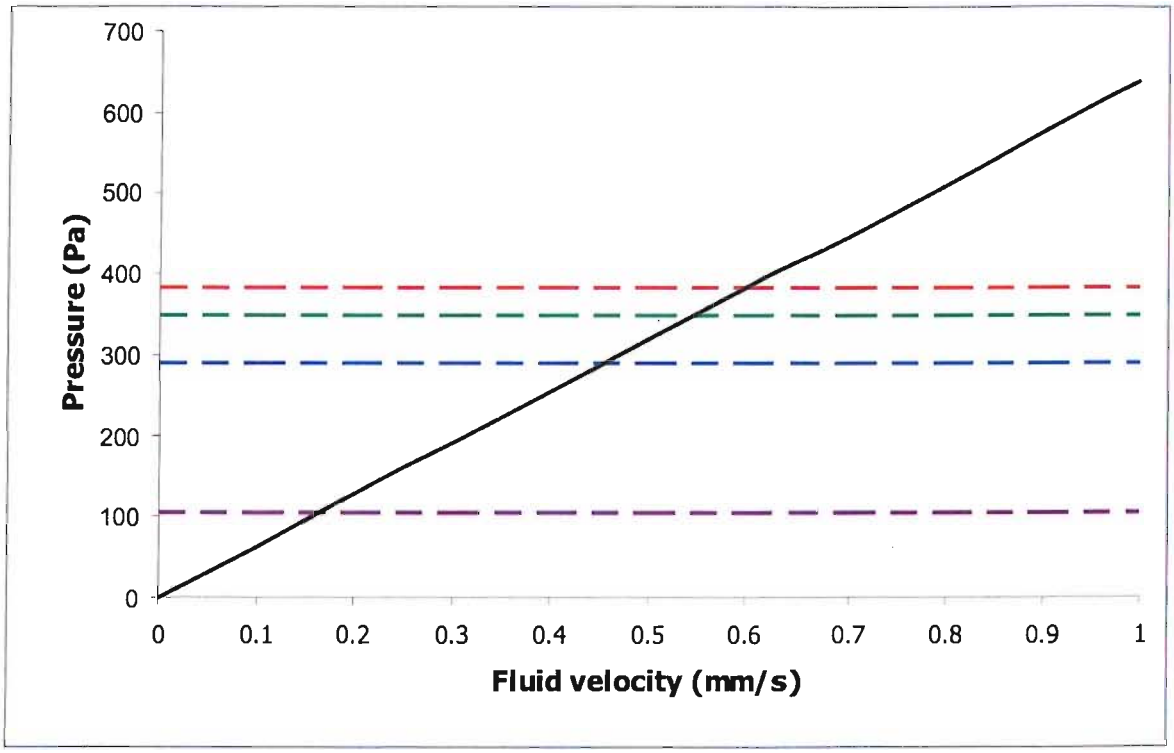

Figure 5.8: Theoretical relationship of velocity dependent theoretical pressure drop across the apparatus fluid channel against average fluid velocity, with the theoretical plug pressures. Illustrating the point at which fluid slip past the bead plug will occur. [===] channel pressure, [===] 12 000 beads, [===] 32 000 beads, [===] 40 000 beads, [===] 48 000 beads.

The impulse of the system was considered because the bead plug and the fluid will be accelerated from stationary to a given velocity up to 2.6 $mm\ s^{-1}$, during the investigation. By predicting the change in linear momentum of the system it is possible to predict the rate of change of the momentum that is required such that the plug force is great enough to displace the fluid from zero to the constant velocity used. For example a minimum time of 4 ms must be allowed to reach a final velocity of 1 $mm\ s^{-1}$. This was estimated using the mass of fluid which is present in the experimental apparatus illustrated in Figure 5.4. If this acceleration time is not allowed the result will be an initial slippage of fluid past the bead plug at the beginning and end of the bead plug movement. The predicted time will obviously increase with the fluid velocity.

During the experiment the magnet was placed beneath and in contact with the channel, such that the centre of the magnet is aligned with the channel, illustrated in Figure 5.4. The movement for the magnet was provided by a Melles Griot motorised linear translation stage ($NanoStep^{TM}$ 1000 linear positioning stage, with an apt^{TM} system stepper motor controller). The stage is used to move the magnet relative to the microchannel, at varying velocities and distances. For the experiment the stage was used to move the magnet a distance of 10 mm and returned. This was done with velocities of 0.2 mms^{-1} and greater and up to 2.6 mms^{-1}. The bead plug was clumped (under the influence of the magnetic field) to form a plunger before the movement of the magnet was started.

The thermal stability of the system was considered. There are two parameters that will alter with temperature; these are the fluid viscosity and the susceptibility of the paramagnetic beads. Firstly the viscosity of the fluid will decrease as the temperature is increased. For water, which has a similar viscosity to the fluid being used during these experiments, the viscosity varies from 1.002 $mPa\ s$ at $20°C$ to 0.467 $mPa\ s$ at $60°C$. The result is that the pressure required to displace the fluid at a given velocity will decrease. The susceptibility of a magnetic material is inversely proportional to temperature and therefore it will also decrease with temperature, resulting in a lower theoretical force and therefore a lower pressure applied to the fluid. This is because the increase in temperature will result in a greater thermal agitation of the molecules within the magnetic material thus reducing the magnetic susceptibility.

5.3.3 Results and discussion

The following series of experiments were performed to understand the behaviour of a paramagnetic bead plug under an applied moving magnetic field to establish optimal conditions for the dispensing technique described in Section 5.2. The experimental apparatus used for these proof of concept studies is illustrated in Figure 5.4. The volume of fluid displaced by the a paramagnetic bead plug moved a distance of 10 mm is plotted in the graph in Figure 5.9. The volume of fluid which is displaced is plotted against the magnet velocity; the magnet is mounted on the motorised translation stage and is moved at velocities from 0.2 $mm\ s^{-1}$. By examining the data presented in the graph in Figure 5.9, it is clear that all of the bead plugs can be used to displace a volume of fluid equal to the volume moved through by the bead plug of 27 nl (apart from the 12 000 bead plug which will be discussed later). At a specific velocity, that is different for all the bead plugs examined here, this 'plugging' is no longer observed and fluid moves through the bead plug, resulting in a lower volume of fluid being displaced. As the velocity of the bead plugs was increased to 2.6 $mm\ s^{-1}$, the volume of fluid displaced decreases, down to volumes less than 15 nl.

The smaller bead plug of 12 000 beads does not exhibit the behaviour described above because the theoretical pressure which can be produced using this plug (105 Pa) is lower than the minimum pressure of 128 Pa required to displace the fluid at velocities from 0.2 $mm\ s^{-1}$.

The estimated and measured fluid slip points are presented in Table 5.1, for the bead plugs investigated here. This shows that the estimated and predicted plug velocity at which fluid will begin to slip through the bead plug are in good agreement. There is a difference of up to 0.2 $mm\ s^{-1}$ in the case of the 48 000 bead plug, however the theoretically estimated slip velocity, was determined using an approximate number of beads. This approximation was determined by visually measuring the bead plug, which is not an accurate technique to determine the number of beads within the plug. The best method would be to remove the bead plug after the experiment and determine how many beads were actually used.

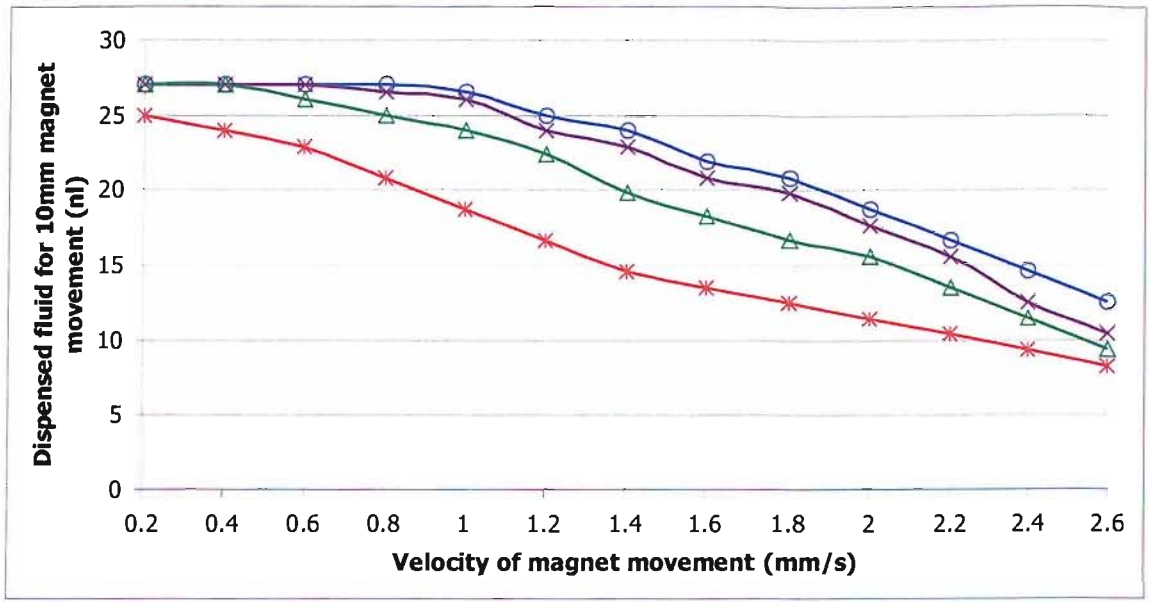

Figure 5.9: Plot of the experimentally determined volume of fluid displaced against the velocity of different size plugs of magnetic beads, for a 10 mm travel distance; the channel used had dimensions of 3 cm x 100 μm x 27 μm (HxWxD), [-∗-] 12 000 beads, [-△-] 32 000 beads, [-x-] 40 000 beads, [-o-] 48 000 beads.

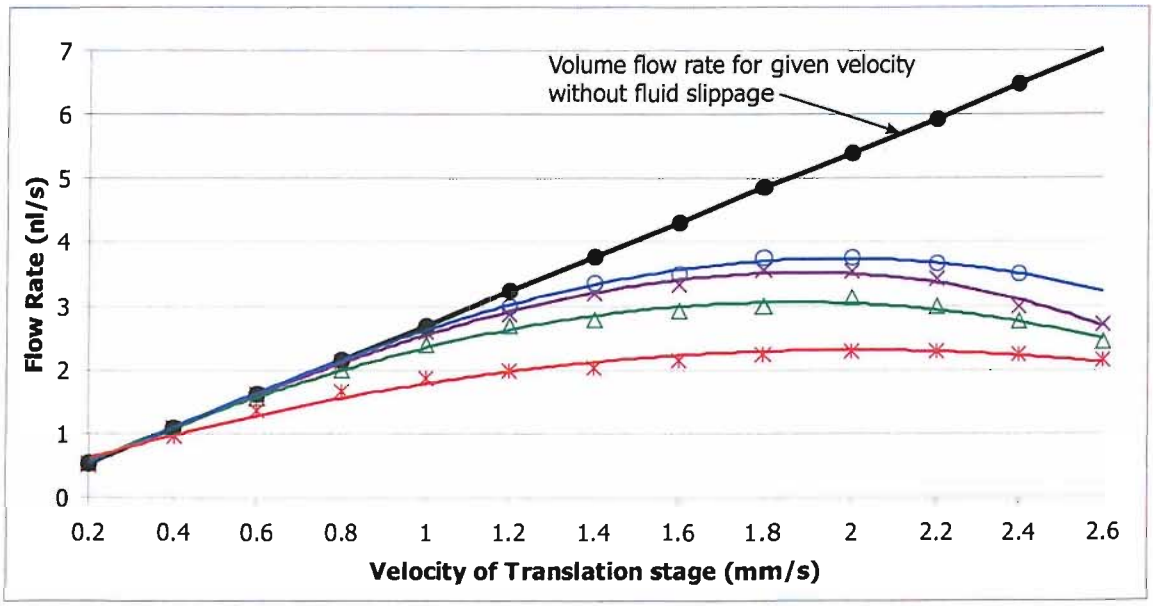

Figure 5.10: Plot of the experimentally determined volume flow rate against the velocity of different size plug of magnetic beads, for a 10 mm travel distance; the channel used had dimensions of 3 cm x 100 μm x 27 μm (HxWxD), [-∗-] 12 000 beads, [-△-] 32 000 beads, [-x-] 40 000 beads, [-o-] 48 000 beads.

Plug size, Plug length $(Beads, mm)$	Theoretical slip point $(mm\ s^{-1})$	Measured slip point $(mm\ s^{-1})$
12 000, 0.25	0.16	< 0.2
32 000, 0.75	0.46	0.4
40 000, 1.00	0.55	0.6
48 000, 1.25	0.6	0.8

Table 5.1: Estimated and measured fluid slip points for the four bead plugs used during this investigation.

The change in the bead plug length of plugs, 12 000 - 48 000, with a dependence on the velocity at which the magnet was moved using the translation stage, is illustrated in Figure 5.11. It is clear from the results described in Figure 5.10 that the volume of fluid displaced by the moving bead plug showed a dependence on the velocity at which the bead plug was displaced. There was an optimum speed for this displacement after which the volume of fluid displaced was reduced rather than increased with the velocity of the bead plug. This demonstrates that fluid is flowing through the bead plug.

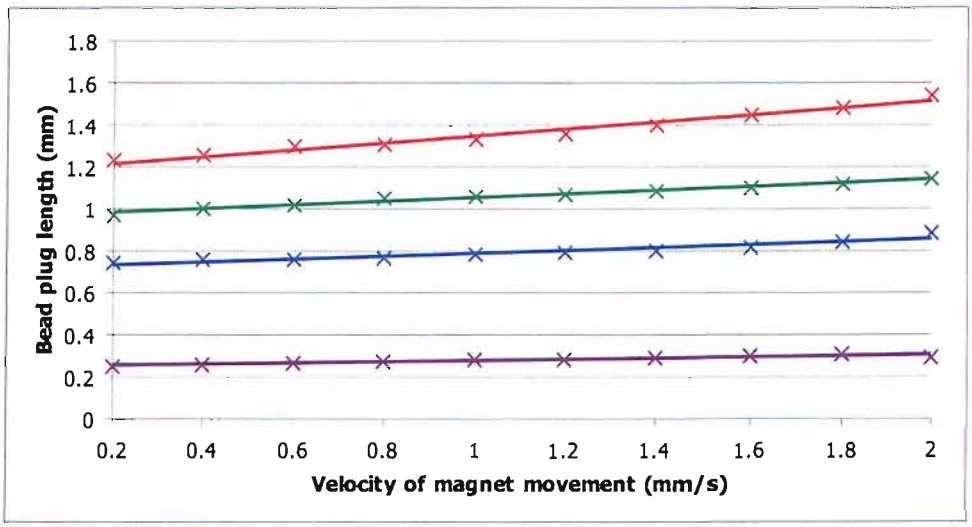

Figure 5.11: Plot of the bead plug length against the velocity of different size plugs of magnetic beads, illustrating bead plug length increase; the channel used had dimensions of 3 cm x 100 μm x 27 μm (HxWxD). The original bead plug lengths were as follows: [-x-] 0.25 mm (12 000 beads), [-x-] 0.75 mm (32 000 beads), [-x-] 1.00 mm (40 000 beads) and [-x-] 1.25 mm (48 000 beads)

It was not clear whether fluid was slipping past the bead plug or how the form of the bead plug altered at higher velocities. The images taken during the second experiment indicated that, as the bead plug velocity was increased the bead plug length increased and the bead density decreased. The graph shown in Figure 5.11 illustrates the measured length of the different bead plugs used in the channel as a function of the magnet velocity.

It has been assumed that all of the bead plugs have a bead density of 74.08 % when stationary, formed on the basis that the beads are in a cubic close pack formation. This had to be assumed, because the density of beads used for the plug make it impossible to obtain an image to confirm the packing density of the beads. The data obtained from the graph, illustrated in Figure 5.11, provides evidence that the bead plugs increase in length, with increasing bead plug velocity. It is clear from the results from these experiments, that the increase in length of the bead plugs and the rate of fluid slippage appear to be linear for each bead plug. The experimental results indicate that once the fluid slippage point has been reached, the fluid will continue to slip through the plug at a linearly increasing value with velocity; this is the same for all bead plugs. However, there is insufficient data to reach a numerical relationship between the bead plug size and the volume of fluid which is displaced.

It has been successfully demonstrated that it is possible to displace fluid using a paramagnetic bead plug. These results show that a paramagnetic bead plug formed and moved using the linear translation of a permanent magnet could be used to dispense variable volumes of fluid by either altering the distance that the bead plug is moved or by varying the velocity of the magnet. Although it has not been demonstrated here, it would be possible to dispense fluid by moving the bead plug slowly toward the outlet (with no fluid slippage), then returning the bead plug to the start position at a higher velocity, thus moving the bead plug through the fluid. This would result in a positive displacement of fluid, whereby more fluid would be dispensed at the outlet on the forward motion of the bead plug, than drawn back on the reverse motion.

5.4 Electromagnet investigation

5.4.1 Introduction

One of the aims of this work is to produce an integrated device. The permanent magnet used for the experiments described in Section 5.3 is to be replaced by integrated microcoils. Microcoils are to be integrated close to the fluidic channel and sequential actuation, which is anticipated to result in a moving magnetic field, as described in Chapter 6. The form of such an integrated device will consist of a series of electromagnets actuated in a linear sequence, one after the other along the length of a microchannel.

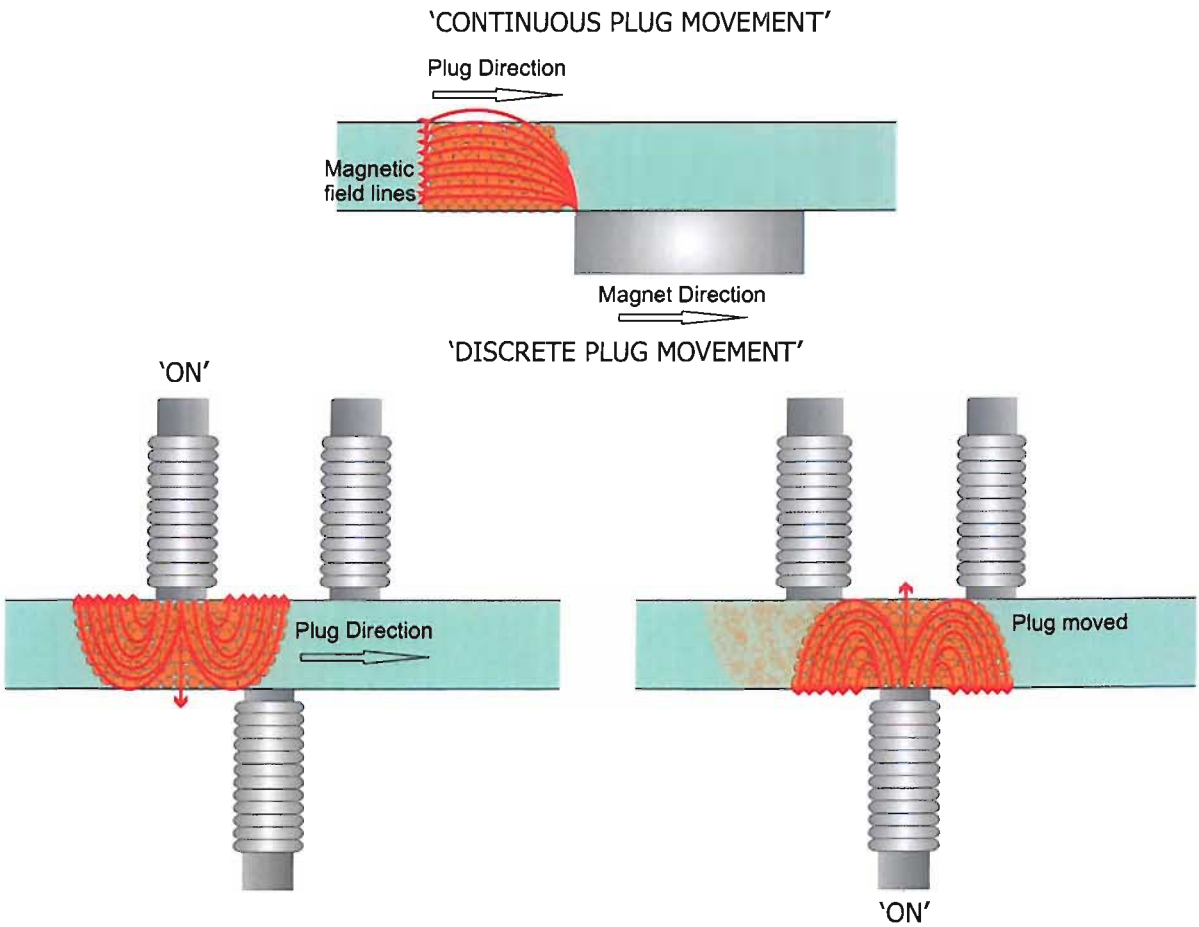

Figure 5.12: Illustration of continuous bead plug movement using a permanent magnet and of discrete plug movement using serial actuation of electromagnets.

The design and subsequent fabrication of an integrated microdevice is a complex task, therefore to test the principle a simple investigation has been carried out using

discrete hand wound electromagnets. It is not possible to create the same moving magnetic field gradient using a series of discrete electromagnets, compared to a translating permanent magnet, as illustrated in Figure 5.12. For the case of the serial actuation of a number of electromagnets the magnetic field will occur at discrete positions along the microchannel, which will result in a 'broken' motion of the bead plug and therefore the bead plug will not form a perfect plug to displace fluid.

5.4.2 Principle

Experiments were performed to establish whether electromagnets can be used to form and transport a paramagnetic bead plug through a fluid filled microchannel. The force which can be produced using a single paramagnetic bead and thus a bead plug, can be estimated using Equation 4.8. The force due to a paramagnetic bead within a magnetic field is dependent on ∇B^2, as discussed in Section 4.2.2. To replace the permanent magnet used previously in Section 5.3.2, it will be necessary to achieve a ∇B^2 of approximately 70 $T^2\ m^{-1}$ (obtained from a magnetic flux density and magnetic gradient of 0.24 T) using the hand wound electromagnets.

The investigation involved the production of a series of hand wound electromagnets. The hand wound electromagnets with 80 turns (two layers of 40 turns each) of copper wire (0.125 mm diameter) wrapped round an iron core (7 mm long and 0.56 mm diameter), had an actuation current of $500mA$. These were placed either side of a fluid capillary (Camag, $1\mu l$, 140 μm diameter) as illustrated in Figure 5.13 such that the end of the core was in contact with the capillary and the edges of the electromagnets were in contact with neighbouring electromagnets, off-set by approximately $0.5mm$ (the radius of the electromagnet). An illustration of the proposed system layout is illustrated later in Section 5.4.2; Figure 5.13. This is similar to a device which has been produced by Joung et al. [167], illustrated in Figure 4.18, page 82.

The proposed design for the system is illustrated in Figure 5.13 which is similar to the device produced by Joung et al. [167] (Figure 4.18), which was used to transport approximately 15 000 beads (Dynal, 2 μm) along a capillary (0.4 mm diameter). The electromagnets used by Joung et al. [167] were much larger than those used for this

investigation, 300 turns around a core (0.15 *mm* diameter, 20 *mm* long), however the magnetic cores extend from the coil by 10 *mm*, where the magnetic flux density is likely to be far less than at the edge of the coil. This system is used to translate a clump of beads (approximated to be 15 000) in a zig-zig pattern along a channel for transportation. Unlike the system used by Joung et al. [167], it was proposed to use a bead plug which fills the channel, therefore more beads are used (approximately ten times). The movement of this plug along the channel must not be in a zig-zag pattern, as in the device produce by Joung et al. [167].

The electromagnetic device consists of a series of electromagnets on either side of a capillary. The proposed sequence of actuation is illustrated, showing how the electromagnets will be used to form and translate a paramagnetic bead plug through the microchannel. To translate the bead plug through the microchannel three electromagnets will be used together to form a bead plug of approximately 1 *mm* long. The first electromagnet is actuated, forming a bead plug at the beginning of the sequence (Initialize system). The second and third electromagnets are actuated, forming a bead plug which extends from the first to the third coil (Sequence ONE). To move the bead plug the first coil will be returned to a 'non-actuated state' and the fourth coil will be actuated (Sequence TWO), thus moving the beads to a position in front of the fourth electromagnet. This sequence is continued, as illustrated in Figure 5.13, to translate the beads to the final electromagnet. Problems with this system have been identified and were considered during the design; heating (actuation current), magnetic remanence (magnet core material), zig-zig bead motion (electromagnet spacing and size).

The sequence for the bead actuation required perfecting to achieve transport of the paramagnetic beads from one electromagnet to the next. A plug of the paramagnetic beads forms within the a magnetic field due to one electromagnet (1) (Scenario A Figure 5.14). If a second electromagnet (2) is actuated such that the magnetic field polarity is the same as that for the first electromagnet (1), the beads trapped in the outer limits of the magnetic field will move toward the second electromagnet (2), providing that the magnetic flux density and gradient is higher at a given point (Scenario B Figure 5.14). However if the second electromagnet (2) is actuated such that the polarity of the induced magnetic field is in the opposite direction, then because the beads are already

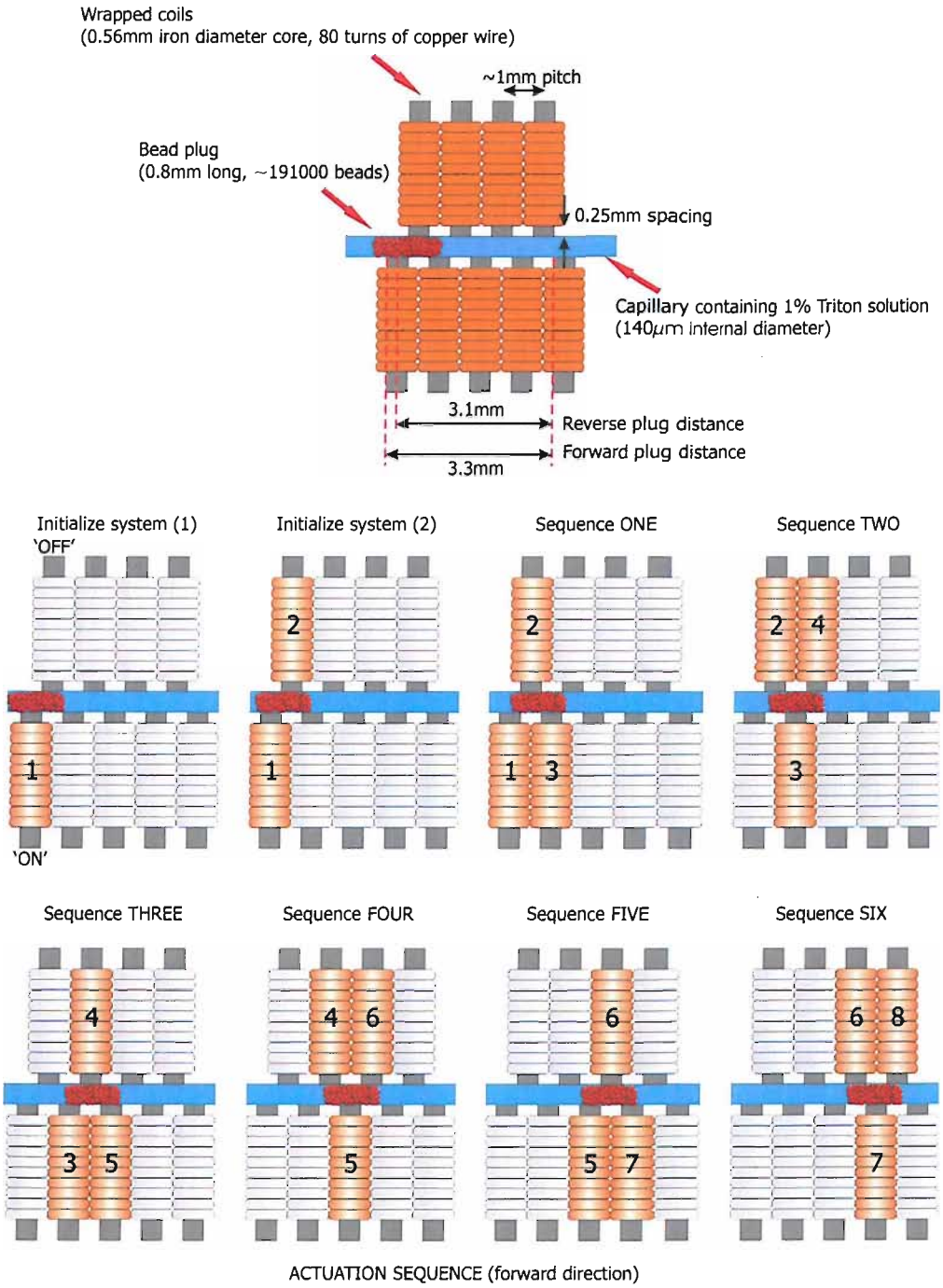

Figure 5.13: Illustration of wrapped electromagnet system to form and transport paramagnetic bead plugs and an illustration to show the coil actuation sequence used to translate a paramagnetic bead plug from left to right through the microcapillary.

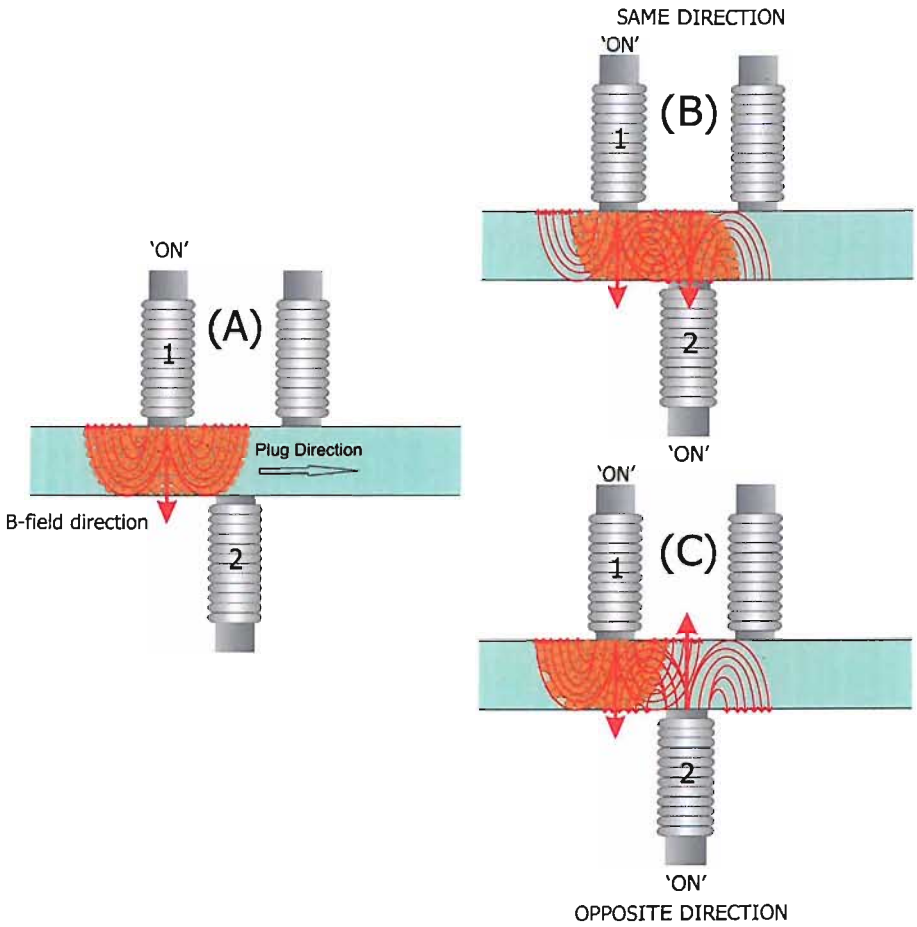

Figure 5.14: Illustration of moving beads from one electromagnet to the next, depending on the direction of the magnetic field from the electromagnet.

'magnetised', the second electromagnet (2) will repel the beads, forming a tighter bead plug (Scenario C Figure 5.14). Indeed, similar observations were made by Greivell and Hannaford [32], using ferrofluid. Unfortunately to move beads from one electromagnet to the next is a non trivial task, because it is difficult to move a bead from one point to another at the same magnetic flux density and gradient when using multiple electromagnets. This problem would be made simpler by only using one electromagnet at a time. It might be possible to improve this by temporarily turning off all the electromagnets before actuating the next electromagnet in the series. This will essentially 'de-magnetise' all of the beads such that repositioning will be easier.

5.4.3 Electromagnet design and evaluation

A structure composed of hand wound electromagnets and a capillary is required to provide a comparable ∇B^2 (approximately 70 $T^2\ m^{-1}$), within the fluid channel, to that which was observed for the evaluation described in Section 5.3 where a permanent magnet was used. In this system issues such as heating effects of the hand wound coils and remanence of the coil cores are considered. The heating of the hand wound coils is due to the power dissipated in the coil windings, which is determined by the actuation current and the wire resistance. The remanence of the electromagnets must be kept to a minimum and this can be achieved by the selection of the electromagnet core materials. The major design constraint is the optimisation of the coil to channel geometry and coil size, to provide a magnetic flux density, where the beads are transported as a plug along the channel. The most appropriate approach was considered to be by producing small diameter electromagnets and reducing the spacing between these. This will effectively produce an overlap of the magnetic flux density yielded from each electromagnet, such that a pseudo-continuous moving magnetic field might be produced.

The first part of the design is based around a suitable core material. The dimensions and relative permeability of the core material will impact upon the magnetic flux density and gradient of the electromagnet which can be produced; the magnetic field is inversely proportional to the radius, see Equation 4.13. The relative permeability of the core material is directly proportional to the magnetic flux density obtained as a result of the actuation of a coil wrapped around this core. There is a need at this time to consider

the remanence of the electromagnet core, because a proportion of the magnetic flux density is retained, as a function of the remanence properties of the material. Once the core material is magnetised, it has the potential to become permanently magnetised due to a re-orientation of the atoms within the structure and this is known as remanence. The core material chosen was iron with a diameter of $0.56mm$ and a predicted relative permeability of up to 200 (typical value). The remanence of the coil will be determined later, when measuring the magnetic flux density of the electromagnet.

The coils were created using enamelled copper wire, where the enamel acts as an insulator to prevent shorting with neighbouring loops. The wire selected for wrapping the coils has a diameter of $0.125mm$. This was selected for practical reasons because it is thick enough to be wrapped easily by hand, but not so thick such that it cannot be tightly wrapped around the iron core. The final parameter which needs to be considered for the wire size is the resistivity; the resistivity of the copper wire used is $16.7\text{x}10^{-9}\ \Omega\ m$. The maximum current density of copper is $1\text{x}10^{9}\ A\ m^2$, which equates to a maximum current of approximately 12 A for any length of this wire used.

The expression in Equation 4.13 was used to predict that a coil with 80 turns, formed in two layers of 40 turns, can be used to produce a magnetic field of $0.1T$ and value for ∇B^2 of 110 $T^2\ m^{-1}$, for an actuation current of $500mA$, at a point 4 mm away from the centre of the core (along the length of the core). This value of ∇B^2, for the electromagnet is greater than the estimated value of 70 $T^2\ m^{-1}$ for the permanent magnet. Figure 5.15 illustrates that the magnetic field from the centre of the electromagnet to a distance 8 mm away along the central axis of the coil. The coil length is 7 mm, so the centre of the core length is at 0 mm on the horizontal axis, which is illustrated by the overlaid transparent coil structure. The data in Figure 5.15 was used to predict the magnetic field gradient along the central axis of the wrapped coil structure. The graph in Figure 5.15 clearly shows that the predicted magnetic flux density is high inside the coil (1.4 T), with a rapid reduction from the end of the coil.

To ensure that the predicted and measured magnetic flux density of the electromagnet were in good agreement, a Hall probe was used to measure the magnetic flux density of the coil, along the axis of the core (see earlier discussion in Section 5.3.2 for Hall probe details). The Hall probe used was packaged in a standard DIL package, where the de-

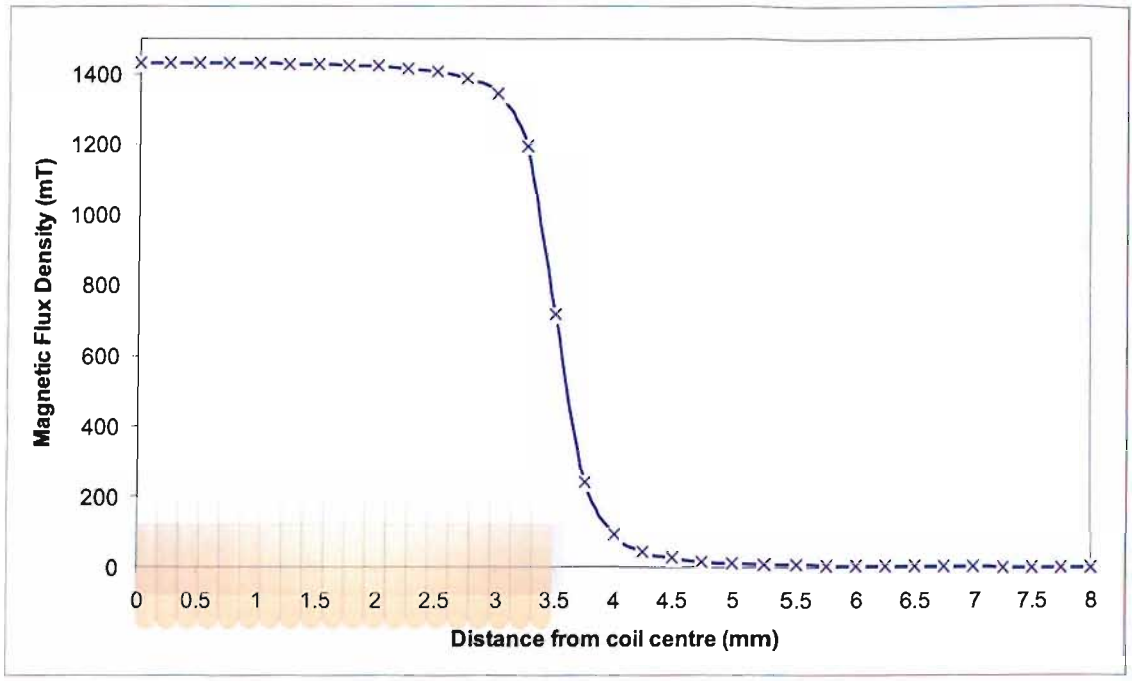

Figure 5.15: Graph of predicted magnetic flux density for a wrapped coil, with 80 turns round an iron core against, the distance from the centre of the coil. Using an actuation current of 500 mA, a core diameter of 0.56 mm and a wire diameter of 0.125 mm.

tector is approximately 500 μm below the package surface. The Hall probe was brought into contact with the end of the coil then moved away at 0.25 mm increments using an optical translation stage. The magnetic flux density was measured at each increment.

Figure 5.16 shows a graph of magnetic flux density values against distance from the centre of the coil, measured using the Hall probe. The first recorded value was measured with the surface of the coil and Hall probe in contact. The actual distance between the Hall probe sensor within the DIL package and the end of the coil was assumed to be $0.75mm$; the iron core extends 0.25 mm from the end of the coil. It is clear that the initial predicted and measured values do not agree to an acceptable level. The initial predicted values were determined using a relative permeability (μ_r) of 200. This was taken as a typical value for pure iron, but the cores used are iron wire and therefore would probably have a lower relative permeability. By reducing the relative permeability to 50, the predicted and measured values of magnetic flux density agree. Using the altered values from the graph in Figure 5.16 ([- -x- -]) the magnetic flux density and ∇B^2 were re-estimated to be 20 mT and 7 $T^2\ m^{-1}$ respectively at a distance of 4 mm from the core centre, as before.

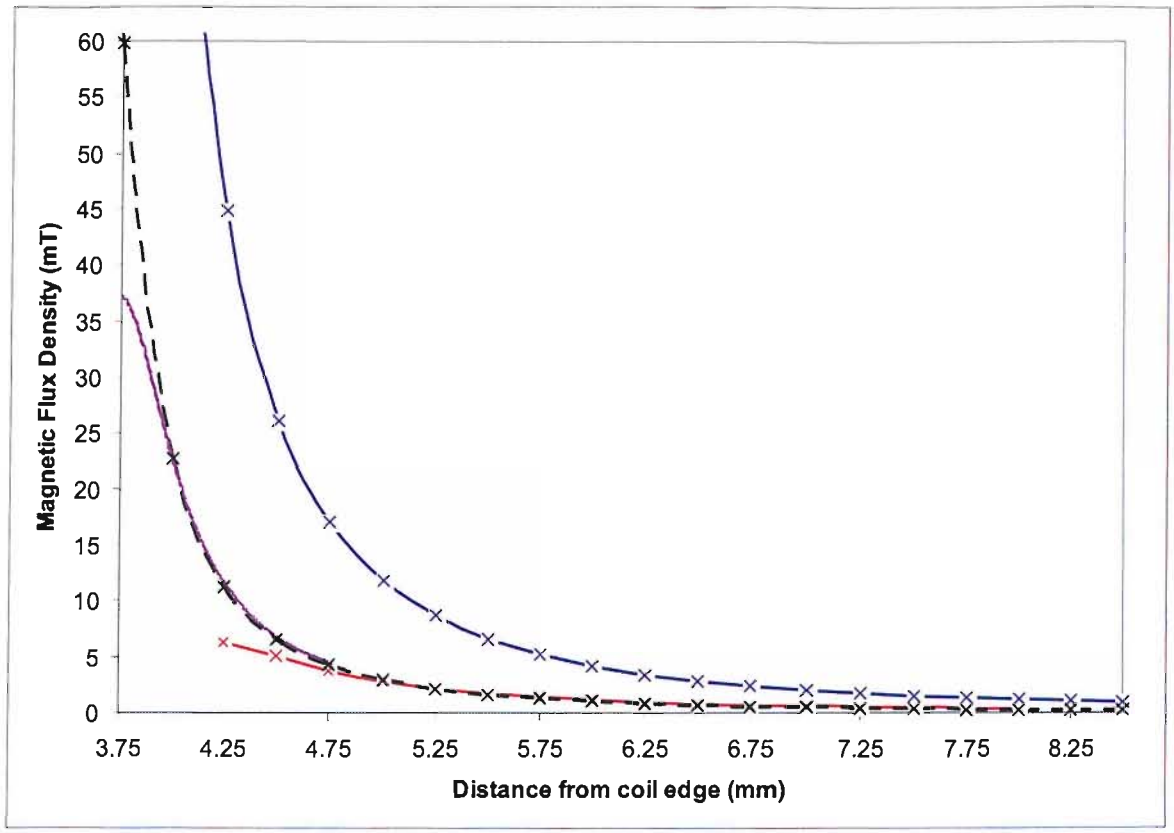

Figure 5.16: Graph of predicted and measured magnetic field for a wrapped coil (0.125 mm diameter wire) with 80 turns, around an iron core (0.56 mm diameter), against distance from the coil centre, using an actuation current of 500 mA.[-x-] B calculated (using $\mu_R = 200$), [--x- -] B calculated (using $\mu_R = 50$), [-x-] B measured and [-x-] FEMLAB simulation

Thus far only the predicted magnetic flux density of the electromagnet has been carried out in one dimension; away from the coil along the central axis of the core. However to estimate the bead plug force, the magnetic field in the direction of the fluid movement must be found. Due to the limitation of the Hall probe (DIL package thickness) it is not possible to measure the magnet flux density that will be achieved in the fluidic channel, perpendicular to the end of the electromagnet. To obtain this a two dimensional magnetostatic simulation was carried out using FEMLAB, with axial symmetry (see Appendix A.1). The important parameter for this model is the electrical conductivity of the material. These were taken as $1\text{x}10^{-13}$, $1.68\text{x}10^{-8}$ $9.61\text{x}10^{-8}$ $S\ m^{-1}$ for the air, copper (wire) and iron (magnetic core) respectively. The predicted magnetic flux density along the central axis of the core, obtained using the simulation, were compared to the measured results and is included in the plot in Figure 5.16. The magnetic flux density across the end of coil was found using the FEMLAB simulation which is illustrated in the plot in Figure 5.17. This shows the magnetic flux density at 100 μm increments from the end of the wrapped coil. As before the point of interest is at about 4 mm away from the coil centre (along the central axis), which is within the capillary in the experimental apparatus shown in Figure 5.18. This is represented by the 4 mm line in the graph in Figure 5.17.

To determine the theoretical plug pressure which can be produced using a bead plug 0.8 mm long, the results in Figure 5.17 were used, in particular the estimated magnetic field at 4 mm away from the centre of the electromagnetic core. As discussed before ∇B^2 is directly proportional to the magnetic force and an average value of this was estimated to be 0.5 $T^2\ m^{-1}$, within the capillary (see Figure 5.18). A theoretical plug force of 47 nN was obtained or a pressure of 3 Pa, using Equation 4.8. The theoretical plug pressure can be used to find the slippage point of the bead plug during translation along the capillary. The capillary used to estimate the fluid slip point, was a 3 mm long glass capillary (140 μm diameter) and two pieces of 1 cm (0.5 mm diameter) long rubber tubing, one at each end of the capillary. The theoretical slippage point was predicted to be 85 $\mu m\ s^{-1}$ using Equation 5.3 and a pressure of 3 Pa.

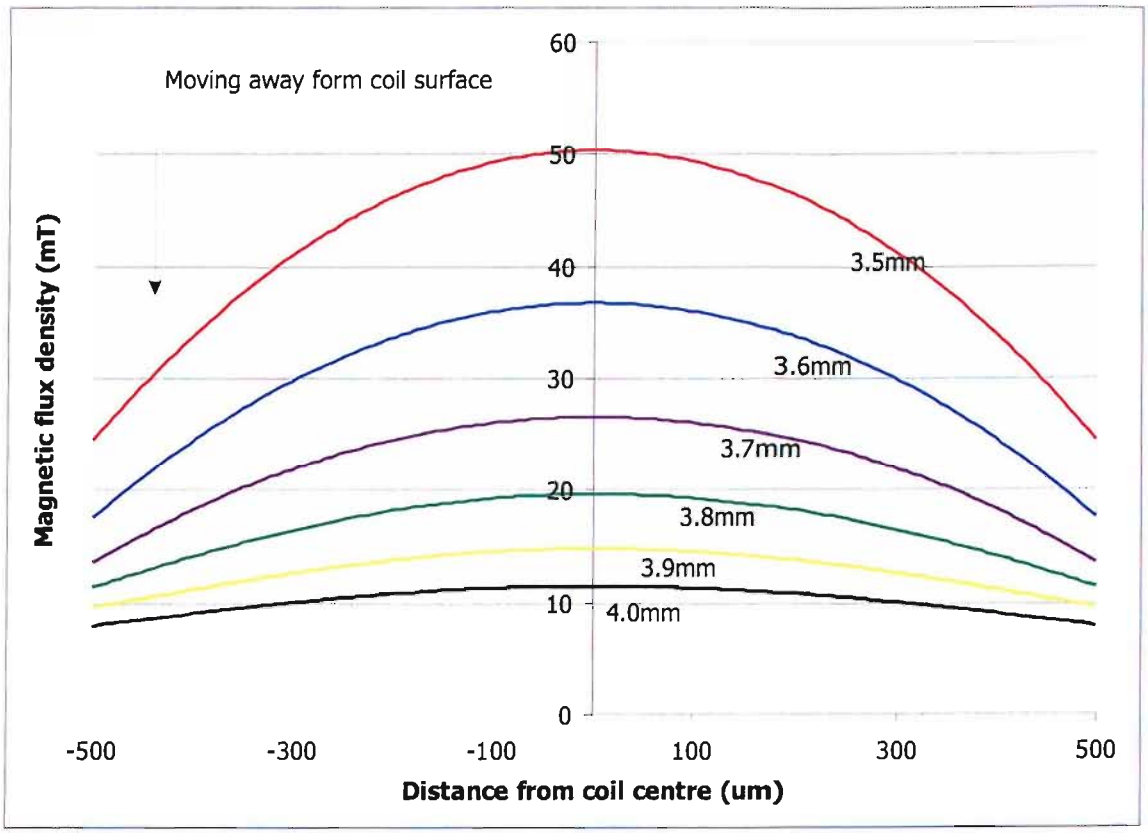

Figure 5.17: Graph of simulated magnetic flux density against distance from the centre of the coil produced using an actuation current of 500 mA. The magnetic flux density is given for incremental steps of 100 μm from the end of the iron core (3.5 mm) to a point of 4 mm away.

Finally the temperature increase is considered for the coil structure. Equation 5.8 was used to determine the temperature increase of the coil structure due to a given power, where P is the power dissipation, ΔT is the increase in temperature, Δt is the time, ρ is the density of the material, C_p is the specific heat capacity of the each material and V is the volume of each material. The material properties are summarised in Table 5.2.

Material	Specific heat capacity $(J/kg\ K)$	Thermal conductivity $(W/m\ K)$	Density (kg/m^3)
Iron	385	400	8700
Copper	444	81	7870

Table 5.2: Material properties used to calculate the temperature increase of the handwound electromagnets.

$$\Delta T = \frac{P\Delta t}{\sum \rho C_p V} \tag{5.8}$$

The wire length used was 20 cm which has a resistance of 0.25 Ω, resulting in a power dissipation of 30 mW due to an actuation current of 500 mA. The iron core was 2 cm long with a diameter of 0.5 mm. The temperature increase due to the applied current of the wrapped coil was estimated to be approximately $2°\ C\ s^{-1}$, using Equation 5.8. This is assuming that the electromagnet is not in contact with any surface. To reduce the heating of the electromagnet the structures will be placed on aluminium. Aluminium has a high thermal conductivity ($250W\ mK^{-1}$). The theoretical temperature increase is considered to be negligible and not to result in any adverse heating problems for applications of the electromagnet structures within the fluid displacing system.

5.4.4 Experimental apparatus and procedure

The fluid displacing system was set up with a series of 9 coils, arranged with 4 and 5 on each side of a glass capillary (Camag, $1\mu l$, 140 μm diameter), illustrated in Figure 5.18.

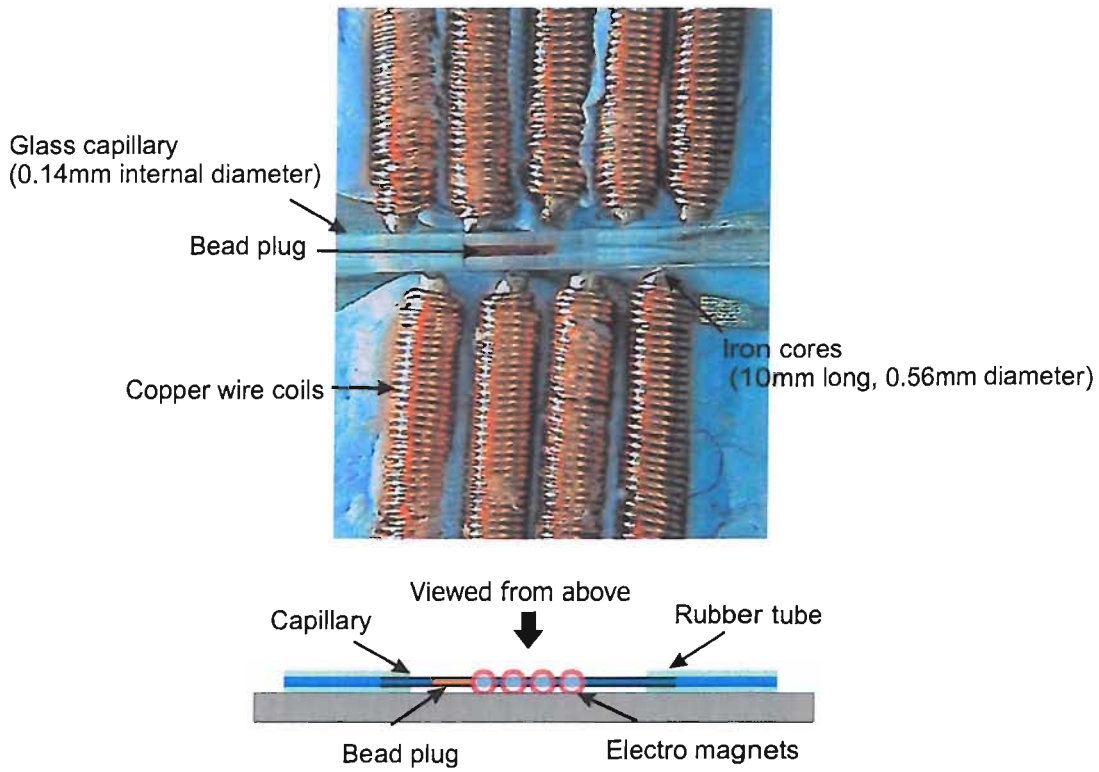

Figure 5.18: Image of the copper coils either side of the glass capillary containing fluid and paramagnetic beads, viewed from above and an illustration of the experiment (BELOW).

The capillary was loaded with a 1% Triton solution to avoid aggregation and adhesion of the paramagnetic beads. Approximately 191 000 beads were added (approximately a $0.8mm$ long bead plug). The number of beads was scaled up by a factor of ten from the permanent magnet system due to the increased cross sectional area of the channel and due to poor predicted performance of the electromagnet device. The glass capillary was attached to a 1 cm long piece of rubber tubing with an internal diameter of $0.5mm$ (SF Medical $0.5mm$ID) at both ends. The contact angle of fluid within the rubber tubing is 80° thus reduced capillary forces will result as compared to the glass capillary; fluid displacement will be a function of the electromagnet device and not capillary action. Figure 5.19 clearly shows a meniscus within the rubber tubing. There is a meniscus present at both ends of the system within the rubber tubing attached to either end of the glass capillary.

Each of the coils was actuated using a current of 500 mA. This was achieved by using a voltage controlled current source, Figure 5.20. The current source was controlled using a digital high (5 v) or low (0 v) signal. The signal for each microcoil was produced using

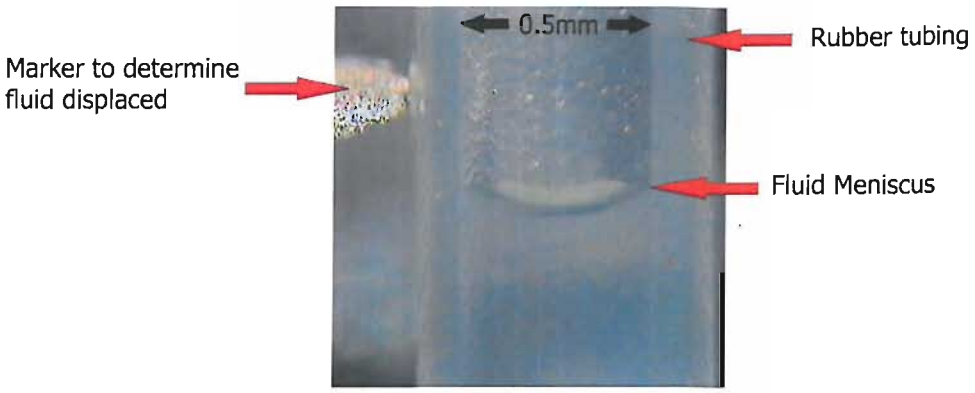

Figure 5.19: Meniscus within rubber tubing used to determine the fluid displacement due to the bead plug movement.

a simple Labview (National Instruments) sequencer used in conjunction with a National Instruments output card (USB6009). The sequencer was programmed to achieve a series of digital signals in parallel with a given time delay of between 2.5 and 0.025 s, from the output card. The time delay is used to alter the velocity by which the bead plug is moved and the sequence used is illustrated in Figure 5.13. The sequence includes an 'initialization stage' which is required to form the bead plug before it is translated along the channel.

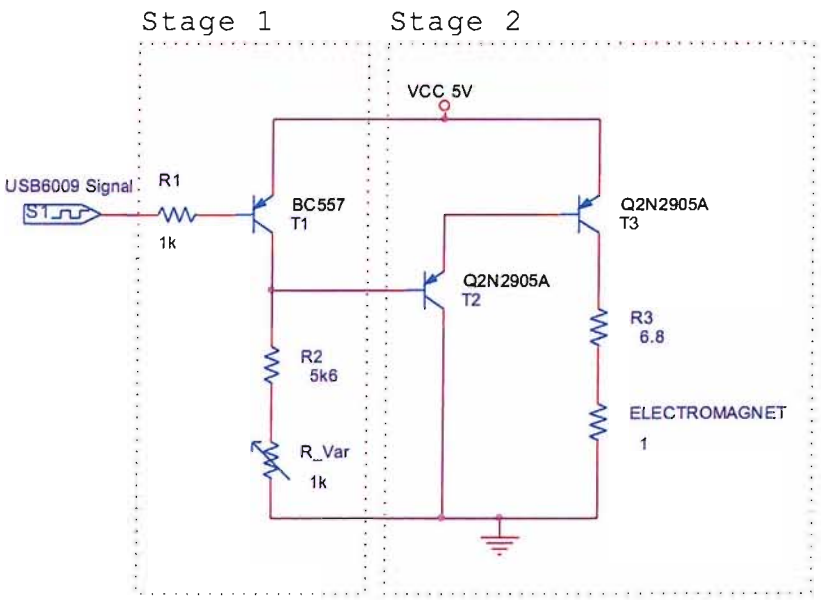

Figure 5.20: Circuit diagram of voltage controlled current source; 500 mA output, with 5 v input.

The bead plug moved along the capillary as a result of the sequential actuation of the electromagnets. The bead plug in the capillary was observed as well as the fluid displacement, by the observation of the fluid meniscus position within the rubber tubing attached to the end of the capillary (illustrated in Figure 5.19).

5.4.5 Results and discussion

A magnetic flux density of 20 mT and ∇B^2 of 7 $T^2\ m^{-1}$ along the central axis of the coil (and ∇B^2 of 0.5 $T^2\ m^{-1}$ perpendicular to the central coil axis) were measured for the electromagnet. This is not close to the original target of 70 $T^2\ m^{-1}$, which was achieved using the permanent magnet used in the experiments in Section 5.3. This means that the bead plug pressure was predicted to be less (3.1 Pa for a 191 000 bead plug) than that which is produced using the permanent magnet (167 Pa for a 12 000 bead plug). Hence the maximum fluid velocity which can be theoretically produced using the bead plug will be substantially lower (85 $\mu m\ s^{-1}$).

By experiment the electromagnets were successfully used to form and translate a bead plug of approximately 0.8mm (191 000 beads) along the capillary over a distance of 3 mm. This bead plug provided sufficient pressure to displace volumes of fluid from 20 to 50 nl in volume when the bead plug was transported at velocities of up to 0.45 $mm\ s^{-1}$. It was noted that during the movement the distance travelled in the forward direction was greater than the distance travelled in the reverse direction (see Figure 5.13). This was due to the relative start position for each direction. Due to this difference the bead plug was moved 3.3 mm in the forward direction and 3.1 mm in the reverse direction. A graph showing the volume of fluid displaced against the relative velocity of the plug is illustrated in Figure 5.21. Also shown in the graph (Figure 5.21) are the ideal volumes of fluid that would be displaced if there was no slippage, for both directions of the bead plug translation.

The theoretical plug force was calculated for the given bead plug and magnetic field (Section 5.4.4). This force was used to calculate the maximum velocity at which the bead plug could be moved before slippage was observed; the maximum velocity was calculated to be 85 $\mu m\ s^{-1}$. The results in Figure 5.21 clearly show that the maximum velocity,

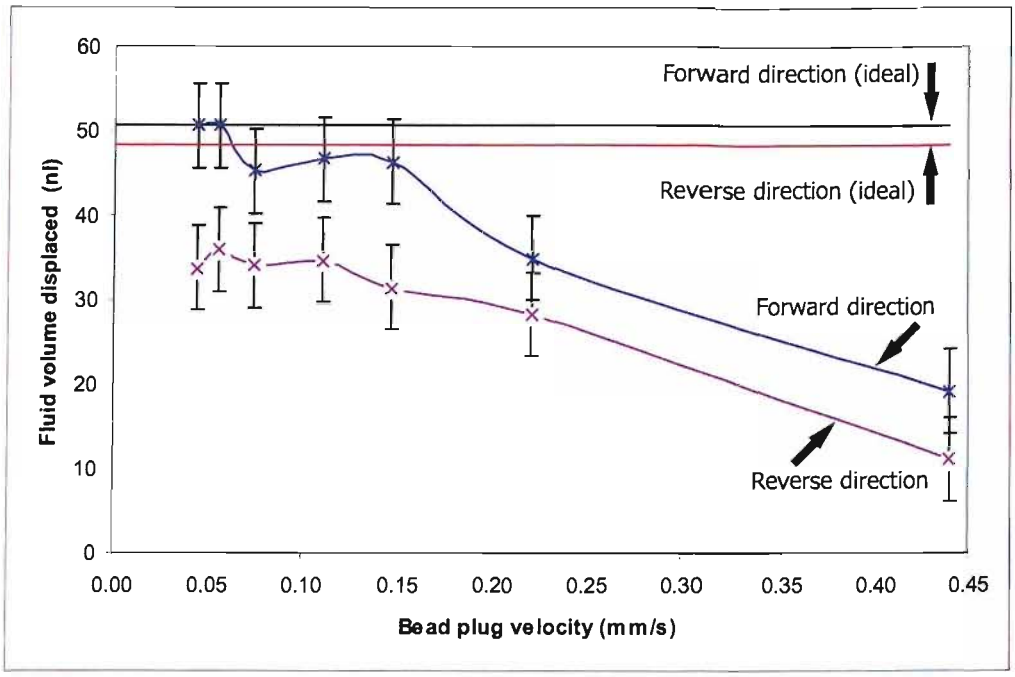

Figure 5.21: Graph of volume displaced against bead plug velocity for both forward and return direction for a bead plug of approximately $0.8mm$, including the ideal displaced volume with no fluid slip.

determined experimentally, was approximately half the predicted value. This difference in predicted and experimental values is thought to be due to the high dispersion of beads due to the limits of the coil spacing.

It is inevitable that the series of electromagnets will result in a 'non-continuous' magnetic field and that the beads would not move seamlessly along the channel. The plug movement is 'controlled' by a series of electromagnets, with an approximate pitch of $1mm$. A zig-zag travel pattern of beads along the capillary was avoided, but instead the bead plug appeared to expand and contract during the translation from one electromagnet to the next. The bead plug doubled in length from 0.8 mm to approximately 1.6 mm during this expansion and contraction. Assuming that the bead plug has a density of 74.08% when clumped together, then an extension that is double the length will result in a bead density of 37%. This will clearly be a less effective plug. The high dispersion of beads during the serial actuation of the electromagnets is considered to be the main contributing factor to the high level of fluid slippage.

Further to the dispersion of the bead plug during translation from one electromagnet to the next, the poor plug performance could also be due to the direction of the magnetic field. The resultant force on the paramagnetic beads may not be in the direction of the fluid movement although there will be a component acting in this direction. As described earlier in this chapter, the bead movement due to the electromagnets differs from the permanent magnet. In the case of the electromagnets the majority of the movement, and therefore the force which will be exerted using the beads, will not be in the direction of the fluid, but toward the outer edge of the capillary, toward the electromagnet.

5.5 Conclusion

A new technique was proposed for fluid displacement, using the magnetic actuation of a plug of paramagnetic beads. This chapter contains the proposal of a new dispensing technique, along with a series of experiments that were carried out to determine whether or not this fluid displacement technique could be used for pipetting nanolitre volumes of fluid.

The confirmation of fluid displacement using a potentially porous bead plug was achieved using a permanent magnet, used to form and control a bead plug within a fabricated microchannel (27 μm x 100 μm x 30 mm). Bead plugs of up to 48 000 beads were used to displace volumes of fluid, from 27 to 8 nl, at velocities up to 2.6 $mm\ s^{-1}$. Variable volumes of fluid were displaced using different bead plugs, despite moving the plugs over a fixed distance. This confirms the proposal made in Section 5.1, that it will be possible to develop this technique to repeatably dispense nanolitre volumes of fluid.

To achieve the aim of fabricating an integrated pipette device, it is the intention to provide the magnetic field required to form and move the paramagnetic bead plug using electromagnets. The use of a series of electromagnets was proposed to achieve a 'moving' magnetic field. Due to the complexity of producing an integrated device, a 'macro' device was produced to establish the feasibility of the approach, consisting of hand wound electromagnets. These electromagnets were actuated in a linear sequence to form and move a paramagnetic bead plug thorough a microchannel (140 μm diameter, 30 mm long). The bead plug of 191 000 beads was used to displace volumes of fluid

from 20 to 50 nl, at fluid velocities up to 0.45 $mm\ s^{-1}$, much lower than those observed when using the permanent magnet.

It has been confirmed that it is possible to displace fluid with a paramagnetic bead plug, controlled using a series of electromagnets. The poorer performance as compared to the paramagnetic bead plug controlled using the permanent magnet (described in Section 5.3), is due to a non-continuous moving magnetic field along the microchannel, as in the case for the system described in Section 5.3 where a moving magnet is used. The non-continuous moving magnetic field resulted in a high dispersion of the paramagnetic bead plug at regions within the bead plug transport and this meant the bead density was decreased by up to 50% (approximately). A less densely packed bead plug does displace the fluid to lesser extent, because more fluid passes through the bead plug. The poor performance is also attributed to a component of the bead force acting perpendicular to the fluid flow direction. To overcome this poor performance, smaller coils could be placed closer together, such that the step between each electromagnet is less. The hand wound devices used here are at the limit of manual fabrication and this is what limits the spacing of the electromagnets. However for the proposed microfabricated device, discussed in Chapter 6, it should be possible to create microcoils on a smaller scale and thus reduce the dispersion of the paramagnetic bead plug upon sequential actuation.

In this chapter the novel technique has been demonstrated and should be possible to exploit to pipette nanolitre volumes of fluid. The design and fabrication of an integrated pipetting device is described in Chapter 6. The pipette device consists of a series of electromagnets fabricated near the microchannel, containing both the paramagnetic bead plug and the sample fluid. Similarly to the electromagnet system, investigated in Section 5.4, the electromagnets will be actuated sequentially to form and move a paramagnetic bead plug in a channel of fluid. By varying the rate of actuation of the electromagnetic coils the velocity of the bead plug will be varied and thus the volume of fluid which is displaced is varied. The outcome will be a positive displacement in one direction, thus dispensing fluid. Application of a reciprocating motion will enable dispensing and refilling of the pipette and this will allow for repeated injection of fluid samples in the nanolitre range.

Chapter 6

Design and fabrication the electromagnetic microdevice

6.1 Introduction

A novel technique for fluid displacement using paramagnetic beads has been demonstrated, see Chapter 5. This technique will be used to provide fluid dispensing of nanolitre volumes of fluid within an integrated microdevice. The integrated microdevice will contain microcoils which will be actuated in a linear sequence to achieve a moving magnetic field. This chapter outlines the design and fabrication of such an integrated microdevice. Following the design of the integrated device, the details of the fabrication are given. This includes the fabrication of the simple fluidic microchannels used in the proof of concept experiments (Chapter 4) and the development of an electromagnetic integrated device with microcoils. The main focus of the fabrication development was to achieve a thin isolation layer between the microcoils, and the fluidic channel (the order of microns), and the fabrication of the microcoils, which is discussed in this chapter.

6.2 Electromagnetic microdevice

It has already been demonstrated that it is possible to transport paramagnetic beads, using microcoils positioned at locations close to a fluid filled microchannel containing paramagnetic beads by Rida et al. [171]. The problem with this design of Rida et al. [171] is that only a few beads (1000) are transported through the microchannel, which would not be sufficient for the system investigated here, where the transportation of a plug of beads is used to displace fluid. Here a device will be designed and fabricated, using a similar structure of a series of microcoils to Rida et al. [171], but a design to enable a bead plug to be transported along the microchannel is proposed. The chosen coil design for the integrated pipetting device is a single turn loop, similar to those produced by Lee et al. [160]. The magnetic flux density which can be produced is higher for a circular loop for similar dimensions than other structures (meander); the magnetic field produced is a result of the sum of the magnetic field from all contributing elements. The single loop coil is the easiest structure to fabricate as this can be created as a planar structure on a single level, unlike a wrapped or multi loop structure. Indeed the maximum magnetic flux density is at the centre of a multi-turn coil, where the magnitude of the magnetic flux density is proportional to $1/R$, see Equation 4.10.

The proposed design for this system is a series of planar coils below a fluid channel in the microdevice. The coils are designed to be as close to the microchannel containing the paramagnetic beads as possible. Figure 6.1 illustrates the configuration of the system. The microcoils will be actuated in a linear sequential way to capture and transport the beads along the microchannel. The serial actuation of hand wound electromagnets around a fluid channel has been demonstrated in the previous chapter (Section 5.4); beads are transported and fluid displaced.

The device will be produced with many single loop coils in series, as illustrated in Figure 6.1. The coils will be actuated in a linear sequence; one after the other, thus translating the beads from one microcoil to the next to achieve a translation distance of approximately 10 mm. The microcoil structure is illustrated in Figure 6.24, on page 159. As in the hand wound electromagnet investigation, multiple coils will be used to achieve a large enough bead plug to displace fluid. The critical design criteria for this will

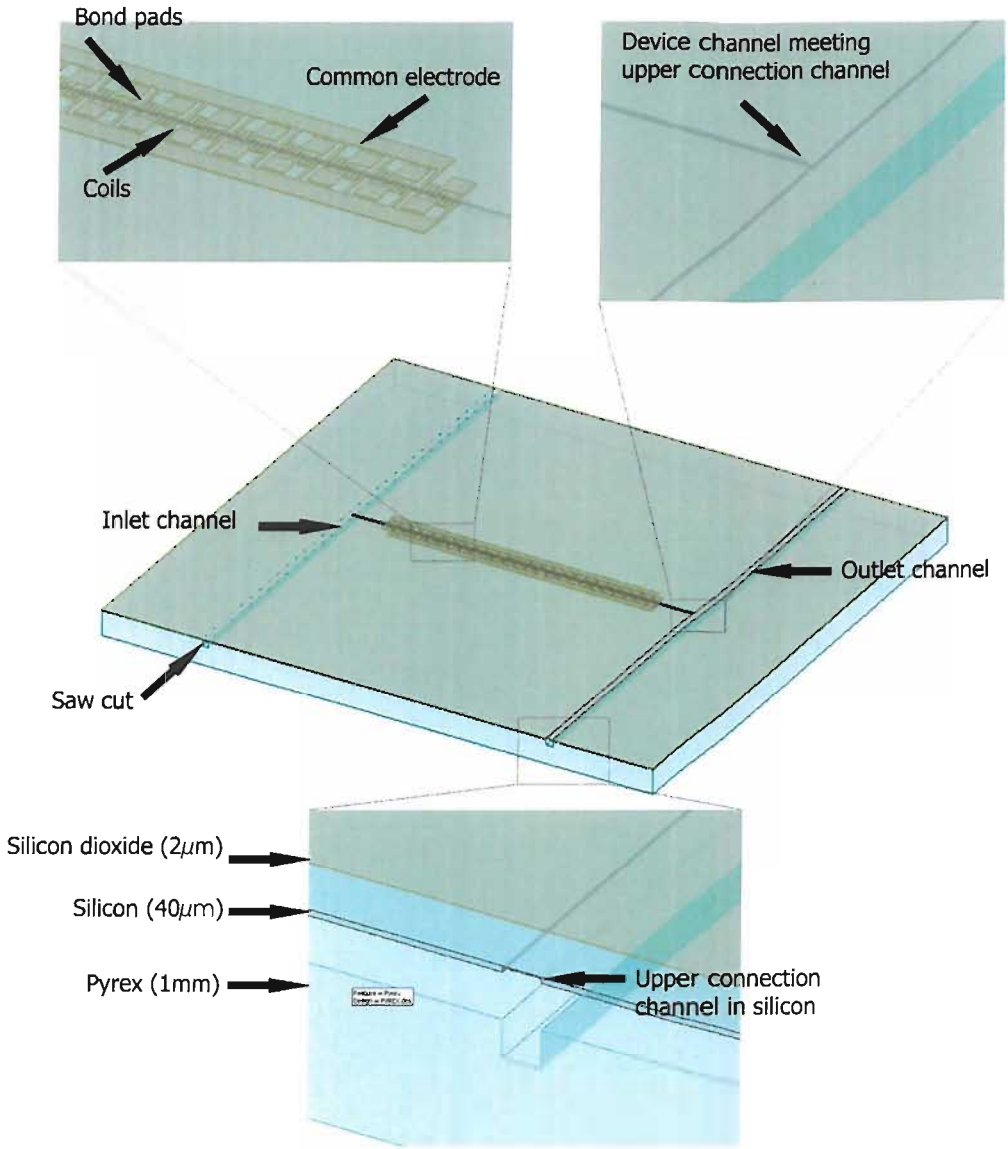

Figure 6.1: Schematic of a coil driven microdevice, consisting of a series of microcoils separated from the fluid channel below with a thin membrane

be to ensure that the magnetic flux density due to each microcoil is high enough to produce movement of the beads from one coil to the next and to ensure there is still a sufficient magnetic field to attract and hold the beads. The coils will be designed such that the magnetic flux density and gradient which can be achieved is similar to that achieved by Joung et al. [167] and Rida et al. [171], as discussed in Section 4.4, both groups achieved bead transportation along a fluid filled channel using electromagnets. To translate the bead plug along the microchannel, the microcoil at the trailing end of the plug will be turned off and the next microcoil at the head of the bead plug will be actuated, as illustrated in Figure 6.2.

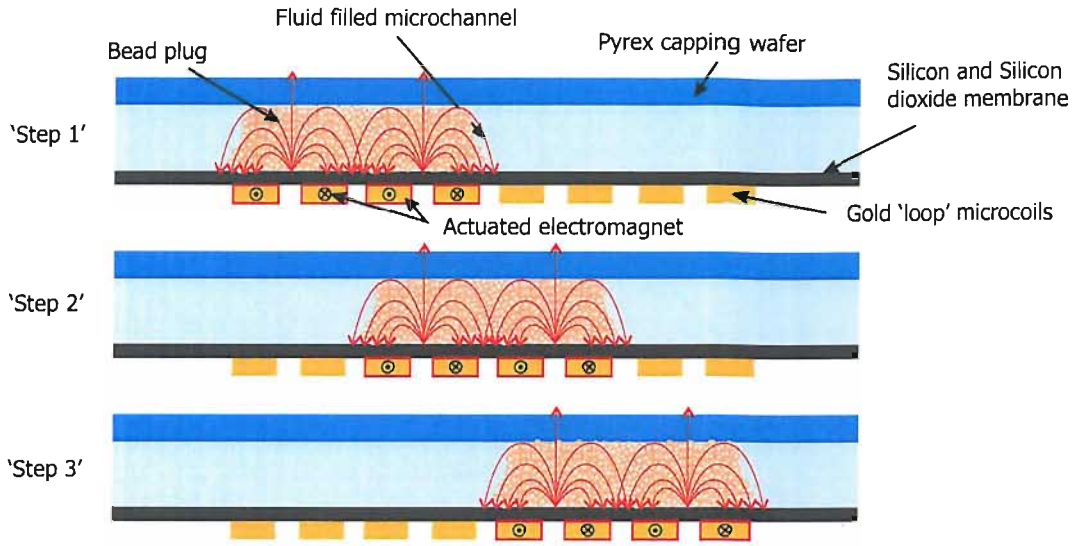

Figure 6.2: Illustration of a plug of beads being transported along the microchannel, using the sequential actuation of two microcoils.

This section will use the relationships discussed earlier to obtain the magnetic fields which can be obtained using single loop coils to design appropriate structures. Due to heating effects inherent in using high currents and thin conductors, thermal considerations are taken into account in the design of the coil and location adjacent to the channel.

6.2.1 Microcoil Design

The results described in Chapter 5 indicate that it is possible to exploit the new paramagnetic bead technique to displace fluid within channels of dimensions $100\,\mu m$ wide and $27\mu m$ deep. The first criterion, considered for the microcoil design, is the size of the microchannel used; this will define the size of the radius of the microcoil. The coil must be large enough to yield a high magnetic flux density throughout the channel. The second design criterion is the dimensions of the conductor. The width and thickness of the conductor will define the overall resistance of the structure and therefore the power dissipation. It is thus desirable to fabricate a thick coil of small radius over the channel (by increasing the thickness of the coil will mean that the electrical resistance will be reduced). However the coil thickness must be uniform and the density of the metal elements must be consistent. Structures that enable a high actuation current to be used

will provide a high magnetic flux density, albeit with a higher power dissipation. Since it is desirable to fabricate coils as close together as possible to provide a moving magnetic field, the coil radius is the defining parameter of the device design.

The design criteria for the microcoils are as follows:

- magnetic flux density $\approx 10\ mT$
- high conductor thickness $\geq 10\ \mu m$
- small outer loop radius $\leq 100\ \mu m$

The magnetic field which can be produced using a single current loop was discussed in Chapter 4 and this method can only be used to estimate the magnetic flux density along the z axis. However to be able to determine the magnetic flux density and ∇B^2 in the direction of the fluid flow, and therefore the direction of the force which needs to be produced, a more complex expression is required. Equations 6.1 and 6.2 can be used to determine the magnitude and the direction of the magnetic field at any point with relation to a current loop. The current loop is illustrated in Figure 6.3, where P is the point of interest, μ is the permeability, I is the current in the loop, θ is the angle between direction of the field and the $z - axis$, α is the radius of the loop and r is the distance between the centre of the loop and P. However these expressions require complete elliptical integrals to solve.

$$B_r = \frac{\mu I \alpha^2 cos\theta}{2(\alpha^2 + r^2)^{3/2}} \left[1 + \frac{15\alpha^2 r^2 sin^2\theta}{4(\alpha^2 + r^2)^2} + ...\right] \tag{6.1}$$

$$B_\theta = \frac{\mu I \alpha^2 sin\theta}{4(\alpha^2 + r^2)^{3/2}} \left[2\alpha^2 - r^2 + \frac{15\alpha^2 r^2 sin^2\theta(4\alpha^2 - 3r^2)}{8(\alpha^2 + r^2)^2} + ...\right] \tag{6.2}$$

Due to the complexity of predicting the magnetic flux density of a current loop in all directions, the structures were simulated using a finite element package; FEMLAB. Two dependant variables were solved; magnetic flux density and temperature. In the first instance a simple two dimensional model with axial symmetry was used, this is illustrated in Figure 6.4. To identify the best design for the microcoils, multiple simulations were completed that predicted both the magnetic flux density and the temperature

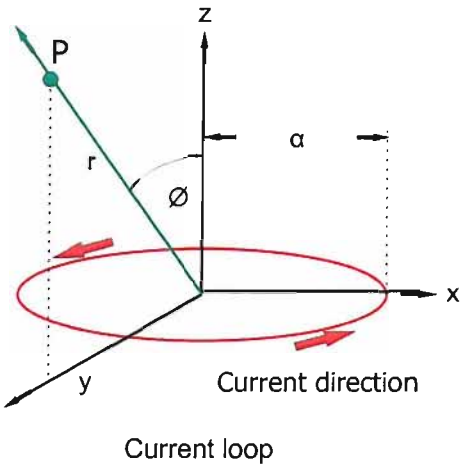

Figure 6.3: Illustration of current loop, including critical dimensions.

for structures with dimensions as illustrated in Figure 6.4, with increasing 'Y' (inner diameter). The outer diameter was fixed at 90 μm, such that microchannels of the same order of magnitude as those used in the experiments in Chapter 5 could be integrated with the microcoil electromagnets. The thickness of the coil was fixed at 10 μm as this is achievable using the electrodeposition process. The properties of the materials used for the simulation are presented in Table 6.1.

	Specific heat capacity ($J\ kg^{-1}\ K^{-1}$)	Thermal conductivity ($W\ m^{-1}\ K^{-1}$)	Density ($kg\ m^{-3}$)	Electrical conductivity (Ω^{-1})
Gold	130	320	19280	$4.7e^{7}$
Silicon	700	148	2330	$1e^{-3}$
Pyrex	900	1	2200	$2.5e^{-5}$
Water	4186	0.6	1000	$1.2e^{-6}$
Silicon dioxide	900	1	2000	$1e^{-13}$
Air	700	0.025	1	$1e^{-13}$

Table 6.1: Material properties used to calculate the magnetic flux density and thermal conduction of the proposed microstructure.

Before the simulations were carried out the input power of the system was determined. To achieve a high magnetic flux density the actuation current for the microcoils was set at 1 A. The resistance of the coils used in the simulation were estimated with a

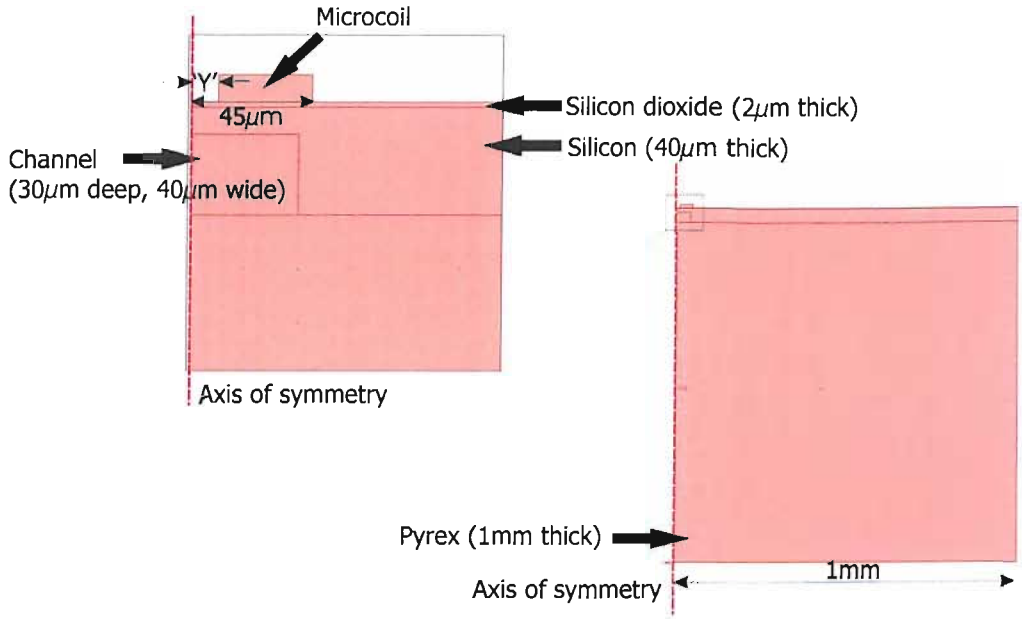

Figure 6.4: Two dimensional model of the microstructure, with axial symmetry.

resistivity of $2.2\text{x}10^{-8}\ \Omega\ m$. The resistance will alter as the inner radius ('Y' illustrated in Figure 6.4) of the microcoils is altered, so the resistance was calculated for each coil dimension. The resistance of the coil was used to determine the power dissipated. For the simulation carried out using FEMLAB, the power was entered as a power density (Heat source), which was obtained by dividing the input power by the volume of the structure.

First a magnetostatic simulation was carried out on the two dimensional model illustrated in Figure 6.4 (Appendix A.1). The simulation was carried out for microcoils with an inner radius from 5 to 25 μm. The results from this simulation are shown in the graph in Figure 6.5. This graph shows that the magnetic flux density parallel to the microcoil, at 12 μm below (in the model the coils are on top), see Figure 6.4. The magnetic flux densities predicted from the simulations are in the region of 12 to 14 mT. This is comparable to the magnetic flux densities achieved by Joung et al. [167]; Rida et al. [171]. It is clear that by increasing the inner radius the predicted magnetic flux density increases. The 15 μm inner radius coil was predicted to achieve the highest magnetic flux density of 13.5 mT for an actuation current of 1 A. For the larger inner diameter microcoils the theoretical values for the magnetic flux density appear to plateau and this is due to the fixed outer radius of the structure.

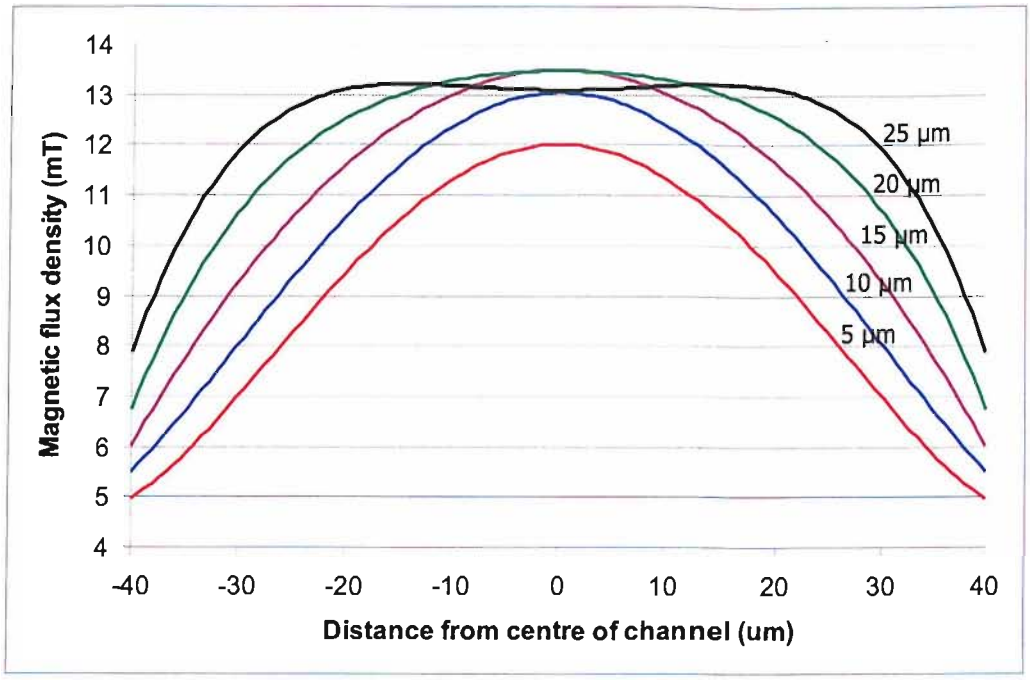

Figure 6.5: Predicted magnetic flux density of microcoils with increasing inner radius ('Y' Figure 6.4) and fixed outer radius ($90\mu m$).

To ensure that heating of the microstructure, due to the microcoil electrical actuation, is kept to a minimum, a transient thermal model was used for the simulation (Appendix A.2) of the two dimensional structure shown in Figure 6.4. It was considered of little point presenting the thermal simulation results as a temperature gradient within the two dimensional structure, because due to the small size of the model used, the temperature was found to be uniform as a result of the power dissipation in the microcoil. The predicted temperature of each modelled structure as a result of the power dissipation is presented in Table 6.2. Along with the temperature results, from the power dissipation, are the resistance and heat source values used for the simulation. Although a higher magnetic flux density would result from the 15 μm inner radius microcoil, the heat generated from this sized structure was considered to be too high for the proposed application. A 10 μm microcoil provides a sufficient magnetic flux density for the application without the potential overheating.

Although the simulations using simplified two dimensional structures provide a reasonable prediction of the magnetic flux density for the current actuation of the microcoils, it was considered advantageous to gain information for the 'real' three dimensional structure. The reason for this is that the simulation from a two dimensional structure

Inner coil radius 'Y' (μm)	Temperature ($^{\circ}K$)	Resistance ($m\Omega$)	Heat source ($W\ m^{-3}$)
25	380	24.20	$5.5e^{11}$
20	360	18.0	$3.52e^{11}$
15	345	13.8	$2.44e^{11}$
10	336	10.9	$1.80e^{11}$
5	328	8.6	$1.37e^{11}$

Table 6.2: Heating, with increasing inner coil radius ('Y'), with an external ambient temperature of $300^{\circ}K$.

can only be used to predict the magnetic flux density due to one coil, whereas the intention here is to use many coils in series. Since the heating effects will be greater when using many microcoils in series, a theoretical approach that allows for the simulation of this design is vital.

The three dimensional structure used for the simulation of magnetic flux density and heating is illustrated in Figure 6.6. The critical dimensions are labelled on the illustration in Figure 6.6 including ten microcoils (10 μm inner radius and 45 μm outer radius). As it is the intention to use ten coils in series to obtain a bead plug of 1 mm this is an appropriate model. This is only a proportion of the actual device that will be fabricated, but by using suitable boundary conditions within the simulation, this will be appropriate. The same magnetostatic and thermal models were applied as described previously (Appendix A.1 and A.2). However in this case, a time dependant thermal simulation was carried out.

The predicted magnetic flux density at 10, 20, 30 and 40 μm from the channel structure (12 μm away from the microcoils), illustrated in Figure 6.6, are plotted in Figure 6.7a. The predicted magnetic flux density has been plotted along the length and through the centre of the microchannel, at a distance of 12 μm from the microcoils. The predicted magnetic flux density is close to that estimated from the two dimensional model (Figure 6.5). It is clear that there are peaks at the centre of the microcoils and troughs between the microcoils. The predicted magnetic flux density through the

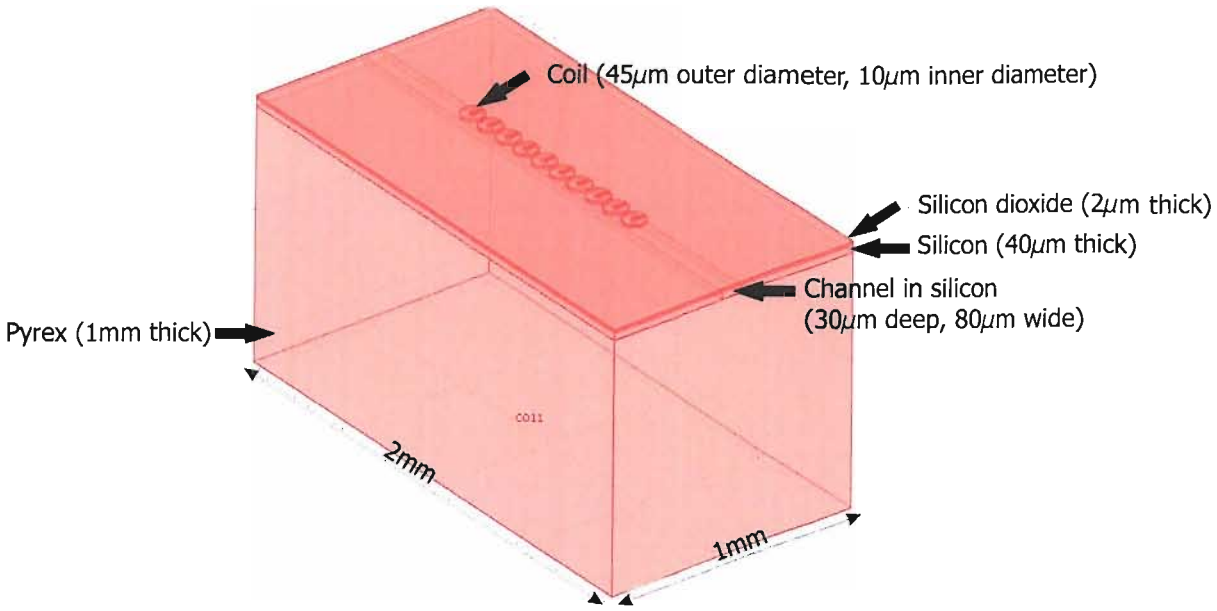

Figure 6.6: Three dimensional model of the microstructure.

channel centre is greater than 2 mT except for the furthest point from the coils within the microchannel. Again this is in good agreement with that calculated for similar structures, as produced by Joung et al. [167] and Rida et al. [171]. As discussed earlier the important factor when calculating the magnetic force is the value of the gradient of the magnetic flux density squared (∇B^2), so this has been calculated from the data in Figure 6.7a, and plotted in Figure 6.7b. This will be used later to determine the magnetic force that can be achieved using a bead plug formed using the actuation the electromagnets.

Each coil will provide a heat source ($W\ m^{-3}$) to the system. A time dependant simulation was carried out, using the model in Appendix A.2, for a period of 10 s. The temperature gradient within the three dimensional structure, after a time period of 10 s, is illustrated in Figure 6.8. It is clear that this is unsuitable as the temperature is predicted to reach 575 $°K$. This high level of heating is due to the high power dissipation in the system and the fact that there is nowhere for the heat to go except into the device. The addition of a heat sink of aluminium of 10 mm thick in contact with the microcoils is sufficient to remove the heat from the system. The simulation was repeated with the addition of a 10 mm thick piece of aluminium, which reduced the temperature increase to 1.52 $°K$, after 10 s, which is acceptable.

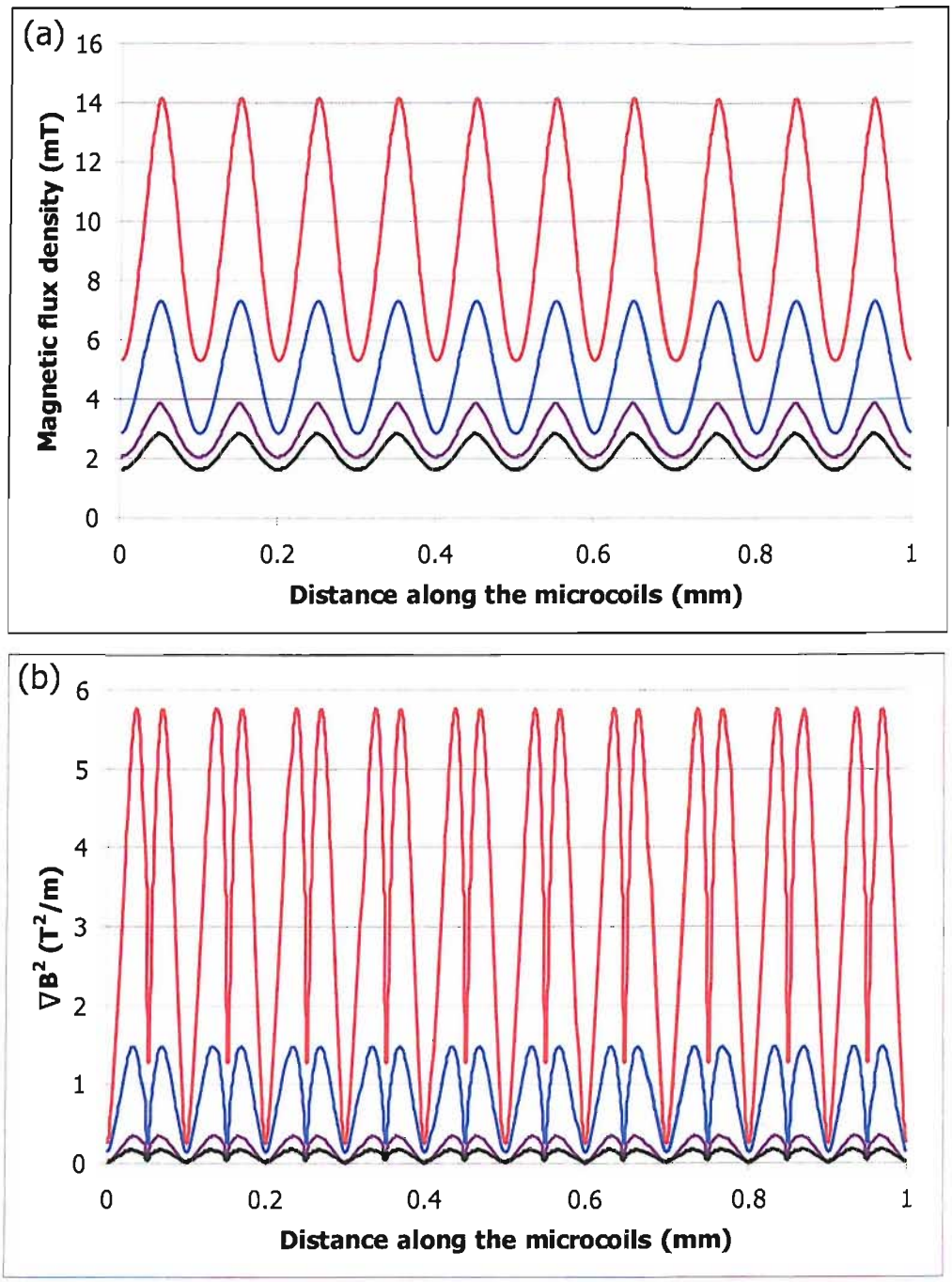

Figure 6.7: Graph of (a) predicted magnetic flux density and (b) predicted ∇B^2, obtained using FEMLAB for the three dimensional structure. The magnetic flux density is shown for the channel surface (12 μm away from the microcoil) and [—], 10 μm [—], 20 μm [—] and 30 μm [—] from the channel surface.

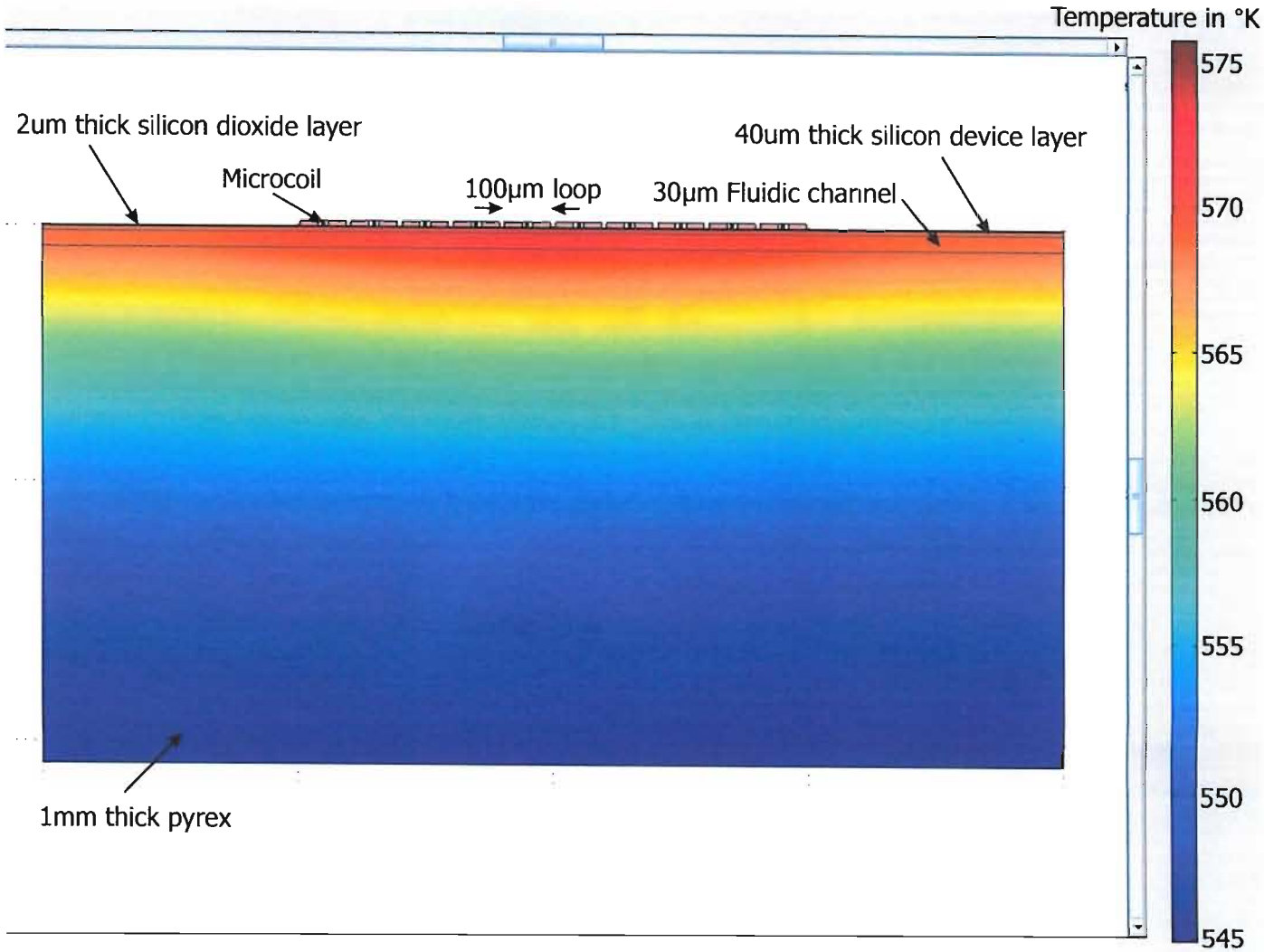

Figure 6.8: Predicted temperature gradient (without heat sink) of a cross section of the of the three dimensional structure due to power dissipation of the microcoils.

6.2.2 Channel design

The channel design for the integrated device is important because the dimensions of the channel will define the pressure drop and therefore the pressure which is required to displace the fluid. In order to calculate the theoretical pressure which can be achieved using a bead plug produced using the microcoils, the magnetic flux density throughout the channel must be known. Firstly the cross-sectional dimensions of the channel must be determined. Due to the size of the microcoil and the thin membrane which will be suspended above the channel, it was decided to use a channel width of 80 μm; slightly less than that used in previous studies (Section 5.3). However the depth of the channel was kept at approximately 30 μm; a reduction in the depth as well as the height would further increase the pressure required to displace the fluid at a given velocity (Equation5.7). To establish the length of the channel, the theoretical pressure which can be produced using a bead plug must be deduced.

The data shown in Figure 6.7b was used to determine the theoretical force of a plug of approximately $1mm$ long, or 37 000 beads assuming a packing density of 74.08 %. It was considered unrealistic to predict the force on each individual bead within the bead plug, therefore an average value of ∇B^2 was found and used to calculate the force on the bead plug. The average value of ∇B^2 was calculated across the depth of the channel, which was then used to calculate the average value of ∇B^2 along the length of the channel (both were calculated through the centre). The average value of ∇B^2 was calculated to be 0.94 $T^2\ m^{-1}$. To obtain the magnetic plug force, Equation 4.8 was used with the calculated value of ∇B^2, with 37 000 beads and a magnetic susceptibility of 1.6. Finally the bead plug force was calculated to be 1.05 μN, with a pressure of 440 Pa within the microfabricated channel (30 μm deep and 80 μm wide). It has already been shown that a reliable prediction for the plug force using electromagnets (Section 5.4) is difficult to obtain because the movement of the beads differs from the permanent magnet case investigated in Section 5.3. Therefore this was considered to be reasonable estimate.

The predicted pressure which can be achieved using a bead plug in the integrated microdevice is of the same order as the magnitude of the pressure which can be achieved

using a bead plug with a permanent magnet ($100 - 400\ Pa$). To ensure that the bead plug of 1 mm (approximately 37 000 beads) in length can be used with the designed microchannel, the theoretical plug velocity at which fluid slip should occur was predicted. Two channel lengths of 10 mm and 15 mm were considered, with theoretical slippage points predicted at 2.4 $mm\ s^{-1}$ and 1.6 $mm\ s^{-1}$ respectively, using Equation 5.7, Section 5.2 with the estimated pressure of 440 Pa.

In addition to ensuring that the fluid can be dispensed using a paramagnetic bead plug actuated using the electromagnetic microcoils, the volume of the pipette was also determined. The aim of this work is to produce a pipette device for injecting nanolitre volumes of fluid. The total internal volume of the pipette devices produced here are 24 nl and 36 nl for the 10 mm and 15 mm long channels respectively. This should allow for a volume of up to 36 nl to be dispensed, depending on the bead plug movement and the amount of fluid slippage past the bead plug.

Thus far the pipette device has been considered as a stand-alone channel. However to form a pipetting device this microchannel must be connected to another channel, into which fluid will be dispensed. To achieve this two channels are located at either end of the pipette channel, as illustrated in Figure 6.1 and discussed in Section 6.3. As well as the fluidic connection (sawn in the Pyrex wafer), an additional channel has been etched in the silicon wafer and this interconnects above the sawn Pyrex channel to form the upper part of the outlet channel. This upper part is illustrated in Figure 6.9a. In order to prevent fluid from leaching out of the pipette device into the outlet channel, the outlet orifice has been reduced to 20 μm wide, illustrated in Figure 6.9b. Because the dimensions of the fluid inlet for the pipette is not so critical, the pipette channel etched in the silicon overlaps the sawn channel in the Pyrex by 80 μm.

The estimated pressure to displace fluid within the pipette channel, without considering any effect from the inlet channel and outlet orifice, has been predicted. As discussed in Section 4.1, the fluid into which the dispensed fluid will be injected will be stationary and miscible. As a result of this there will be no pressure difference at the outlet orifice and thus no reason to prevent the fluid from being dispensed. The outlet orifice will not provide any pressure differential, this is because only low fluid velocities are investigated. The pressure drop due to a gradual contraction (outlet orifice, see Fig-

ure 6.1) can be predicted using Equation 3.13, from Section 3.3.3. For a fluid velocity of up to 2.4 $mm\ s^{-1}$ (the predicted fluid slippage velocity) the pressure drop due to a gradual contraction, is predicted as being 300 pPa. This is negligible compared to the theoretical bead plug pressure.

A number of techniques were discussed in Section 3.4 to stop or restrict fluid flow, however no such techniques were implemented in this design. Physical valves were not included because these would make the fabrication of the device more complicated. Indeed, dynamic valves would not result in any pressure differential effect because the fluid velocities here are too low. Valve structures could be included in the channel design if required, at a later date once the results obtained from this pipetting device have been evaluated; this will be discussed in the future work sections of the thesis.

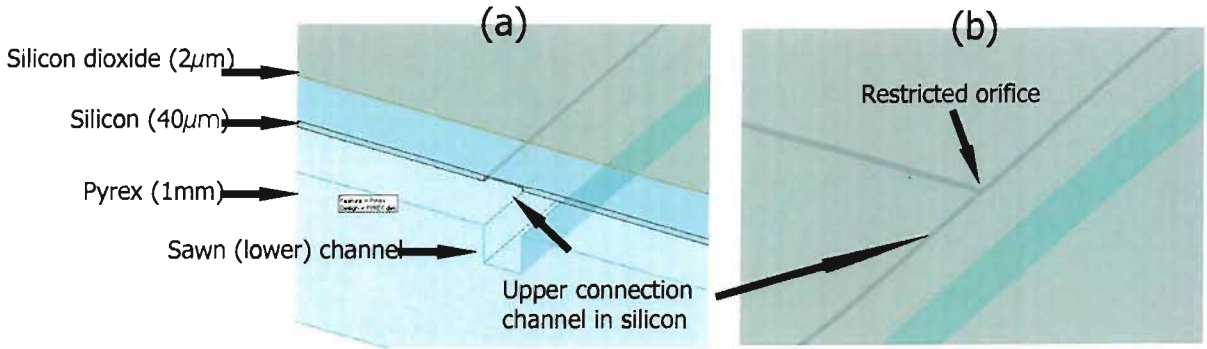

Figure 6.9: Illustration of the lower Pyrex channel (a) below the upper outlet channel formed in the silicon at the end of the pipette channel with reduced orifice (b).

6.3 Device Fabrication

The fabrication of three devices has been achieved:

1. The first fabricated structures were produced without any integrated electromagnets and were used in the experiments in Section 5.3.

2. The second device was fabricated as a test structure for the fabrication of microcoils separated by a thin silicon membrane.

3. The final fabricated devices include the same microcoil fabrication technique with an integrated microchannel as described in Section 6.2.

6.3.1 Test channel fabrication

The main aim of this work is to produce an integrated microdevice, capable of being used to pipette an aliquot of fluid of nanolitre scale. MEMS silicon fabrication techniques will be used to produce the final pipetting device, therefore to ensure the integrity of the technique the proof of concept experiments were also carried out using silicon fabricated microchannels (Section 5.3). Full details of this fabrication are in Appendix B.1.

To be able to test the proposed fluid displacement technique, straight channels were produced with fluidic access at each end. The channels are 27 μm deep, 100 μm wide and 30 mm long. For ease of production, the channels were etched by deep reactive ion etching (DRIE) in a silicon substrate (500 μm thick), thus producing a rectangular channel profile. To achieve the fluidic connections to the etched channel, channels were sawn in a Pyrex (1 mm thick) wafer, which was bonded to the silicon wafer by anodic bonding. The etched channels in the silicon substrate and the sawn channels in the Pyrex substrate are perpendicular to each other (see Figure 5.3, Section 5.3.1).

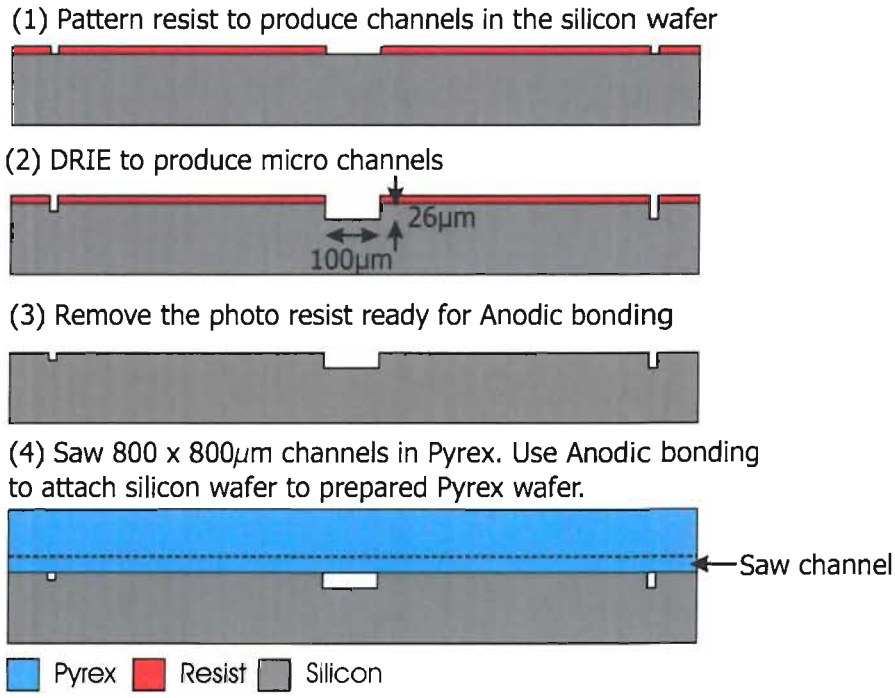

Figure 6.10: Test channel fabrication process used to create microchannels.

The fabrication involved four process steps, which are shown Figure 6.10.
(Step 1) Pattern photoresist (Shipley SPR220, 2.2 μm) with a dark field mask to produce the channel structures.
(Step 2) Deep reactive ion etch to a depth of 27 μm.
(Step 3) Resist strip in fuming nitric acid (FNA).
(Step 4) Finally, anodic bonding was used to cap the microchannels in the silicon wafer with a Pyrex wafer. Sawing was used to produce trenches in the Pyrex (800 by 800 μm), to be used for fluidic connections for the microchannels within the silicon. The two ends of the microchannel etched in the silicon overlap the sawn channels when the two wafers are anodically bonded to form the fluid connections for an inlet and outlet.

6.3.2 Microcoil fabrication with straight fluidic channel

The literature review of the current state of the art microcoil structures (Section 4.5) identified that the most common fabrication technique for producing microcoils was electrodeposition. A planar coil, without a core, is the simplest to fabricate. The fabrication techniques used to produce the microcoils for this work are as follows; firstly a gold seed layer for electrodeposition is deposited. The seed layer is patterned using either wet etching or ion beam milling. A mould is formed on top of the seed layer using photoresist. The coil is then grown using electrodeposition within the resist mould, to define the shape of the structure on the exposed seed layer.

Electrodeposition has been used to produce coil structures of gold of up to a thickness of 25μm, as discussed in Section 4.5. The resistance of the conducting gold structure is inversely proportional to the area (and therefore to the thickness). By increasing the thickness of the electrodeposited conductors, the resistance is reduced, as compared to thinner structures created by sputtering or evaporation (the limit in thickness of these techniques is 5 μm). As discussed in Section 6.2.1, by reducing the resistance of the structure, the power dissipated will be decreased, which will reduce heating. This electrodeposition technique allows for conductors to be produced with high aspect ratios, which is defined by the photoresist mould. The proposed coil structure is shown in detail in Figure 6.11.

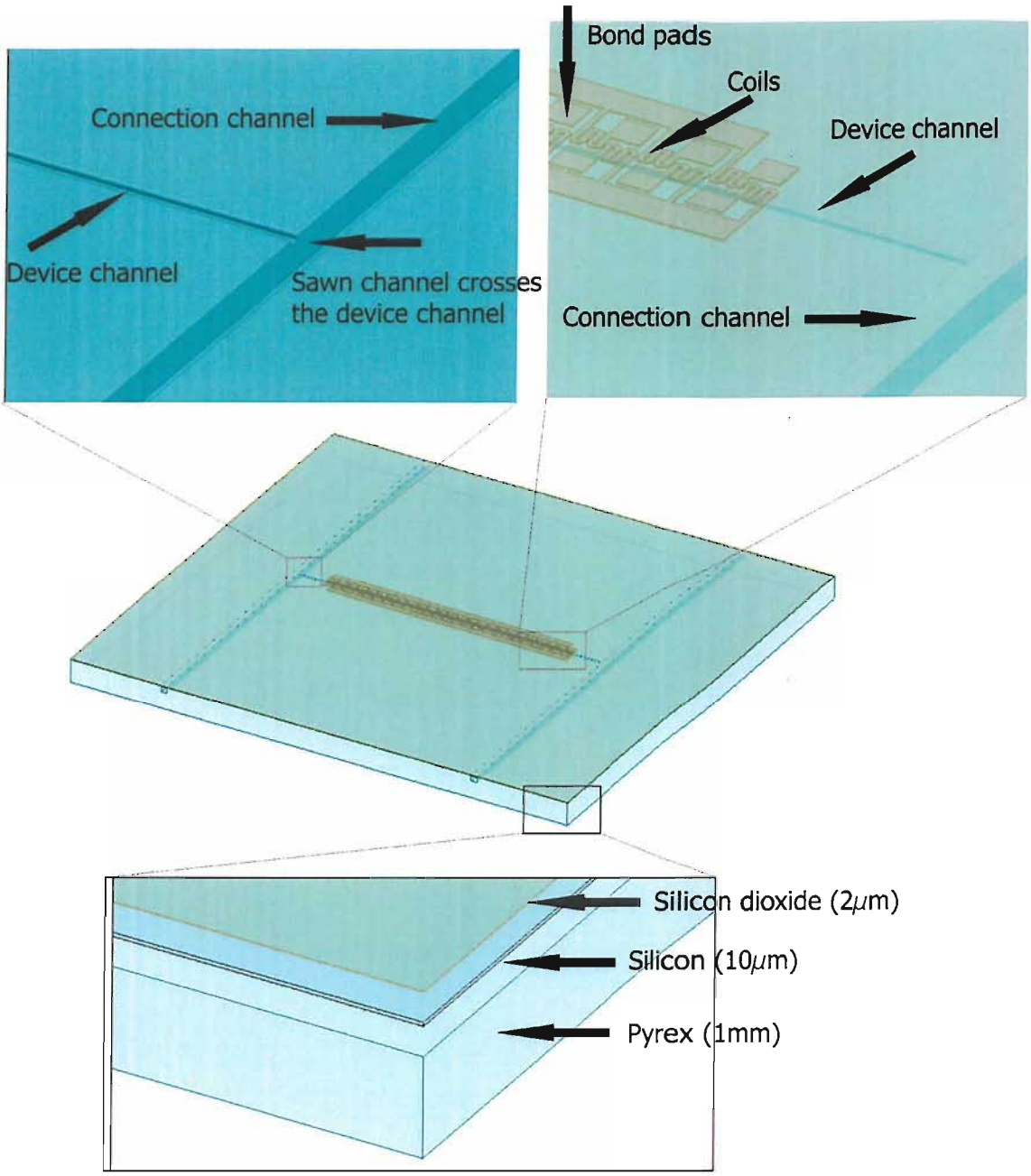

Figure 6.11: Test structure to obtain microcoils above a fluid microchannel with a thin ($12\mu m$) membrane.

The proposed microcoil design has been predicted to produce a magnetic flux density of 14 mT at a distance of 12 μm, as discussed in Section 6.2.1. A fabricated structure was proposed such that the microcoils are fabricated close to the fluidic channel (within 12 μm) containing the paramagnetic bead plug and fluid. Examples of integrated microcoils have been fabricated, where the microcoils are within 1 μm of the fluidic microchannel [161], as discussed Section 4.4. However in this example the coils were encapsulated in Polyimide to make the overall structure rigid. This design is not suitable for this work because the microcoils must be cooled (it has already been predicted that the microcoils in this work will require cooling during actuation). Therefore a fabrication technique was required to be able to produce microcoils on the surface of a rigid structure containing a microchannel.

The fabricated structure which was proposed to achieve the microcoil design, consists of a thin silicon membrane of approximately $12 \mu m$ which is used to separate the gold microcoils and the fluidic channel containing the beads. The proposed design is based around the use of a silicon on insulator (SOI) wafer. SOI wafers typically consist of a three layer stack; a silicon handle wafer, a silicon dioxide insulating layer and a silicon device layer (the SOI). These are conventionally used for the fabrication of semiconductor devices to reduce the leakage current, however the use of these wafers for the fabrication of MEMS devices is increasing. These are usually fabricated by direct bonding of two silicon wafers, one of which has silicon dioxide grown on it prior to bonding to form the insulation layer. Once the wafers are bonded the silicon wafer is ground and polished to the desired thickness, forming the device layer. The full process list for the fabrication of this microcoil device is in Appendix B.2.

The device is fabricated using two wafers, a Pyrex wafer (7440) and an SOI wafer. Pyrex 7440 is used because its thermal expansion coefficient is close to that of silicon. Figure 6.12 illustrates the Pyrex process flow; the Pyrex wafer was used to create the fluidic channel.

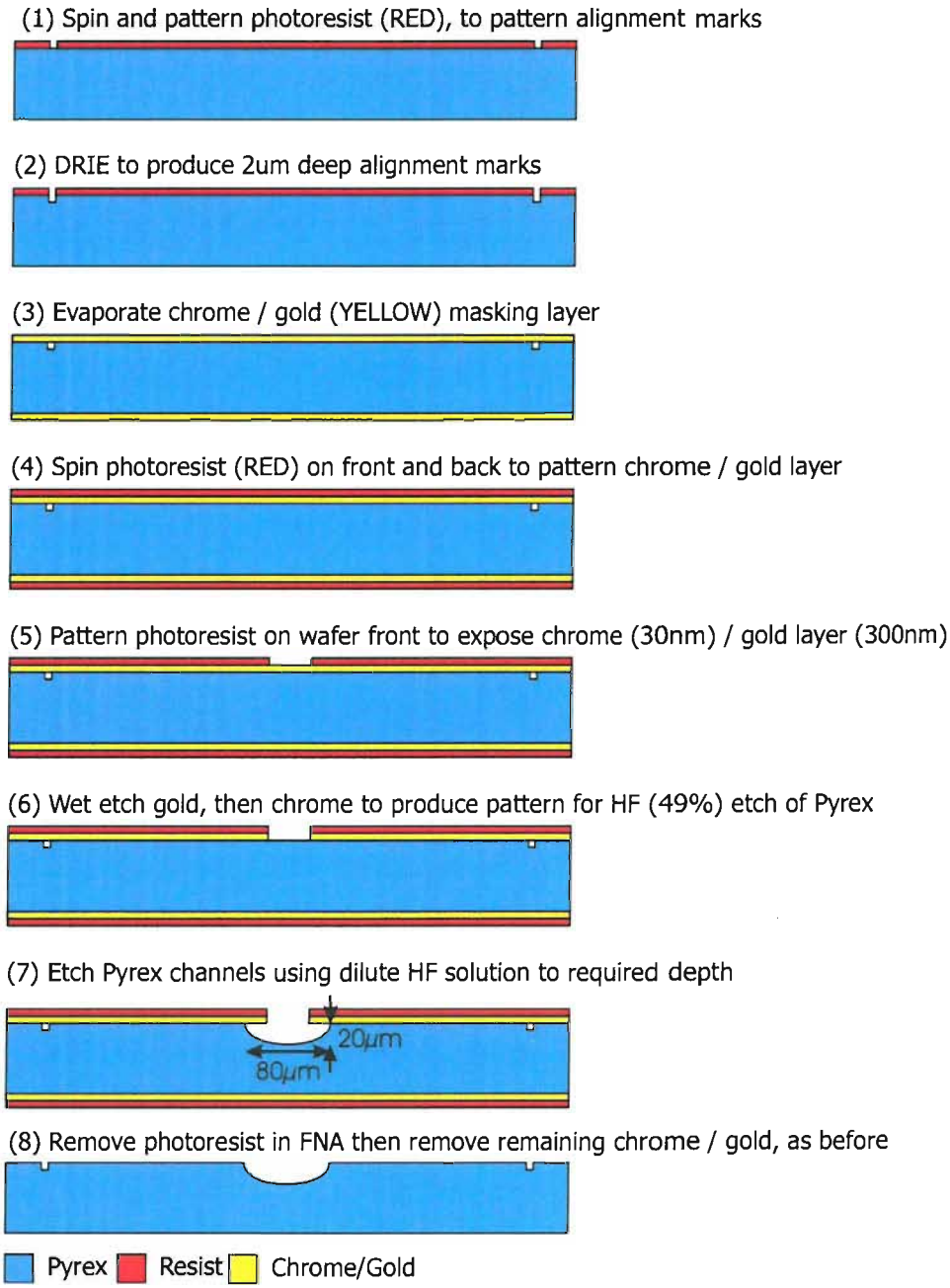

Figure 6.12: Pyrex wafer fabrication process flow, 1 *mm* thick Pyrex wafer.

(Step 1) A 1 mm thick Pyrex wafer is first cleaned using a standard fuming nitric acid (FNA) clean. Shipley S1818, photoresist is patterned on the front of the wafer only.
(Step 2) Alignment marks are produced using DRIE, to a depth of 2 μm (using a Surface Technology Systems (STS) Advanced Silicon Etch (ASE)). This is of sufficient depth for the marks to be visible, DRIE etching of silicon dioxide (SiO_2) using an STS ASE is extremely slow (approximately 1 μm an hour).

To etch the channels in the Pyrex a wet etch was selected; the creation of deep channels of 20 μm using DRIE is unrealistic, because the typical etch rate using a STS ASE is $1\mu m$ an hour. To mask the wafer for the wet etch, gold/chrome masking for etching the 20 μm channel is used. If the Pyrex is etched any more than a few microns, using a wet etch (i.e. buffered hydrochloric acid) in conjunction with a standard resist mask, the resist mask is prone to peel off [29].
(Step 3) Chrome (30 nm)/gold (300 nm) is evaporated on both sides of the wafer; chrome is evaporated to improve the poor adhesion of gold to the Pyrex substrate.
(Step 4-5) Photoresist (S1818) is spun on both sides of the wafer and patterned on the front of the wafer using a standard contact mask.
(Step 6) The exposed gold followed by the chrome is etched using an aqueous KI_3 solution and ceric ammonium nitrate and nitric acid solution respectively.
(Step 7) The channels are etched using a 2 : 1 solution of deionised water to hydrofluoric acid (HF,49%), obtaining an etch rate of 2 μm a minute. The channel is undercut by 20 μm to yield a channel of 80 μm wide.
(Step 8) The photoresist is removed using a FNA clean. The same gold/chrome etch process used in (Step 5) is repeated to remove the gold and chrome masking layers. The final result is illustrated in Figure 6.13, which shows the end of one of the channels, which is approximately 80 μm wide and 20 μm deep.

One of the problems which needed to be overcome was the integration of fluidic connections once fabrication is complete. Ideally the fluidic connection is required in the same plane as the device to limit fluidic pressure in the channel. If the fluidic connection was instead made from above the microchannel, a head of water would result and this could lead to pressure induced displacement of the fluid within the microdevice. To overcome this problem, channels have been sawn into the Pyrex substrate at either

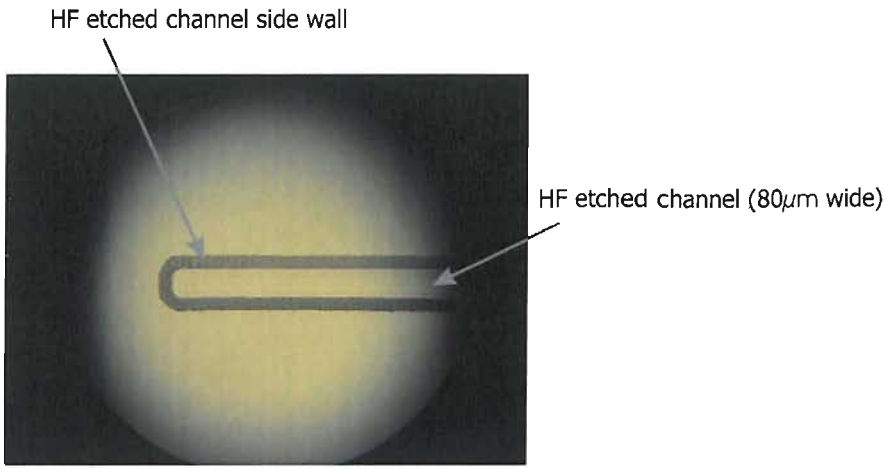

Figure 6.13: Image of the end of a wet etched channel in Pyrex, approximately $80\mu m$ wide.

end of the etched channel. One of these sawn connection channels is illustrated in Figure 6.14. The sawn connection channel will allow the use of a fused glass capillary with an external diameter of up to $700\mu m$ to be inserted for the use as an inlet.

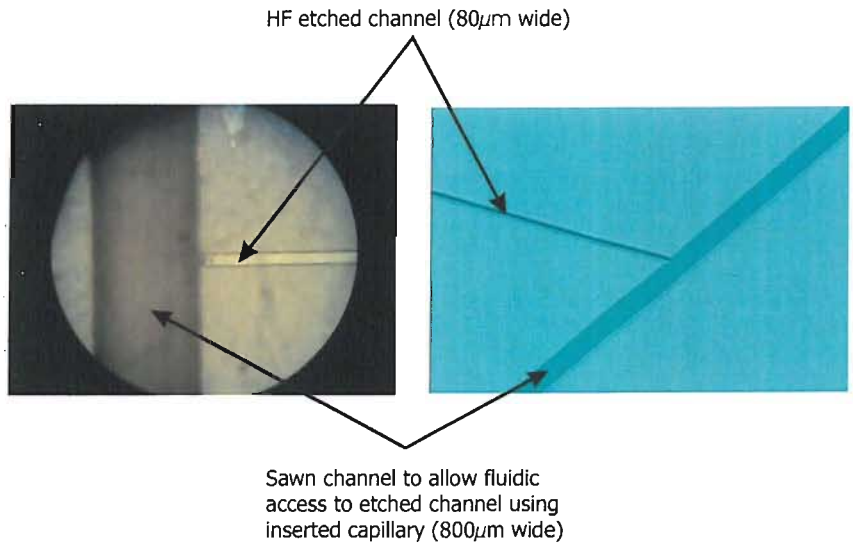

Figure 6.14: Sawn channel for fluidic access at the end of the HF etched channel, in the plane of the microdevice

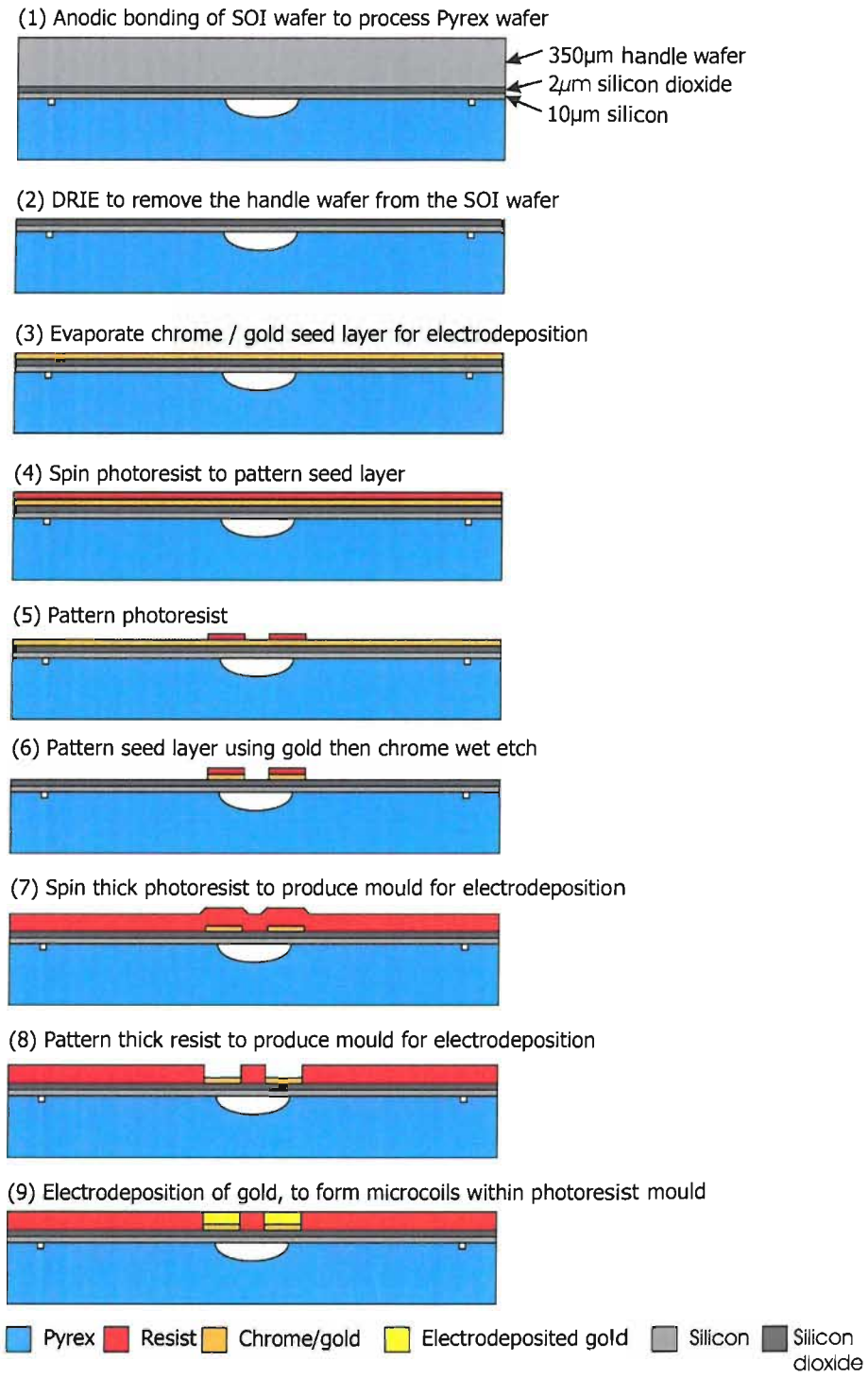

Figure 6.15: Bonded SOI wafer process flow

The second part of the fabrication process relates to the SOI wafer. The SOI wafer used for this work is a standard silicon wafer with a 2 μm silicon dioxide layer and a 10 μm device layer of silicon, obtained from ICEMOS. The process flow is illustrated in Figure 6.15.

(Step 1) The first step of the process is a FNA clean of the wafers. The SOI is then

bonded to the processed Pyrex wafer by anodic bonding, such that the device layer is bonded to the processed surface of the Pyrex wafer. The channels etched in the Pyrex are now sealed within the bonded structure.

(Step 2) To form the thin membrane over the microchannel, the handle wafer is removed using DRIE. DRIE was chosen because only the wafer front (the handle wafer) will be exposed to the plasma, therefore the rest of the wafer will be protected and the silicon dioxide will act as an etch stop due to the difference in etch rate (silicon 1500 $nm\ min^{-1}$, silicon dioxide 29 $nm\ min^{-1}$ [187]) . However there is a problem in the usage of the DRIE equipment available (STS ASE). The wafer is clamped at the periphery with eight small clips. The area under these eight clips will not be etched and therefore once etching is complete, eight 500 μm pillars will remain at the periphery of the wafer. If there was no further processing involved this would not be an issue, but as subsequent photolithography steps are required, a mask will be prevented from contacting with the wafer. To over come this, two etch steps were performed; one to etch eight small isolated areas at the periphery of the wafer (to go under the clamps during the second etch) and the second etch step on the remaining part of the wafer after removing the photoresist mask.

Next, further steps are required for the fabrication of the microcoils on top of the silicon dioxide layer which remains after the DRIE. The oxide which acts as an etch stop, is used as a layer for electrical isolation between each of the coils.

(Step 3-5) The first part of the microcoil fabrication is to produce a seed layer for the deposition of the gold. The seed layer of gold (150 nm) is evaporated onto the silicon dioxide, over a chrome (30 nm) adhesion layer. Photoresist (S1818) was spun onto the evaporated chrome/gold seed layer and patterned.

(Step 6) The chrome/gold layer is then patterned. Ideally this would be carried out using ion beam milling, because no under cutting of the evaporated layer should occur. For this process this was not possible because it was thought that the wafer was not strong enough due to the deep connection channels. Therefore the seed layer was etched using a wet etch approach similar to that used for the Pyrex processing. The mask is then removed and the patterned seed layer is shown in Figure 6.16.

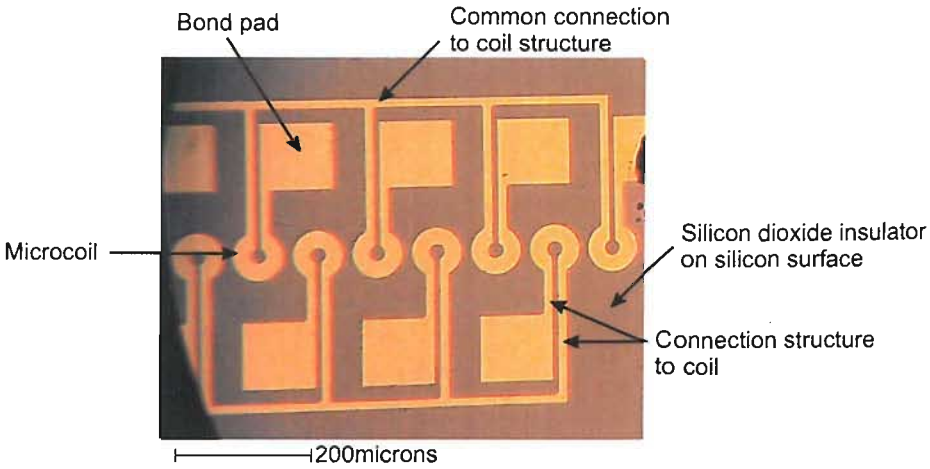

Figure 6.16: Patterned seed layer before gold electrodeposition

The final step of the fabrication process is the deposition of the thick gold wires by electrodeposition into a thick resist mould. The purpose of the thick resist mould was discussed in Section 6.3.4. The resist mould production and electrodeposition of the gold will be discussed in Section 6.3.4.

6.3.3 Microcoil fabrication with pipette device

The fabrication steps, described in Section 6.3.2 were used to create a test structure. This device was used to demonstrate that it was possible to fabricate a series of microcoils, which were separated from a fluidic channel by a 12 μm thick layer. This was successfully achieved, however problems occurred during the fabrication of the microcoils, as is discussed in Section 6.3.4. The fabrication steps used for creating the second 'pipette' device are similar to those described in Section 6.3.2. An SOI wafer was anodically bonded to a Pyrex wafer to achieve the thin separation layer, as before, but with one minor alteration which is illustrated in Figure 6.1, page 129. In this case the fabrication of the 'pipette' channel was not done using a wet etch (2:1 HF) of the Pyrex wafer. For this device, the 'pipette' channel contains a restriction at the outlet. This structure was considered too difficult to achieve using the wet etch method, this is due to undercutting observed in wet etch Pyrex and because the sawing technique is not accurate enough to align the fluid restriction with the connection channel. Therefore an alternative fabrication technique was proposed. Instead of producing the pipette in

the Pyrex wafer, it was etched in the device layer of the SOI wafer before the anodic bonding. Fluidic connections were still sawn in the Pyrex wafer, but the alignment is not so critical. However this would require a thicker device layer to enable the etching of a 30 μm deep channel. The proposed fabrication process to produce the pipette channel is DRIE. This can be used to achieve the structure for the fluidic restriction and subsequent upper connection channel without any undercutting. Full details of this fabrication are in Appendix B.3.

The alternative fabrication steps are illustrated in Figure 6.17. The wafers used for this process are a $1mm$ thick Pyrex wafer and an SOI wafer (ICEMOS) with a $350\mu m$ handle wafer, a $40\mu m$ device layer and a $2\mu m$ layer of silicon dioxide.
(Step 1-3) Spin photoresist (Shipley SPR220, 2.2 μm) onto the front side of the SOI wafer to pattern the device layer. The pipette channels are etched into the device layer by DRIE and the photoresist mask is removed is FNA.
(Step 4) Alignment marks are etched into the Pyrex by DRIE to allow for alignment of the sawn channels and the devices in the SOI wafer. Before bonding the two wafers, channels are sawn in the Pyrex along the patterned marks which will be used for fluidic connections. Once this is complete the SOI and Pyrex wafers are bonded using anodic bonding.
(Step 6) Once the two wafers are bonded the handle wafer is removed to expose the thin silicon layer covered with silicon dioxide. The removal of the handle wafer is carried out using DRIE. An electrostatic clamping system was used for the DRIE (STS ASE), so that the entire handle wafer was removed without leaving any unetched points. This is unlike the DRIE process steps described in Section 6.3.2 for the test structure, where the DRIE equipment has a system where the wafers are held in place by clips. It is important to ensure that the entire handle wafer is removed because of the subsequent photolithography steps which were carried out on the back of the silicon layer using contact masks.

The remainder of the fabrication process (Step 7-10) is as described in Section 6.3.2. The patterned gold seed layer is illustrated in Figure 6.19.

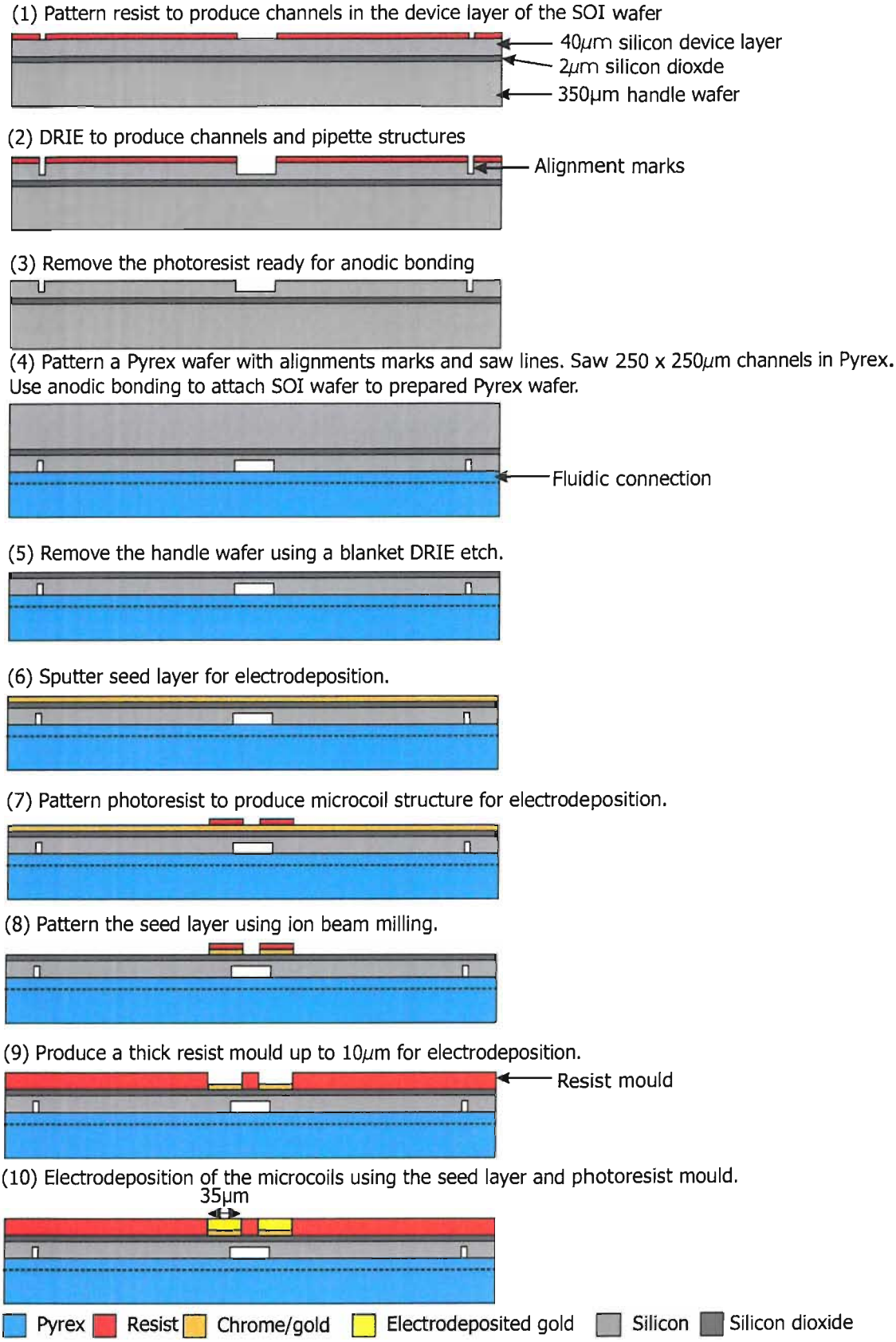

Figure 6.17: Fabrication process to produce pipette devices with integrated microcoils.

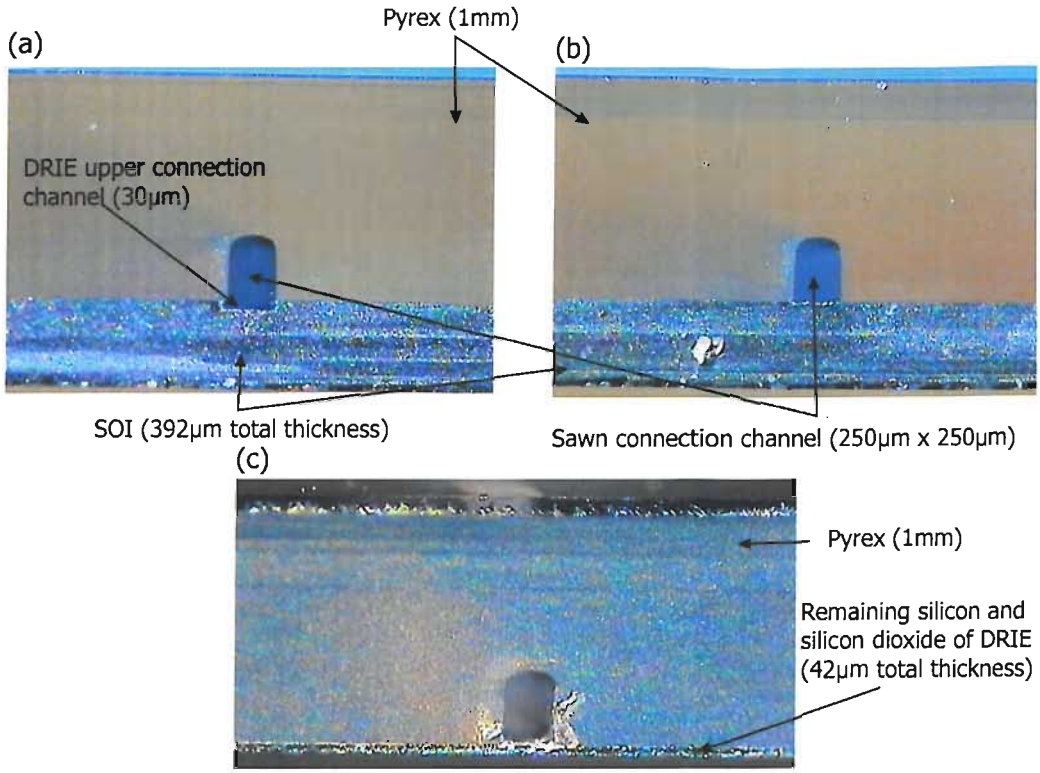

Figure 6.18: Image of (a) bonded device with etched upper channel, (b) bonded device and (c) after DRIE to remove the handle wafer.

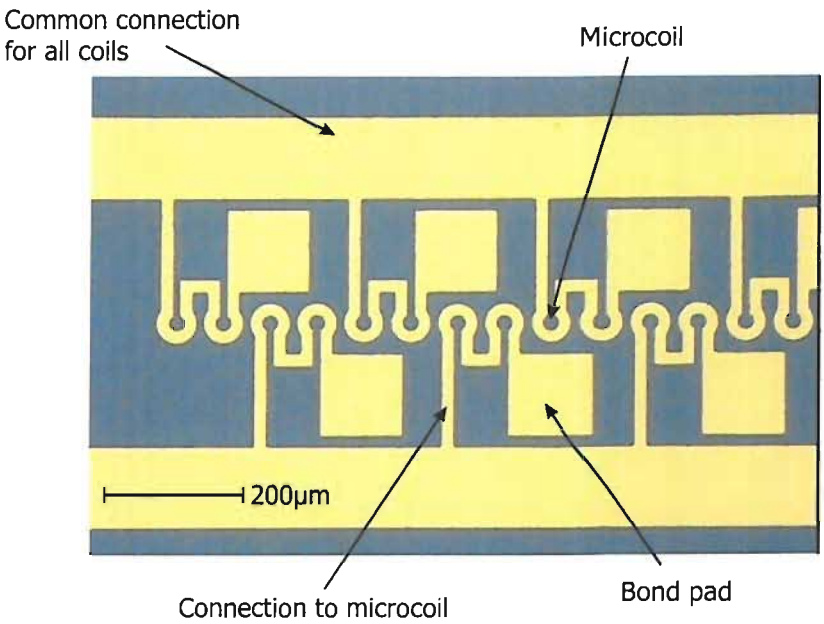

Figure 6.19: Patterned seed layer, with improved mask design.

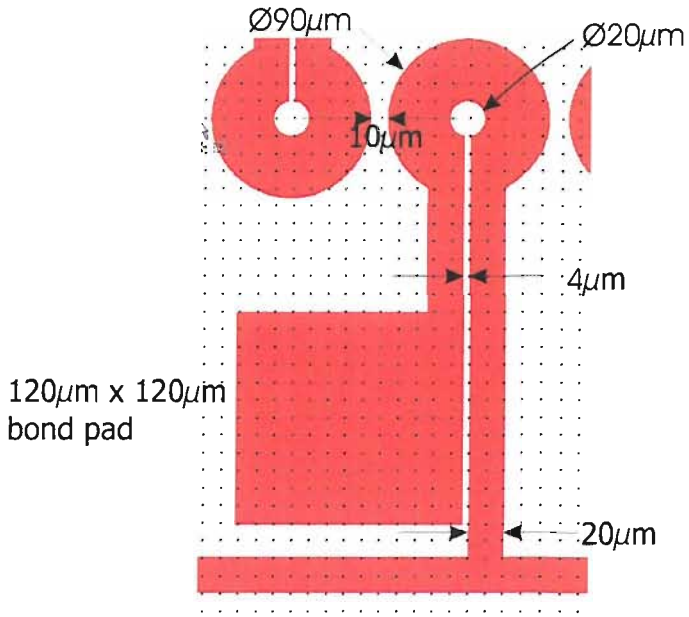

Figure 6.20: Original microcoil design.

6.3.4 Electroplating microstructures

Initial electrodeposition

As identified in Chapter 4 the most common technique for producing thick metal structures is by using electrodeposition. A thick resist mould is required to define the shape of the electrodeposited metal over the seed layer. This mould is achieved using a $20\,\mu m$ thick photoresist (SPR220). The first attempt was to create the thick resist mould, with the coil pattern for the structures shown in Figure 6.20. Unfortunately these structures were unstable, as illustrated in Figure 6.21. This is due to the high aspect ratio of the resist structures between the linking contacts to the coils of approximately 5 : 1 (height: width). These high aspect ratio structures collapsed during the development of the exposed photoresist pattern. Another reason for the collapse of the resist structures between the linking contact structures is due to lack of support at end of the structure. It was considered that the inclusion of suitable anchor points would result in better success in the stability of such thin ridges. To complete the process, using the coil design in Figure 6.20, and to create more stable structures the resist thickness was reduced to $5\mu m$, such that the electrodeposition could be done (Step 7 and 8 of Figure 6.15).

The final step of the fabrication process is to deposit gold to produce thick conductors

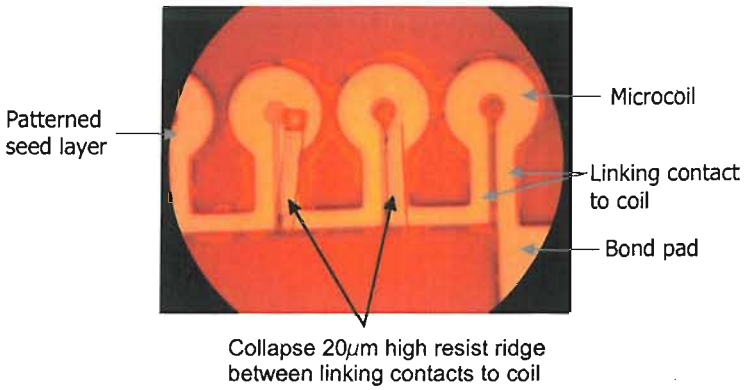

Figure 6.21: Resist ridge collapsing, with a height of $20\mu m$ and width of $4\mu m$.

to form the microcoils. The deposition was carried out using a non-cyanide plating solution (Metalor, ECF64D). To produce the gold structures a constant current was used, while agitating and heating the plating solution at 50 $°C$, to ensure a uniform deposition (further information on the gold deposition can be found in Chapter 4). The electrodeposition set up that was used is illustrated in Figure 4.24.

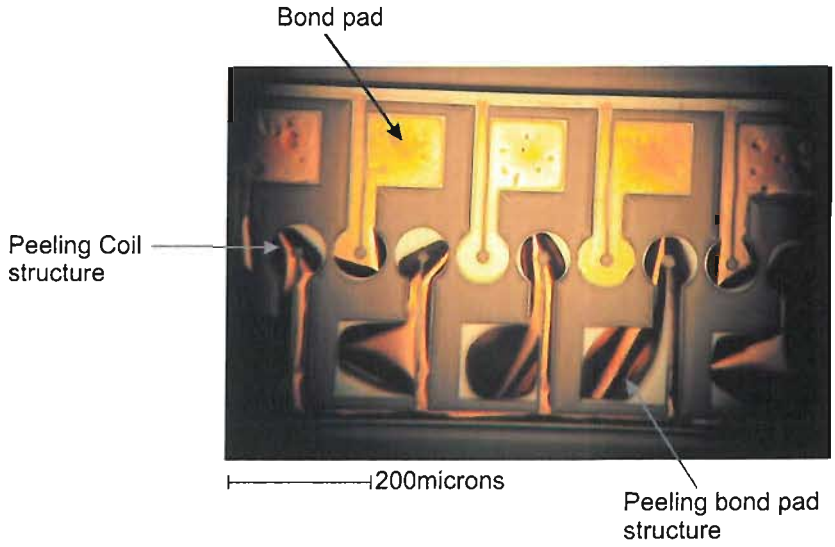

Figure 6.22: Peeling microcoils as a result of tensile stress in the deposited metal due to incorrect plating conditions being used. Due to the poor success of the previous electrodeposition stages

As discussed in Chapter 4, the deposition current can effect the resulting metal structure and the stress in the deposited metal. The recommended current density for the plating solution used is specified as 50 $A\ m^{-1}$ by the manufacturer (Metalor). If the current density used is below this, there is an increased risk of the structure peeling from the surface due to tensile stress. An image of peeling gold structures is shown in

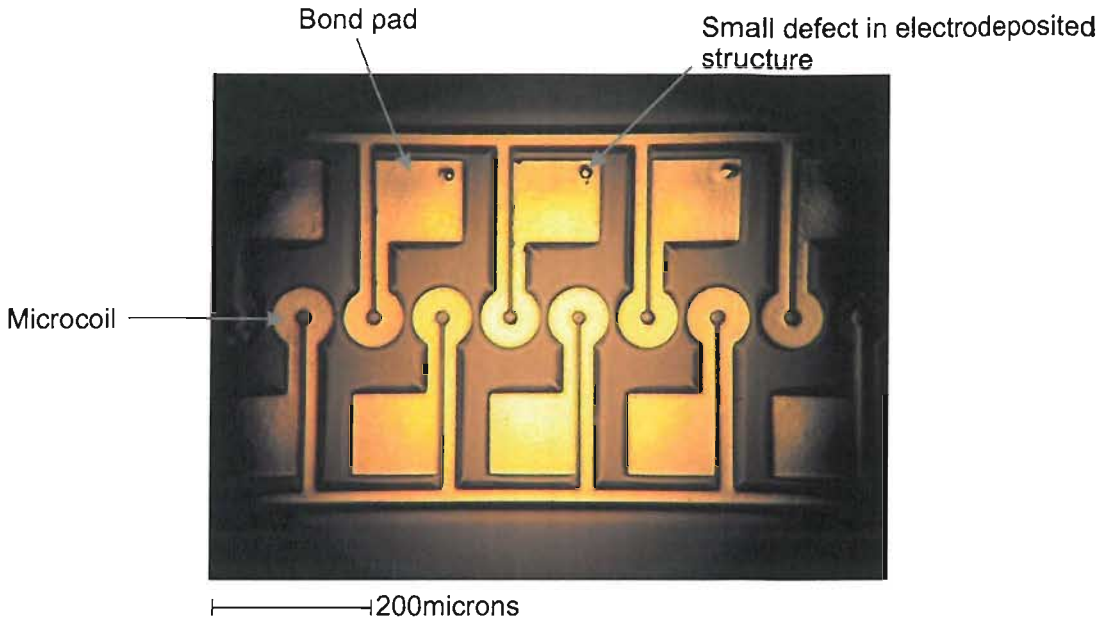

Figure 6.23: Gold plated microcoils, with an approximate thickness of 5 μm.

Figure 6.22, which was produced using a current density of 20 $A\ m^{-2}$. These structures are less than 1 μm thick, indeed it was clear that the structures were peeling so the deposition was stopped.

The coils were successfully deposited using a current density of 50 $A\ m^{-2}$. The coils were plated until the gold reached the top of the photoresist mould, which are approximately 5 μm thick. The completed coils are illustrated in Figure 6.23.

The completed microcoils need to be electrically connected such that current can be applied. To achieve this the devices were sawn up and attached to pre-fabricated headers. These headers are 3x3 cm pieces of alumina, with screen printed gold tracks (800 μm wide, 200 μm spacing) on the surface. The microcoils were wire bonded to the headers, via the bond pads (see Figure 6.23). During this final stage of the processing it was apparent that the coil structures had poor adhesion to the surface. When the wire bonding was attempted the structures were lifted off the surface. Due to the failing of the wire bonding step no further testing was done.

The poor adhesion was thought to be due to either a (i) poor adhesion of the evaporated chrome/gold seed layer or (ii) a degradation of the seed layer during patterning or electrodeposition, resulting in the unwanted lift off. Unfortunately, the adhesion of the evaporated chrome/gold layer was not tested before patterning and therefore this

may or may not be the cause of the microcoil 'lift off'. The seed layer could have been damaged during the patterning stage, because a wet etch had to be used. The wet etch might have resulted in a undercutting of the structures which made the structures fragile. Alternatively damage to the seed layer might have been a result of the electrodeposition and this would result in the final devices being weak. At the beginning of the electrodeposition, the plating set up is allowed to equilibrate before the current is applied. The equilibrium state, as discussed in Section 4.5, is a transfer of ions from the seed layer into the plating solution at the surface of the working electrode (sample), which could have weakened the seed layer. Alterations were made to the microcoil production stage of the fabrication process, which are discussed in the following section, 'Improved electrodeposition'

Improved electrodeposition

To improve the adhesion of the electrodeposited microcoils, alterations were made to both the fabrication process and the mask design. To improve the resist mould patterning, the thin ridges which separate the linking contacts to the microcoils (see Figure 6.21) were increased in width from $4\mu m$ to 10 μm; the new microcoil mask design is illustrated in Figure 6.24. The inner radius of the microcoils was increased from 10 μm to 15 μm to help 'anchor' the ridges at one end, while the length of the problematic ridges was reduced. The bonds pads were increased in size from $120nm$ x $120nm$, to $200nm$ x $200nm$. Finally an area within the bond pad has been masked during the electrodeposition, which will not be electrodeposited with gold. If the weakness in the microcoils was a result of the electrodeposition, this region of the bond pad will not be effected, and will allow for the wire bonds to be made directly to the gold seed layer.

It is clear from the mask design in Figure 6.24, that two microcoils are connected together and thus both will be actuated at the same time. This was done for two reasons. Firstly, this made it possible to reduce the length of the problematic resist ridge (that collapsed in the previous design, on page 156). Secondly, it will also make the actuation of the microcoils easier, because pairs of microcoils will be actuated at the same time.

To improve on the success of the microcoils, the thickness of the seed layer was

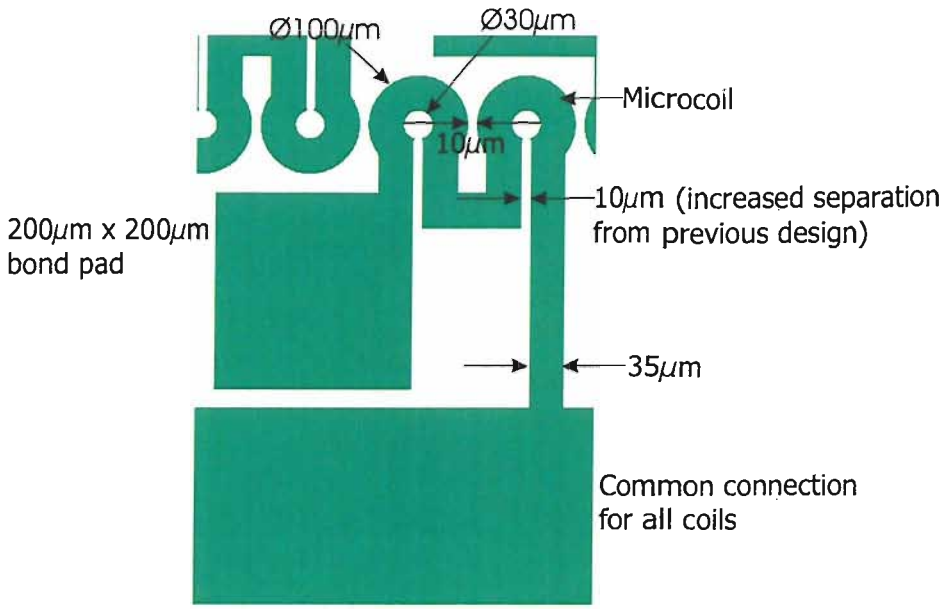

Figure 6.24: Improved microcoil design, with double loop and reduced length and width of problematic resist ridge.

increased from $150nm$ to $500nm$. By increasing the thickness of the seed layer, it is thought that even if a transfer of ions occurs from the seed layer to the plating solution (during the first equilibrium stage), there will be a substantial seed layer remaining which is undamaged.

The resist mould for the 'Improved electrodeposition' was fabricated using AZ4562 photoresist (Clariant), with a spin speed of 1200 rpm, resulting in a measured thickness of 13.1 μm. An image of the resist mould pattern is shown in Figure 6.25. Despite making alterations to the design of the mask to increase the yield, some of the thin ridges between the connection wires (10 μm wide) to the microcoils were still damaged post development of the photoresist. The damage to the resist has resulted in these thin ridges being washed away, which are critical for the success of the electrodeposition. Without the presence of the photoresist ridges between the connecting wires, the two connecting wires will be shorted during the electrodeposition and no current will flow through the coil loop. An image of the photoresist pattern, where some of the thin ridges have been washed away, is shown in Figure 6.26.

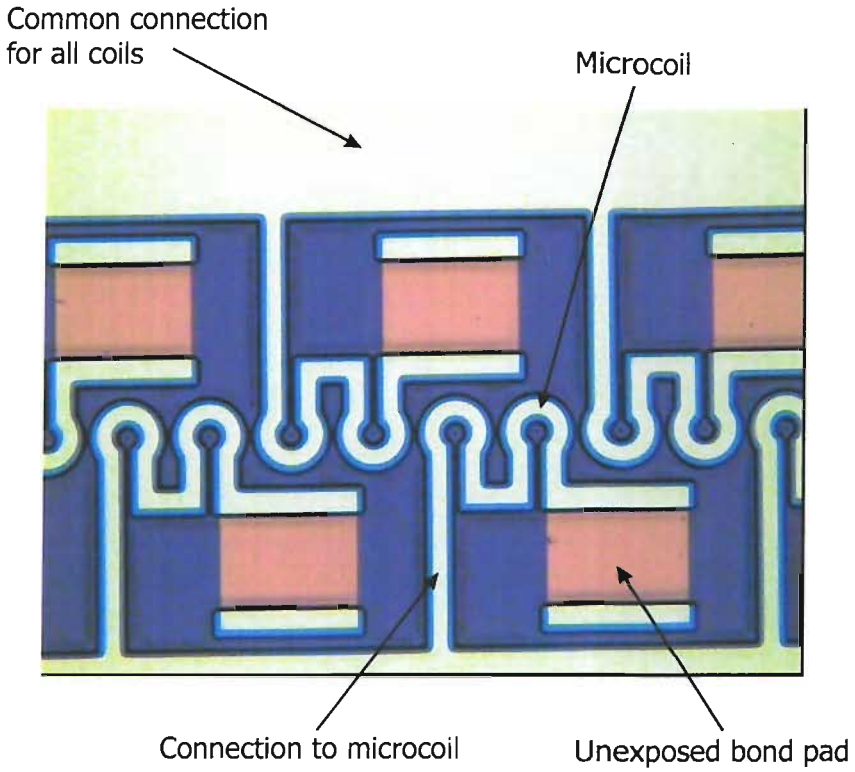

Figure 6.25: Image of 13.1 μm thick resist mould before electrodeposition.

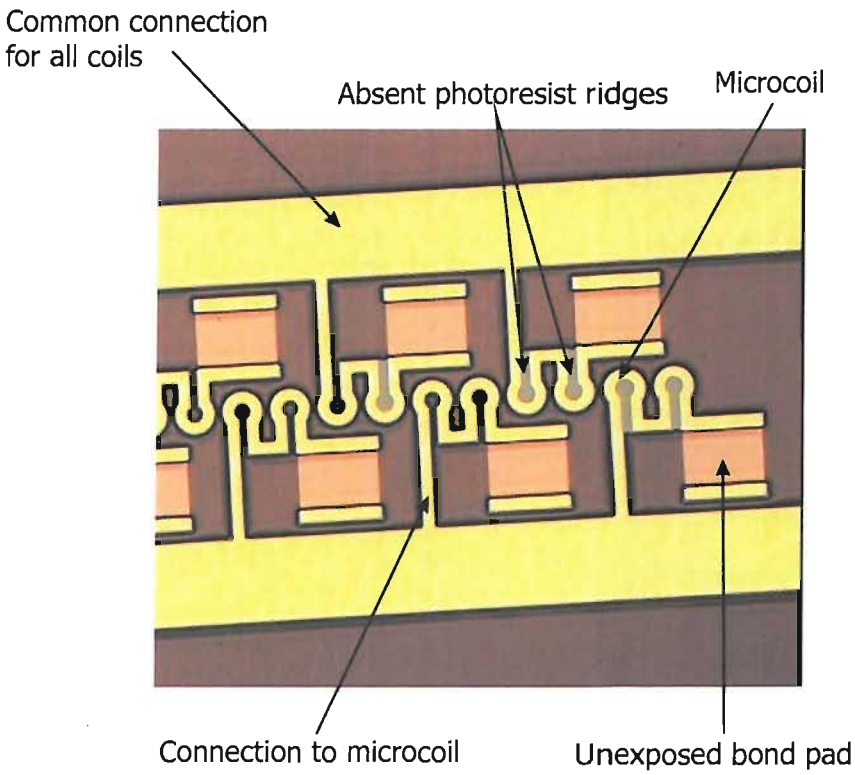

Figure 6.26: Image of 13.1 μm thick resist, where some of the photoresist ridges have been washed away during development.

The electrodeposition of the microcoils was carried out using the same set up as before, which is illustrated in Figure 4.24, Chapter 4. The plating solution used for the electrodeposition was ECF64D from Metalor, which was agitated and heated at 50 $°C$. As before the current used for the deposition was calculated using the current density recommended by the manufacturer of 50 $A\ m^{-2}$.

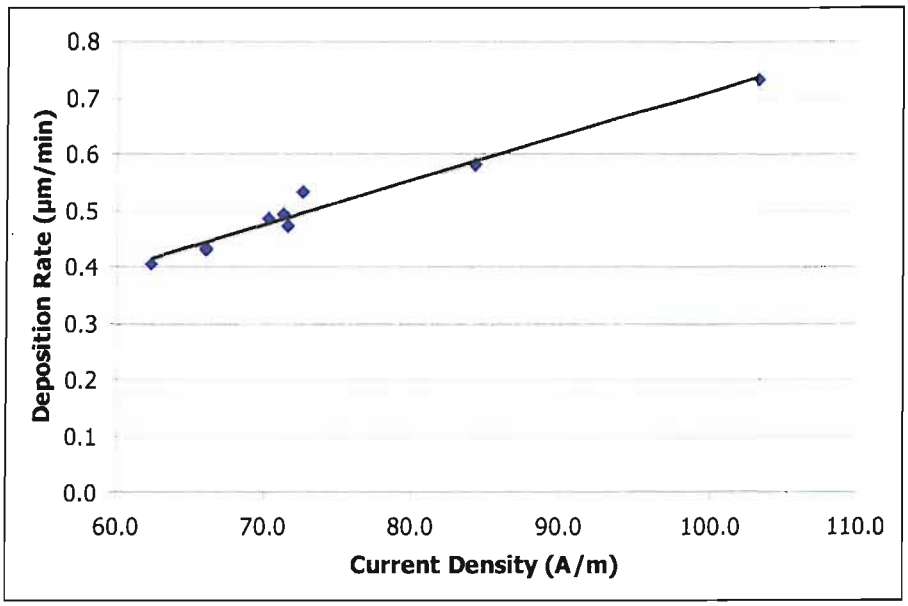

Figure 6.27: Graph of deposition rate of the gold against the current density for ECF64D, for the devices illustrated in Figure 6.25.

Due to the poor success of the previous electrodeposition stages (page 156), this time the wafers were sawn up into chips before the deposition of the thick gold layer. This provided more structures to test for the optimal deposition conditions and thus increased the probability of achieving a working device. The area of the microcoil patterns were accurately calculated from the mask design. The area was calculated to be $1.5\text{x}10^{-5}\ m^2$ and this required a deposition current of approximately 1 mA (using the a current density of 50 $A\ m^{-2}$ from the manufacturer), which was used. Before the microcoils on the 'final' devices were fabricated, some test structures were used to determine the deposition rate. These test structures were the same patterned gold structures of sputtered gold on silicon wafers, with the same thick photoresist mould, as those used on the 'final' devices. Figure 6.27 shows a graph of deposition rate against current density, which was achieved from these 'test' structures.

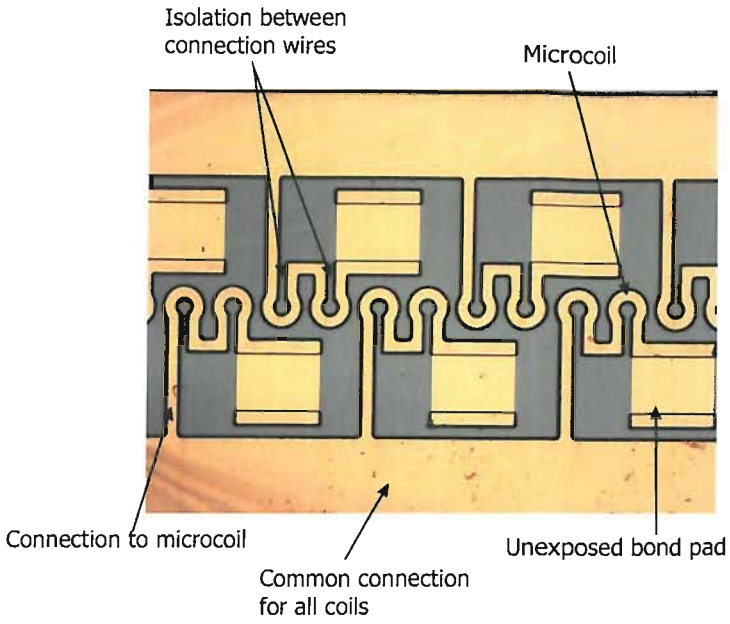

Figure 6.28: Electrodeposited gold of 12.5 μm thick.

It is clear from the graph in Figure 6.27 that the rate of deposition varies for each test structure measured. The deposition current of 1 mA was calculated using the recommended current density of 50 $A\ m^{-2}$ and the calculated deposition area. However during the actual deposition, the area which was submersed in the plating solution varied and therefore the current density increased, for the deposition current of 1 mA. An approximate deposition rate of 0.45 $\mu m\ min^{-1}$ was determined from Figure 6.27, which was used to fabricate a gold thickness of approximately 12 μm, using a current 1 mA for 1600 s, shown in Figure 6.28.

Once the electrodeposition fabrication stage was complete the resist was removed by dissolving it in acetone. To allow for electrical connections to be made to the microcoils, headers are attached to the devices using epoxy glue (B&Q, repositionable epoxy glue), which are subsequently wire bonded (WestBond 5400) using 25 μm diameter gold wire. The headers consist of 3x3 cm pieces of alumina, with screen printed gold tracks (800 μm wide, 200 μm spacing) on the surface. The microcoils have been designed to be actuated with 1 A, therefore two wire bonds had to be made for each microcoil, because the fuse current of 25 μm diameter bond wire is approximately 0.5 A at 10 mm long. An image of the assemble microdevice is show in Figure 6.29, including the successful wire bonding to the bond pads.

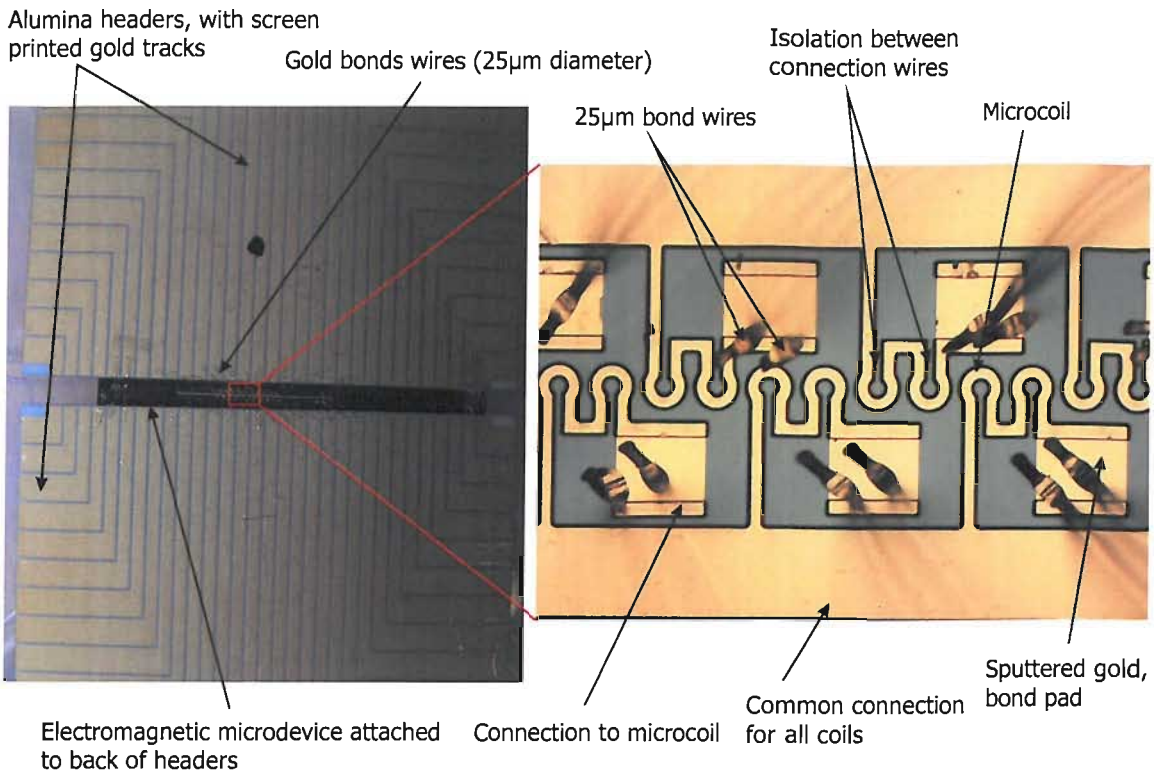

Figure 6.29: Wire bonded microcoils with 25 μm bond wire attached to the pre-fabricated alumina headers.

To ensure that the bond wires did not fuse during the actuation of the microcoils, the fuse current of the bond was determined experimentally. A single bond wire of approximately 5 mm long was bonded to the header between two tracks. Current was passed through the bond wire, until the bond wire fused. Although the manufacturer specification for the fuse current of the wire is approximately 0.5 A, experimentally the bond wire fused at 1 A. Indeed it is not ideal to use the bond wires close to the fusing current, thus the wires were tested. A single bond wire was used to sink a current of 0.8 A for one hour and no damage was found. Therefore two bond wires will be sufficient to sink 1 A, for each microcoil.

6.4 Conclusion

The design and fabrication of an integrated microdevice, for manipulating paramagnetic beads, to displace fluid was described in Chapter 6. The integrated device includes microcoils which have been predicted to produce a magnetic flux density of 14 mT,

when actuated with a current of 1 A. The microcoils consist of two current loops in series, which each have an outer diameter of 100 μm and a spacing of 10 μm. The fluidic channels are configured in a 'H-shape' such that an inlet and outlet connection channel butt each end of the 'device' channel, as illustrated in Figure 7.1. The device channel is 30 μm deep, 80 μm wide and 15 mm long. It has been predicted that it should be possible to displace fluid at velocities up to 2.4 $mm\ s^{-1}$, without fluid slip past or through the bead plug.

The use of SOI wafers made it possible to achieve the small separation of 12 μm between the microcoils and the fluidic channel. The thinning of the SOI wafers was used to achieve this separation, which was developed during this fabrication, such that it was possible to use contact masks on the remaining silicon and silicon dioxide layer.

The fabrication process was developed such that 12 μm thick gold conductors could be fabricated on the surface of the microdevice. Problems with the electrodeposition of the microcoils occurred as a result of the production of the thick resist moulds and the adhesion of the metal on the silicon dioxide surface. These problems were resolved by modifying both the mask design of the microcoils and the parameters used to fabricate these microcoils. The successful fabrication of the thick gold conductors was thanks to the thick resist patterns of 13 μm that were achieved with an aspect ratio of 2:1.

Chapter 7

Evaluation of the integrated electromagnetic device

7.1 Introduction

The design and fabrication of an integrated microdevice, for manipulating paramagnetic beads, to displace fluid was described in Chapter 6. In this chapter the magnetic flux density and magnetic force that can be produced by the actuation of the microcoils, with paramagnetic beads in the fluid filled channel is investigated. Two experiments are carried out, whereby the electromagnetic device is used to both separate and transport beads within the fluidic channel. The measured magnetic field and the magnetic force, is compared to that evaluated theoretically (Chapter 6) and studies are done to establish the application of the device for pipetting nanolitres of fluid.

The integrated device includes microcoils which have been predicted to produce a magnetic flux density of 14 mT, when actuated with a current of 1 A. The microcoils consist of two current loops in series, which each have an outer diameter of 100 μm and a spacing of 10 μm. The fluidic channels are configured in a 'H-shape' such that an inlet and outlet connection channel butt each end of the 'device' channel, as illustrated in Figure 7.1. The device channel investigated here is 30 μm deep, 80 μm wide and 15 mm long.

The results obtained using the integrated microdevice, are presented and discussed in this chapter.

7.2 Experimental apparatus and procedures

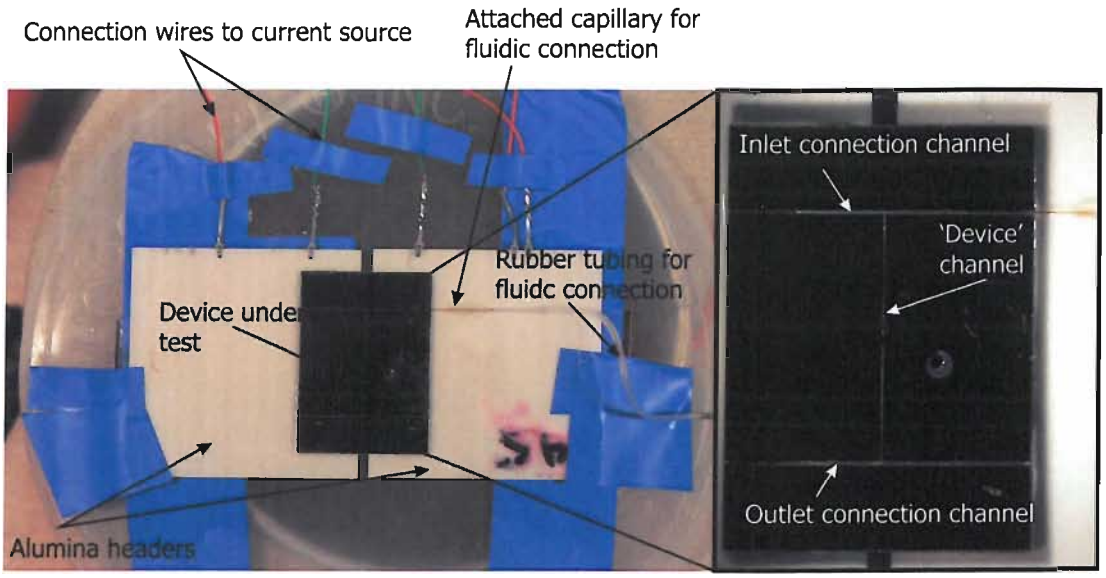

Figure 7.1: An image of the completed microdevice (Pyrex side) showing the electrical and fluidic connections, which were necessary to investigate the device operation.

The microdevice required both electrical actuation and fluidic connections to carry out the following experiments. The individual microcoils were wire bonded to headers allowing for electrical connections to be made, as described in Chapter 6, Section 6.3.4 (Figure 6.29). These headers allow for easy electrical connections to be made, with wide (1 *mm*) screen printed gold tracks. Each of the microcoils could be actuated individually and were connected to independent current sources. A constant current source was required in order to keep the magnetic field constant. Joule heating of the microcoils will cause resistance variations which have to be accommodated. Each current source was switched using a high (5 v) or low signal (0 v) from digital outputs of a data acquisition card (National Instruments USB-6019). The digital outputs are switched manually via a simple Labview program. Figure 7.2 shows a schematic diagram of the current source circuit which was used to actuate each of the microcoils.

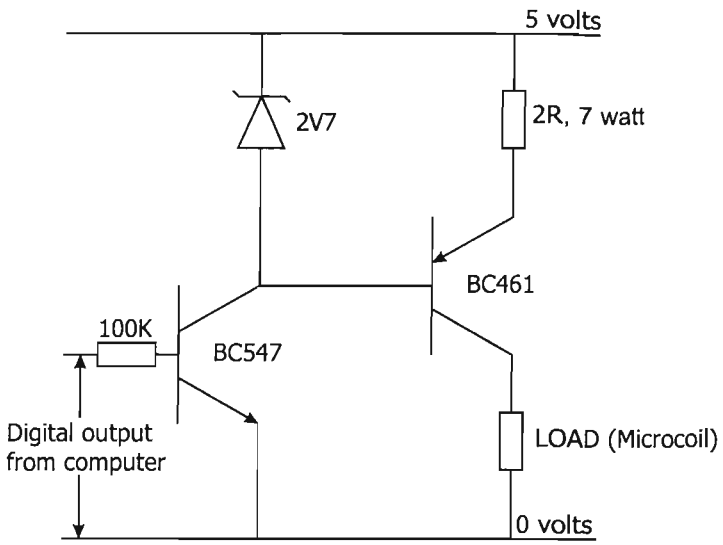

Figure 7.2: Circuit diagram of the voltage controlled current source used to actuate each of the microcoils

The device channel is configured in a 'H-shaped' design with the inlet and outlet, which is illustrated in Figure 7.1. A capillary tube (Polymicro, 75 μm inner diameter, 150 μm outer diameter) was fixed into the inlet channel of the integrated device, using epoxy glue (B&Q, repositionable epoxy glue). The opposite end of the sawn connection channel was plugged with epoxy glue. This was done to allow for the paramagnetic beads to be injected into the microdevice and so that the microchannel could be flushed before and after experiments, to ensure that no beads remained in the fluidic channel. The overall experimental set up is shown in Figure 7.3, including the syringe pump, current source and multimeter (Fluke 187) used to measure the actuation current.

During initial testing of the integrated microdevice, it was observed that the paramagnetic beads were sticking to the surface of the silicon microchannel. The exact cause of the bead adhesion was not investigated, however steps were taken to prevent this happening and these are discussed in more detail in Section 7.2.3. Two experiments determined the feasibility of this design for future use as a paramagnetic bead plug device for dispensing fluid. These experiments were carried out to determine what forces could be applied, using a magnetically actuated paramagnetic bead plug, to the fluid in the microchannel, within the integrated microdevice and also determined the magnetic flux density that could be achieved using the microcoil design fabricated here.

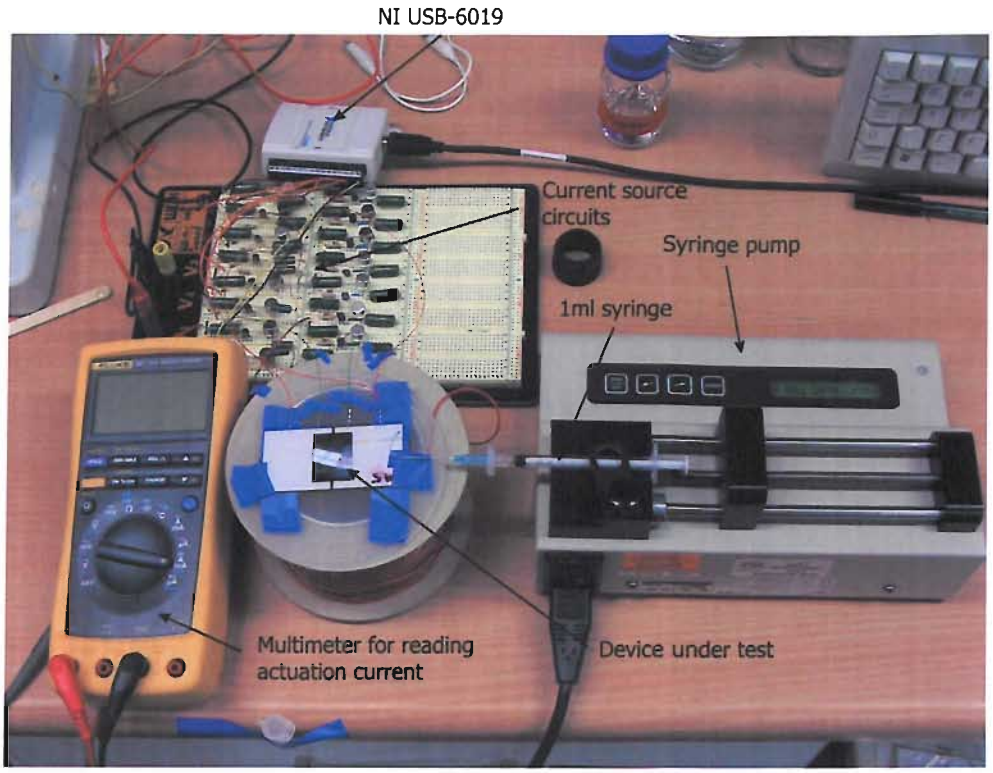

Figure 7.3: An image of the experimental set up used to investigate the integrated device operation.

7.2.1 Bead separation

Paramagnetic beads (Invitrogen, M-450 4.5 μm diameter) were pumped through the microdevice in an aqueous solution of 1% Triton X-100 (Sigma Aldrich) with a bead density of approximately 10^6 $beads\ ml^{-1}$. One of the microcoils was actuated using the current obtained from a current source, as illustrated in Figure 7.2. The velocity of the bead solution, flowing through the microchannel, was kept constant by using a 1.0 ml syringe, connected to the device via a piece of rubber tubing (SF Medical, 0.5 mm internal diameter). The 1.0 ml syringe was clamped into a syringe pump (KDS Scientific, KDS-100-CE) which was used to control the velocity at which the syringe plunger is moved. The syringe pump is illustrated in Figure 7.3. The volume flow rate of the fluid exiting the syringe is set using the syringe pump, which yields a fixed fluid velocity within the microchannel of the integrated device. The microcoil actuation current was increased linearly from 0 A and the microchannel was observed until beads were trapped at the surface of the silicon, at a location above the actuated electromagnet. The actuation current to trap the beads (above the electromagnet) was

recorded. The flow velocity of the injected bead solution was then increased and the experiment was repeated, to establish the required microcoil actuation current to trap the beads. Likewise, the actuation current whereby the beads are released was also determined as a function of fluid velocity, by gradually reducing the microcoil actuation current, until the beads were released and flowed away.

7.2.2 Bead transportation

Approximately 100 paramagnetic beads (Invitrogen, M-450 4.5 μm diameter) were loaded into the microchannel in an aqueous solution (1% Triton). These beads were moved back and forth between two microcoils. Firstly the beads were trapped above one microcoil, then the second coil was actuated and the first coil was turned off. An illustration of the two adjacent coils used for this investigation is show in Figure 7.4. The actuation current used for the two microcoils was the same. This was repeated for different actuation currents between 0.4 A and 1.0 A. As the actuation current is increased, the time taken for the beads to be moved between the microcoils decreases. A higher current will result in a higher magnetic flux density gradient, and therefore a higher magnetic force is exerted by the beads. By equating the magnetic force and the fluidic drag force exerted on the beads, the time taken to move the beads between two points, can be predicted. A series of experiments was done where the applied actuation current and the time taken for the beads to be transported between the two microcoils were recorded.

Although approximately 100 beads were used during this experiment, it was only the movement of individual beads that was of interest. By considering only single beads, the drag force and magnetic force can be easily predicted to compare to the measured values. These results are discussed in Section 7.3

7.2.3 Bead adhesion

The adhesion of the paramagnetic beads is a problem that had already been addressed in Chapter 5. It was eliminated by ensuring that the microchannel was clean and by

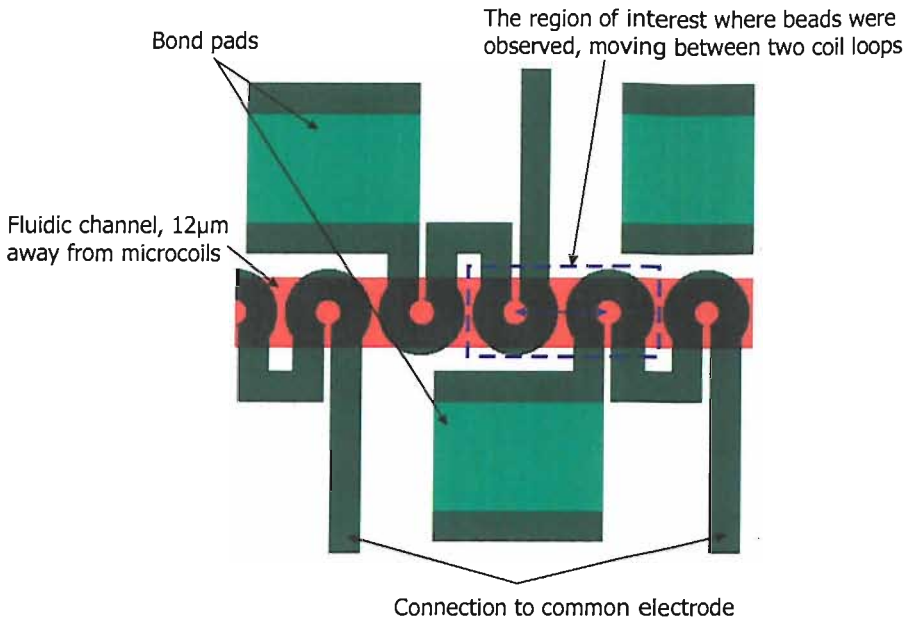

Figure 7.4: An illustration of two adjacent microcoils, which were used to transport paramagnetic beads between two current loops.

using a 1% Triton aqueous solution in the microchannel. Visual inspections showed that the microchannels in the integrated devices were not clean (after the fabrication process was complete). During fabrication, steps were taken to clear the channels after any 'wet' processing steps, however this was not always possible, because the device consists of many channels. Due to the layout of the wafer, the more centrally located devices on the wafer are less affected by this problem, because the fluids used during the process steps do not penetrate deep into the channels. Each wafer contained 14 devices, which are interconnected by the sawn channels. The fabrication chemicals would not go into all of the channels, especially not the microchannels located in the centre of the wafer.

Once the fabrication of the channels was complete, attempts were made to remove the debris from the channel surfaces. Unfortunately, the exact chemical composition of the debris was not known and this made it difficult to determine what could be used to dissolve or remove it. Various solvents and acids were used, including acetone, potassium hydroxide and commercial chrome etch. Care also had to be taken during the attempted cleaning of the channels because the microchannels are fabricated in silicon and Pyrex and the microcoils are fabricated in gold and titanium. Indeed gold and titanium is etched by aggressive cleaning solutions, such as aqua regia (hydrochloric and nitric acid) and piranha (sulphuric acid and hydrogen peroxide at 130 $^{\circ}C$) [187].

Ideally the device would be contained within the bonded wafers and thus the channels are sealed until sawing is done. This would eliminate chemicals from entering the channels in the device. However the fluidic connection channels were produced using sawing and the only way to do this for the saw channel to run the length of the Pyrex wafer. These connection channels could, in future similar devices, be made using an alternative technique, such as wet etching (as in Section 6.3.2) and the connection channels could be produced to provide sealed channels after the structure had been bonded. However process conditions would need to be considered so that damage to the silicon and silicon dioxide membrane between the microcoils and the fluidic channel was not caused; the air in the channels could expand during processing that required large thermal stress on the device. In hind sight for the system investigated here the channels could be coated with photoresist, after the anodic bonding (Figure 6.17), which could be removed once the devices were completed.

7.3 Results and discussion

It was demonstrated that the paramagnetic beads were separated from fluid at the highest magnetic flux density point of an actuated microcoil, as illustrated in Figure 7.5. However, when the actuation current was removed the beads remained on the surface and could not be moved when either adjacent microcoil was actuated.

The first experiment was carried out to ensure that a magnetic field sufficient to separate beads from fluid flow could be achieved using the actuated microcoils. Both the current required to trap the beads on the surface and the current at which the beads were released was recorded. An image of the microchannel above the microcoil, is shown in Figure 7.5, before and after the beads were separated from the solution. The results from this experiment are shown in the graph in Figure 7.6.

A graph of current applied to trap and release the beads against the fluid velocity is shown in Figure 7.6. It is clear that the microcoil actuation current required to release beads is less than that for the beads to be trapped. This confirms our hypothesis that the beads adhere to the surface of the silicon after being separated from the fluid. If the beads did not adhere to the surface of the silicon, it is assumed that the beads would

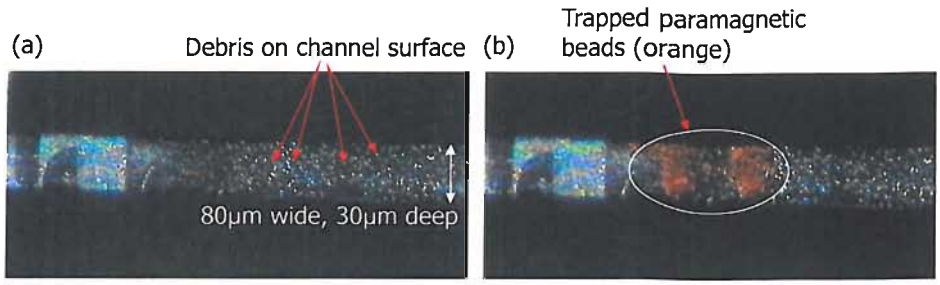

Figure 7.5: An image of a section of the fluidic channel above the actuated microcoil (a) before trapping and (b) once the beads have been trapped.

move away due to the exerted fluid flow (by the syringe), once the current applied to the microcoil was reduced below the trapping current. This cannot be due to remanence in the microcoil, because the materials used to fabricate the microcoils and the substrate are diamagnetic (discussed in Chapter 4).

To determine the force which can be achieved theoretically using a single paramagnetic bead, Equation 4.8 (Chapter 4) was used, with the predicted magnetic flux density from Chapter 6, which was obtained using FEMLAB with a magnetostatic model (Appendix A.1). It was observed experimentally that the beads were only trapped from the fluid bulk at the surface of the silicon, under which the microcoils are positioned. Other beads, which were further away from the microcoil in the microchannel, flowed over. The magnetic force exerted on the beads, closest to the microcoils (approximately 12 μm), was therefore calculated. Although the exact location of the microcoil is not known (because the silicon is not transparent), it was assumed that the beads were separated at a point where the magnetic flux density and gradient was the highest. The force on a single bead was predicted for microcoil actuation currents up to 1 A, which is the limit of the actuation system defined by the 2 Ω emitter resistor used in the actuation circuit. The predicted magnetic force on the bead above the coil is shown in the graph in Figure 7.7, by the solid black line. The magnetic susceptibility used to predict the bead force, was taken as 1.6, from the graph in Figure 4.3, in Chapter 4. Although the value for the magnetic susceptibility is higher than that used in our previous evaluations in Chapter 5, in this case the applied magnetic field is much lower.

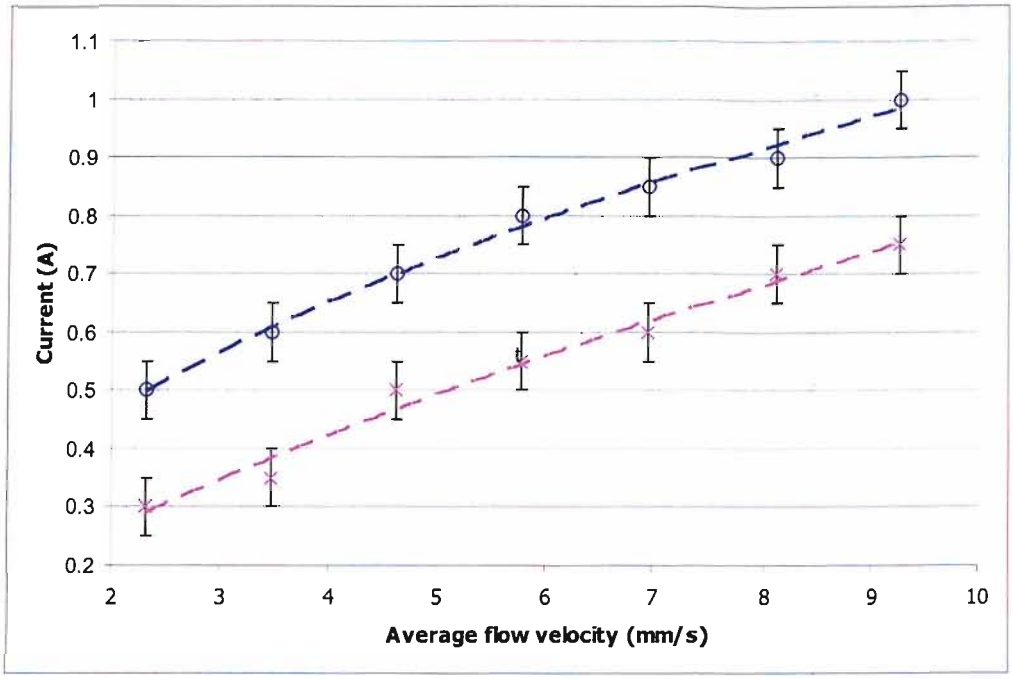

Figure 7.6: A graph of the microcoil actuation current against the average flow velocity for [– o –] the trapping of the beads and [–x–] the release of the beads. The dashed lines have been fitted to the data.

A comparison was made of the predicted magnetic force and the estimated value for the drag force, obtained from the experimental results, of a single bead under the conditions investigated and described above, (see Figure 7.6). To obtain a value for the drag force, the fluid velocity near the surface of the microchannel, where the bead was trapped, was estimated using Equation 7.1 [86]; where ν_y is the velocity at a distance of y from the surface of the channel, ν_m is the maximum velocity in the centre of the channel and b is the channel height. The average flow velocity was found using Equation 7.1, by integrating the flow velocity over a distance of 4.5 μm (bead diameter) from the surface of the channel. This was done because the diameter of the paramagnetic bead (4.5 μm) is the same order of magnitude as the microchannel height (30 μm), therefore it will be travelling in a region of the microchannel where the pressure driven fluid flow is travelling at different velocities. (The fluid flow will be laminar due to the small Reynolds number of the device). Although Equation 7.1 is defined for the theoretical solution of two parallel plates and not for a closed channel, an approximation of the flow velocity in the central section of the channel (away from the side walls) using this equation is considered to be reasonable.

$$\nu_y = 4\nu_m y \frac{(y-b)}{b^2} \tag{7.1}$$

The bead solution was pumped through the microchannel using a syringe pump (KDS Scientific, KDS-100-CE) and a 1.0 ml syringe. The syringe pump was configured to be used with a 1.0 ml syringe, such that the volume flow rates were correct for this particular syringe. The flow velocity was then calculated using the volume flow rate within the microchannel (80 μm height, 30 μm deep). The investigated flow velocities (calculated from the volume flow rates from the syringe pump, see Section 7.2.1) were taken as the average flow velocity, where the average velocity is $2/3$ of the maximum velocity (ν_m).

Stokes' Law was used to obtain an approximate value for the drag force of a single bead. However Stokes' law can only be applied to obtain the drag force of a bead in an unbounded system, with low Reynolds number (< 0.1) [86]. The Reynolds number for a single bead was calculated using Equation 3.1 and found to be $<< 0.1$ for the fluid velocities investigated here. If the system is bounded, as in the case of the system investigated here, it has been shown that the drag force increases as a result of an increase of the diffusion coefficient, which is inversely proportional to the fluid viscosity [188; 189]. This can result in an increase of the effective viscosity of up to three times that of the normal value. Stokes' law is given in Equation 7.2 to estimate the drag force (F_{Drag}), where η is the fluid viscosity, ν is the fluid velocity and R_B is the bead radius. Values for the predicted drag force for a single bead have been calculated and are plotted in the graph in Figure 7.7. It was assumed that for the beads to be trapped within the magnetic field of the actuated microcoil, the magnetic force on the bead must be greater than or equal to the drag force ($F_B \geq F_{Drag}$). The force on the bead is known (F_B), therefore the drag force (F_{Drag}) can be proven to be correct.

$$F_{Drag} = 6\pi\eta\nu R_B \tag{7.2}$$

The experimental and predicted data are plotted and shown in the graph in Figure 7.7. The predicted drag force on the bead was calculated using experimental fluid velocities at which the beads were trapped, for a given microcoil actuation current.

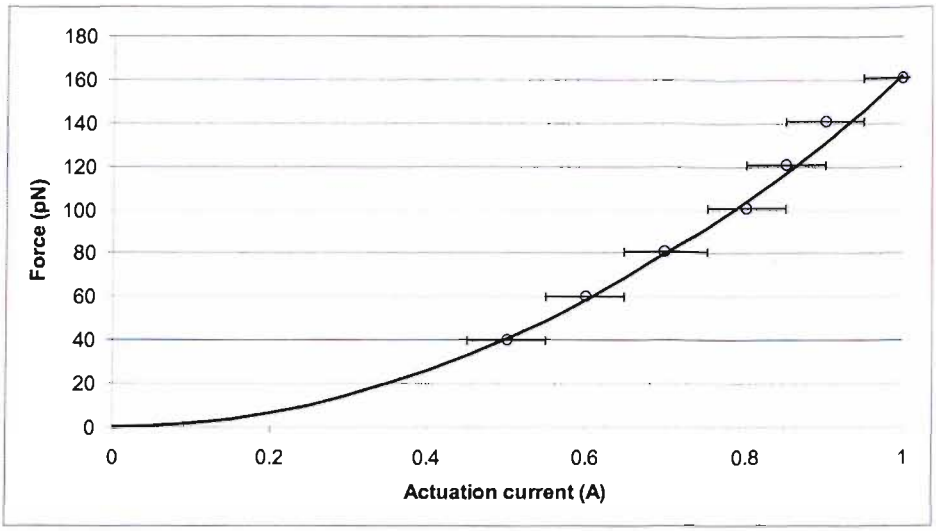

Figure 7.7: Graph of the [—] predicted magnetic bead force obtained using Equation 4.8 and [○] the drag force, obtained using the measured data from Figure 7.6 and Equation 7.7, against the microcoil actuation current.

There is an error in the recorded actuation current, because the recorded actuation currents are within ± 0.5 A of the average actuation current. Using the data in Figure 7.7, this error equates to an overall error of approximately $\pm 12\%$ between the predicted force and the force derived from the recorded data. The predicted trapping forces are in good agreement with the observed trapping forces.

There are potentially two sources of error in determining the drag force on the bead. Firstly the drag force on a bead in fluid increases as it gets closer to a surface, because the effective viscosity of the fluid increases [188; 189]. At the surface this can be as high as three times the drag force which has been calculated here. Secondly the bulk velocity of the fluid that was pumped through the microchannel is known and was controlled using a syringe pump. However the actual velocity of the fluid at the surface of the channel, and therefore the bead velocity, was predicted using Equation 7.1. The predicted values for the drag force for the bead, shown in the graph in Figure 7.7, were calculated using the average velocity in the channel, which was calculated from the silicon surface (12 μm from the microcoils) to a height of 4.5 μm (the diameter of a single bead). However, it is thought that the bead velocity could be much lower than this at the surface. Overall, the drag force will be higher for a given bead velocity. However, because it is believed that the bead velocity is lower that than predicted, the

overall drag force will not change.

The paramagnetic beads were found to adhere irreversibly to some of the surfaces of the channel and this prevented any long distance transport along the microchannel. However, the adhesion of the paramagnetic beads was not observed to occur at all locations in the microchannel, thus movement of beads from one microcoil location to another could be demonstrated.

To demonstrate that beads can be transported between two microcoils as a result of the induced magnetic field, an experiment was carried out as described in Section 7.2.2. Clumps of approximately 100 beads were observed to be moved, as shown in Figure 7.8, between two electromagnets, using an actuation current of $1\,A$. As seen in Figure 7.8c the beads form a self aligned cubic packed structure under the influence of the magnetic field, as discussed earlier. The results obtained for the time for beads to travel from one coil to the next, under different actuation currents, are shown in the graph in Figure 7.9; the graph shows both the measured and predicted time taken to move a single paramagnetic bead between two microcoils. During this experiment the movement of individual beads was recorded and it was observed that the average distance that these beads moved was 40 μm. Although the distance between the microcoil centres is 110 μm, once the majority of the beads had moved between the two coils, further beads were prevented from transport to this region. Thus the distance of the transports of beads was 40 μm and shorter. The location of the coils (with respect to the channel) used to move the beads between to adjacent electromagnets are illustrated in Figure 7.4.

To obtain the average time taken for single beads to be moved from one actuated microcoil to the next, a number of beads (25) were monitored. The distance moved and the time taken for the individual beads was recorded. However the path which each of the beads moved along was not always the same. To accurately predict the time taken to move a single bead over an observed distance of 40 μm, a representative sample of different paths were considered. These paths were taken as a straight line from a point above the first microcoil to a point above the second microcoil, of a distance of 40 μm. These paths were selected to represent the majority of the paths along which the beads moved. Once the predicted times were found for each path, an average time was recorded and this was used in the graph in Figure 7.9. As discussed previously, the

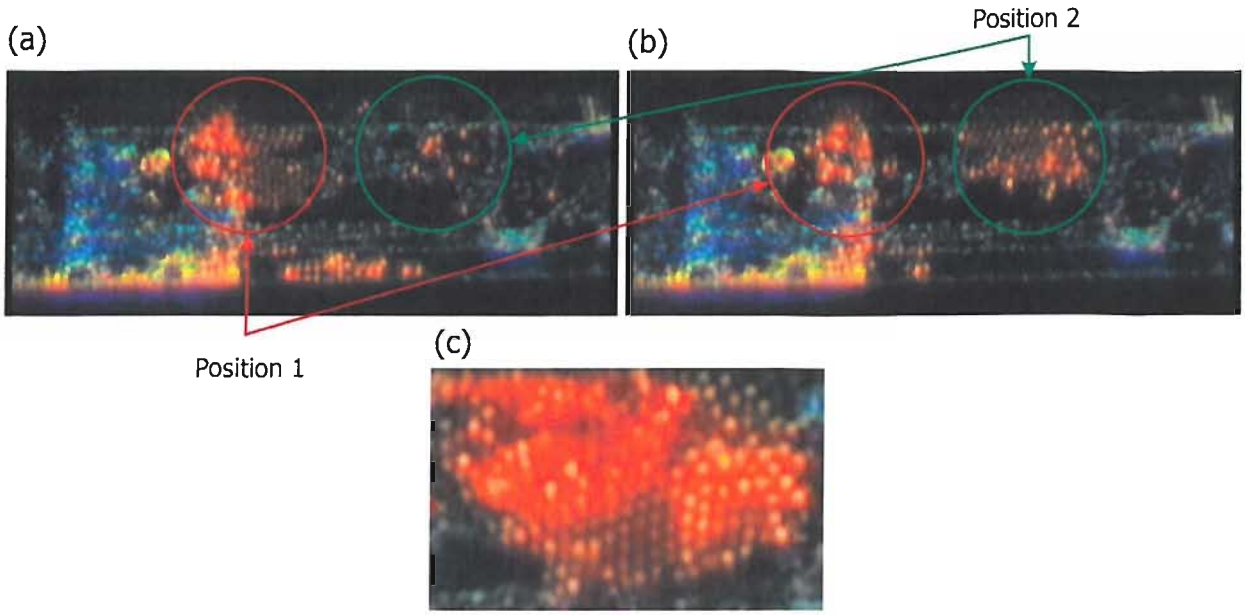

Figure 7.8: An image of a clump of approximately 100 beads, which was moved move from one electromagnet (a) to an adjacent electromagnet (b) by the alternate actuation of two neighbouring microcoils. (c) is a magnified image of the 4.5 μm beads in a cubic close pack structure.

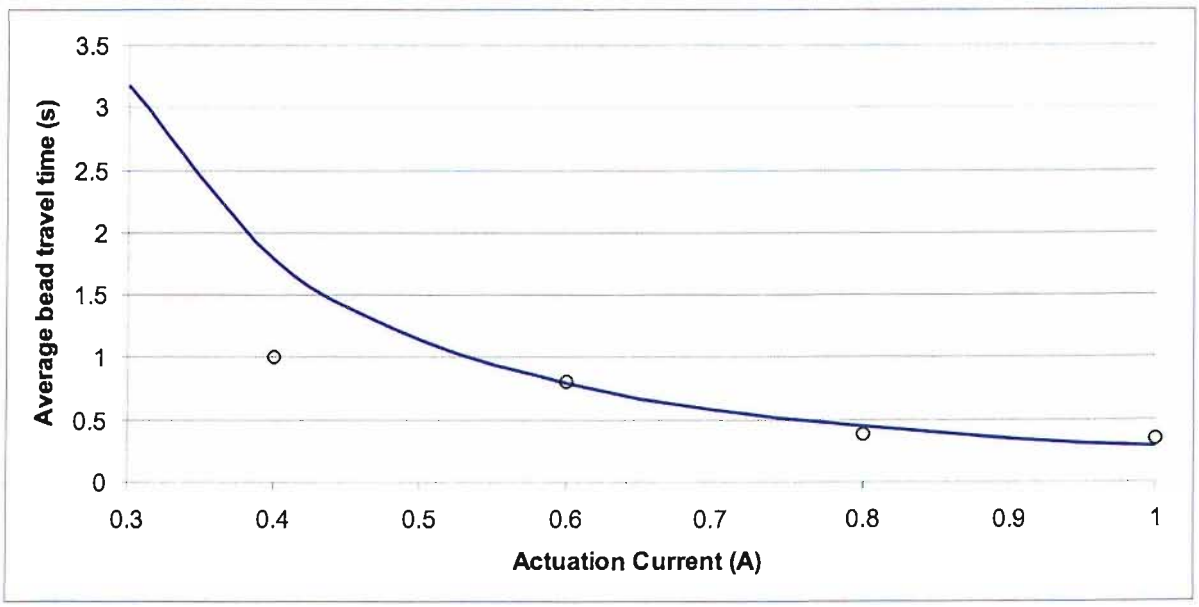

Figure 7.9: Graph of the average time taken for a single bead to be moved over an average distance 40 μm against the coil actuation current [—] predicted, [o] measured

bead drag force was equated to the magnetic force on a bead ($F_B = F_{Drag}$) to predict the time taken for the beads to move over a distance of 40 μm (assuming that the bead is moving at its terminal velocity when $F_B = F_{Drag}$). The time taken for a single bead to move along a number of observed routes was predicted, which was then averaged to achieve the theoretical times shown in Figure 7.9.

The values for the Stokes' drag, in Equation 7.2, need to be corrected for beads moving close to the channel surface, due to an increase in the effective viscosity. The beads were observed to be moving at the surface of the microchannel, so the maximum correction factor of 3 was used [188; 189], to achieve the predicted times in the graph in Figure 7.9. This was done here, and not in the previous measurements (Figure 7.7) for the separation of the beads, because the velocity of the beads was measured.

The measured time values appear to fit the predicted values well except for the observed time taken for a bead to be moved between two coils, using an actuation current of 0.4 A. As discussed earlier the single beads were observed to move over an average distance of 40 μm. However when a microcoil actuation current of 0.4 A was used, an average distance of only 20 μm was observed to be moved by the beads. This was because, when an actuation current of 0.4 A was used, there were more beads in the vicinity of the electromagnet than for the other actuation currents. During the experiment there were more than 100 beads within the channel, so it was difficult to prevent these additional beads entering the region of the microchannel under investigation.

Even though a bead plug could be formed, and this was the same size as the actuated microcoil coil below, fluid continued to flow over the plug. The height of the bead plug within the channel is unknown, however it is considered to be three to four beads in height ($\approx 20\ \mu m$) and the channel height is 30 μm. Although it is possible to form, and move a plug of beads, using the integrated microcoil and channel design, fluid cannot be displaced, because it is not possible to block the entire channel with beads under the influence of the actuated electromagnet. It is thought that this is because the magnetic flux density is not great enough in the upper half of the channel to trap the beads. The theoretical magnetic flux density at the top of the fluidic channel is approximately 2.8 mT ($\nabla B^2 = 0.3\ T^2\ m^{-1}$) (Figure 6.7) with an actuation current of 1 A, which would produce a single bead force of approximately 9 pN, this is 20 times lower than that at

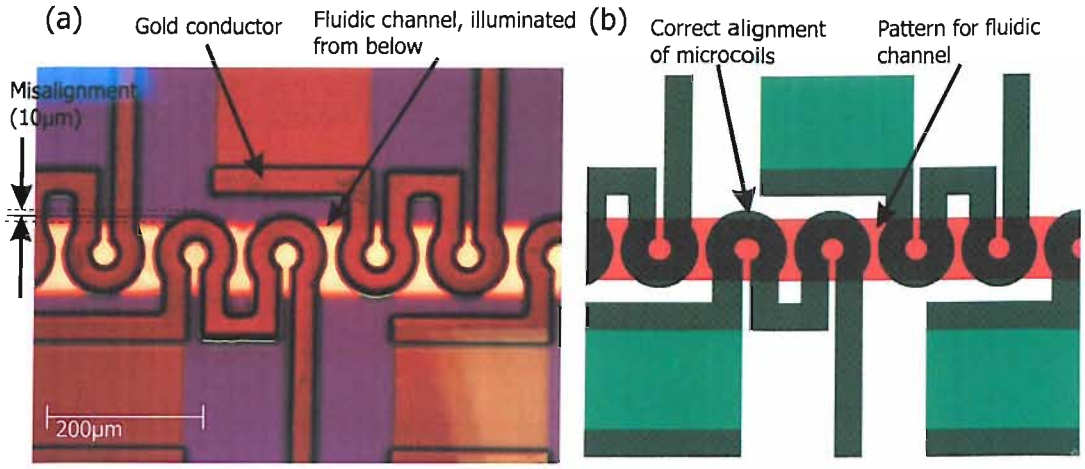

Figure 7.10: (a) An image of the microcoil structures on the silicon surface illustrating the misalignment of the electromagnets with the fluidic channel and (b) is the mask design used to produce the microcoils illustrating the correct alignment of the microcoils.

the bottom of the silicon channel.

It was not possible to directly measure the magnetic flux density produced by the actuation of the microcoils, Figure 6.29 (inside the channels). However it has been possible to indirectly estimate the magnetic flux density using the two experiments discussed in Section 7.2. The experimental and theoretical data in Figures 7.9 and 7.7 are in good agreement, thus the predicted magnetic flux density and the ∇B^2 is close to that achieved using the microcoils due to the good fit between the experimental and predicted data. Therefore the magnetic flux density is estimated to be approximately 14 mT ($\nabla B^2 = 5.5\ T^2\ m^{-1}$) at the channel surface, closest to the magnetic coils, using an actuation current of 1 A.

It was observed that during the actuation of the coils, the beads appeared to be trapped closer to one side of the microchannel. Firstly this was thought to be because the magnetic flux density was higher in a region of the microcoil, rather than at the centre of the current loop. However, this phenomenon was observed at adjacent coil positions, where the microcoils are rotated through 180° (see Figure 7.10), therefore this was attributed to the misalignment of the photolithography mask used to pattern the seed layer, which defined the position of the microcoils. To confirm this, an image of the microdevice was taken while illuminating the structure from below. Due to the thin membrane, 12 μm, between the coils and the microchannel, the microchannel can

be clearly seen in Figure 7.10a, showing a misalignment of approximately 10 μm. To illustrate how the microcoils and fluidic channel should have been aligned, Figure 7.10b shows an image of the mask design used to fabricated the device.

The transport of paramagnetic beads between two single coil loops has been demonstrated. However, it was not possible to transport beads over a longer distance, due to the bead adhesion and the coil design. The coil design consists of two current loops, which was chosen to reduce the number of microcoils for ease of actuation and to improve the yield of the microcoil fabrication process. The length of the thin ridge between the microcoil connections was reduced to prevent it from collapsing during the development stage (Section 6.3.4). It was not possible to completely move beads from one double loop structure to the next, because the magnetic field from one double loop structure does not overlap the entire neighbouring double loop coil. It has been demonstrated that only the beads from two adjacent current loops can be transported. However, if the microcoils were fabricated with just single loops, it would be possible to transport beads over the range of the microcoils. This will be discussed in more detail in Chapter 8.

Previous examples of magnetic microdevices have already been discussed in Section 4.4. Lee et al. [160] produced a single loop trap, which was used to achieve a magnetic flux density of 2.7 mT, with an actuation current of 0.35 A. In comparison the device produced here can be used to produce a higher magnetic flux density of 6 mT (correcting for an actuation current of 0.35 A). Other similar devices, which have been produced to transport beads, have only been shown to achieve a magnetic flux density of $1 - 4$ mT, despite using multiple loop coils [171].

Rida et al. [171] has reported the transport of clusters of beads of velocities up to 1 $mm\ s^{-1}$, using overlapped multiple loop coils, with additional permanent magnets. This is more rapid than demonstrated here (115 $\mu m\ s^{-1}$) with an actuation current of 1 A. However, these results achieved here were obtained using single current loops, with no external magnetic fields. Additionally the investigation carried out by Rida et al. [171], demonstrated the transport of clumps of beads. Although it has not been investigated here, it is likely that a cluster of beads will move at a higher velocity, because the drag force will increase to a lower degree than the total magnetic force, if more beads are used.

A system was produced by Joung et al. [167], which consists of external electromagnets, for bead pumping. Although the system was demonstrated to transport beads at velocities of approximately 0.8 $mm\ s^{-1}$, the reported magnetic flux density of 12 mT, is comparable to the device investigated here. This illustrates that it is possible to achieve similar magnetic forces using electromagnetic microcoils, as for larger 'macro' devices [167]. This is mainly due to the fact that it is possible to produce the electromagnets and fluidic channel in such close proximity (12 μm) which cannot be achieved when using larger components.

Although many beads will be used to form a plug, if the beads do not fill the entire channel, it will not be possible to displace fluid. It would be possible to effectively block the channel using a bead plug formed using this microcoil design, if the height of the microchannel is reduced. However this has implications on the fluidic resistance within the microchannel, which will be discussed in more detail in Chapter 8.

7.4 Conclusion

The actuation of the electromagnets in the integrated microdevice has been successfully demonstrated. This device can be used to move paramagnetic beads through a microchannel. Unfortunately, due to debris within the microchannels, it has not been possible to demonstrate the long distance transportation of paramagnetic beads. It is also not possible to displace fluid using a plug of paramagnetic beads. This is in part due to the design of the microcoils, which are two current loops wired in series. If single current loops were used, which are individually addressable, the transport of paramagnetic beads over long distances should be possible. However it has been demonstrated that the magnetic flux density of the electromagnets, obtained experimentally, is close to the predicted value of 14 mT, which translates to a value of ∇B^2 of 5.5 $T^2\ m^{-1}$ at the surface of the microchannel. This is a critical parameter for predicting the magnetic force which could be applied to the fluid.

The force on a single bead, under the influence of the magnetic flux density from the microcoils, was determined experimentally to be approximately 160 pN. This would translate to a force of approximately 6.4 μN if a plug of 37 000 beads (1 $mmlong$)

was used. However, this magnetic force is based upon the expected force at the silicon surface above the electromagnet in the channel. An actual bead plug would experience a much lower force, because the magnetic flux density is lower in the upper part of the microchannel (furthest from the microcoil). Therefore the predicted maximum force that can be applied using a plug of 40 000 paramagnetic beads within the microchannel will be approximately 1.05 μN, as discussed in Section 6.2.2.

It has been demonstrated that this device can be used for separating paramagnetic beads from fluid and that the magnetic field, which can be achieved using the electromagnetic loop design (100 μm outer diameter), is sufficient to be used to form an integrated device for moving plugs of paramagnetic beads. However, the overall design of the microdevice must be improved if this is to be realised. If the same device structure was used i.e. planar microcoils, individual current loops would have to be fabricated on the surface with the same spacing of 10 μm. By altering the coil design it should be possible to transport beads. However, to form and move a plug of paramagnetic beads, the height of the channel must also be reduced.

Chapter 8

Conclusion and suggestions for future work

8.1 Conclusion

The aim of this thesis work was to produce an integrated pipetting device, which can be used to dispense nanolitre volumes of fluid, into another miscible fluid in an integrated microchannel, in an accurate and repeatable fashion. It is essential that the fluid being dispensed is not exposed to high temperatures by the actuation technique. The samples to be injected are biological fluids which can be denatured at temperatures greater than $\approx 50°C$. This work has included the first proof of concept experiments using paramagnetic beads to displace fluid and the design, fabrication and testing of an integrated microdevice.

During the initial stages of this research, an investigation was carried out on a peristaltic micropump, because during the early stages of this thesis work it was thought that actuation using a PZT on a membrane could be used to produce the pipetting device, similar to those used for inkjet printing, as discussed in Section 3.3 on page 41. A piezo electric element was used to produce a diaphragm deflection and a micropump was designed and fabricated, as part of a PCR device, to manipulate a 1 μl droplet through three thermal chambers. The micropump is a peristaltic air pump, which is used to move a droplet of fluid using the pneumatic pressure produced using the pump

diaphragms. To achieve air pumping within the microdevice, an actuation system was designed and built. Subsequently this device used to demonstrate a volume flow rate of 835 $\mu l\ min^{-1}$ at 80 Hz.

Further investigations into the micropump operation included the design and production of a Michelson interferometer, which was used to determine the dynamic deflection of the individual diaphragms of the micropump. The key problem which was solved during the interferometer set up was the detection method. Although the overall actuation frequency of the micropump was up to 80 Hz, the central region of the diaphragms were displaced upwards a distance of 9 μm ($\pm 0.633\ \mu m$) in 3 ms. This equates to the Michelson interferometer output having a 'fringe' frequency of approximately 10 kHz.

The pump and interferometer data were used to determine the overall performance of the micropump. The pumping rate of the device was demonstrated to be 647 $\mu l\ min^{-1}$ above the theoretical pump rate of 188 $\mu l\ min^{-1}$. This is in part due to the diaphragm deflection being nearly two times greater than predicted and that the maximum pump rate was achieved at a much higher frequency of 80 Hz. However if the actual deflection of the micropump is considered (9 μm), the demonstrated pump rate is only 41% of the theoretical pump rate. This investigation was carried out in the early stage of this thesis, although the device enabled precise manipulation of droplets, the high temperatures resulting from the PZT actuation were considered a potential problem for an application using biomolecules.

After reviewing existing fluid displacement techniques, including diaphragm pumps/ injectors, a new device whereby the actuation of paramagnetic beads is used for fluid displacement to produce a pipetting device was proposed. This device would be far simpler and easier to fabricate than a PZT based pipetting system. The proposed technique consists of a plug of paramagnetic beads ($1000's$) within a fluid filled microchannel. This was proposed because there are essentially no moving parts within the device, the beads are bio-compatible and the magnetic field to actuate the beads can be applied externally. By moving the beads along the microchannel, fluid is displaced both in front and behind the bead plug. In this simple form, the technique can be used like a syringe to dispense the volume of fluid contained in the microchannel. Once the microchannel is empty the device can no longer be used to dispense fluid. However this technique can

be used to dispense volumes of fluid which are smaller than the volume of the microchannel, by only moving the bead plug through a fraction of the microchannel. It was considered that unlike other similar techniques which contain magnetic fluids, it should be possible to refill the device by moving the bead plug back to the start position, while the fluid remains stationary in the microchannel. The device could then be used for a fresh injecting stroke.

To confirm that it is possible to displace fluid using a paramagnetic bead plug, proof of concept experiments were carried out. One of the aims of this research is to dispense nanolitre volumes of fluid; so a microchannel was designed and fabricated in silicon and Pyrex that had an internal volume of 81 nl. Bead plugs of up to 48 000 beads were used to displace volumes of fluid using a 10 mm linear translation of a permanent magnet to move the bead plug. The bead plug was formed and translated along the channel using a permanent magnet in contact with the device surface. The velocity of the bead plug was increased up to 2.6 $mm\ s^{-1}$ and volumes of fluid between 8 and 27 nl were displaced. This confirmed that it was possible to displace fluid, with 100% efficiency and that increasing the velocity of the bead plug, caused less fluid to be displaced. It was confirmed that the velocity at which fluid began to slip through the bead plug was possible to predict theoretically. This fluid slip point, occurs when the total magnetic force of the bead plug, which is used to apply pressure to the fluid, is equal to the fluidic pressure in the microchannel for a given velocity. Following the demonstrated use of this bead plug technique to dispense variable volumes of fluid, by altering the velocity of the bead plug, it was proposed that this technique could be used to displace a volume of fluid and then the microchannel can be refilled.

Neither the fluid displacement nor the variable displacement of fluid using paramagnetic beads has been demonstrated before. The fluid dispensing system achieved here is comparable with the magnetically actuated devices produced by Greivell and Hannaford [32] and Ahn et al. [14]; however this technique offers the ability to carry out repeatable dispensing of fluid without the addition of complicated valves and with no risk of contamination, unlike the ferrofluid equivalent. This technique is 100 % efficient, simple and there are no moving parts. If the paramagnetic beads become damaged during operation, the microchannel can be flushed through and a new bead plug can be

loaded into the device.

The aim of this research is to produce an integrated device. To achieve this it was proposed to fabricate a series of electromagnets which, when actuated in a linear sequence, would produce a moving magnetic field. Such an integrated device was designed and fabricated; however, a 'macro' device was also produced to establish the feasibility of the pipetting approach. The macro device consisted of a series of nine hand wound electromagnets. These electromagnets were designed such that a magnetic flux density of 20 mT could be achieved using an actuation current of 500 mA. The overall size of the microcoils was limited, because it was considered necessary to achieve a continuous (or close to continuous) magnetic field and for this reason the electromagnets must be as close together as possible. A plug of 191 000 paramagnetic beads was successfully translated along a glass capillary, using the sequentially actuated electromagnets and used to displace volumes of fluid from 20 to 50 nl, at fluid velocities up to 0.45 $mm\ s^{-1}$.

Based on the previously demonstrated concepts, an integrated microdevice was designed and fabricated. The microdevice consists of two main components which are a microfluidic channel and a series of gold microcoils. These two components are separated by a 12 μm silicon/ silicon dioxide membrane. It was critical to ensure that the microcoils were as close as possible to the fluidic channel containing the paramagnetic beads. This was achieved using an SOI wafer, anodically bonded to a Pyrex wafer. Ultimately thinning of the SOI wafer was used, by removing the silicon handle wafer, leaving only the device layer (40 μm thick) containing the fluidic channel (30 μm deep). The device remained rigid, due to the use of a 1 mm thick anodically bonded Pyrex wafer. The gold microcoils were then electroplated on the silicon dioxide surface (of the SOI wafer), into thick resist moulds ($\approx$ 13 μm thick). The silicon dioxide served as both an electrical isolation layer and as an etch stop during the wafer thinning process. Electroplating was used because it was possible to produce microcoil structures of up to 12 μm thick, allowing a high actuation current to be used, without producing unwanted heating.

Similar devices have been produced by Liakopoulos et al. [172], Lee et al. [160] and Rida et al. [171], where the separation between the electromagnets and the fluidic channel is much greater than 12 μm. Although Choi et al. [161] have produced

a magnetic microdevice, with only a 1 μm separation between the microcoils and the microchannel. However the coils are encapsulated and this makes it difficult to make electrical connections to the coils and to cool the coils. The fabrication technique researched here, was used to successfully produce a microdevice, where the microcoils and the fluidic channel were separated by only 12 μm, thus allowing for the magnetic field close to the electromagnets to be utilised. Such a fabrication process has not been used for this type of device before.

The predicted magnetic flux density for the microcoil design was 14 mT, with a value of ∇B^2 of 5.5 $T^2\ m^{-1}$, for an actuation current of 1 A at the surface of the microchannel. The integrated microdevice was attached to alumina headers and wire bonded, to make electrical connections to the microcoils. However, due to the size and complexity of the completed devices, it was not possible to directly measure the magnetic flux density using conventional techniques, such as a Hall probe. Therefore two experiments were carried out to determine whether or not the predicted magnetic flux density could be achieved by the actuation of the microcoils. Single paramagnetic beads were observed to be moved a distance of 40 μm, between two adjacent microcoils, and paramagnetic beads were trapped from within fluid flow with velocities of up to 9 $mm\ s^{-1}$. The movement and the trapping of paramagnetic beads were used to indirectly determine the magnetic field from the actuated coils. These experiments confirmed that the theoretical magnetic flux density (and ∇B^2) of the integrated microdevices was in good agreement with the estimated magnetic flux density, obtained from the measured velocity and travel time of individual beads.

Numerous attempts were made using the actuation of the microcoils in the microdevice, to produce a paramagnetic bead plug to displace fluid. However, this was not possible because debris, which is present on the surface of the microchannels, resulted in the paramagnetic beads adhering to the silicon surface. Additionally, it was not possible to move beads from one coil to the next, because the magnetic field of one actuated microcoil was not sufficient to move all of the beads from the neighbouring microcoil.

The planar microcoils produced here, consisted of a single layer of electrodeposited gold, which was achieved using a 13 μm thick resist layer. Single beads were transported between two neighbouring microcoils, with velocities up to 115 $\mu m\ s^{-1}$ for an actuation

current of 1 A. By separating the beads from the fluid it was possible to determine a magnetic force of 160 pN for a single bead, at the surface of the microchannel, using an actuation current of $1A$. This demonstrates that beads can be transported using the sequential actuation of single current loop microcoils, like the ones fabricated here (100 μm diameter, with 10 μm spacing). A similar bead transport device, produced by Rida et al. [171], consists of overlapped multi-turn coils, with the addition of external permanent magnets, which is a far more complicated structure than the microcoils fabricated for this thesis work.

Here it has been demonstrated that a magnetic pipetting device can be produced using the actuation of a paramagnetic bead plug. This was achieved both through the use of permanent magnets and a series of electromagnets. An integrated microdevice was fabricated to achieve a similar result. The integrated microdevice was used to confirm that the relatively simplistic single current loop microcoil can be used to separate paramagnetic beads from fluid and to transport beads between neighbouring microcoils.

8.2 Future work

Testing of the electromagnetic microdevice that was fabricated during this thesis work was problematic because of debris on the surface of the microchannels. To be able to determine the exact composition of the debris or to determine if surface of the channel has been modified, the channels could be cleaved and investigated. If the debris on the surface of the channel can be identified, it might then be possible to remove it or to deposit a film in the channel that will provide a surface that the paramagnetic beads will not adhere to. If this fabrication process was repeated, a coating should be deposited on the channel surface during fabrication to prevent this problem from occurring.

It was not possible to directly measure the magnetic flux density that could be achieved by the actuation of the microcoils, due to the size and complexity of the structure. However, it might be possible to use a different strategy to measure the magnetic field than those used during this work. Ideally an access hole could be made in the Pyrex wafer, through to the microchannel. Unfortunately to make a large enough hole to gain access to the microchannel (with a Hall probe for example) would be very

difficult because of the rigid Pyrex wafer. Any weakening of this Pyrex wafer could cause the silicon membrane to collapse. However it might be possible to measure the magnetic field at the back of the microcoils, on the surface of the silicon. The device does not have to be attached to alumina headers, as it was during this work. Instead a suitable bond could be made to a single microcoil, with a single wire, which would still allow access to the microcoil to measure the magnetic field, using a Hall probe. The Hall probe used for this work is contained within a DIL package; however other Hall probes are available which are much smaller and are not contained within a DIL package. Prior to using the electromagnetic device investigated here, it is essential that the magnetic flux density is directly measured, such the limitations of the device for pipetting can be determined.

It has been shown in Chapter 5 of this thesis that the actuation of electromagnets on either side of the microchannel can be used to move a paramagnetic bead plug to displace fluid. Although the design considered here only has microcoils on one side of the microchannel, it would be possible to copy this earlier system of electromagnets and fabricate microcoils both above and below the fluidic microchannel containing the paramagnetic beads. This could be achieved by fabricating the first set of microcoils in etched trenches in the Pyrex wafer, similar to those produced by Velten et al. [177], as discussed in Section 4.5. These microcoils would then be within microns of the fluidic channel. A second set of microcoils could be produced, similar those fabricated here on the opposite side of the channel. The draw back of this approach is the first set of coils will be encapsulated in the Pyrex wafer, making electrical connection and cooling more complicated.

In contrast to the design and fabrication of planar coils, the ideal design would be a series of single current loops, which are wrapped around the microchannel. Such free standing structures have been produce by Yoon et al. [178], for RF inductors and therefore no information is given about the magnetic field which could be achieved with these structures. However if the dimensions of these current loops were kept similar to the microcoil dimensions investigated here, it will be possible to achieve a similar magnetic flux density of 14 mT. The advantage of positioning the coils in such a way is that the magnetic field in the centre of the loop will be utilised, which could be as

high as 20 mT (35 μm radius, with 1 A actuation current). There would also be no insulation layer between the channel and the planar surface of the coil and therefore the microcoils could be spaced up to 20 or 30 μm apart. Finally although there is a magnetic gradient across the surface of the planar coils, as demonstrated in this work, the magnetic gradient perpendicular to the coil surface will be higher and therefore a higher magnetic force could be exerted on the paramagnet beads in the microchannel. This type of fabrication would be very difficult, because it would require multiple wafers and multiple layers of electroplating.

Although it has been shown that a paramagnetic bead plug can be used to dispense fluid within a microchannel, it will not be possible to refill the device, without drawing some fluid back into the pipetting chamber. This is because, although the majority of the fluid will not be moved as the bead plug is returned to the starting position (through the fluid), some of the dispensed fluid will be drawn back into the pipette channel. A valve structure must be included within the microchannel, in order to produce a better refilling device. Ideally this should not be an active valve, because this would complicate the fabrication. The obvious choice would be to use a second bead plug at the exit of the pipette device which is simply moved into place, to stop fluid being drawn back into the pipette, as the bead plug is returned to the starting position.

The paramagnetic beads selected for this work are biocompatible, so the simple technique investigated here can be used for a number of applications, where biomaterials are handled. Mixing devices have already been produced by Suzuki et al. [81], where paramagnetic beads are actuated using integrated electromagnets to effect mixing. This mixing technique, using paramagnetic beads, could be combined with the dispensing/pumping technique investigated here to form a complete fluidic system. Moreover an entire lab-on-a-chip system could be produced, which contained many electromagnets with which a number of bead 'devices' could be controlled and a complete magnetic fluidic system can be realised.

Appendix A

FEMLAB simulation models

A.1 Magnetostatic

For the magnetic analysis FEMLAB was used to solve Equation A.1. The symbols are summarised in Table A.1.

$$\nabla \times (\mu_0^{-1} \nabla \times \mathbf{A} - \mathbf{M}) - \sigma \mathbf{v} \times (\nabla \times A) = \mathbf{J}^e \tag{A.1}$$

Variable	Units	Description
μ_0	$N\ A^{-2}$	Permeability of a vacuum
$\mathbf{A}$	$W\ m^{-1}$	Magnetic vector potential
$\mathbf{M}$	$A\ m^2\ Kg^{-1}$	Magnetization
$\mathbf{J}^e$	$A\ m^{-2}$	Externally generated current density

Table A.1: Magnetostatic model terms, units and description.

The boundary condition used during the solution is shown in Equations A.2.

$$\mathbf{A} = 0 \tag{A.2}$$

A.2 Conductive heat transfer

For the Conductive heat transfer analysis FEMLAB was used to solve Equation A.3. The symbols are summarised in Table A.2.

$$Q = \rho C \frac{\delta T}{\delta t} - \nabla.(k \nabla T) \tag{A.3}$$

Variable	Units	Description
C	$J\ kg^{-1}\ K^{-1}$	Heat capacity
C_{const}	$W\ m^{2}$	Radiative heating constant
h	$W\ m^{-2}\ K^{-1}$	Heat transfer coefficient
k	$W\ m^{-1}\ K^{-1}$	Thermal conductivity
T_{inf}	K	Temperature of surrounding environment
T	K	Temperature dependant variable
Q	$W\ m^{-3}$	Heat source
q_0	$W\ m^{-2}$	Inward heat flux
ρ	$kg\ m^{-3}$	Density

Table A.2: Conductive heat transfer model terms, units and description.

The boundary conditions used with this model are shown in Equations A.4 and A.5.

$$n.(k \nabla T) = q_0 + h(T_{inf} - T) \tag{A.4}$$

$$n.(k \nabla T) = 0 \tag{A.5}$$

Appendix B

LMS process listing

B.1 Test channel fabrication

ID	Description
K2860	BH Etch channels in silicon wafers and bond to Pyrex
P-EM	E-BEAM Mask/Reticle writing
G-S12	Title page: 10 wafers, Material 3x Silicon 3xPyrex
W-C2	Fuming Nitric acid clean, 2nd pot only
F7-0	Furnace 7: Load in N2, horizontally, 400 $^{\circ}C$ for 1 hour PYREX ONLY
S-SX	Saw fluidic channels into PYREX ONLY, 500 μm deep and wide
P-G2	Photolith mask KB68M-PLY, Dark Field: 2.2 μm resist SILICON ONLY
P-RHBD	Hard bake for DRIE etch SILICON ONLY
DS-S0X	ASE Deep Silicon Etch less then 200 μm (no baking wafer required) 30 μm deep etch SILICON ONLY
P-RSGX	Resist strip SILICON ONLY
W-C3X	Fuming nitric acid clean SILICON ONLY
S-AB	Anodic bonding. Bond patterned silicon wafers to Pyrex wafers
S-SX	Saw wafers into chips along scribe lanes

B.2 Microcoil fabrication with straight channel

ID	Description
K2773	BH Etch channels in Pyrex, bond to SOI wafers and produce microcoils
P-EM	E-BEAM Mask/Reticle writing
G-S12	Title page: 10 wafers, Material 5xSOI and 5xPyrex
W-C2	Fuming Nitric acid clean, 2nd pot only
F7-0	Furnace 7: Load in N2, horizontally, 400 $^{\circ}C$ for 1 hour PYREX ONLY
MS-0	Evaporate 30 nm of Cr and 300 nm of gold on both sides for masking PYREX ONLY
P-G2	Photolith mask KB51-L1, Dark Field: nom. 2.2 μm resist, to produce fluidic channels on FRONT, spin 2.2 μm resist on BACK PYREX ONLY
P-RHBX	Hard bake for wet etch 140 $^{\circ}C$ 1 hour
WM-0	Remove Au and Cr (wet etch) to pattern metal mask PYREX ONLY
WH-E1X	Wet etch oxide: 2:1 HF, 10 minutes for 20 μm deep channel PYREX ONLY
S-SX	Saw wafers along end of etched channels, 250 μm wide and 250 μm deep PYREX ONLY
P-RSGX	Resist strip PYREX ONLY
WM-0	Remove Au and Cr (wet etch) PYREX ONLY
S-AB	Anodic bonding. Bond SOI wafers to Pyrex wafers using alignment marks Bonding SOI device layer to patterned Pyrex face
P-G0X	Photolithmask KB51-L2, dark field:SPR220 10 μm thick to define regions at edge of wafer
P-RHBD	Hard bake for DRIE etch
DS-S0X	ASE Deep Silicon Etch more then 200 μm (no baking wafer required) 500 μm deep etch to remove 8 regions at the edge of the wafer for clamps
P-RSGX	Resist strip
DS-S0X	ASE Deep Silicon Etch more then 200 μm (no baking wafer required) 500 μm deep etch to remove remaining handle wafer

ME-0X	Evaporate 30 nm Cr and 150 nm Gold on silicon side
P-G0X	Photolithmask KB51-L3, light field:S1818 2.2 μm thick
P-RHBX	Hard bake 140 $^{\circ}C$ for wet etch
WM-0	Remove exposed Au and Cr to produce seed layer (wet etch)
P-RSGX	Resist strip
W-C3X	Fuming nitric acid clean
P-G0X	Photolithmask KB51-L4, dark field:SPR220 5 μm thick
G-3	Gold plating 50 $A\ m^{-1}$ with ECF64D

B.3 Microcoil fabrication with pipette channel

B.3.1 Pyrex wafer

ID	Description
K4040	BH Pattern Pyrex wafers then saw connection channels
P-EM	E-BEAM Mask/Reticle writing
G-S12	Title page: 10 wafers, Material 10xPyrex
W-C2	Fuming Nitric acid clean, 2nd pot only
F7-0	Furnace 7: Load in N2, horizontally, 400 $^{\circ}C$ for 1 hour
P-G2	Photolith mask KB98-SAW, Dark Field: nom. 2.2 μm resist, to produce alignment marks and saw lines for fluidic connections
P-RHBX	Hard bake for wet etch 140 $^{\circ}C$ 1 hour
WH-E1X	Wet etch oxide: 7:1 BHF, 30 minutes for 1 μm deep, alignment marks
S-SX	Saw wafers along etched lines, 250 μm wide and 250 μm deep
P-RSGX	Resist strip
W-C3X	Fuming nitric acid clean
G-3	Transfer to K4046 for anodic bonding

B.3.2 SOI wafer

ID	Description
K4046	BH DRIE channels bond to Pyrex, remove handle wafer and produce coils
P-EM	E-BEAM Mask/Reticle writing
G-S12	Title page:20 wafers, Material 10xSOI ICEMOS, 10xPyrex K4040
W-C2	Fuming Nitric acid clean, 2nd pot only **10x SOI wafers**
P-G2	Photolith mask KB98-DRY, Dark Field: nom. 2.2 μm resist, to produce alignment marks and pipette channels
P-RHBD	Hard bake for DRIE etch
DS-S0X	ASE Deep Silicon Etch less then 200 μm (no baking wafer required) 30 μm deep etch
G-3	Add Pyrex wafers from K4040 Batch
S-AB	Anodic bonding. Bond SOI wafers to Pyrex wafers using alignment marks Bonding SOI device layer to Sawn Pyrex face
WH-D1X	Dip etch silicon dioxide in 7:1BHF 25 $°C$ to strip all oxide to
MS-0	Sputter of 30nm of Cr on Pyrex side for electrostatic clamping
DS-S0X	ASE Deep Silicon Etch more then 200 μm (no baking wafer required) 350 μm deep etch to Silicon dioxide to remove handle wafer
WM-0	Remove Cr (wet etch)
W-C3X	Fuming nitric acid clean
ME-0X	Veeco sputter 30nm Titanium and 500nm Gold on silicon side
P-G0X	Photolithmask KB98-CLL, light field: nom. 2.2 μm thick
P-RHBX	Hard bake 140 $°C$ for ion beam mill
B-0	Ion beam mill: Remove all exposed Ti/Au to SiO2. Check back pressure
P-RSGX	Resist strip
W-C3X	Fuming nitric acid clean
P-G0X	Photolithmask KB98-CLD, dark field: AZ4562 $>$ 10 μm thick
S-SX	Saw wafers into chips along scribe lanes
G-3	Gold plating 1 mA for 1600 s with ECF64D

Appendix C

Publications

1. B. Husband, M. Bu, V. Aspostoloupoulos, T. Melvin and A. G. R. Evans. Investigation for the operation of an integrated peristaltic micropump. *In Proceedings of 14th MicroMechanics Europe Workshop, MME, Delft, The Netherlands*, pp. 115-118 2003.

2. M. Bu, B. Husband, T. Melvin, G. J. Ensell, N. P. Pham, P. M. Sarro, J. S. Wilkinson and , J. S. and A. G. R. Evans. Fabrication of a microfluidic chip for PCR applications. *In Proceedings of 14th MicroMechanics Europe Workshop, MME, Delft, The Netherlands*, pp. 119-122 2003.

3. B. Husband, M. Bu, A. G. R. Evans and T. Melvin. Investigation for the operation of an integrated peristaltic micropump, *Journal of Micromechanics and Microengineering* 14(9) pp. S64-S69 2004.

4. B. Husband, M. Bu, V. Aspostoloupoulos, A. G. R. Evans and T. Melvin. Novel actuation of an integrated peristaltic micropump. *Microelectronic Engineering* 73-74 pp. 858-863 2004.

5. B. Husband, T. Melvin and A. G. R. Evans. Fluidic Control Using Superamagnetic Beads. *In Proceedings of 15th Micromechanics Europe Workshop, MME, Leuven, Belgium*, pp. 179-183 2004.

6. B. Husband, A. G. R. Evans and T. Melvin. A Superparamagnetic bead driven fluidic device, *Submitted to Microtechnologies for the New Millennium 2005, Seville, Spain.*

7. B. Husband, A. G. R. Evans and T. Melvin. Fluid Dispensing using Superparamagnetic Beads. *In Proceedings of 16th MicroMechanics Europe Workshop, MME, Gothenburg, Sweden*, pp. 338-341 2005.

References

[1] P. Gravesen, J. Branebjerg, and O. S. Jensen. Microfluidics-a review. *Journal of Micromechanics and Microengineering*, 3(4):168–182, 1993.

[2] N.-T. Ngyuyen, X. Huang, and T. K. Chuan. MEMS - micropumps : a review. *Transactions of the ASME*, 124:384–392, 2002.

[3] D. J. Laser and J. G. Santiago. A review of micropumps. *Journal of Micromechanics and Microengineering*, 14(4):R35–R64, 2004.

[4] T. Chovan and A. Guttman. Microfabricated devices in biotechnology and biochemical processing. *Trends in Biotechnology*, 20(3):116–121, 2002.

[5] M. J. Felton. Lab on a chip: poised on the brink. *Analytical Chemistry*, 75(23): 505A–508A, 2003.

[6] R. H. Liu, J. Yang, R. Lenigk, J. Bonanno, and P. Grodzinski. Self-contained, fully integrated biochip for sample preparation, polymerase chain reaction amplification, and DNA microarray detection. *Analytical Chemistry*, 76(7):1824 - 1831, 2004.

[7] J. Voldman, M. L. Gray, and M. A. Schmidt. An integrated liquid mixer / valve. *Journal of Microelectromechanical Systems*, 9(3):295–302, 2000.

[8] J.-H. Tsai and L. Lin. Active microfluidic mixer and gas bubble filter driven by thermal bubble micropump. *Sensors and Actuators*, A97-98:665–671, 2002.

[9] P. Woias. Micropumpspast, progress and future prospects. *Sensors and Actuators*, B105(1):28–38, 2005.

[10] H. Andersson, W. van der Wijngaart, P. Griss, F. Niklaus, and G. Stemme. Hydrophobic valves of plasma deposited octafluorocyclobutane in DRIE channels. *Sensors and Actuators*, 1-2(B75):136–141, 2001.

[11] R. H. Liu, J. Bonanno, J. Yang, R. Lenigk, and P. Grodzinski. Single-use, thermally actuated paraffin valves for microfluidic applications. *Sensors and Actuators*, B98(2-3):328–336, 2004.

[12] A. Luque, J. M. Quero, C. Hibert, P. Flckiger, and A. M. Gan-Calvo. Integrable silicon microfluidic valve with pneumatic actuation. *Sensors and Actuators*, A118 (1):144–151, 2005.

[13] I. Papautsky, J. Brazzle, H. Swerdlow, R. Weiss, and A. B. Frazier. Micromachined pipette arrays. *Transactions on Biomedical Engineering*, 47(6):812–819, 2000.

[14] J.J. Ahn, J. Oh, and B. Choi. A study on the novel type of ferrofluid magnetic pipette. *Nanotech 2003*, 1:226–229, 2003.

[15] R. A. Askeland, W. D. Childers, and W. R. Sperry. The second-generation thermal inkjet structure - effects of materials and processes changes. *Hewlett-Packard Journal*, August:27–31, 1988.

[16] J. S. Aden, J. H. Bohorquez, D. M. Collins, M. D. Crook, A. Garcia, and U. E. Hess. The third-generation HP thermal inkjet printhead - design of HP DeskJet 1200C and HP DeskJet 1200C/PS printers. *Hewlett-Packard Journal*, February, 1994.

[17] C. P. Steinert, I. Goutier, O. Gutmann, H. Sandmaier, M. Daub, B. de Heij, and R. Zengerle. A highly parallel picoliter dispenser with an integrated, novel capillary channel structure. *Sensors and Actuators*, A116(1):171–177, 2004.

[18] A. Kuoni, M. Boillat, and N. F. de Rooij. A highly parallel piezoelectric printing device for micro-array technology. *presented at the 17th IEEE International Conference on Micro Electro Mechanical Systems 2004 (MEMS), Neuchatel, Switzerland.*, pages 466–469, 2004.

[19] P. Calvert. Inkjet printing for materials and devices. *Chemistry of Materials*, 13 (10):3299 - 3305, 2001.

[20] T. Xu, J. Jin, C. Gregory, J. J. Hickman, and T. Boland. Inkjet printing of viable mammalian cells. *Biomaterials*, 26(1):93–99, 2005.

[21] E. A. Roth, T. Xu, M. Das, C. Gregory, J. J. Hickman, and T. Boland. Inkjet printing for high-throughput cell patterning. *Biomaterials*, 25(17):3707–3715, 2004.

[22] W. C. Wilson(Jr.) and T. Boland. Cell and organ printing 1: protein and cell printers. *The Anatomical Record Part A: Discoveries in Molecular, Cellular, and Evolutionary Biology*, 272(2):491–496, 2003.

[23] L. Pardo, W. C. Wilson(Jr.), and T. Boland. Characterization of patterned self-assembled monolayers and protein arrays generated by the ink-jet method. *Langmuir*, 19(5):1462–1466, 2003.

[24] S. H. Wong, M. C. L. Ward, and C. W. Wharton. Micro T-mixer as a rapid mixing micromixer. *Sensors and Actuators*, B100(3):359–379, 2004.

[25] T. Nisisako, T. Torii, and T. Higuchi. Droplet formation in a microchannel network. *Lab Chip*, 2(1):24–26, 2002.

[26] P. Garstecki, M. J. Fuerstman, H. A. Stone, and G. M. Whitesides. Formation of droplets and bubbles in a microfluidic T-junctionscaling and mechanism of break-up. *Lab on a Chip*, 6(3):437–446, 2006.

[27] Y.-C. Tan, V. Cristini, and A. P. Lee. Monodispersed microfluidic droplet generation by shear focusing microfluidic device. *Sensors and Actuators*, B114(1): 350–356, 2006.

[28] M. Bu, T. Melvin, G. Ensell, J. S. Wilkinson, and A. G. R. Evans. Design and theoretical evaluation of a novel microfluidic device to be used for PCR. *Journal of Micromechanics and Microengineering*, 13(4):S125–S130, 2003.

[29] M. Bu, B. Husband, T. Melvin, G. J. Ensell, N. P. Pham, P. M. Sarro, J. S. Wilkinson, and A. G. R. Evans. Fabrication of a microfluidic chip for PCR applications. *presented at the 14th MicroMechanics Europe Workshop 2003, Delft, The Netherlands*, pages 119–122, 2003.

[30] S.-H. Lee, C.-S. Lee, B.-G. Kim, and Y.-K. Kim. Qantitatively controlled nanoliter liquid manipulation using hydrophobic valving and control of surface wettability. *Journal of Micromechanics and Microengineering*, 13(1):89–97, 2003.

[31] S.-H. Lee, S. I. Cho, C.-S. Lee, B.-G. Kim, and Y.-K. Kim. Microfluidic chip for biochemical reaction and electrophoretic separation by quantitative volume control. *Sensors and Actuators*, B110(1):164–173, 2005.

[32] N. E. Greivell and B. Hannaford. The design of a ferrofluid magnetic pipette. *Transactions on Biomedical Engineering*, 44(1):129–135, 1997.

[33] M. A. M. Gijis. Magnetic bead handling on-chip: new oppurtunities for analytical applications. *Microfluidics and Nanofluidics*, 1(1):22–40, 2004.

[34] M. Slovakova, N. Minc, Z. Bilkova, C. Smadja, W. Faigle, C. Ftterer, M. Taverna, and J.-L. Viovy. Use of self assembled magnetic beads for on-chip protein digestion. *Lab on a Chip*, 5(9):935–942, 2005.

[35] Q. Ramadan, V. Samper, D. P. Poenar, and C. Yu. An integrated microfluidic platform for magnetic microbeads separation and confinement. *Biosensors and Bioelectronics*, 21(9):1693–1702, 2006.

[36] E. Verpoorte and N. F. De Rooij. Microfluidics meets MEMS. *Proceedings of the IEEE*, 91(6):930–953, 2003.

[37] M. Bu. *Design and fabrication of a microfluidic device for polymerase chain reaction application.* Phd thesis, Universty of Southampton, Electronics and Computer Science, 2004.

[38] M. U. Kopp, H. J. Crabtree, and A. Manz. Developements in technology and applications of microsystems. *Current Opinion in Chemical Biology*, 1(3):410–419, 1997.

[39] Z. Zhang and A. Grishini. Characterization of piezoelectric shear mode inkjet actuator. *Integrated Ferroelectrics*, 69:401–415, 2005.

[40] S. S. Baek, H. T. Lim, H. Song, Y. S. Kim, K. D. Bae, C. H. Cho, C. S. Lee, J. W. Shin, S. J. Shin, K. Kuk, and Y. S. Oh. T-jet: a novel thermal inkjet printhead with monolithically fabricated nozzle plate on soi wafer. *presented at*

the 12th International Conference on Transducers, Solid-State Sensors, Actuators and Microsystems, 2003, Boston, pages 472–475, 2003.

[41] Y. Feng, Z. Zhou, X. Ye, and J. Xiong. Passive valves based on hydrophobic microfluidics. *Sensors and Actuators*, A108(1-3):138–143, 2003.

[42] K. Hoshino, S. Triteyaprasert, k. Matsumoto, and I. Shimoyama. Electrowetting-based pico-liter liquid actuation in a glass-tube microinjector. *Sensors and Actuators*, A114(2-3):473–477, 2004.

[43] M. U. Kopp, A. J. de Mello, and A. Manz. Chemical amplification : continuous-flow PCR on a chip. *Science*, 280(5366):1046–1048, 1998.

[44] I. Schneegass, R. Brautigam, and J. M. Kohler. Minitatirized flow-through PCR with different template types in a silicon chip thermocycler. *Lab on a Chip*, 1(1): 42–49, 2001.

[45] A. I. K. Lao, T. M. H. Lee, I.-M. Hsing, and N. Y. Ip. Precise temperature control of microfluidic chamber for gas and liquid phase reactions. *Sensors and Actuators*, 84(1-2):11–17, 2000.

[46] E. T. Lagally, C. A. Emrich, and R. A. Mathies. Fully integrated PCR-capillary electrophoresis microsystem for DNA analysis. *Lab on a Chip*, 1(2):102–107, 2001.

[47] A. Olsson, P. Enoksson, G. Stemme, and E. Stemme. Micromachined flat-walled valveless diffuser pumps. *Journal of Microelectromechanical Systems*, 6(2):161–166, 1997.

[48] M. Koch, A. G. R. Evans, and A. Brunnschweiler. The dynamic micropump driven with a screen printed PZT actuator. *Journal of Micromechanics and Microengineering*, 8(2):119–122, 1998.

[49] D. Maillefer, S. Gamper, B. Frehner, P. Balmer, H. van Lintel, and P. Renaud. A high-performance silicon micropump for disposable drug delivery systems. *presented at the 14th IEEE International Conference on Micro Electro Mechanical Systems 2001*, pages 413–417, 2001.

[50] N.-T. Nguyen and X. Huang. Miniature valveless pumps based on printed circuit board technique. *Sensors and Actuators*, A88(2):104–111, 2001.

[51] C. G. J. Schabmueller, M. Koch, M. E. Mokhhtari, A. G. R. Evans, A. Brunnschweiler, and H. Sehr. Self-aligning gas / liquid micropump. *Journal of Micromechanics and Micorengineering*, 12(4):420–424, 2002.

[52] A. Hatch, A. E. Kamholz, G. Holman, P. Yager, and K. F. Bohringer. A ferrofluidic magnetic micropump. *Journal of Microelectromechanical Systems*, 10(2):215–221, 2001.

[53] H. Hartshorne, C. J. Backhouse, and W. E. Lee. Ferrofluid-based microchip pump and valve. *Sensors and Actuators*, B99(2-3):592–600, 2004.

[54] C. Yamahata, M. Chastellain anad V. K. Parashar, A. Petri, H. Hofmann, and M. A. M. Gijs. Plastic micropump with ferrofluidic actuation. *Journal of Microelectromechanical Systems*, 14(1):96–102, 2005.

[55] C. Grosjean and Y.-C. Tai. A thermopneumatic peristaltic micropump. *Technical Digest of Transducers*, 1999.

[56] A. Wego and L. Pagel. A self-filling micropump based on PCB technology. *Sensors and Actuators*, A88(3):220–226, 2001.

[57] J.-H. Kim, K.-H. Na, C. J. Kang, and Y.-S. Kim. A disposable thermopneumatic-actuated micropump stacked with PDMS layers and ITO-coated glass. *Sensors and Actuators*, A120(2):365–369, 2005.

[58] C. G. Cooney and B. C. Towe. A thermopneumatic dispensing micropump. *Sensors and Actuators*, A116(3):519–524, 2004.

[59] W. H. Song and J. Lichtenberg. Thermo-pneumatic, single-stroke micropump. *Journal of Micromechanics and Microengineering*, 15(8):1425–1432, 2005.

[60] Z. Yin and A. Prosperetti. A microfluidic 'blinking bubble' pump. *Journal of Micromechanics and Microengineering*, 15(3):643–651, 2005.

[61] Z. Yin and A. Prosperetti. 'blinking bubble' micropump with microfabricated heaters. *Journal of Micromechanics and Microengineering*, 15(9):1683–1691, 2005.

[62] S. Santra, P. Holloway, and C. D. Batich. Fabrication and testing of a magnetically actuated micropump. *Sensors and Actuators*, B87(2):358–364, 2002.

[63] J. M. Berg, R. Anderson, M. Anaya, B. Lahlouh, M. Holtz, and T. Dallas. A two-stage discrete peristaltic micropump. *Sensors and Actuators*, A104(1):6–10, 2003.

[64] S. Zeng, C.-H. Chen, J. C. Mikkelsen, and J. G. Santiago. Fabrication and characterization of electroosmotic micropumps. *Sensors and Actuators*, B79(2-3).

[65] P. Selvaganapathy, Y.-S. L. Ki, P. Renaud, and C. H. Mastrangelo. Bubble-free electrokinetic pumping. *Journal of Microelectromechanical Systems*, 11(5):448–453, 2002.

[66] T. T. Veenstra, J. W. Berenschot, J. G. E. Gardeniers, R. G. P. Sanders, M. C. Elwenspoek, and A. van den Berg. Use of selective anodic bonding to create micropump chambers with virtually no dead volume. *Journal of The Electrochemical Society*, 148(2):G68–G72, 2001.

[67] R. Zengerle, J. Ulrich, S. Kluge, M. Richter, and A. Richter. A bidirectional silicon micropump. *Sensors and Actuators*, A50(1-2):81–86, 1995.

[68] M. Koch, N. Harris, A. G. R. Evans, N. M. White, and A. Brunnschweiler. A novel micromachined pump based on thick-film peizoelectric actuation. *Sensors and Actuators*, A70(1-2):98–103, 1998.

[69] E. Meng, X.-Q. Wang, H. Mak, and Y.-C. Tai. A check-valved silicone diaphragm pump. *presented at the Thirteenth Annual International Conference on Micro Electro Mechanical Systems, MEMS 2000*, pages 62–67, 2000.

[70] J. A. Folta, N. F. Raley, and E. W. Hee. Design, fabrication and testing of a miniature peristaltic membrane pump. *presented at Solid-State Sensor and Actuator Workshop 5th Technical Digest, IEEE*, pages 186–189, 1992.

[71] M. Koch, A. Evans, and A. Brunschweiler. *Microfluidic technology and applications.* Baldock: Research Study Press Ltd, 2000.

[72] B. Husband, A. G. R. Evans M. Bu, and T. Melvin. Investigation for the operation of an integrated peristaltic micropump. *Journal of Micromechanics and Microengineering*, 14:S64–S69, 9.

[73] B. Husband, M. Bu, V. Apostolopoulus, T. Melvin, and A.G.R. Evans. Novel actuation of an integrated peristaltic micropump. *Microelectronic Engineering*, 73-74:858–863, 2004.

[74] E. Hecht. *Optics.* Addison-Welsey Publishing Company, 1987.

[75] T. S. J. Lammerink, M. Elwenspoek, and J. H. J. Fluitman. Integrated microliquid DOSING system. *IEEE Proceedings of Micro Electro Mechanical Systems, MEMS '93*, pages 254–259, 1993.

[76] T. Thorsen, S. J. Maerkl, and S. R. Quake. Microfluidic large-scale integration. *Science*, 298:580–584, 2002.

[77] M. J. Heller. Dna microarray technology : devices, systems and applications. *Annual Review Biomedical Engineering*, 4:129–153, 2002.

[78] P. Mitchell. Microfluidics - downsizing large-scale biology. *Nature Biotechnology*, 19(8):717–721, 2001.

[79] T. J. Johnson, D. Ross, and L. E. Locascio. Rapid microfluidic mixing. *Analytical Chemistry*, 74(1):45–51, 2002.

[80] L.-H. Lu, K. S. Ryu, and C. Liu. A magnetic microstirrer and array for microfluidic mixing. *Journal of Microelectromechanical Systems*, 11(5):462–469, 2002.

[81] H. Suzuki, C.-M. Ho, and N. Kasagi. A chaotic mixer for magnetic bead-based micro cell sorter. *Journal of Microelectromechanical Systems*, 13(5):779–790, 2004.

[82] J. M. Khler and T. Kirner. Nanoliter segment formation in micro fluid devices for chemical and biological micro serial flow processes in dependence on flow rate and viscosity. *Sensors and Actuators*, A119(1):19–27, 2005.

[83] M. Joanicot and A. Ajdari. Droplet control for microfluidics. *Science*, 309(5736): 887–888, 2005.

[84] D. J. Beebe, G. A. Mensing, and G. M. Walker. Physics and applications of microfluidics in biology. *Annual Review of Biomedical Engineering*, 4:261–286, 2002.

[85] F. M. White. *Viscous fluid flow.* McGraw-Hill, 1994.

[86] B. S. Massey. *Mechanics of Fluids.* Van Nostrand Reinhold (UK) Co. Ltd., 1983.

[87] D. Gobby, P. Angeli, and A. Gavriilidis. Mixing characteristics of T-type microfluidic mixers. *Journal of Micromechanics and Microengineering*, 11(2):126–132, 2001.

[88] G. P. Hatch and R. E. Stelter. Magnetic design considerations for devices and particles used for biological high-gradient magnetic separation (hgms) systems. *Journal of Magnetism and Magnetic Materials*, 225(1-2):262–276, 2001.

[89] C. D. Costin and R. E. Synovec. Microscale-molecular weight sensor: probing molecular diffusion between adjacent laminar flows by refractive index gradient detection. *Analytical Chemistry*, 74(17):4558–4565, 2002.

[90] A. Hatch, E. Garcia, and P. Yager. Diffusion-based analysis of molecular interactions in microfluidic devices. *Proceedings of the IEEE*, 92(1):126–139, 2004.

[91] P. G. Wapner and W. P. Hoffman. Utilization of surface tension and wettability in the design and operation of microsensors. *Sensors and Actuators*, B71(1-2): 60–67, 2000.

[92] P. F. Man, C. H. Mastrangelo, M. A. Burns, and D. T. Burke. Microfabricated capillarity-driven stop valve and sample injector. *presented at The Eleventh Annual International Workshop on Micro Electro Mechanical Systems, MEMS 98, Delft, The Netherlands*, pages 45–50, 1998.

[93] A. D. Stroock, S. K. Dertinger, G. M. Whitesides, and A. Ajdari. Patterning flows using grooved surfaces. *Analytical Chemistry*, 74(20):5306–5312, 2002.

[94] B. Zhao, J. S. Moore, and D. J. Beebe. Surface-directed liquid flow inside micro channels. *Science*, 291:1023–1026, 2001.

[95] J.-D. Lee, H.-D. Lee, H.-J. Lee, J.-B. Yoon, K.-H. Han, J.-K. Kim, C.-K. Kim, and C.-H. Han. A monolithic thermal inkjet printhead utilizing electrochemical etching and two-step electroplating techniques. *presented at The International Electron Devices Meeting, 1995*, pages 601–604, 1995.

[96] P. Krause, E. Obermeier, and W. Wehl. A micromachined single-chip inkjet printhead. *Sensors and Actuators*, A53(1-3):405–409, 1996.

[97] J.-D. Lee, J.-B. Yoon, J.-K. Kim, H.-J. Chung, C.-S. Lee, H.-D. Lee, H.-J. Lee, C.-K. Kim, and C.-H. Han. A thermal inkjet printhead with a monolithically fabricated nozzle plate and self-aligned ink feed hole. *Journal of Microelectromechanical Systems*, 8(3):229–236, 1999.

[98] S. S. Baek, H.-T. Lim, H. Song, Y.-S. Kim, K.-D. Bae, C.-H. Cho, C.-S. Lee, J.-W. Shin, S.-J. Shin, K. Kuk, and Y.-S. Oh. A novel back-shooting inkjet printhead using trench-filling and soi wafer. *Sensors and Actuators*, A114(2-3):392–397, 2004.

[99] S. J. Shin, K. Kuk, J. W. Shin, C. S. Lee, Y. S. Oh, and S. O. Park. Thermal design modifications to improve firing frequency of back shooting inkjet printhead. *Sensors and Actuators*, A114(2-3):387–391, 2004.

[100] A. V. Lemmo, D. J. Rose, and T. C. Tisone. Inkjet dispensing technology : applications in drug discovery. *Current Opinion in Biotechnology*, 9(6):615–617, 1998.

[101] X. B. Chen and J. Kai. Modeling of positive displacement fluid dispensing processes. *Transactions on Electronics Packaging Manufacturing*, 27(3):157–163, 2004.

[102] R. Zengerle, J. Ducree, and P. Koltay. Microfluidics: pipetting, dispensing and microarrays. *FSRM-Course*, pages 12–14, 2001.

[103] J. Brunahl and A. M. Grishin. Piezoelectric shear mode drop-on-demand inkjet actuator. *Sensors and Actuators*, A101(3):371–382, 2002.

[104] P.-H. Chen, H.-Y. Peng, H.-Y. Liu, S.-L. Chang, T.-I. Wu, and C.-H. Cheng. Pressure response and droplet ejection of a piezoelectric inkjet printhead. *International Journal of Mechanical Sciences*, 41(2):235–248, 1999.

[105] T. Laurell, L. Wallman, and J. Nilsson. Design and development of a silicon microfabricated flow-through dispenser for on-line picolitre sample handling. *Journal of Micromechanics and Microengineering*, 9(4):369–376, 1999.

[106] P. Luginbuhl, P.-F. Indermuhle, M.-A. Grtillat, F. Willemin, N. F. de Rooij, D. Gerber, G. Gervasio, J.-L. Vuilleumer, D. Twerenbold, M. Duggelin, D. Mathys, and R. Guggenheim. 'Femtoliter injector for DNA mass spectrometry.

[107] J. Bergkvist, T. Lilliehorn, J. Nilsson, S. Johansson, and T. Laurell. Miniaturized flowthrough microdispenser with piezoceramic tripod actuation. *Journal of Microelectromechanical Systems*, 14(1):134–140, 2005.

[108] K.H. Lam, H. L. W. Chan, H. S. Luo, Q. R. Yin, and Z. W. Yin. Piezoelectrically actuated ejector using PMNPT single crystal. *Sensors and Actuators*, A121(1): 197–202, 2005.

[109] W. Streule, T. Lindemann, G. Birkle, R. Zengerle, and P. Koltay. PipeJet: a simple disposable dispenser for the nano- and microliter range. *Journal of the Association for Laboratory Automation*, 9(5):300–306, 2004.

[110] D. Westberg and G. I. Andersson. A novel cmos-compatible inkjet head. *presented at the International Conference on Solid State Sensors and Actuators, 1997. Transducers '97*, 2:813 - 816, 1997.

[111] S. A. Curry and H. Portig. Scale model of an ink jet. *IBM Journal of Research and Development*, 21(1):10–20, 1977.

[112] R. H. Darling, C.-H. Lee, and L. Kuhn. Multiple-nozzle ink jet printing experiment. *IBM Journal of Research and Development*, 28(4):300–306, 1984.

[113] J. E. Fromm. Numerical calculation of the fluid dynamics of drop-on-demand jets. *IBM Journal of Research and Development*, 28(3):322–333, 1984.

[114] F.-G. Tseng, C.-J. Kim, and C.-M. Ho. A novel microinjector with virtual chamber neck. *presented at The Eleventh Annual International Workshop on Micro Electro Mechanical Systems, MEMS 98*, pages 57–62, 1998.

[115] F.-G. Tseng, C.-J. Kim, and C.-M. Ho. A high-resolution high-frequency monolithic top-shooting microinjector free of satellite drops - part i: concept, design, and model. *Journal of Microelectromechanical Systems*, 11(5):427–436, 2002.

[116] F.-G. Tseng, C.-J. Kim, and C.-M. Ho. A high-resolution high-frequency monolithic top-shooting microinjector free of satellite drops - part ii: fabrication, implementation, and characterization. *Journal of Microelectromechanical Systems*, 11(5):437–447, 2002.

[117] S. S. Baek, B. Choi, and Y. Oh. Design of a high-density thermal inkjet using heat transfer from CVD diamond. *Journal of Micromechanics and Microengineering*, 14(5):750–760, 2004.

[118] K. D. Bae, S. S. Baek, H. T. Lim, K. Kuk, and K. C. Ro. Development of the new thermal inkjet head on SOI wafer. *Microelectronic Engineering*, 78-79:158–163, 2005.

[119] P.-H. Chen, W.-C. Chen, P.-P. Ding, and S. H. Chang. Droplet formation of a thermal sideshooter inkjet printhead. *International Journal of Heat and Fluid Flow*, 19(4):382–390, 1998.

[120] P.-H. Chen, W.-C. Chen, and S.-H. Chang. Bubble growth and ink ejection process of a thermal ink jet printhead. *International Journal of Mechanical Sciences*, 39 (6):683–695, 1997.

[121] Ferrotec. URL `https://www.ferrotec.com/`.

[122] P. Koltay, R. Steger, B. Bohl, and R. Zengerle. The dispensing well plate: a novel nanodispenser for the multiparallel delivery of liquids (DWP Part I). *Sensors and Actuators*, A116(3):483–491, 2004.

[123] J. Ducree, H. Gruhler, N. Hey, M. Muller, S. Bekesi, M. Freygang, H. Sandmaiser, and R. Zengerle. Topspot-a new method for the fabrication of microarrays. *presented at the Thirteenth Annual International Conference on Micro Electro Mechanical Systems, MEMS 2000*, pages 317–322, 2000.

[124] B. de Heij, C. Steinert, H. Sandmaier, and R. Zengerle. A tuneable and highly-parallel picolitre-dispenser based on direct liquid displacement. *Sensors and Actuators*, A103(1-2):88–92, 2003.

[125] P. Koltay, B. Bohl, S. Taoufik, R. Steger, S. Messner, H. Sandmaier, and R. Zengerle. Dispensing well plate (DWP): a highly integrated nanoliter dispensing system. *presented at the 12th International Conference on Transducers, Solid-State Sensors, Actuators and Microsystems*, 1:16–19, 2003.

[126] F. Takagi, R. Kurosawa, D. Sawaki, S. Kamisuki, M. Takai, K. Ishihara, and M. Atobe. Pico liter dispenser with 128 independent nozzles for high throughput biochip fabrication. *presented at the 17th IEEE International Conference on Micro Electro Mechanical Systems (MEMS)*, pages 276–279, 2004.

[127] K. Handique, D. T. Burke, C. H. Mastrangelo, and M. A. Burns. Nanoliter-volume disctrete drop injection and pumping in microfabrificated chemical analysis system. *presented at Solid-State Sensor and Actuation Workshop, South Carolina*, June 1998.

[128] K. Handique, D. T. Burke, C. H. Mastrangelo, and M. A. Burns. Nanolitre liquid metering in microchannels using hydrophobic patterns. *Analytical Chemistry*, 72 (17):4100–4109, 2000.

[129] K. Handique, D. T. Burke, C. H. Mastrangelo, and M. A. Burns. On-chip thermopnuematic pressure for discrete drop pumping. *Analytical Chemistry*, 73(8): 1831–1338, 2001.

[130] M. A. Burns, C. H. Mastrangelo, T. S. Sammarco, F. P. Man, J. R. Webster, B. N. Johnson, B. Foerster, D. Jones, Y. Fields, A. R. Kaiser, and D. T. Burke. Microfabricated structures for integrated DNA analysis. *Proceedings of the National Academy of Sciences of the United States of America*, 93(11):5556–5561, 1996.

[131] M. A. Burns, B. N. Johnson, S. N. Brahmasandra, K. Handique, J. R. Webster, M. Krishnan, T. S. Sammarco, P. M. Man, D. Jones, D. Heldsinger, C. H. Mastrangelo, and D. T. Burke. An integrated nanoliter DNA analysis device. *Science*, 282(5388):484–487, 1998.

[132] K. Hosokawa, T. Fujii, and I. Endo. Handling of picoliter liquid samplers in a poly(dimethylsiloxane)-based picorfluidic device. *Analytical Chemistry*, 71(20): 4781–4785, 1999.

[133] K Hosokawa, T Fujii, and I Endo. Formation and active mixing of metered nano/picoliter liquid droplets in a microfluidic device. *presented at the 4th International Syposium on Micro Total Analysis Systems (uTAS 2000)*, 2000.

[134] K Hosokawa, T Fujii, and I Endo. Droplet-based nano/picoliter mixer using hydrophobic microcapillary vent. *presented at the 4th International Symposium on Micro Total Analysis Systems (uTAS 2000)*, May 2000.

[135] J. Melina, N. Roxhed, G. Gimenez, P. Griss, W. van der Wijngaart, and G. Stemme. A liquid-triggered liquid microvalve for on-chip flow control. *Sensors and Actuators*, B100(3):463–468, 2004.

[136] T. Ohori, S. Shoji, K. Miura, and A. Yotsumoto. Partly disposable three-way microvalve for a medical micro total analysis system (μTAS). *Sensors and Actuators*, A64.

[137] N. Vandelli, D. Wroblewski, M. Velonis, and T. Bifano. Development of a MEMS microvalve array for fluid flow control. *Journal of Microelectromechanical Systems*, 7(4):395–403, 1998.

[138] P. K. Xuen, L. J. Kricka, and P. Wilding. Semi-disposable microvalves for use with microfabricated devices or microchips. *Journal of Micromechanical and Microengineering*, 10(4):401–409, 2000.

[139] P. M. Pilarskia, S. Adamiab, and C. J. Backhouse. An adaptable microvalving system for on-chip polymerase chain reactions. *Journal of Immunological Methods*, 305(1):48–58, 2005.

[140] W. H. Grover, A. M. Skelley, C. N. Liu, E. T. Lagally, and R. A. Mathies. Monolithic membrane valves and diaphragm pumps for practical large-scale integration into glass microfluidic devices. *Sensors and Actuators*, B89(3):315–323, 2003.

[141] M. Capanu, J. G. Boyd, and P. J. Hesketh. Design, fabrication, and testing of a bistable electromagnetically actuated microvalve. *Journal of Microelectromechanical Systems*, 9(2):181–189, 2000.

[142] S. Bohm, G. J. Burger, M. T. Korthorst, and F. Roseboom. A micromachined silicon valve driven by a miniature bi-stable electro-magnetic actuator. *Sensors and Actuators*, A80(1):77–83, 2000.

[143] E. T. Carlen and C. H. Mastrangelo. Surface micromachined paraffin-actuated microvalve. *Journal of Microelectromechanical Systems*, 11(5):408–420, 2002.

[144] B. J. Kirby, T. J. Shepodd, and E. F. Hasselbrink. Voltage-addressable on / off microvalves for high-pressure microchip separations. *Journal of Chromatography*, 979:147–154, 2002.

[145] A. Menz, W. Benecke, R. Perez-Castillejos, J. A. Plasza, J. Esteve, N. Garcia, J. Higuero, and T. Diez-Caballero. Fluidic components based on ferrofluids. *presented at the 1st Annual International, Conference On Microtechnologies in Medicine and Biology 2000*, 2000.

[146] Invitrogen. URL `https://www.invitrogen.com/`.

[147] B. I. Bleaney and B. Bleaney. *Electricity and magnetism*. Oxford University Press, 1976.

[148] J. A. Olsen. Small beads make big medicine. *Gemini,*, 1993/1994. URL `http://www.ntnu.no/gemini/1993-dec/34.html/`.

[149] Seradyn. URL `http://www.seradyn.com/`.

[150] Polyscience. URL `http://www.polysciences.com/`.

[151] M. Zborowski, L. Sun, L. R. Moore, P. S. Williams, and J. J. Chalmers. Continuous cell separation using novel magnetic quadrupole flow sorter. *Journal of Magnetism and Magnetic Materials*, 194(1-3):224–230, 1999.

[152] L. Lagae, R. Wirix-Speetjens, C. X. Liu, W. Laureyn, G. Borghs, S. Harvey, P. Galvin, H. A. Ferreira, D. L. Graham, P. P. Freitas, L. A. Clarke, and M. D. Amaral. Magnetic biosensors for genetic screening of cystic fibrosis. *IEE Proceedings on Circuits, Devices and Systems*, 152(4):393–400, 2005.

[153] G. Fonnum, C. Johansson, A. Molteberg, S. Mrup, and E. Aksnes. Characterisation of Dynabeads by magnetization measurements and Mssbauer spectroscopy. *Journal of Magnetism and Magnetic Materials*, 293(1):41–47, 2005.

[154] F. Ilievski, T. Tepper, and C. A. Ross. Optical and magnetic properties of γ-iron oxide made by reactive pulsed laser deposition. *Transactions on Magnetics*, 39(5): 3172–3174, 2003.

[155] C. P. Hunt, B. M. Moskowitz, and S. K. Banerjee. Magnetic properties of rocks and minerals. *American Geophysical Union*, pages 189–204.

[156] A. O. Ivanov and O. B. Kuznetsova. Magnetic properties of dense ferrofluids. *Journal of Magnetism and Magnetic Materials*, 252:3172–3174, 2002.

[157] N. Minc, C. Ftterer, K. D. Dorfman, A. Bancaud, C. Gosse, C. Goubault, and J.-L. Viovy. Quantitative microfluidic separation of DNA in self-assembled magnetic matrixes. *Analytical Chemistry*, 76(13):3770–3776, 2004.

[158] N. Minc, P. Bokov, K. B. Zeldovich, C. Ftterer, J.-L. Viovy, and K. D. Dorfman. Motion of single long DNA molecules through arrays of magnetic columns. *Electrophoresis*, 26(2):362–375, 2005.

[159] T. C. Hales. A proof of the kepler conjecture. *Annals of Mathematics*, 162(3): 1065–1185, 2005.

[160] C. S. Lee, H. Lee, and R. M. Westervelt. Microelectromagnets for the control of magnetic nanoparticles. *Applied Physics Letters*, 79(20):3308–3310, 2001.

[161] J.-W. Choi, C. H. Ahn, S. Bhansali, and H. T. Henderson. A new magnetic bead-based, filterless bio-separator with planar electromagnet surfaces for integrated bio-detection systems. *Sensors and Actuators*, B68(1-3):34–39, 2000.

[162] C. H. Ahn, M. G. Allen, W. Trimmer, Y.-N. Jun, and S. Erramilli. A fully integrated micromachined magnetic particle separator. *Journal of Microelectromechanical Systems*, 5(3):151–158, 1996.

[163] J.-W. Choi, T. M. Liakopoulos, and C. H. Ahn. An on-chip magnetic bead separator using spiral electromagnets with semi-encapsulated permalloy. *Journal of Biosensors and Bioelectronics*, 16(6):409–416, 2001.

[164] T. Deng, G. M. Whitesides, M. Radhakrishnan, G. Zabow, and M. Prentiss. Manipulation of magnetic microbeads in suspension using micromagnetic systems fabricated with soft lithography. *Applied Physics Letters*, 78(12):17751777, 2001.

[165] K. Smistrup, P. T. Tang, O. Hansen, and M. F. Hansen. Microelectromagnet for magnetic manipulation in lab-on-a-chip systems. *Journal of Magnetism and Magnetic Materials*, 300(2):418–426, 2006.

[166] M. N. O. Sadiku. *Elements of electromagnetics*. Saunders College Publishing, 1994.

[167] J. Joung, J. Shen, and P. Grodzinski. Micropumps based on alternating high-gradient magnetic fields. *Transactions on Magnetics*, 36(4):2012–2014, 2000.

[168] M. A. Hayes, N. A. Polson, and A. A. Garcia. Active control of dynamic supra-particle structures in microchannels. *Langmuir*, 17:2866–2871, 2001.

[169] M. A. Hayes, N. A. Polson, A. N. Phayre, and A. A. Garcia. Flow-based microimmunoassay. *Analytical Chemistry*, 73(24):5896–5902, 2001.

[170] P. S. Doyle, J. Bibette, A. Bancaud, and J.-L. Viovy. Self-assembled magnetic matrices for DNA separation Chips. *Science*, 295(5563):2237, 2002.

[171] A. Rida, V. Fernandez, and M. A. M. Gijs. Planar coil-based microsystem for the long-range transport of magnetic beads. *presented at Solid-State Sensors, Actuators and Microsystems, 12th International Conference on Transducers*, pages 292–295, 2003.

[172] T. M. Liakopoulos, J.-W Choi, and C. H. Ahn. A bio-magnetic bead separator on glass chips using semi-encapsulated spiral electromagnets. *presented at the International Conference on Solid State Sensors and Actuators*, 1:485–488, 1997.

[173] A.-L. Coutrot, E. Dufour-Gergam, E. Martincic, J.-P. Gilles, J.-P. Grandchamp, J.-M. Quemper, A. Bosseboeuf, F. Alves, and B. Ahamada. Electromagnetic micro-device realized by electrochemical way. *Sensors and Actuators*, A91(1-2): 80–84, 2001.

[174] B. Wagner, M. Kreutzer, and W. Benecke. Permanent magnet micromotors on silicon substrates. *Journal of Microelectromechanical Systems*, 2(1):23–29, 1993.

[175] N. Yamada, Y. Yokoyama, and H. Tanaka. Fabrication of wrapped micro coils wound around a magnetic core. *presented at the 8th international conference on Solid state sensors and actuators and EurosensorsIX, Stockholm, Sweden*, June 1995.

[176] D. Sadler, T. M. Liakapoulos, and C. H. Ahn. A universal electromagnetic microactuator using magnetic interconnection concepts. *Journal of Microelectromechanical Systems*, 9(4):460–468, 2000.

[177] T. Velten, D. Stefan, and E. Obermeier. Micro-coil with movable core for application in an inductive displacement sensor. *Journal of Microelectromechanics and Microengineering*, 9(2):119–122, 1999.

[178] J.-B. Yoon, B.-I. Kim, Y.-S. Choi, and E. Yoon. 3-D construction of monolithic passive components for RF and microwave ICs using thick-metal surface micro machining technology. *Transactions on Microwave Theory and Techniques*, 51(1): 279–288, 2003.

[179] C. H. Ahn and M.G. Allen. A planar micromachined spiral inductor for integrated magnetic microactuator applications. *Journal of Micromechanics and Microengineering*, 3(2):37–44, 1993.

[180] D. J. Sadler, S. Gupta, and C. H. Ahn. Micromachined spiral inductors using UV-LIGA techniques. *Transactions on Magnetics*, 37(4):2897 –2899, 2001.

[181] M. Sclesinger and M. Paunovic. *Modern Electroplating*. John Wiley and Sons, INC., 2000.

[182] B. Margesin, A. Bagolini, V. Guarnieri, F. Giacomozzi, A. Faes, R. Pal, and M. Decarli. Stress characterization of electroplated gold layers for low temperature surface micromachining. *presented at a Symposium on Design, Test, Integration and Packaging of MEMS/MOEMS 2003*, pages 402–405, 2003.

[183] J. D. Jackson. *Fundamentals of electrochemical deposition.* John Wiley & Sons, 1998.

[184] T. Inoue, Y. Hamsaki, I. Shimoyama, and H. Mirua. Micromanipulation using a microcoil array. *presented at the IEEE International Conference on Robotics and Automation, Minneapolis, Minnesota*, pages 2208–2213, 1996.

[185] J. Do, J.-W. Choi, and C. H. Ahn. Low-cost magnetic interdigitated array on a plastic wafer. *Transactions on Magnetics*, 40(4):3009–3011, 2004.

[186] K. Smistrup, O. Hansen, H. Bruus, and M. F. Hansen. Magnetic separation in microfluidic systems using microfabricated electromagnetsexperiments and simulations. *Journal of Magnetism and Magnetic Materials*, 293(1):597–604, 2005.

[187] K. R. Williams, K. Gupta, and M. Wasilik. Etch rates for micromachining processing-partii. *Journal of Microelectromechanical Systems*, 12(6):761–778, 2003.

[188] J. Happel and H. Brenner. *Low reynolds number hydrodynamics.* Martinus Nijhoff Publisher, 1983.

[189] A. Pralle, E. L. Florin, E. H. K. Stelzer, and J. K. H. Hrber. Local viscosity probed by photonic force microscopy. *Applied Physics*, A66:S71S73, 1998.